

Theoretical and experimental study of spin-1 antiferromagnetic Bose-Einstein Condensates

Lingxuan Shao

▶ **To cite this version:**

Lingxuan Shao. Theoretical and experimental study of spin-1 antiferromagnetic Bose-Einstein Condensates. Quantum Gases [cond-mat.quant-gas]. Ecole Normale Supérieure, 2014. English. NNT : . tel-01104387

HAL Id: tel-01104387
https://theses.hal.science/tel-01104387

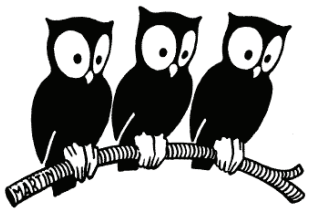
Submitted on 16 Jan 2015

HAL is a multi-disciplinary open access archive for the deposit and dissemination of scientific research documents, whether they are published or not. The documents may come from teaching and research institutions in France or abroad, or from public or private research centers.

L'archive ouverte pluridisciplinaire **HAL**, est destinée au dépôt et à la diffusion de documents scientifiques de niveau recherche, publiés ou non, émanant des établissements d'enseignement et de recherche français ou étrangers, des laboratoires publics ou privés.

DÉPARTEMENT DE PHYSIQUE
DE L'ÉCOLE NORMALE SUPÉRIEURE

LABORATOIRE KASTLER BROSSEL





THESE DE DOCTORAT DE L'ÉCOLE NORMALE SUPÉRIEURE

Spécialité: Physique Quantique

présentée par

Lingxuan SHAO

pour obtenir le grade de

DOCTEUR de L'ÉCOLE NORMALE SUPÉRIEURE

Theoretical and experimental study of spin-1 antiferromagnetic Bose-Einstein Condensates

---

Devant être soutenue le 4 juillet 2014
devant le jury composé de :

Mme Anna MINGUZZI	Rapporteur
M. Daniel COMPARAT	Rapporteur
M. Denis BOIRON	Examinateur
M. Thomas COUDREAU	Examinateur
M. Jean DALIBARD	Directeur de Thèse

Contents

Contents **3**

Introduction **7**

1 Mean-field theory of spinor Bose-Einstein Condensates **11**
1.1 Introduction . . . 11
1.2 Elements for scalar condensate . . . 12
1.2.1 The ideal Bose gas . . . 12
1.2.2 Bose gas with interactions . . . 14
1.2.3 Calculation for scalar interacting Bose gas . . . 17
1.3 Spinor BEC : Pure condensate at zero temperature . . . 20
1.3.1 Hyperfine structure of ^{23}Na . . . 20
1.3.2 Hamiltonian of the interacting spin-1 Bose gas . . . 20
1.3.3 Mean-field approach to the spinor Hamiltonian - H_{SMA} . . . 25
1.4 Spinor BEC : Condensate with thermal cloud at finite temperature . . . 27
1.4.1 Semi-ideal HF approximation for spinor BEC . . . 28
1.4.2 Simulation results for $m_z = 0$ . . . 29
1.5 Conclusion . . . 33

2 Experimental realization and diagnosis of spinor Bose-Einstein Condensates **35**
2.1 Introduction . . . 35
2.2 Vacuum system and experimental control . . . 36
2.3 Evaporative cooling to BEC . . . 36
2.3.1 Elements of evaporative cooling . . . 38
2.3.2 Experimental setup of the Small-CDT . . . 39
2.3.3 Two-step evaporation . . . 40
2.4 Spinor condensate preparation and diagnosis . . . 43
2.4.1 Magnetic field control . . . 43
2.4.2 Magnetization controlled spinor gas preparation . . . 45
2.4.3 Spin diagnosis . . . 47
2.5 Imaging . . . 49
2.5.1 Absorption imaging . . . 51
2.5.2 Imaging systems . . . 52
2.5.3 Kinetics mode . . . 53
2.6 Image analysis . . . 55

2.6.1 Fitting . . . 55
2.6.2 Counting spin populations . . . 58
2.6.3 Imaging noises . . . 58
2.6.4 Methods to reduce structural noise . . . 60
2.7 Conclusion . . . 63

3 Phase diagram of spin 1 antiferromagnetic Bose-Einstein condensates 65
3.1 Introduction . . . 65
3.2 Experimental configuration . . . 67
3.3 Experimental results and interpretation . . . 68
3.4 Conclusion and perspectives . . . 72

4 Collective fluctuations of spin-1 antiferromagnetic Bose-Einstein condensates 75
4.1 Introduction . . . 75
4.2 Quantum analysis of a spin-1 antiferromagnetic BEC . . . 78
4.2.1 Formulation in the basis of total spin eigenstates $|N, S, M\rangle$ . . . 78
4.2.2 Thermal equilibrium for $\langle \hat{S}_z \rangle = 0$ . . . 82
4.2.3 Broken-symmetry approach . . . 84
4.3 Generalization to arbitrary distribution of M . . . 88
4.4 Hartree-Fock Approach . . . 90
4.4.1 Semi-ideal Hartree Fock approximation for spinor BEC . . . 92
4.4.2 Simulation results and analysis . . . 93
4.5 Analysis of experimental results . . . 97
4.5.1 Data analysis . . . 97
4.5.2 Experimental results of temperature during evaporation . . . 98
4.5.3 Experimental results of temperature during hold time . . . 100
4.5.4 Fluctuation of magnetization Δm_z at $q = 0$ . . . 101
4.6 Discussion of the results . . . 104
4.7 Conclusion . . . 105

Conclusion and perspectives 107

A Magneto-Optical Trap (MOT) 111
A.1 Elements of Doppler cooling and MOT . . . 111
A.2 589 nm laser system . . . 113
A.3 Sodium MOT . . . 115

B Loading the Large Crossed Dipole Trap (Large-CDT) 117
B.1 Elements of optical dipole traps . . . 118
B.2 Experimental setup . . . 119
B.2.1 Configuration of the Large-CDT . . . 119
B.2.2 Feedback system of the Large-CDT . . . 120
B.3 Loading the Large Crossed Dipole Trap . . . 122
B.3.1 Optimization of the MOT lasers . . . 122
B.3.2 Optimization of the Large-CDT power . . . 123
B.4 Compression in the Large-CDT . . . 124

C Supplementary Material : Phase diagram of spin 1 antiferromagnetic Bose-Einstein condensates **127**
C.1 Sample preparation 127
C.2 Stern-Gerlach expansion 128
C.3 Spin interaction energy 129
C.4 Conservation of magnetization 130

D Calculation details for Broken symmetry picture **133**
D.1 Spin nematic states $|N : \mathbf{\Omega}\rangle$ 133
D.2 Calculation of $\hat{\rho}$ in section 4.3 133
D.3 Fluctuation of magnetization Δm_z at $q = 0$ 135

E Published articles **137**

Bibliography **157**

Introduction

Bose Einstein condensation (BEC) is a statistical phenomena which was first predicted in 1925 by A.Einstein [1, 2] based on the work of S.N.Bose. Below a certain critical temperature T_c, macroscopic number of atoms will occupy the ground state of the system, leading to a macroscopic quantum state. This condensation caused directly by the quantum statistics of Bosons, Bose-Einstein statistics, can happen even in the system without inter-atomic interactions [3]. However, the extremely low critical temperature T_c makes BEC very difficult to realize. In 1980s, with the help of the techniques of laser cooling, alkali atoms are first time cooled below milli-Kelvin, which makes a large step towards BEC. S. Chu, C. Cohen-Tannoudji and W. D. Phillips are awarded Nobel Prize for physics in 1997 for this contribution [4, 5, 6]. In 1995, combining the laser cooling and the evaporative cooling techniques, BEC is realized in dilute gases of alkali atoms in JILA [7] and MIT [8]. In 2001, E. Cornell, W. Ketterle and C. Wieman are awarded Nobel Prize for physics for this achievement [9, 10].

The realization of the Bose-Einstein condensation in ultra-cold dilute gases not only achieves the prediction by Bose and Einstein in 1905, more importantly, this new macroscopic quantum state opens a large area of research [11, 12]. Compare to the other macroscopic quantum systems, *e.g.* ^{4}He superfluid, the ultra-cold dilute gases have several distinct features. First, ultra-cold dilute gas is a weakly-interacting system. The inter-atomic interactions can be modelized by a single parameter, the scattering length a [3, 12]. This weakly-interacting system can be well described by Bogoliubov mean-field theory, which is proved to be very effective in describing many aspects of the condensate, for instance, the density distribution, the excitation modes, and the vortices [3, 12]. Second, the inter-atomic interactions can be tuned by Feshbach resonance [13, 14, 15]. This allows one to reach the strongly correlated regime by increasing the scattering length a [16, 17] or even change the nature of the interactions (repulsive or attractive) [16]. Finally, various kinds of atoms are suitable for the formation of BEC [7, 8, 18, 19, 20, 21, 22, 23], which gives many choices for the experiments. Besides the realization of the Bose-Einstein condensation in ultra-cold Bose gases, ultra-cold Fermi gases [24] and molecule condensation are also studied [25].

In this thesis, we focus on the so-called spinor condensate, which is a condensate with multiple internal degrees of freedom, spin [26]. Early experimental work on the spinor condensate in ultracold Bose gases started in 1998 [27, 28], followed by theoretical analysis on the spin-1 interacting Bose gases [29, 30]. Using an optical trap, all sub-Zeeman levels of a certain hyperfine state can be trapped, independent with the spin states. Because of this supplementary degree of freedom, the interaction with external magnetic

field is important in the spinor condensate system. The interplay between the internal interactions between atoms and the interaction with external field provides rich physics to study, such as spin texture [28], coherent spin mixing dynamics [31], *etc.* In our experiment, we work with ^{23}Na atoms, total spin $F = 1$ in the hyperfine ground states with 3 Zeeman sub-levels, $m_F = (+1, 0, -1)$. We concentrate mainly on two aspects: the phase diagram of spin-1 condensate and collective spin fluctuations. The later needs a many-body quantum analysis, instead of the mean-field theory, which describes very well most of the experiments.

Plan of thesis

This thesis consists of 4 chapters.

In chapter 1, we introduce the basic theory of the spinor Bose-Einstein condensate in our experiment. We begin with the simple scalar case and then introduce the spinor case. We concentrate, in this chapter, on the mean-field description of the condensate which agrees well with most of the experiments [3] and a more detailed theory will be discussed in chapter 4. Briefly speaking, according to mean-field approach, the condensate can be described by an order parameter $\Phi(\mathbf{r})$ (in spin-1 case, the order parameter is a 3 component vector $(\Phi_{+1}(\mathbf{r}), \Phi_0(\mathbf{r}), \Phi_{-1}(\mathbf{r}))$), obeying the Gross-Pitaevskii equation, which determines the properties of the condensate. Moreover, in our experiment, it is reasonable to apply the single mode approximation, which decouples the spin and the spatial degrees of freedom and supposes all spin components share the same spatial wave function. We predict a phase transition for the condensate, which will be studied experimentally in chapter 3. However, at finite temperature, the thermal atoms are always present. We use the so-called semi-ideal Hartree-Fock approximation [3], which neglects the correlations between the condensate and the thermal cloud, to calculate the distributions of the condensate and the thermal cloud in each spin state ($m_F = +1, 0, -1$) with the presence of the interactions between condensate and thermal cloud. In fact, in this thesis, we always use this approximation to describe the system when both condensate and thermal cloud are present.

In chapter 2, we introduce step by step how we realize, control, detect and analyze our spin-1 Bose-Einstein condensate. The realization of BEC takes several steps, including the cooling in the Magneto-Optical Trap (MOT), compression and evaporation in dipole traps. At the end of the evaporation, we obtain an almost pure condensate with about 5000 atoms in the trap. We explain how to use spin distillation and depolarization process to control the magnetization m_z between 0 and 0.9 ($m_z = n_{+1} - n_{-1}$)[1], which is important for the phase diagram experiment described in chapter 3. Finally, we introduce several methods to reduce the noise of the absorption image and the model to analyze the image, from which we can get important informations, including total atom number, temperature, condensate fraction, *etc.*

[1] we denote N_i ($i = +1, 0, -1$) the atom number in $m_F = i$ state, and $n_i = N_i/N$ the relative atom number in $m_F = i$ state, with $N = N_{+1} + N_0 + N_{-1}$ the total atom number

In chapter 3, we study the phase diagram of the spinor gas at very low temperatures, where the atomic sample is purely condensed. We observe a phase transition between a so-called antiferromagnetic phase, which is characterized by the absence of the $m_F = 0$ component, and a so-called broken-asymmetry phase, which is characterized by the presence of the $m_F = 0$ component. When comparing with the SMA theory of chapter 1, we find a good agreement between the mean-field theory prediction in chapter 1 and our experiment. We also remark abnormal large fluctuations at low magnetic fields and low magnetizations. In fact, these large fluctuations, which can not be explained by the mean-field theory, is the subject in the next chapter.

In chapter 4, we study the large collective fluctuations mentioned in chapter 3 both in theory and in experiment. We first give a quantum analysis (replacing the mean-field solution in chapter 1) of SMA Hamiltonian $\hat{H}_{\mathrm{SMA}}$, which describes the condensate. We develop a so-called "broken symmetry approach", precise enough compared with the exact diagonalization and much faster. However, two major differences are noticed between the SMA theory and the experimental measurements. Therefore, we generalize the SMA theory by generalizing the distribution of magnetization and taking the thermal atoms into account, which use the semi-ideal Hartree-Fock approximation introduced in chapter 1. We plot, as in chapter 1, $1 - \langle n_0 \rangle$ as a function of q, additionally we also plot Δn_0 as a function of q. These curves give many important information of the system, including the temperature, the condensate fraction, *etc.* We use the theory developed above to fit the $1 - \langle n_0 \rangle$ and Δn_0 curves measured in the experiment and obtain the temperatures and condensate fraction of our system. We find that the "spin temperature" is much smaller than the "kinetic temperature" and we discuss the possible reasons in the end.

Chapter 1

Mean-field theory of spinor Bose-Einstein Condensates

1.1 Introduction

Bose-Einstein condensation is a phase transition predicted by Einstein in 1924 [1, 2]. A macroscopic number of atoms occupy the fundamental state of the system when they are cooled down below certain critical temperature [32]. This phenomena is a perfect illustration of quantum statistics: Bose-Einstein statistics in this case. After 71 years of the prediction, in 1995, Bose-Einstein condensation was first time realized in dilute gases by E. Cornell, C. Wieman, and W. Ketterle [7, 8, 18].

Ordinary Bose-Einstein condensate (BEC), or scalar BEC, is a BEC with only one component. This kind of BEC can be described by a scalar wave function (order parameter) $\phi(r)$ [3]. In the first realizations of BEC experiments, magnetic traps are generally adopted to cool down and conserve the cold atoms. In fact, the magnetic trap conserves only the atoms in the so-called "weak field seeking" hyperfine states [33, 34]. As a result, the internal degree of freedom, spin, is frozen. This is an example of scalar BEC. A spinor BEC is a condensate with multiple internal degrees of freedom, spin [26]. With the help of far-off resonance optical traps, which interact with atoms almost spin independently, all spin states can be conserved in the trap [28]. Spinor BEC, can be described by a vector wave function (order parameter) which consists of several components. In our experiment, the atoms of sodium are in $F = 1$ $m_F = \{+1, 0, -1\}$ hyperfine spin state [35]. As a result, the condensate is described by a three components vector $(\phi_{+1}, \phi_0, \phi_{-1})$, each component corresponds to one of the Zeeman sub-levels.

In this chapter, we focus on the theory of the BEC, especially the mean-field theory which agrees very well with most of our experiments [3]. We begin with the theory of the scalar BEC in section 1.2, first in ideal case then in the case with interactions. We calculate the critical temperature and condensate fraction in both cases. At finite temperature, the thermal atoms are always present in addition to the BEC. We describe the interactions between thermal atoms and the condensate by the "semi-ideal" Hartree-Fock approximation [36, 37, 3]. This approximation will also be adopted for spinor gases as well. In section 1.3, we turn to the spinor BEC at zero temperature. First, we give a brief

introduction to the energy structure of the atom, ^{23}Na, which we use in the experiment, and we write down explicitly the Hamiltonian of our system including the spin-dependent interactions between atoms and the Zeeman effects in a magnetic field B. Then we use the mean-field approach to calculate the behavior of the spinor condensate in response to the magnetic field and predict the existence of a phase transition [38]. In the last section, we use the "semi-ideal" Hartree-Fock method mentioned above to calculate the properties of the spinor gas at finite temperatures. We will focus on the atom number in each Zeeman states ($m_F = +1, 0, -1$) state as a function of the magnetic field, which is easy to measure in the experiment, and reveals many informations of our spinor condensate system.

1.2 Elements for scalar condensate

1.2.1 The ideal Bose gas

We begin with the ideal Bose gas, which means we neglect the interactions between atoms. In the experiment, atoms are normally confined in a trap which can be magnetic or optical. The trap can be well approximated by the harmonic potential nearby the minimum of the trap [12]:

$$V_{\text{ext}}(\mathbf{r}) = \frac{1}{2}m(\omega_x^2 x^2 + \omega_y^2 y^2 + \omega_z^2 z^2). \tag{1.1}$$

Here m denotes the mass of the atom, ω_i with $i = (x, y, z)$ the pulsation in (x, y, z) directions. Since we consider Bose gas without interactions, the many-body Hamiltonian is simply the sum of N harmonic oscillator Hamiltonian

$$H_{\text{sp}}(\mathbf{r}, \mathbf{p}) = \frac{\mathbf{p}^2}{2m} + V_{\text{ext}}(\mathbf{r}), \tag{1.2}$$

with single-particle eigenvalues

$$\varepsilon_{n_x n_y n_z} = (n_x + \frac{1}{2})\hbar\omega_x + (n_y + \frac{1}{2})\hbar\omega_y + (n_z + \frac{1}{2})\hbar\omega_z, \tag{1.3}$$

Here (n_x, n_y, n_z) are non-negative integers. The ground state $\phi(\mathbf{r}_1, ..., \mathbf{r}_N)$ for N noninteracting bosons is the product wave function $\phi(\mathbf{r}_1, ..., \mathbf{r}_N) = \prod_i \varphi_0(\mathbf{r}_i)$ [12], where the single-particle ground state $\varphi_0(\mathbf{r})$ is given by

$$\varphi_0(\mathbf{r}) = \Big(\frac{m\bar{\omega}}{\pi\hbar}\Big)^{3/4} \exp\Big(-\frac{x^2}{2\sigma_x^2} - \frac{y^2}{2\sigma_y^2} - \frac{z^2}{2\sigma_z^2}\Big). \tag{1.4}$$

Here $\bar{\omega} = (\omega_x\omega_y\omega_z)^{1/3}$, and $\sigma_i = \sqrt{\hbar/m\omega_i}$, with $i = x, y, z$.

If the temperature T is large compared with the level spacing (constant in the harmonic trap case), $k_B T \gg \hbar\omega_i$ $(i = x, y, z)$, we can adopt the "semi-classical" approximation which considers the atoms as classical particles possessing a position $\mathbf{r}$ and a momentum

$\mathbf{p}$ and evolving in the classical phase space. As a result, the phase space density function for bosons is determined by the Bose-Einstein distribution [3]:

$$f_{\mathrm{BE}}(\mathbf{r},\mathbf{p}) = \frac{1}{h^3}\cdot\frac{1}{e^{\beta(\varepsilon(\mathbf{r},\mathbf{p})-\mu)}-1}, \tag{1.5}$$

evaluated at the classic energy $\varepsilon(\mathbf{r},\mathbf{p}) = \mathbf{p}^2/2m + V_{\mathrm{ext}}(\mathbf{r})$, where $\beta = 1/k_BT$, and μ the chemical potential.

Integrating the phase space density distribution (Eq. (1.5)) over momentum space, we obtain the distribution only in the coordinate space which is the atom spatial density in the confining potential $V_{\mathrm{ext}}(\mathbf{r})$:

$$n_{\mathrm{th}}(\mathbf{r}) = \frac{1}{\Lambda_{\mathrm{db}}^3} g_{3/2}(e^{\beta(\mu - V_{\mathrm{ext}}(\mathbf{r}))}). \tag{1.6}$$

Integrating again the spatial density $n_{\mathrm{th}}(\mathbf{r})$ over the coordinate space. We obtain the total atom number:

$$N_{\mathrm{th}} = \int n_{\mathrm{th}}(\mathbf{r})\,\mathrm{d}^3\mathbf{r} = \Big(\frac{k_BT}{\hbar\bar{\omega}}\Big)^3 g_3(e^{\beta\mu}). \tag{1.7}$$

In Eq. (1.6) and (1.7), g_α denotes the Bose function defined by $g_\alpha(u) = \sum_{k=1}^{\infty} u^k/k^\alpha$, and $\Lambda_{\mathrm{dB}} = h/\sqrt{2\pi m k_B T}$ the thermal De Broglie wavelength.

In Eq. (1.7), we remark that N_{th} has a upper bound with $(N_{\mathrm{th}})_{\max} = g_3(1)(k_BT/\hbar\bar{\omega})^3$ (because the chemical potential $\mu < 0$). Once the temperature T is below certain critical temperature T_c, the exited states are saturated, which means a macroscopic number of atoms have to be "condensed" to the single-particle ground state. This phenomena is known as Bose-Einstein condensation, which is predicted originally by A. Einstein [2] base on the work of S. N. Bose [1]. Essentially, it is a phase transition between the "normal" phase and the "condensed" phase in which a macroscopic number of atoms occupy the single-particle ground state.

According to the discussions above, the phase transition temperature T_c^{id} ("id" denotes "ideal") is given by the condition $N = (N_{\mathrm{th}})_{\max}$, or :

$$k_BT_c^{\mathrm{id}} = \hbar\bar{\omega}\Big(\frac{N}{g_3(1)}\Big)^{1/3} \approx \hbar\bar{\omega}\Big(\frac{N}{1.202}\Big)^{1/3}. \tag{1.8}$$

Below T_c^{id}, atoms are condensed to the ground state. The condensate fraction f_c, which is the ratio between condensed atom number and the total atom number, is given by

$$f_c = \frac{N_c}{N} = 1 - \Big(\frac{T}{T_c^{\mathrm{id}}}\Big)^3. \tag{1.9}$$

We estimate the spatial size of the condensate and of the thermal cloud as follows. The size of the condensate is the size of the ground state (Eq. (1.4)):

$$R_c^{\mathrm{id}} \sim a_{\mathrm{ho}} \equiv \sqrt{\hbar/(m\bar{\omega})}. \tag{1.10}$$

The size of the thermal cloud (Eq. (1.6)) is

$$R_{\rm th}^{\rm id} \sim \sqrt{k_B T/(m\bar{\omega}^2)}. \tag{1.11}$$

As $k_B T \gg \hbar\bar{\omega}$, the thermal cloud is much more extended than the condensate.

Another important parameter is the phase space density which is defined as the product between thermal spatial density $n_{\rm th}(\mathbf{r})$ and the cubic power of the thermal De Broglie wavelength:

$$\mathcal{D}(\mathbf{r}) = n_{\rm th}(\mathbf{r})\Lambda_{\rm dB}^3. \tag{1.12}$$

At the critical point, the phase space density at the center of the trap

$$\mathcal{D}_c(0) = n(0)\Lambda_{\rm dB}^3(T_c^{\rm id}) = g_{3/2}(1) \approx 2.612. \tag{1.13}$$

It gives us a simple physical picture to better understand the Bose-Einstein condensation [33]. When distances between atoms approach the thermal De Broglie wavelength, the condensation begins, which also means strong statistical correlations between atoms. The picture of individual atoms appropriate to a thermal gas begins to be replaced by the picture of a macroscopic wave function which describes all the atoms in the condensate as a whole. This will be discussed in detail in the next few sections.

1.2.2 Bose gas with interactions

1.2.2.1 Definition, One-body density matrix

In section 1.2.1, we have discussed the ideal Bose gas. In a noninteracting system, the ground state of the whole system is simply the product of single-particle wave functions [12]. However, in the case of many interacting particles, the notion of a single-particle ground state is ill defined. We should re-define the Bose-Einstein condensation differently by the one-body density matrix [34, 3]

$$\rho_1(\mathbf{r}', \mathbf{r}, t) = \langle \hat{\Psi}^\dagger(\mathbf{r}', t)\hat{\Psi}(\mathbf{r}, t)\rangle. \tag{1.14}$$

Here, $\hat{\Psi}(\mathbf{r}, t)$, and $\hat{\Psi}^\dagger(\mathbf{r}, t)$ denote field annihilation and creation operator respectively.

The one-body density matrix is Hermitian. Therefore, it can be diagonalized with real eigenvalues as

$$\rho_1(\mathbf{r}', \mathbf{r}, t) = \sum_i n_i(t)\chi_i^*(\mathbf{r}', t)\chi_i(\mathbf{r}, t). \tag{1.15}$$

If one or more eigenvalues $n_i(t)$ is of the order of the total atom number N, the system undergoes *Bose-Einstein condensation*. If only one eigenvalue is of order N, it is a *scalar* BEC. If several eigenvalues are of order N, it is a *fragmented* BEC [39], which is the main subject of this thesis. There are many important aspects in the one-body density matrix such as long range order [3], but we will not discuss in detail here.

1.2.2.2 Interactions between atoms

Here, we recall briefly how to modelize the interactions between atoms. The interactions between atoms are in general very complicated. But for dilute cold atom gases, it can be simplified. Because of the low temperature of the gases, we can consider only the s-wave scattering, which is described by a single parameter, the s-wave scattering length a. Because of the diluteness of the gases, which satisfy $n|a|^3 \ll 1$, we can consider only the pair-wise interactions. As a result, the interaction potential between two atoms in $\mathbf{r}_1$ and $\mathbf{r}_2$ can be modelized by a contact potential V_{int}, and irrelevant with the detail of the interactions [40, 12].

$$V_{\text{int}}(\mathbf{r}_1, \mathbf{r}_2) = g\delta(\mathbf{r}_1 - \mathbf{r}_2), \tag{1.16}$$

where $g = 4\pi\hbar^2 a/m$ is obtained from the Born approximation, with δ the Dirac distribution. The interactions are repulsive if $a > 0$ and attractive if $a < 0$. In this thesis, we always consider $a > 0$.

The condition of diluteness $n|a|^3 \ll 1$ means the inter-atomic distances are large compared with scattering length. But it does *not* mean that the interactions are not important [12]. On the contrary, as we shall see later, the interactions change significantly the properties of the gas and *determine* the nature of the phase diagram for spinor gases.

1.2.2.3 Gross-Pitaevskii equation

The general Hamiltonian of interacting bosons confined by the external potential V_{ext} in second quantization representation is [3]:

$$\begin{aligned} \hat{H} = &\int \mathrm{d}^3\mathbf{r}\, \hat{\Psi}^\dagger(\mathbf{r})\Big[-\frac{\hbar^2}{2m}\nabla^2 + V_{\text{ext}}(\mathbf{r})\Big]\hat{\Psi}(\mathbf{r}) \\ &+ \frac{1}{2}\int \mathrm{d}^3\mathbf{r}\mathrm{d}^3\mathbf{r}'\, \hat{\Psi}^\dagger(\mathbf{r})\hat{\Psi}^\dagger(\mathbf{r}')\hat{V}_{\text{int}}(\mathbf{r}-\mathbf{r}')\hat{\Psi}(\mathbf{r}')\hat{\Psi}(\mathbf{r}), \end{aligned} \tag{1.17}$$

where $\hat{V}_{\text{int}}(\mathbf{r} - \mathbf{r}')$ is the interaction potential between two atoms.

The field operator $\hat{\Psi}(\mathbf{r})$ obeys the Heisenberg equation of motion:

$$i\hbar\frac{\partial}{\partial t}\hat{\Psi}(\mathbf{r}, t) = [\hat{\Psi}, \hat{H}]. \tag{1.18}$$

Assuming a condensate is present in the system, we can decompose the field operator $\hat{\Psi}(\mathbf{r}, t)$ as [3]

$$\hat{\Psi}(\mathbf{r}, t) \approx \Phi(\mathbf{r}, t) + \delta\hat{\Psi}(\mathbf{r}, t), \tag{1.19}$$

In Eq. (1.19), the field operator $\hat{\Psi}(\mathbf{r}, t)$ is decomposed into two parts. The *function* $\Phi(\mathbf{r}, t)$ is called the macroscopic wave function of the condensate and plays the role of an order parameter. This complex function is characterized by its modulus and phase [3]

$$\Phi(\mathbf{r}, t) = |\Phi(\mathbf{r}, t)|\mathrm{e}^{iS(\mathbf{r},t)}. \tag{1.20}$$

Its modulus fixes the condensate spatial density $n_c(\mathbf{r},t) = |\Phi(\mathbf{r},t)|^2$. The other term $\delta\hat{\Psi}(\mathbf{r},t)$ describes the non-condensate component. For very low temperature, as a zero-order approximation, we neglect the depletion term $\delta\hat{\Psi}(\mathbf{r},t)$. This is a reasonable approximation for small depletion of condensate (weak interaction $n|a|^3 \ll 1$) [33]. Substituting Eq. (1.19), (1.16) and (1.17) in Eq. (1.18), we have:

$$\left[-\frac{\hbar^2}{2m}\nabla^2 + V_{\text{ext}}(\mathbf{r}) + g|\Phi(\mathbf{r},t)|^2\right]\Phi(\mathbf{r},t) = i\hbar\frac{\partial}{\partial t}\Phi(\mathbf{r},t), \tag{1.21}$$

where μ is the chemical potential. This equation, known as Gross-Pitaevskii (GP) equation [3], describes the behavior of condensate by a macroscopic wave function $\Phi(\mathbf{r},t)$. The GP equation is essentially a mean-field theory. The interactions between atoms are considered as a mean field potential gn_c in the GP equation, neglecting all correlations.

In the stationary case, $\Phi(\mathbf{r},t) = \phi(\mathbf{r})\,\mathrm{e}^{-i\mu t/\hbar}$, the GP equation becomes [3, 12]:

$$\left[-\frac{\hbar^2}{2m}\nabla^2 + V_{\text{ext}}(\mathbf{r}) + g|\phi(\mathbf{r})|^2\right]\phi(\mathbf{r}) = \mu\phi(\mathbf{r},t). \tag{1.22}$$

Here, we can define an important dimensionless parameter [12]

$$\chi = Na/a_{\text{ho}}. \tag{1.23}$$

This determines the ratio between the interaction and the kinetic energies [12],

$$E_{\text{int}}/E_{\text{kin}} \sim \chi. \tag{1.24}$$

This is thus the parameter expressing the importance of the interactions compared with the kinetic energy. It can be much larger than 1 even if $n|a|^3 \ll 1$ (condition of diluteness). As a result, dilute gases can also exhibit an important non-ideal behavior as we will see in section 1.2.2.4.

1.2.2.4 Thomas-Fermi approximation

If $\chi \gg 1$, which means the interaction energy is much larger than the kinetic energy, we can neglect the kinetic energy term $-(\hbar^2/2m)\nabla^2$ to simplify the GP Eq. (1.22). The density distribution is thus [12]:

$$n(\mathbf{r}) = |\phi(\mathbf{r})|^2 = \frac{1}{g}\max(\mu - V_{\text{ext}}(\mathbf{r}), 0). \tag{1.25}$$

According to Eq. (1.1), the density profile is a inverted parabola where $\mu - V_{\text{ext}}(\mathbf{r}) > 0$, and zero elsewhere. Integrating Eq. (1.25), we get the relation between the chemical potential μ and the total atom number N:

$$\mu = \frac{\hbar\bar{\omega}}{2}\Big(\frac{15Na}{a_{\text{ho}}}\Big)^{2/5}. \tag{1.26}$$

As $\chi \gg 1$, we have $\mu \gg \hbar\bar{\omega}$.

From Eq. (1.25), the size of the condensate under Thomas-Fermi approximation is

$$R_c^{\text{TF}} = \sqrt{\frac{2\mu}{m\bar{\omega}^2}}. \tag{1.27}$$

Combining Eq. (1.27), (1.10) with condition $\mu \gg \hbar\bar{\omega}$, we have $R_c^{\mathrm{TF}} \gg R_c^{\mathrm{id}}$. Here, we can see clearly that "strong" interactions dramatically change the form of the condensate even if the gas is "dilute".

1.2.3 Calculation for scalar interacting Bose gas

In section 1.2.2, we get the GP equation for the condensed part. But the pure condensate only exists when $T \sim 0$. We should also consider the problem that condensate and thermal cloud coexist at $T < T_c$.

Solving the problem in general with both condensate and the thermal cloud is very complicated. Near T_c, $\delta\hat{\Psi}$ is no longer small compared with Φ, making the expansion Eq. (1.19) suspect. In principle, we should use Eq. (1.17), (1.18) to deal with the depletion part $\delta\hat{\Psi}$ and the order parameter Φ at the same time.

Here, we simplify the problem by separating the system into two parts, condensate and thermal cloud, and solving them step by step. Both condensate and thermal cloud behave as confined in a *effective* potential V^{eff}, which is composed by the trap potential V_{ext} and a mean-field interaction potential generated by condensate and thermal cloud. This mean-field approach, known as Hartree-Fock approximation [36, 3], neglects the correlations between the condensate and thermal cloud. This makes the calculation at finite temperature much more accessible.

In this section, we will calculate the condensate fraction and density profile below T_c for the scalar gas. This method is subsequently adopted in the spinor case in section 1.4.

1.2.3.1 Semi-ideal Hartree-Fock approximation

According to the Hartree-Fock approximation, interactions are simplified as a mean-field effective potential. For thermal atoms, the effective potential $V_{\mathrm{th}}^{\mathrm{eff}}$ is the sum of the trapping potential V_{ext} and the mean-field potential of interactions with all the other atoms $2gn(\mathbf{r})$. Here $n(\mathbf{r})$ denotes the total spatial density : $n(\mathbf{r}) = n_c(\mathbf{r}) + n_{\mathrm{th}}(\mathbf{r})$. So

$$V_{\mathrm{th}}^{\mathrm{eff}} = V_{\mathrm{ext}}(\mathbf{r}) + 2g[n_c(\mathbf{r}) + n_{\mathrm{th}}(\mathbf{r})]. \tag{1.28}$$

The factor of 2 in Eq. (1.28) is a consequence of quantum statistics. It arises from collisions between thermal atoms, or a thermal atom and a condensate atom. It is however absent for condensate-condensate interactions (in Eq. (1.29)), since the exchange term is absent when the 2 particles wave function is directly symmetric [41].

For condensate, the effective potential is the sum of the trap potential V_{ext}, the mean-field potential of interactions by condensate gn_c, which is the interaction term in GP equation, and the potential by thermal atoms $2gn_{\mathrm{th}}$.

$$V_{\mathrm{c}}^{\mathrm{eff}} = V_{\mathrm{ext}}(\mathbf{r}) + gn_c(\mathbf{r}) + 2gn_{\mathrm{th}}(\mathbf{r}). \tag{1.29}$$

As a result, the density distribution of condensed and thermal clouds are determined by the two coupled equations below:

$$n_{\rm c}(\mathbf{r}) = \frac{1}{g}\max\Big(\mu - (V_{\rm ext}(\mathbf{r}) + 2gn_{\rm th}(\mathbf{r})), 0\Big), \tag{1.30}$$

$$n_{\rm th}(\mathbf{r}) = \frac{1}{\Lambda_{\rm dB}^3} g_{3/2}\Big(\mathrm{e}^{\mu-(V_{\rm ext}+2gn(\mathbf{r}))/k_BT}\Big). \tag{1.31}$$

We denote this method the "complete" Hartree-Fock approximation. Remember that Eq. (1.30) is obtained under Thomas-Fermi approximation and Eq. (1.31) is obtained under semi-classical approximation.

The "semi-ideal" Hartree-Fock approximation neglect also the influence of the thermal cloud to the condensate [37], assuming that the spatial density of the condensate is much larger than that of the thermal cloud, even if the condensate atoms number is less than the number of thermal atoms. As a result, the Eq. (1.30) and (1.31) are simplified as follows:

$$n_{\rm c}(\mathbf{r}) = \frac{1}{g}\max\Big(\mu - V_{\rm ext}(\mathbf{r}), 0\Big), \tag{1.32}$$

$$n_{\rm th}(\mathbf{r}) = \frac{1}{\Lambda_{\rm dB}^3} g_{3/2}\Big(\mathrm{e}^{\mu-(V_{\rm ext}+2gn_c(\mathbf{r}))/k_BT}\Big). \tag{1.33}$$

In order to justify the validity of the "semi-ideal" approximation, we can always check the spatial density for both thermal cloud and the condensate *a posteriori*. Here, a simple estimation of the peak values of density profile for both components can give us some confidences. For the condensate, the peak density $n^c(0) \approx \mu/g$. For thermal cloud, the peak density $n^{\rm th}(0) \approx g_{3/2}(e^{\beta\mu})/\Lambda_{\rm dB}^3$. If we use $T \approx 0.9\,T_c^{\rm id}$, $N \approx 5000$, we have

$$\frac{n^c(0)}{n^{\rm th}(0)} \approx 0.2 \cdot \Big(\frac{a_{\rm ho}}{a}\Big)^{3/5}. \tag{1.34}$$

Since $a_{\rm ho} \gg a$, we have $n^c(0)/n^{\rm th}(0) \gg 1$, which means the peak density of the condensate is indeed much larger than that of the thermal cloud. It shows the validity of the semi-ideal approximation in a broad temperature range. However, near T_c, the condensate atom number will drop dramatically and the approximation fails.

Given a certain temperature T and total atom number $N_{\rm t}$, we want to calculate the condensate fraction and the spatial density profiles for condensate and thermal cloud. Using Eq. (1.32) and (1.33), the simulation is an iteration which consists of several steps

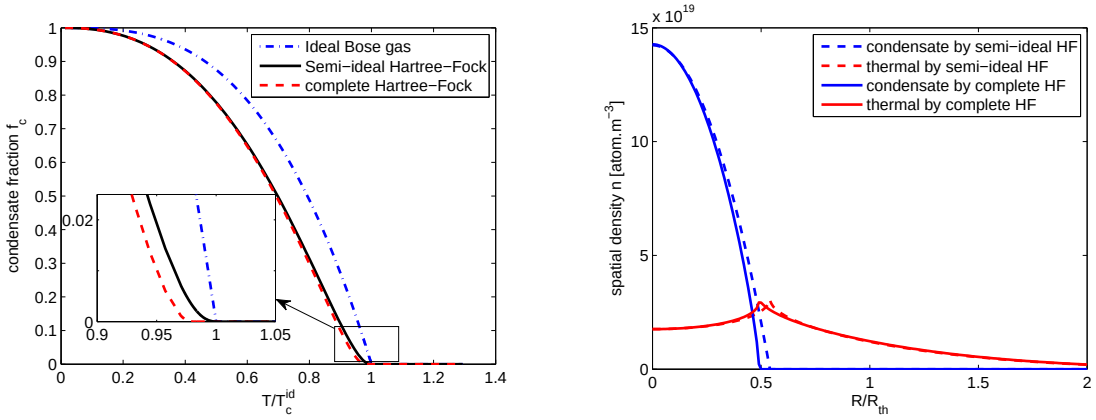
- We begin with certain chemical potential μ_0, calculate the condensate density profile $n_c(\mathbf{r})$ by Eq. (1.32).
- Integrating $n_c(\mathbf{r})$, we get the condensed atom number. In fact, for a given chemical potential μ, the condensed atom number N_c is given by Eq. (1.26)

$$N_c = \frac{a_{\rm ho}}{15a}\Big(\frac{2\mu}{\hbar\bar{\omega}}\Big)^{5/2}, \tag{1.35}$$

- Calculate thermal spatial density $n_{\rm th}(\mathbf{r})$ by Eq. (1.33) in using $n_c(\mathbf{r})$ obtained above.
- Integrating $n_{\rm th}(\mathbf{r})$, we get the total thermal atom number $N_{\rm th}$.
- We adjust the chemical potential μ so that the total atom number calculated $N_c + N_{\rm th}$ equals to the given total atom number within some precision (typically better than 10^{-3}).

1.2.3.2 Simulation results

Here, we show in Fig. 1.1 an example of the simulation where total atom number $N = 5000$. Atoms are confined in an isotropic harmonic trap $\bar{\omega} = \omega_x = \omega_y = \omega_z = 2\pi \times 1000$ Hz. We use the sodium atom mass $m_{\rm Na} = 3.82 \times 10^{-26}$ Kg [35], and a scattering length $a \approx 2.59\,$nm [42].



(a) (b)

Figure 1.1: (a) Condensate fraction f_c as a function of $T/T_c^{\rm id}$. Dash-dot line: Ideal Bose gas by Eq. (1.9). Solid line: simulation by semi-ideal Hartree-Fock approximation. Dashed line: simulation by complete Hartree-Fock approximation.
(b) Spatial density profile for thermal and condensed atoms as a function of $R/R_{\rm th}$, at $T/T_c^{\rm id} = 0.9$, with $f_c \approx 0.1$. Blue solid and dased line: condensate density distribution by complete and semi-ideal Hartree-Fock approximation, respectively. Red solid and dashed line: thermal cloud density distribution by complete and semi-ideal Hartree-Fock approximation, respectively. This plot show the validity of the semi-ideal Hartree-Fock approximation, which neglect the influence of the thermal atoms on the condensate.

In Fig. 1.1a, we plot the condensate fraction as a function of $T/T_c^{\rm id}$ by complete and semi-ideal Hartree-Fock approximation and ideal Bose gas formula Eq. (1.8). At the critical temperature, the spatial density distribution of the thermal cloud is not changed compared with the ideal case because of the absence of the condensate. As a result, the critical temperature predicted by semi-ideal Hartree-Fock approximation is not changed compared with the ideal case. However, the critical temperature predicted by complete Hartree-Fock approximation is slightly lower than that of the ideal case, because the influence of the thermal cloud on the condensate is no longer neglected.

In Fig. 1.1b, we plot the spatial density of the condensate and the thermal cloud as a function of $R/R_{\rm th}$ by both complete and semi-ideal Hartree-Fock approximation, where R is the radius coordinate, $R_{\rm th}$ is defined as Eq. (1.11). The temperature for this plot is $T/T_c^{\rm id} = 0.9$, where the condensate fraction $f_c \sim 0.1$. Here we can verify *a posteriori* that the size of the thermal cloud is much larger than that of the condensate and that the amplitude of the condensate is much larger than that of the thermal cloud (even if only 10% of atoms are in the condensate).

Finally, we compare the results obtained by the "semi-ideal" and the "complete" Hartree-Fock methods [43]. The condensate fraction and the density profile of both components calculated by semi-ideal and complete HF are close, if the condensate fraction is sufficiently large, typically above 10%. We conclude that the "semi-ideal" approximation is a simple but very effective description of a mixed cloud.

1.3 Spinor BEC : Pure condensate at zero temperature

1.3.1 Hyperfine structure of ^{23}Na

In our experiment, we work with ^{23}Na atoms. The energy structure is shown in Fig. 1.2 [35]. As the other alkali atoms, because of the spin-orbit coupling, the electronic $3P$ level is split into $3^2P_{1/2}$ and $3^2P_{3/2}$ manifolds, which constitutes the fine structure of Sodium. The optical transition between the electronic ground state $3^2S_{1/2}$ and $3^2P_{1/2}$ is called the D_1 line, and the one between $3^2S_{1/2}$ and $3^2P_{3/2}$ is called the D_2 line. In our experiment, laser cooling operates on the D_2 line. This will be discussed in details in the next chapter.

Moreover, because of the interactions between electronic angular momentum and the nuclear spin, the energy levels of the fine structure, $3^2S_{1/2}$, $3^2P_{1/2}$, $3^2P_{3/2}$, are all split into several sub-levels by hyperfine interaction, which is also shown in Fig. 1.2. The electronic ground state $3^2S_{1/2}$ is split into two hyperfine levels, which are marked by the total spin F, with $F = 1$ and $F = 2$. Altogether, the electronic ground state for ^{23}Na is $3^2S_{1/2}$, $F = 1$, with three Zeeman sub-levels, $m_F = (+1, 0, -1)$. This hyperfine spin manifold is used in our experiment to realize spinor condensate, which consists of three Zeeman components and thus are described by a 3-component order parameter, $(\hat{\psi}_{+1}, \hat{\psi}_0, \hat{\psi}_{-1})$.

1.3.2 Hamiltonian of the interacting spin-1 Bose gas

1.3.2.1 Interaction of collision

In section 1.2.2.2, we have discussed the interaction between atoms in scalar case. In spinor case, the interactions between atoms depend on the spin. We begin with two atoms with spin $s = 1$. Suppose as in Eq. (1.16) a contact potential for the spatial part.

$$\hat{V}(\mathbf{r}_1, \mathbf{r}_2) = \hat{V}_s \cdot \delta(\mathbf{r}_1 - \mathbf{r}_2). \tag{1.36}$$

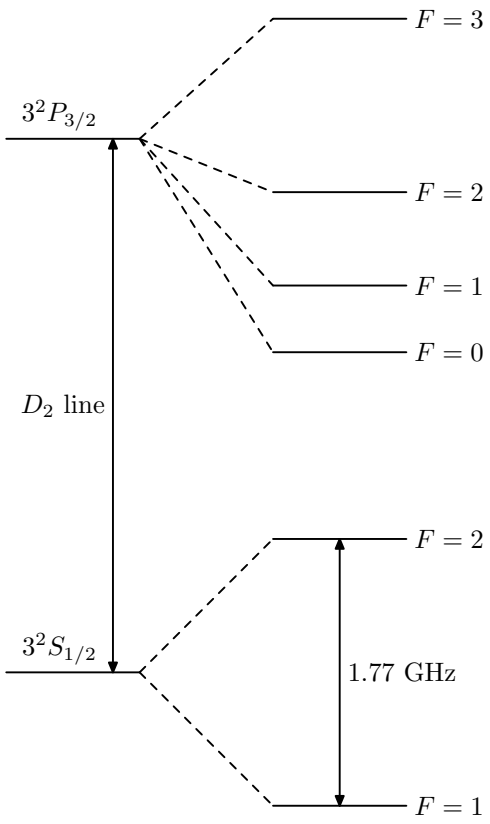


Figure 1.2: Sodium D_2 line hyperfine structure.

Here, $\hat{V}_s$ denotes the spin-dependent interaction. The interaction potential mainly comes from the electrostatic interactions between the electron clouds repulsion, which are invariant by spin rotation. The two spins combine to a total angular momentum $S = 0, 1, 2$, with projection $m_S = -S, ..., S$. Due to the rotational invariance in spin space, S is a conserved quantity in the collision. $\hat{V}_s$ can thus be written as [29, 30, 26]:

$$\hat{V}_s = \sum_{S.m_S} g_S \hat{\mathcal{P}}_S. \tag{1.37}$$

Here, $\hat{\mathcal{P}}_S = \sum_{m_S} |S, m_S\rangle\langle S, m_S|$ projects onto the subspace with total spin S, $g_s = 4\pi\hbar^2 a_S/m$, and a_S is the S-channel scattering length.

In addition, when the spatial wave function is symmetric in the s-wave scattering regime, only even values for S are allowed for bosons. So the interaction

$$\begin{aligned} \hat{V}(\mathbf{r}_1, \mathbf{r}_2) &= (a_0\mathcal{P}_0 + a_2\mathcal{P}_2) \otimes \delta(\mathbf{r}_1 - \mathbf{r}_2). \\ &= (\bar{g}\mathbf{1} + g_s\mathbf{s}_1 \cdot \mathbf{s}_2) \otimes \delta(\mathbf{r}_1 - \mathbf{r}_2). \end{aligned} \tag{1.38}$$

Here, $\mathbf{s}_1$ and $\mathbf{s}_2$ are the spin operators for each atom, $\bar{g}$ the spin-independent coupling constant:

$$\bar{g} = \frac{4\pi\hbar^2}{m}\frac{a_0 + 2a_2}{3}, \tag{1.39}$$

and g_s the spin-dependent coupling constant:

$$g_s = \frac{4\pi\hbar^2}{m}\frac{a_2 - a_0}{3}. \tag{1.40}$$

The spin-dependent interaction is called "anti-ferromagnetic" if $g_s > 0$, and "ferromagnetic" if $g_s < 0$ [29, 30, 26]. It means two interacting spins lower their energy by forming the anti-aligned (aligned) configuration if the interaction is anti-ferromagnetic (ferromagnetic). This coefficient is crucial for the nature of the quantum gas. For sodium, $a_2 = 2.89\,\mathrm{nm}$, and $a_0 = 2.69\,\mathrm{nm}$ [42], therefore $g_s > 0$. Sodium atoms present anti-ferromagnetic interactions in the electronic ground state, one of the reasons why we work with sodium in our experiment [44].

From Eq. (1.38), we can write the Hamiltonian for N interacting atoms in second quantization representation. The total interaction Hamiltonian consists of two parts: spin-dependent and spin-independent part, $\hat{H}_{\mathrm{int}} = \bar{H} + \hat{H}_s$, where

$$\bar{H} = \frac{\bar{g}}{2} \int d^3\mathbf{r}\, \hat{n}^2(\mathbf{r}), \tag{1.41}$$

and

$$\hat{H}_s = \frac{g_s}{2} \int d^3\mathbf{r}\, \hat{S}^2(\mathbf{r}). \tag{1.42}$$

In Eq. (1.41), (1.42), $\hat{n}(\mathbf{r})$ is the density operator, and $\hat{S}^2(\mathbf{r})$ is the total spin operator.

$$\begin{aligned} \hat{n}(\mathbf{r}) &= \hat{n}_{+1}(\mathbf{r}) + \hat{n}_0(\mathbf{r}) + \hat{n}_{-1}(\mathbf{r}) \\ &= \hat{\Psi}^\dagger_{+1}(\mathbf{r})\hat{\Psi}_{+1}(\mathbf{r}) + \hat{\Psi}^\dagger_0(\mathbf{r})\hat{\Psi}_0(\mathbf{r}) + \hat{\Psi}^\dagger_{-1}(\mathbf{r})\hat{\Psi}_{-1}(\mathbf{r}). \end{aligned} \tag{1.43}$$

where $(\hat{\Psi}_{+1}(\mathbf{r}), \hat{\Psi}_0(\mathbf{r}), \hat{\Psi}_{-1}(\mathbf{r}))$ are the annihilation operators for $m_F = +1, 0, -1$ Zeeman sub-levels at position $\mathbf{r}$ respectively.

The total spin operator $\hat{S}(\mathbf{r})^2 = \hat{S}_x(\mathbf{r})^2 + \hat{S}_y(\mathbf{r})^2 + \hat{S}_z(\mathbf{r})^2$ is obtained from

$$\hat{S}_x(\mathbf{r}) = \frac{1}{\sqrt{2}}(\hat{\Psi}^\dagger_{+1}(\mathbf{r})\hat{\Psi}_0(\mathbf{r}) + \hat{\Psi}^\dagger_{-1}(\mathbf{r})\hat{\Psi}_0(\mathbf{r}) + \hat{\Psi}^\dagger_0(\mathbf{r})\hat{\Psi}_{+1}(\mathbf{r}) + \hat{\Psi}^\dagger_0(\mathbf{r})\hat{\Psi}_{-1}(\mathbf{r})) \tag{1.44}$$

$$\hat{S}_y(\mathbf{r}) = -\frac{i}{\sqrt{2}}(\hat{\Psi}^\dagger_{+1}(\mathbf{r})\hat{\Psi}_0(\mathbf{r}) + \hat{\Psi}^\dagger_{-1}(\mathbf{r})\hat{\Psi}_0(\mathbf{r}) - \hat{\Psi}^\dagger_0(\mathbf{r})\hat{\Psi}_{+1}(\mathbf{r}) - \hat{\Psi}^\dagger_0(\mathbf{r})\hat{\Psi}_{-1}(\mathbf{r})) \tag{1.45}$$

$$\hat{S}_z(\mathbf{r}) = \frac{1}{\sqrt{2}}(\hat{\Psi}^\dagger_{+1}(\mathbf{r})\hat{\Psi}_{+1}(\mathbf{r}) - \hat{\Psi}^\dagger_{-1}(\mathbf{r})\hat{\Psi}_{-1}(\mathbf{r})) = \hat{n}_{+1}(\mathbf{r}) - \hat{n}_{-1}(\mathbf{r}). \tag{1.46}$$

As a result:

$$\begin{aligned} \hat{S}(\mathbf{r})^2 = \hat{n}(\mathbf{r}) + \hat{n}_0(\mathbf{r}) + 2\hat{n}_0(\mathbf{r})(\hat{n}_{+1} + \hat{n}_{-1}) + (\hat{n}_{+1}(\mathbf{r}) - \hat{n}_{-1}(\mathbf{r}))^2 + \\ 2(\hat{\Psi}^\dagger_{+1}(\mathbf{r})\hat{\Psi}^\dagger_{-1}(\mathbf{r})\hat{\Psi}_0(\mathbf{r})\hat{\Psi}_0(\mathbf{r}) + \hat{\Psi}^\dagger_0(\mathbf{r})\hat{\Psi}^\dagger_0(\mathbf{r})\hat{\Psi}_{+1}(\mathbf{r})\hat{\Psi}_{-1}(\mathbf{r})). \end{aligned} \tag{1.47}$$

In Eq. (1.47), we divide the terms into two lines. The first line lists the terms describing the *spin-preserving* collisions which do not change the internal Zeeman sub-levels of the atoms involved in the collisional process. The second line lists the terms describing *spin-flip* collisions which change the internal states. As shown in Fig. 1.3, there are two terms in the *spin-flip* process. A pair of $m = 0$ states are converted to $m = +1$ and $m = -1$ or inversely. As a result, the magnetization ($m_z = (N_{+1} - N{-}1)/N$) is conserved during the atom collisions described by the Hamiltonian H_{int}.

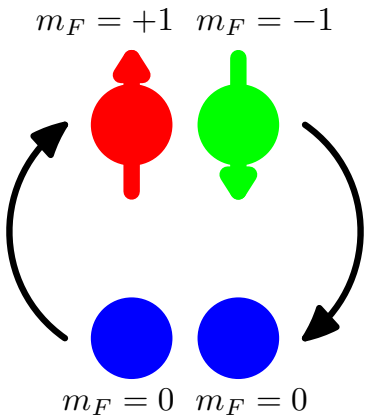


Figure 1.3: Spin-flip collisions processes in Eq. (1.47). The magnetization m_z is conserved.

1.3.2.2 Magnetic field effects

The Hamiltonian of one alkali atom in a magnetic field is given by Breit-Rabi formula [45, 41]. For Zeeman splittings small compared to the hyperfine energy, it reduces to the magnetic Hamiltonian

$$\hat{h}_{\text{mag}} = p\hat{s}_z + q(\hat{s}_z^2 - 4). \tag{1.48}$$

Here, $\hat{s}_z$ is the spin operator in z direction, p and q the coefficients of linear and quadratic Zeeman effect respectively:

$$p = g_F \mu_B \times B, \tag{1.49}$$

$$q = \frac{(g_F \mu_B)^2}{\hbar \omega_{\text{hf}}} \times B^2, \tag{1.50}$$

where g_F is the Landé factor, μ_B the Bohr magneton, and ω_{hf} the hyperfine splitting between $F = 1$ and $F = 2$ of the electronic ground state $3^2S_{1/2}$ (see Fig. 1.2). For sodium, $3^2S_{1/2}$, $F = 1$ hyperfine level, $g_F = -1/2$, and $\omega_{\text{hf}} = 2\pi \times 1.77$ GHz [35], therefore

$$p = -700\,\text{kHz/G} \times B \quad \text{and} \quad q = 276.4\,\text{Hz/G}^2 \times B^2. \tag{1.51}$$

In Fig. 1.4, we illustrate the linear and quadratic Zeeman effect. The linear Zeeman effect shifts the $m_F = +1$ and $m_F = -1$ energy level by $+p$ and $-p$ respectively relative to $m_F = 0$ sub-level. The quadratic Zeeman effect shifts both the $m_F = +1$ and $m_F = -1$ energy level by $+q$ relative to $m_F = 0$ sub-level.

The Hamiltonian for N atoms in the magnetic field B can be rewritten as

$$\begin{aligned} \hat{H}_{\text{mag}} &= p(\hat{N}_{+1} - \hat{N}_{-1}) + q(\hat{N}_{+1} + \hat{N}_{-1} - 4\hat{N}) \\ &= -q\hat{N}_0 - 3q\hat{N} + p(\hat{N}_{+1} - \hat{N}_{-1}) \end{aligned} \tag{1.52}$$

Here, $\hat{N}_{+1}, \hat{N}_0, \hat{N}_{-1}$ are the number operator of $m_F = +1, 0, -1$ respectively.

There are three terms in Eq. (1.52). The first term is the quadratic Zeeman effect which plays a crucial role in the following discussions. The second term depends only

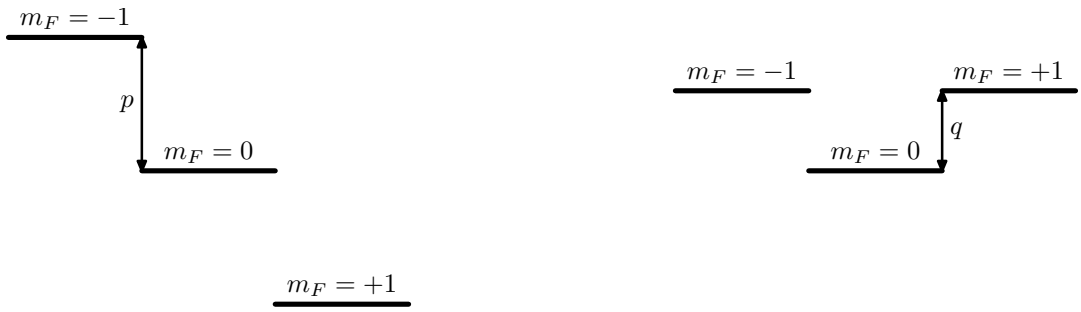


Figure 1.4: Linear and quadratic Zeeman effects

on total atom number, and normally we can simply omit it. Last term is the linear Zeeman effect proportional to magnetization which is conserved, so the last term is also a constant. Up to an overall energy shift, we thus have

$$\hat{H}_{\text{mag}} = -q\hat{N}_0. \tag{1.53}$$

1.3.2.3 Total Hamiltonian of the spin-1 Bose gas

According to sections above, the total Hamiltonian of our system consists of several parts: the kinetic energy, potential energy, the interactions between atoms, and quadratic Zeeman effect.

$$\hat{H}_{\text{tot}} = \int d^3\mathbf{r}\, \hat{\Psi}_i^\dagger(\mathbf{r})\Big(-\frac{\hbar^2}{2m}\nabla^2 + V_{\text{ext}}(\mathbf{r})\Big)\hat{\Psi}_i(\mathbf{r}) + \bar{H} + \hat{H}_s + \hat{H}_{\text{mag}}. \tag{1.54}$$

1.3.2.4 Single Mode Approximation (SMA)

In order to find the properties of a spinor BEC at $T = 0$, we introduce first the single mode approximation (SMA) which supposes that all the spin components share the same spatial wave function. This approximation was first introduced in [29, 46, 30], and studied in [47]. The SMA is valid mainly because the spin-dependent interaction is much smaller than the spin-independent interaction $g_s \ll \bar{g}$. As a result, the vector order parameter can be decomposed by a spin part which is still a vector and a spatial part which is a scalar function

$$\{\hat{\Psi}_{+1}(\mathbf{r}), \hat{\Psi}_0(\mathbf{r}), \hat{\Psi}_{-1}(\mathbf{r})\} = \Phi_{\text{SMA}}(\mathbf{r}) \times \{\hat{a}_{+1}, \hat{a}_0, \hat{a}_{-1}\}. \tag{1.55}$$

Here $\hat{a}_{+1}, \hat{a}_0, \hat{a}_{-1}$ denote the annihilation operator for $m_F = +1, 0, -1$ respectively. $\Phi_{\text{SMA}}(\mathbf{r})$ is the common spatial mode which is described by the Gross-Pitaevskii equation:

$$\Big(-\frac{\hbar^2}{2m}\nabla^2 + V_{\text{ext}}(\mathbf{r}) + \bar{g}N|\Phi_{\text{SMA}}(\mathbf{r})|^2\Big)\Phi_{\text{SMA}}(\mathbf{r}) = \mu\Phi_{\text{SMA}}(\mathbf{r}), \tag{1.56}$$

and is normalized to unity, $\int d^3\mathbf{r}\, |\Phi_{\text{SMA}}(\mathbf{r})|^2 = 1$.

The Hamiltonian for the spin part $|\zeta\rangle$ is:

$$\hat{H}_{\text{SMA}} = \frac{U_s}{2N}\hat{S}^2 - q\hat{N}_0, \tag{1.57}$$

with

$$U_s = g_s N \int d^3\mathbf{r}\, |\Phi_{\mathrm{SMA}}(\mathbf{r})|^4. \tag{1.58}$$

and

$$\hat{S}^2 = \hat{N} + \hat{N}_0 + 2\hat{N}_0(\hat{N}_{+1} + \hat{N}_{-1}) + (\hat{N}_{+1} - \hat{N}_{-1})^2 + 2(\hat{a}_{+1}^\dagger \hat{a}_{-1}^\dagger \hat{a}_0^2 + \hat{a}_0^{\dagger 2} \hat{a}_{+1} \hat{a}_{-1}). \tag{1.59}$$

In next subsection, we will adopt the mean-field approach to solve the H_{SMA}.

1.3.3 Mean-field approach to the spinor Hamiltonian - H_{SMA}

The first level of approximation is to try a mean-field many-body wave function of the form $\propto (a_{\vec{\zeta}}^\dagger)^N|0\rangle$ where the condensate operator $a_{\vec{\zeta}}^\dagger$ creates an atom in the single-particle spin state $\vec{\zeta}$ which is a normalized vector. In the mean-field approach, the operator is approximated by a C-number as Eq. (1.19). So the normalized spin-dependent wave function is:

$$|\zeta\rangle_N = \frac{1}{\sqrt{N}} \begin{pmatrix} \sqrt{N_{+1}}\, \mathrm{e}^{i\theta_{+1}} \\ \sqrt{N_0}\, \mathrm{e}^{i\theta_0} \\ \sqrt{N_{-1}}\, \mathrm{e}^{i\theta_{-1}} \end{pmatrix} = \frac{1}{\sqrt{2}} \begin{pmatrix} \sqrt{x + m_z}\, \mathrm{e}^{i\theta_{+1}} \\ \sqrt{2(1-x)}\, \mathrm{e}^{i\theta_0} \\ \sqrt{x - m_z}\, \mathrm{e}^{i\theta_{-1}} \end{pmatrix} \tag{1.60}$$

where $N_{+1,0,-1}$ are the atom number in $m_F = +1, 0, -1$ respectively, $\theta_{+1,0,-1}$ the phase of the three spin components, m_z the magnetization $m_z = (N_{+1} - N_{-1})/N$ and $x = (1 - N_0/N)$.

Substituting Eq. (1.60) to the SMA Hamiltonian Eq. (1.57), we have:

$$\frac{E_{\mathrm{spin}}}{U_s} = \left[\frac{m_z^2}{2} + x(1-x) + \cos(\theta_m)(1-x)\sqrt{x^2 - m_z^2}\right] + (q/U_s) \cdot x. \tag{1.61}$$

where $\theta_m = \theta_{+1} + \theta_{-1} - 2\theta_0$. In this equation, the first term at the right side describes the anti-ferromagnetic interaction and the second term describes the quadratic Zeeman effect.

We have to minimize the energy in order to solve the ground state of the Hamiltonian Eq. (1.57) under mean-field approximation, we have first $\cos(\theta_m) = -1$, which means

$$\theta_m = \theta_{+1} + \theta_{-1} - 2\theta_0 = \pi. \tag{1.62}$$

In our experiment, the magnetization m_z is fixed once the sample is prepared. So, we minimize the Eq. (1.61) as follows: for a fixed m_z, we search for the $x_{\min}$ to minimize the energy Eq. (1.61) for each q value (magnetic field).

We plot the results for this calculation in Fig. 1.5. For each magnetization, we remark that there exists a critical magnetic field q_c below which $N_0 = 0$. Only if $q > q_c$ atoms begin to occupy the $m_z = 0$ state. The critical magnetic field is given by:

$$q_c/U_s = 1 - \sqrt{1 - m_z^2}. \tag{1.63}$$

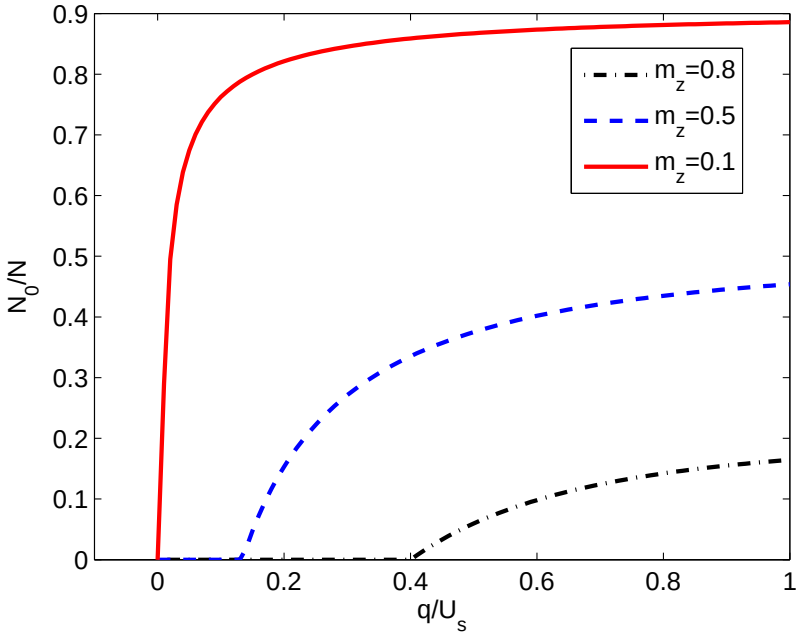


Figure 1.5: phase transition at q_c between anti-ferromagnetic and broken axisymmetry state.

- if $q < q_c$, E_{spin} is minimized at $x = 1$, which means $N_0 = 0$. The spin ground state is

$$|\zeta\rangle = \frac{1}{\sqrt{2}} \mathrm{e}^{i\theta_0} \begin{pmatrix} \sqrt{1+m_z}\, \mathrm{e}^{i\phi} \\ 0 \\ -\sqrt{1-m_z}\, \mathrm{e}^{-i\phi} \end{pmatrix} \tag{1.64}$$

  where $\phi = \theta_{+1} - \theta_0$. This state is known as "anti-ferromagnetic" state [29].

- if $q > q_c$, E_{spin} is minimized at $x = x_0$, with x_0 the solution to the equation:

$$(1-2x_0)(\sqrt{x_0^2 - m_z^2} - x_0) + (q/U_s)\sqrt{x_0^2 - m_z^2} = m_z^2. \tag{1.65}$$

  And the spin ground state is

$$|\zeta\rangle = \frac{1}{\sqrt{2}} \mathrm{e}^{i\theta_0} \begin{pmatrix} \sqrt{x_0+m_z}\, \mathrm{e}^{i\phi} \\ \sqrt{2}\cdot\sqrt{1-x_0} \\ -\sqrt{x_0-m_z}\mathrm{e}^{-i\phi} \end{pmatrix}. \tag{1.66}$$

  This state is known as "broken axisymmetry" state.

From the physical point of view, this phase transition originates from the competition between the anti-ferromagnetic interactions and the quadratic Zeeman effect. In considering Eq. (1.62), the anti-ferromagnetic interaction part in Eq. (1.61) is

$$\frac{E_{\text{spin}}^{\text{int}}}{U_s} = \frac{m_z^2}{2} + (1-x)(x - \sqrt{x^2 - m_z^2}). \tag{1.67}$$

If $m_z \neq 0$, the minimum of $E_{\text{spin}}^{\text{int}}$ is at $x = 1$, which means $N_0 = 0$. Therefore, the anti-ferromagnetic interaction prefers the atoms in $m_F = +1$ and $m_F = -1$ states (for $m_z \neq 0$). However the quadratic Zeeman effect prefers the atoms in the $m_F = 0$ state. If the magnetic field is not sufficiently large, the anti-ferromagnetic interactions dominate, thus we have $N_0 = 0$. But when magnetic field is comparable or large enough compared with the anti-ferromagnetic interactions, atoms begin to occupy the $m_F = 0$ state. This is a phase transition between the anti-ferromagnetic phase to the broken axisymmetry phase which are mentioned above. The case $m_z = 0$ is special. At $q = 0$, all states in the family of Eq. (1.66) are degenerate. This means going from one to another will be easy and fluctuations can be expected. We will study this situation in detail in chapter 4.

In chapter 3, we will compare the experiment results with the mean-field theory prediction calculated in this section.

1.4 Spinor BEC : Condensate with thermal cloud at finite temperature

In this section, we combine the two aspects seen previously and consider the case: spinor condensate at finite temperatures. We adopt here the same idea in section 1.2.3, separating the condensate and the thermal part and neglecting the influence of the thermal part on the condensate. This approximation, as mentioned in section 1.2.3, is called the semi-ideal Hartree-Fock approximation. Here, in the spinor case, the condensate is described by the mean-field solution discussed in section 1.3.

Several phenomena can be discussed by this method including the different critical temperatures for different spin components in different magnetic fields [48]. However, we will focus here on N_0, the occupation number in the $m_F = 0$ state. More precisely, we calculate N_0 as a function of magnetic field (or quadratic Zeeman energy q) for a given magnetization m_z. The reason for this calculation is that the atom number in each spin component is the simplest quantity to measure in the experiment and as we will see in this section, the $N_0(q)$ curve can reveal several important informations of the spin system, including the temperature T, characterizing the thermal cloud at equilibrium, and the condensate fraction f_c. This calculation can also be extended to describe condensate spin fluctuations which will be discussed in detail in chapter 4.

We focus in this part on the special case where the magnetization $m_z = 0$. As we will see in chapter 3, at small magnetization and low magnetic field, the fluctuations of N_0 are "abnormally" large. However, the mean-field theory in section 1.3.3 indicate that the phase transition happens at $B = 0$ for $m_z = 0$, which also means an infinitesimal small magnetic field can always force all the atoms to $m_F = 0$ state. In order to explain this inconsistency, we will develop in chapter 4 a full quantum solution for H_{SMA}. In fact, the deviation between the mean-field approach and the full quantum solution becomes large at small magnetization, which makes it interesting for us to focus on $m_z = 0$ case.

We divide this section into two parts. In the first part, we will write down explicitly

the formalism of the semi-ideal Hartree-Fock approximation for the spinor BEC at finite temperatures. In the second part, we will focus on the $m_z = 0$ case and calculate how N_0 and condensate fraction f_c depend on the magnetic field B.

1.4.1 Semi-ideal HF approximation for spinor BEC

In section 1.2.3, we have introduced the semi-ideal Hartree-Fock approximation for the case of a single-component BEC. Here, we will generalize it to spinor BEC.

We assume that the density distribution of condensate is not influenced by the thermal distribution and determined by the ground state calculated in section 1.3.3. This leads to

$$n^c_{+1}(\mathbf{r}) = N^c_{+1} \cdot |\Phi_{\mathrm{SMA}}(\mathbf{r})|^2, \tag{1.68}$$
$$n^c_{0}(\mathbf{r}) = N^c_{0} \cdot |\Phi_{\mathrm{SMA}}(\mathbf{r})|^2, \tag{1.69}$$
$$n^c_{-1}(\mathbf{r}) = N^c_{-1} \cdot |\Phi_{\mathrm{SMA}}(\mathbf{r})|^2. \tag{1.70}$$

where $n^c_{+1}(\mathbf{r})$, $n^c_0(\mathbf{r})$, $n^c_{-1}(\mathbf{r})$ are the density profile for $m_F = +1, 0, -1$ respectively, N^c_{+1}, N^c_0, N^c_{-1} are condensed atom number in $m_F = +1, 0, -1$ respectively, and $\Phi_{\mathrm{SMA}}(\mathbf{r})$ is the SMA function defined by Eq. (1.56). Here, in accordance with the SMA, we also neglected spin-dependent interactions between the condensate and the thermal cloud, because $g_s \ll \bar{g}$. We solve this equation using the Thomas-Fermi approximation,

$$\Phi_{\mathrm{SMA}}(\mathbf{r}) = \frac{1}{\bar{g}} \max(\mu - V_{\mathrm{ext}}(\mathbf{r}), 0). \tag{1.71}$$

The free energy G of the ideal spin 1 Bose gas with magnetic field and magnetization fixed can be written as

$$\begin{aligned} G &= H_0 - \mu N - \eta M_z - qN_0 \\ &= (H_0 - qN) - (\mu + \eta - q)N_{+1} - \mu N_0 - (\mu - \eta - q)N_{-1}. \end{aligned} \tag{1.72}$$

As a result, the "effective" chemical potentials for each component are given by

$$\mu_{+1} = \mu + \eta - q, \tag{1.73}$$
$$\mu_0 = \mu, \tag{1.74}$$
$$\mu_{-1} = \mu - \eta - q. \tag{1.75}$$

Compared to Eq. (1.33), the density profiles of the thermal clouds $n^{\mathrm{th}}_i(\mathbf{r})$ (with $i = +1, 0, -1$) are:

$$n^{\mathrm{th}}_i(\mathbf{r}) = \frac{1}{\Lambda^3_{\mathrm{dB}}} g_{3/2}(\mathrm{e}^{(\mu_i - V^{\mathrm{eff,th}}_i(\mathbf{r}))/k_B T}), \tag{1.76}$$

with

$$V^{\mathrm{eff,th}}_i(\mathbf{r}) = V_{\mathrm{ext}}(\mathbf{r}) + \bar{g}|\Phi_{\mathrm{SMA}}(\mathbf{r})|^2(N^c + N^c_i). \tag{1.77}$$

Here, μ is the chemical potential which serves to fix the total atom number, and η is the Lagrangian multiplier to fix the magnetization m_z. The interaction terms are obtained as follows. Take $n^{\mathrm{th}}_{+1}(\mathbf{r})$ for example. The thermal cloud in $m_F = +1$ interacts with all

condensed spin components, but differently. The thermal atoms in $m_F = +1$ and the condensed atoms in $m_F = +1$ are in principle indistinguishable. As a result, the effective potential for $n^{\rm th}_{+1}(\mathbf{r})$ is

$$\begin{aligned} V^{\rm eff,th}_{+1}(\mathbf{r}) &= V_{\rm ext}(\mathbf{r}) + \bar{g}|\Phi_{\rm SMA}(\mathbf{r})|^2(2N^c_{+1} + N^c_0 + N^c_{-1}) \\ &= V_{\rm ext}(\mathbf{r}) + \bar{g}|\Phi_{\rm SMA}(\mathbf{r})|^2(N^c + N^c_{+1}), \end{aligned} \tag{1.78}$$

with $N^c = N^c_{+1} + N^c_0 + N^c_{-1}$, total condensed atom number. $n^{\rm th}_0(\mathbf{r})$ and $n^{\rm th}_{-1}(\mathbf{r})$ can be obtained by the same way.

The simulation is similar to the one performed in section 1.2.3. Given a certain temperature T, total atom number $N_{\rm t}$, and magnetization m_z, the simulation is an iteration which consists of several steps.

1. We begin with certain chemical potential μ_0 and a certain η_0,
2. we calculate the SMA function $\Phi_{\rm SMA}(\mathbf{r})$ by Eq. (1.71),
3. we calculate N^c_{+1}, N^c_0, N^c_{-1} by minimizing the mean-field energy Eq. (1.61) in the same way as in section 1.3.3,
4. we calculate the $n^{\rm th}_{+1}(\mathbf{r})$, $n^{\rm th}_0(\mathbf{r})$, $n^{\rm th}_{-1}(\mathbf{r})$ by Eq (1.76),
5. we integrate $n^{\rm th}_{+1}(\mathbf{r})$, $n^{\rm th}_0(\mathbf{r})$, $n^{\rm th}_{-1}(\mathbf{r})$, we get the thermal atom numbers in $m_F = +1, 0, -1$, which we denote $N^{\rm th}_{+1}$, $N^{\rm th}_0$, $N^{\rm th}_{-1}$,
6. we calculate the total atom number $N = N^c + N^{\rm th}$ and total magnetization $m_z = (N^c_{+1} + N^{\rm th}_{+1} - N^c_{-1} - N^{\rm th}_{-1})/N$,
7. we adjust μ and η respectively so that the total atom number (resp. magnetization) calculated above equals to the given total atom number (resp. magnetization) within certain precision (typically better than 10^{-3}).

In the next subsection, we focus on the situation where $m_z = 0$ which means the Lagrange multiplier $\eta = 0$. The simulation steps are simplified without η adaptation. We will show some results and discuss their physical meanings.

1.4.2 Simulation results for $m_z = 0$

We show in Fig. 1.6 an example of the calculated N_0. Here, the total atom number $N = 5000$. Sodium atoms are confined in an isotopic harmonic trap $\bar{\omega} = \omega_x = \omega_y = \omega_z = 2\pi \times 1000\,\text{Hz}$. We plot in each figure with $T = 200$, 300, 500 nK and B varied. We denote $n_i = N_i/N$ the relative atom number in the $m_F = i$ Zeeman sub-level.

In Fig. 1.6, we plot $1 - n_0$ as a function of q (see Eq. (1.51)) for three different temperatures, $T = 200, 300, 500$ nK. There are several important features in this figure.

First, for each temperature, as the magnetic field B increase, $1 - n_0$ decreases because of the quadratic Zeeman effect. For $q > 0$, all the condensed atoms occupy the $m_F = 0$

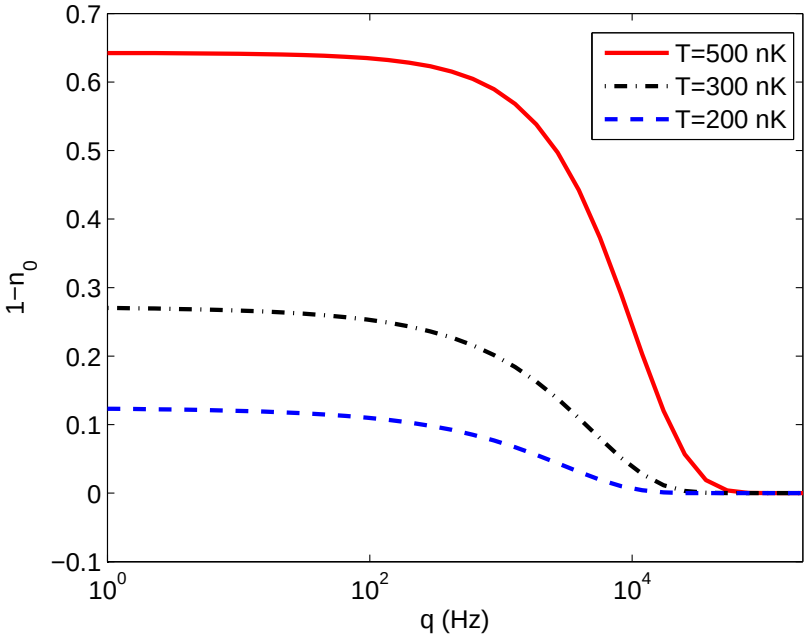


Figure 1.6: $1 - n_0$ as a function of q.

state, which means as q increase, more *thermal atoms* occupy the $m_F = 0$ state. As a result, the $1 - n_0$ curve will decrease drastically when quadratic Zeeman effect is comparable with the thermal energy, which means $q_{1/2} \sim k_B T$. Here $q_{1/2}$ means the Half width at Half Maximum of $1 - n_0$. As shown in Fig. 1.6, $q_{1/2}$ is larger for higher temperatures. At extremely high q, the quadratic Zeeman effect forces all the atoms to the $m_F = 0$ state, therefore, $(1 - n_0) \to 0$.

Second, the $1 - n_0$ value at low q decreases as temperature T decreases. To explain this, we suppose the spin isotropy of the thermal clouds, which means $N_{+1}^{\rm th} = N_0^{\rm th} = N_{-1}^{\rm th}$. We will test this hypothesis *a posteriori*. In contrast, the condensed atoms always occupy the $m_F = 0$ state for $q > 0$ ($m_z = 0$). As a result, as the atom number of the condensate increases for lower temperatures, the value of $1 - n_0$ at low q decreases.

In Fig. 1.7, we show the deviation of the spin isotropy of the thermal clouds as a function of q. We define the deviation parameter

$$Q = \frac{N_{+1}^{\rm th} + N_{-1}^{\rm th} - 2N_0^{\rm th}}{N}. \tag{1.79}$$

If $Q = 0$, the spin isotropy of the thermal clouds is perfectly satisfied, which means $N_{+1}^{\rm th} = N_0^{\rm th} = N_{-1}^{\rm th}$. As shown in Fig. 1.7, at low q, the spin isotropy for different temperatures is well satisfied. At extremely high q, as almost all the atoms, thermal and condensed, occupy the $m_F = 0$ state, the spin isotropy is completely destroyed. Note that this is different from the case of the condensate, where both spin interactions and quadratic Zeeman energy concur to maximize the population in $m_F = 0$. For thermal atoms and in our Hartree-Fock model, spin isotropy breaks down due to a "paramagnetic" effect of alignment in the external field. In chapter 4, we will see that at low q, collective

spin fluctuation of the condensate will completely restore the spin isotropy as $q \to 0$. Here, because we work within the mean-field framework, the condensate is anisotropic (all atoms are in $m_F = 0$ state). Even then, the spin anisotropy of the thermal cloud is small at low q.

We conclude that despite the complete spin anisotropy of the condensate and the interactions with condensate, the spin isotropy of the thermal clouds are well satisfied in a relatively large interval of q.

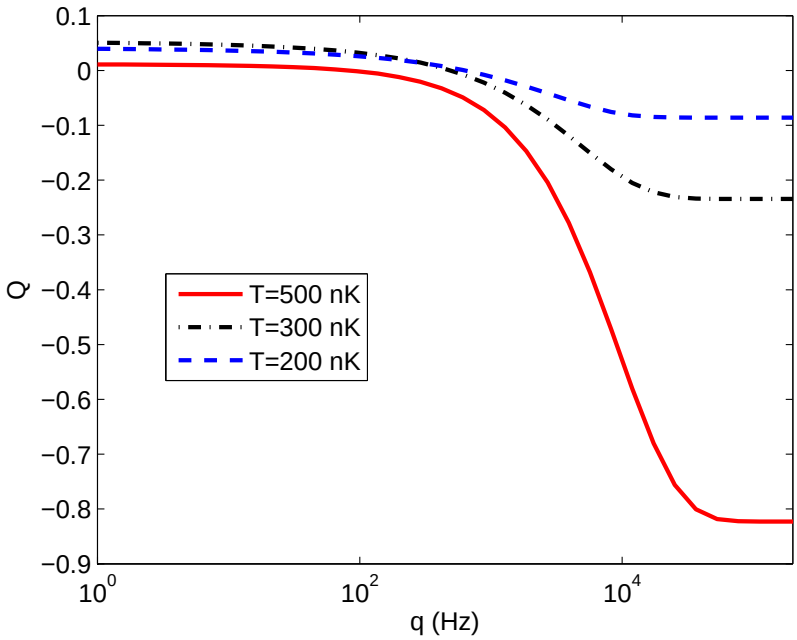


Figure 1.7: Deviation of the thermal clouds from spin isotropy. $Q = (N_{+1}^{\rm th}+N_{-1}^{\rm th}-2N_0^{\rm th})/N$ quantifies this deviation. $Q = 0$ means perfect spin isotropy. At low q, the spin isotropy for different temperatures is well satisfied. However, when q is sufficiently large, the spin isotropy will be broken.

Third, if the spin isotropy of the thermal atoms is satisfied, the condensate fraction f_c is related directly to the $1 - n_0$ value at low q, which we denote c.

$$f_c^{\rm iso} = \frac{N_0^c}{N} = 1 - 3c/2. \tag{1.80}$$

with $c = 1 - (N_0^c + N^{\rm th}/3)/N$.

We show in Fig. 1.8, the "calculated" condensate fraction $f_c^{\rm cal}$ as a function of q. We also compare in Fig. 1.9, the "calculated" $f_c^{\rm cal}$ at low q with the $f_c^{iso} = 1 - 3c/2$ which suppose the spin isotropy of the thermal clouds. We find a good agreement within 5%.

In conclusion, the $1 - n_0$ curve reveals many useful informations about the spin system,

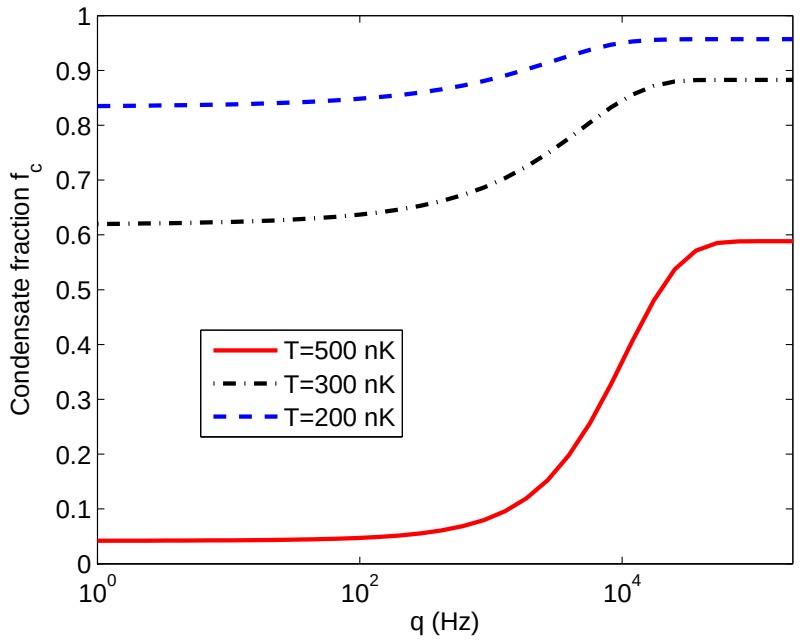


Figure 1.8: Condensate fraction f_c as a function of q.

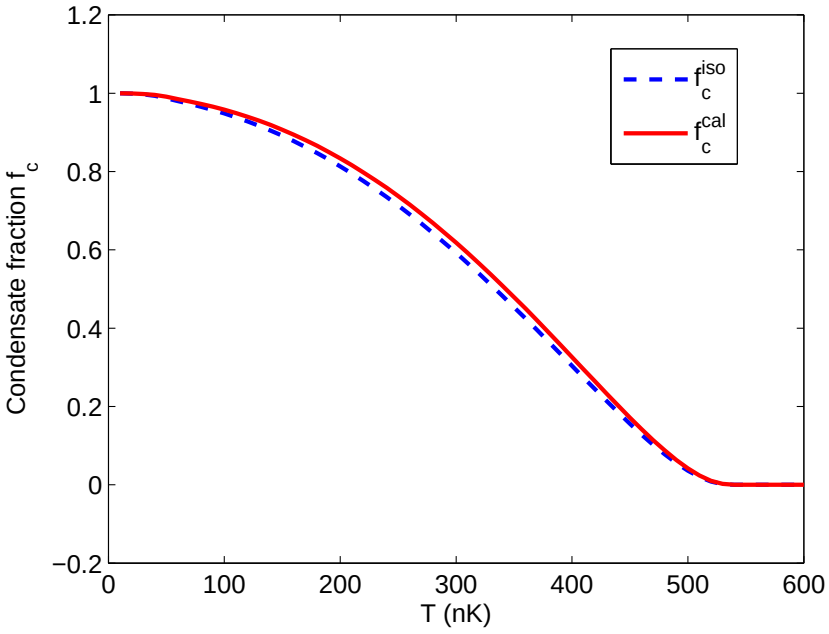


Figure 1.9: Comparison between f_c^{cal} and f_c^{iso} at $q = 0$.

including the temperature T and the condensate fraction f_c. In the experiment, the measurement of $1-n_0$ curve *does not* require to distinguish the condensate from the thermal clouds. We only need to count the total atom number in $m_F = 0$ state. We will discuss the experimental realization in chapter 2.

We must remind here again that this is a mean-field calculation, which neglect completely the fluctuations. In fact, as we will see in chapter 4, fluctuation will change the behavior of $1-n_0$ curve at low q. But the qualitative conclusions in this section are still valid, and the semi-ideal Hartree-Fock approximation will be also adopted.

1.5 Conclusion

In this chapter, we have discussed the basic theory of the spinor Bose-Einstein condensate. We begin with the simple scalar case, and introduce the semi-ideal Hartree-Fock method to describe the interactions between condensate and thermal clouds. This method, proven to be simple but effective, is also used in the simulation of spinor BEC.

Because of the supplementary degree of freedom, spin, the spinor BEC shows rich physics even near zero temperature. In section 1.3, we deal with the ground state of the condensate by mean-field approach. Essentially, this approach replaces the field operator of each spin component directly by a complex number, which neglect the quantum fluctuations of the system. Under this approximation, we find out a phase transition at some critical magnetic field $B_c(m_z)$. Below B_c the system is in the "anti-ferromagnetic" state with $N_0 = 0$, and above B_c the system is in the "broken-axisymmetry" state with $N_0 > 0$. This phase transition has been already observed in the experiment [38], and will be discussed in detail in chapter 3. A full quantum solution at $T = 0$ will be developed in chapter 4.

In section 1.4, we combine the results about the ground state of the condensate in section 1.3 and the semi-ideal Hartree-Fock approximation used in section 1.2.3 to calculate the behavior of the spinor BEC at finite temperatures. We still focus on N_0 as a function of magnetic field B, although now it is given by a condensate contribution plus a thermal contribution, $N_0 = N_0^c + N_0^{\text{th}}$. We plot $1-n_0$ as a function of B and find out

- the value of $1-n_0$ at low q is related to the condensate fraction f_c.
- the HWHM $q_{1/2}$ is related to the temperature T.

This quantity is easy to measure in the experiment, because we do not need to distinguish the condensed and thermal component in each Zeeman sub-level, which can be difficult to do especially for small atom numbers and tight traps [49, 43]. In chapter 4, we will first complement this calculation by adopting the full quantum solution of the H_{SMA} mentioned above and realize the measurements.

Chapter 2

Experimental realization and diagnosis of spinor Bose-Einstein Condensates

2.1 Introduction

Achieving the Bose-Einstein condensation (BEC) requires several important techniques in the experiment [33], including laser cooling and trapping, evaporative cooling, *etc.* Laser cooling was developed in 1980s [5, 4, 6], and allows one to decrease the temperature of an atomic sample from the room temperature directly to mK regime [33]. Laser cooling inside a magnetic field gradient, forms a so-called Magneto-Optical Trap (MOT) [50] which proved to be ideal as the pre-cooling technique to reach BEC. Evaporative cooling, which is the second crucial technique to reach BEC, was first developed in 1990s [51]. It can dramatically improve the phase space density of the pre-cooled sample after the MOT and finally reach the BEC regime [10, 9]. Briefly speaking, our experiment will adopt this "MOT and Evaporative cooling" process. Because we focus on the spinor condensate, we will also talk about the techniques to prepare and diagnose the spinor condensate. The detail of each step will be discussed in the following sections.

In this chapter, we will explain how we achieve Bose-Einstein condensation in our experiments, and the techniques related to the control and diagnosis of the spinor condensate. We begin with a brief introduction of our vacuum system and experimental control system in section 2.2. The first step to the Bose-Einstein condensation is the Magneto-optical trap (MOT). After the MOT stage, we load the atoms from the MOT to the far-off resonance dipole trap. These two steps were extensively discussed in the PHD thesis of Emmanuel Mimoun [44] and David Jacob [43], and we defer a detailed discussion to the appendix A and B, including how to load the MOT, how to load the trap and how to force the atoms to the trap center. In section 2.3, we will talk about the evaporative cooling which is the last step to reach the Bose-Einstein condensation. At the end of the evaporation stage, we obtain the almost pure condensate with about 5000 atoms. In section 2.4, we discuss the experimental techniques related to spinor condensates control and diagnosis. In section 2.5, we will focus on the imaging system. At the end of this chapter in the section 2.6, we will talk about the image analysis, first discussing how

to extract useful informations from the fitting, and then how to reduce the noise in the image to improve its quality.

2.2 Vacuum system and experimental control

In Fig. 2.1, we show an overall view of the setup around the science chamber. Six crossed beams of 589 nm laser combined with the anti-Helmholtz coils form the Magneto-Optical Trap, which will be discussed in section A. Two crossed beams of 1064 nm infrared laser form the Large-Crossed dipole trap, which will be discuss in section B. Pumps (not shown in Fig. 2.1) are used to maintain the vacuum inside the science chamber. A Bose-Einstein condensation experiment requires very high vacuum in the science chamber. The collisions between trapped cold atoms and atoms of the residual gas at room temperature will immediately "kick" the cold atoms out of the trap. Such collisions thus decrease the life time of the trapped cloud and must be avoided. Normally, in our experiment, the background pressure in the science chamber is about 10^{-11} mbar [52, 43], which is maintained by two sets of pumps, a getter pump and an ion pump.

The science chamber is made of Titanium which is paramagnetic with a low magnetic susceptibility. This is crucial for the spinor condensate experiment because of the sensitivity to magnetic field. The science chamber is equipped with several viewports allowing wide optical access, antireflection coated for 589 nm (MOT and imaging) and 1064 nm (optical dipole trap). Lateral viewports (CF25) gives access for the six MOT beams and optical dipole trap beams. Two larger viewports (CF63) along the vertical axis allow us to install a large numerical aperture (NA) objective for high resolution imaging [52].

A Bose-Einstein condensation experiment requires also very precise response timing of each optical and electronic elements, for example, the timing of the switch on/off of current in the coil for the magnetic field. We use the input/output cards made by National Instrument to communicate between a computer, giving the commands, and the instruments. The precise sequence of instructions is managed by a software from MIT (Cicero, Atticus) which also handles the communication with the National Instrument cards [53]. These cards, analog or digital, are all synchronized with a precision better than 1 μs which guarantees the response timing.

2.3 Evaporative cooling to BEC

The first step to the Bose-Einstein condensation is the Magneto-Optical Trap (MOT), which is summarized in appendix A. After the MOT, we have about 2×10^7 atoms with temperature $T \approx 200$ μK. After the MOT, we load the atoms into the large crossed dipole trap and do the compression, which is summarized in appendix B. After the compression, we have about 1.4×10^5 atoms with temperature $T \approx 100$ μK.

After the compression in the Large-CDT, we start evaporative cooling. Evaporative cooling is proved to be very efficient for many kinds of atoms [54, 55, 22]. During the evaporation, we will reach the regime of Bose-Einstein condensation. The most crucial

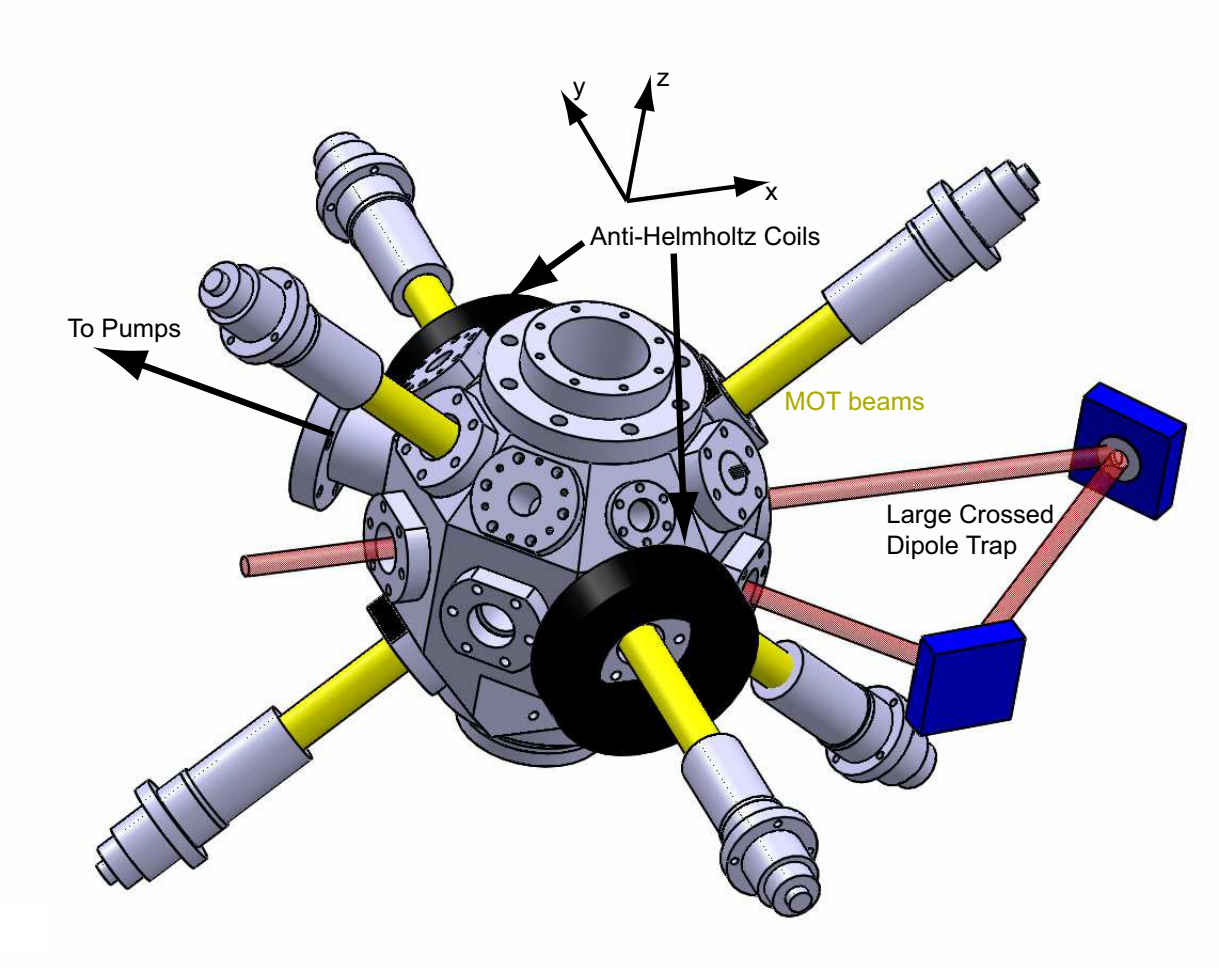


Figure 2.1: Sketch by CATIA illustrating the experimental configuration around the science chamber, showing the six beams of the 589 nm cooling laser, the pair of anti-Helmholtz coils for the MOT, and the Large Crossed Dipole Trap.

point in the evaporative cooling is to keep the elastic collision rate high which helps us to evaporate the hot atoms out of the trap [33]. In our experiment, as the evaporation goes on, the Large-CDT can not keep the efficiency always high. This is the reason why we introduce the second evaporation in the more confined, deeper composite dipole trap, Small Crossed Dipole Trap (Small-CDT), which is composed by a Small Vertical Dipole Trap (Small-VDT) and a Small Horizontal Dipole Trap (Small-HDT). At the end of the evaporation in the Small-CDT, we realize an almost pure Bose-Einstein Condensate with about 5000 atoms.

In this section, we begin with the introduction of the basic ideas of the evaporative cooling. In the second part, we introduce our experimental configuration of the Small-CDT, which is composed by Small-VDT and Small-HDT. In the third part, we introduce our two steps evaporation. In the first step, the evaporation carries out mainly in the Large-CDT in order to fill the atoms to the Small-CDT. It helps to increase the phase space density $\mathcal{D}$ (detail in section 2.3.1), and in the second step, the evaporation is realized purely in the Small-CDT until we reach the BEC regime.

2.3.1 Elements of evaporative cooling

We consider here an equilibrium gas with N atoms and temperature T confined in the harmonic potential with trap frequency ω. During evaporative cooling, the system evaporates the "hotter" atoms and reaches the new equilibrium state. The crucial point is that whether the system can reach the new equilibrium sufficiently quickly. Elastic collisions play the central role to drive the system towards equilibrium. The elastic collision rate Γ_e can be expressed as follows [56]

$$\Gamma_e = \sqrt{\frac{2}{\pi}} n_0 \sigma \bar{v} = \frac{m\omega^3 \sigma}{2\pi^2 k_B} \cdot \frac{N}{T}. \tag{2.1}$$

with n_0 the spatial density, σ the cross section, $\bar{v}$ the mean velocity and m the mass of the atom. In order to keep the evaporative cooling effective, we must first ensure a sufficiently large Γ_e in order to let the system reach the new equilibrium quickly enough.

The total energy of a non-degenerate gas in a harmonic trap, including kinetic and potential energy, is given by

$$E = 3Nk_BT. \tag{2.2}$$

If we evaporate $\mathrm{d}N$ atoms with energy larger than the trap depth $U = \eta k_B T$, atom evaporated having energy $(\eta + \kappa)k_BT$ on average, the lost energy of the system is

$$\mathrm{d}E = \mathrm{d}N\,(U + \kappa k_B T) = \mathrm{d}N\, k_B T(\eta + \kappa) \quad \rightarrow \quad \frac{\mathrm{d}E}{E} = \frac{\eta + \kappa}{3}\frac{\mathrm{d}N}{N}. \tag{2.3}$$

As a result, $N - \mathrm{d}N$ atoms continue to re-thermalize in the trap in the help of the elastic collisions. They reach a new equilibrium state with temperature $T - \mathrm{d}T$ which can be determined by Eq. (2.2).

$$E - \mathrm{d}E = 3(N - \mathrm{d}N)k_B(T - \mathrm{d}T) \quad \rightarrow \quad \frac{\mathrm{d}T}{T} = \frac{\eta + \kappa - 3}{3}\frac{\mathrm{d}N}{N}. \tag{2.4}$$

According to Eq. (2.4), the temperature will decrease if $\eta + \kappa > 3$.

The phase space density $\mathcal{D}$ scales as N/T^3 [33], thus we have

$$\frac{\mathrm{d}\mathcal{D}}{\mathcal{D}} = \frac{\mathrm{d}N}{N} - 3\frac{\mathrm{d}T}{T} = -(\eta + \kappa - 4)\frac{\mathrm{d}N}{N}. \tag{2.5}$$

According to Eq. (2.5), the phase space density will increase if $\eta + \kappa > 4$, which imposes a higher condition if we want to increase the phase space density during the evaporation. A more complete study based on kinetic theory [51] indicates that $\kappa \sim 1$ under typical conditions.

Special difficulty for the optical trap In magnetic traps, the depth and the frequency of the trap are two independent parameters. We can control one of them without changing the other. A typical evaporation experiment in a magnetic trap starts with low Γ_e, increasing in time as the cloud gets colder and colder [51]. However, the situation is different for optical traps, because there is only one control parameter in the experiment:

the laser power. The trap frequency and the trap depth are both related to the beam power. If we decrease the power, the depth of the trap will decrease, but at the same time the trap frequency will also decrease ($\omega \sim \sqrt{U}$) which will decrease the elastic collision rate (Eq.(2.1)) and decrease the efficiency of the evaporative cooling.

In fact, in our experiment, we have tried to evaporate only in the Large-CDT. We realize a power ramp from 36 W to 200 mW exponentially. At the end of the evaporation, the phase space density $\mathcal{D} \approx 10^{-3}$ which is still far from the BEC threshold ($\mathcal{D}_{\mathrm{BEC}} \approx 2.6$). We also observed that the elastic collision rate decrease rapidly during the evaporation, which accords with the analysis above.

Therefore, in order to overcome this difficulty, we introduce a Small-Crossed Dipole Trap (Small-CDT) composed by a 1064 nm and a 1070 nm laser. These two traps are more confined, with the waist about 10 μm. We realize the evaporation in two steps, first, evaporate in the Large-CDT, at the same time, this will fill the Small-CDT, second, evaporate in the Small-CDT. This will solve the problem of the low collision rate, because the frequency of the Small-CDT is much larger than that of the Large-CDT, which make the evaporative cooling always efficient.

2.3.2 Experimental setup of the Small-CDT

In Fig. 2.2, we illustrate the configuration of the Small-CDT together with the Large-CDT by a view from the top. The Small-VDT propagates in the $+z$ direction, and the Small-HDT propagates in the $+u$ direction. Both Small-VDT and Small-HDT are focused and crossed at the waist of each beams at the center of the science chamber, the same as the Large-CDT.

2.3.2.1 Small Vertical Dipole Trap (Small-VDT)

The dipole trap "Small-VDT" is generated by a 500 mW laser with wavelength $\lambda_D = 1064$ nm, the same wavelength as the fiber laser for the Large-CDT. The laser is focused by a large numerical aperture (NA) objective into the science chamber. This objective also serves for imaging system, which will be discussed in section 2.5.2. The trap can be switched off rapidly by a Acousto-Optical Modulator (AOM) within several μs. In order to stabilize the power of the Small-VDT, we realize a power feedback system, which is similar to that of the Large-CDT, by measuring the power by a photo-diode (before the laser enters the science chamber) as the feedback signal. We measure the waist of the Small-VDT trap by parametric oscillation [57], which gives the size of the waist of Small-VDT

$$w_{\mathrm{SV}} \approx 9.05 \pm 0.02\ \mu\mathrm{m}. \tag{2.6}$$

2.3.2.2 Small Horizontal Dipole Trap (Small-HDT)

The dipole trap "Small-HDT" is generated by a 20 W fiber laser with wavelength $\lambda_{\mathrm{SH}} = 1070$ nm. The laser is focused by a $f = 200$ mm lens as illustrated in Fig. 2.2. As the Small-VDT trap, the Small-HDT is also controlled by a AOM and a power feedback system (feedback signal is measured after the laser passing the science chamber). The

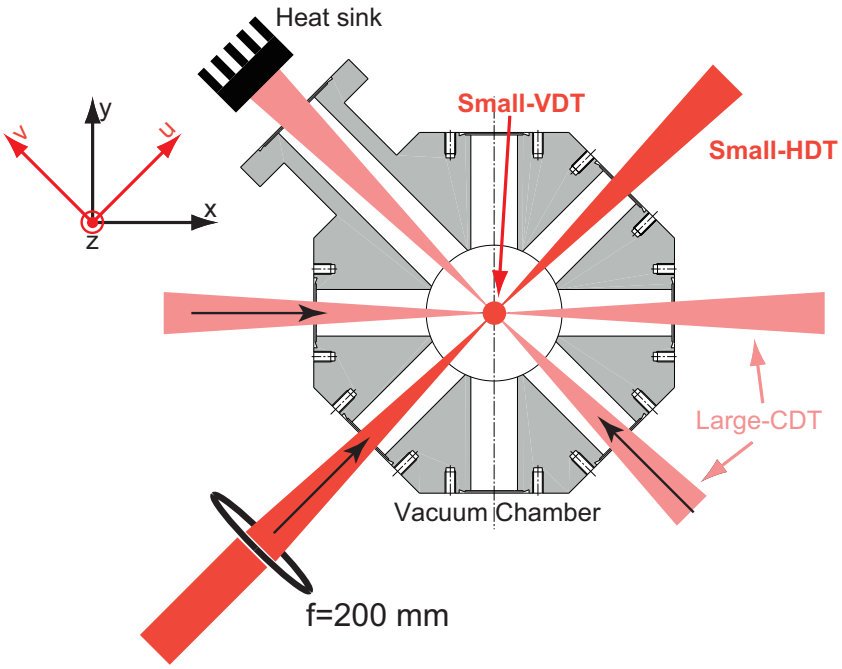


Figure 2.2: Large-CDT, Small-VDT and Small-HDT with the science chamber. (top view)

waist of Small-HDT trap is measured together with the Small-VDT trap by parametric oscillation [57], which gives the size of the waist of Small-HDT

$$w_{\mathrm{SH}} \approx 11.00 \pm 0.01\ \mu\mathrm{m}. \tag{2.7}$$

2.3.3 Two-step evaporation

As discussed in section 2.3.1, our evaporative cooling is realized by two steps. We illustrate in Fig. 2.3 the global view of the laser powers of the three dipole traps as a function of t (t=0 means the beginning of the evaporation) during the experiment, including the Large-CDT loading, compression, the first and the second evaporation. The sub-figure (a), (b), (c) represent the power of the Large-CDT, Small-VDT and Small-HDT, respectively.

2.3.3.1 First evaporation

The first evaporation lasts 2 seconds. The main purpose of this process is to fill the atoms from the Large-CDT to the Small-CDT. In Fig. 2.4, we plot the composed potential of the Small-VDT+Large-CDT (blue line) and the potential of the Large-CDT only (red line). We suppose the power of the Large-CDT $P_{\mathrm{CDT}} = 1.5$ W and the power of the Small-VDT $P_D = 250$ mW, which corresponds to the powers around the middle of the first evaporation ($t = 1.5\ s$ in Fig. 2.3). We can see clearly from Fig. 2.4 that when we decrease the power of the Large-CDT, the trap depth of the Small-VDT is much larger than that of the Large-CDT. As the temperature decreases during the evaporative cooling, atoms will gradually fill in the more confined, deeper trap, the Small-VDT.

The first evaporation is composed by two stages. During the first second, as shown in

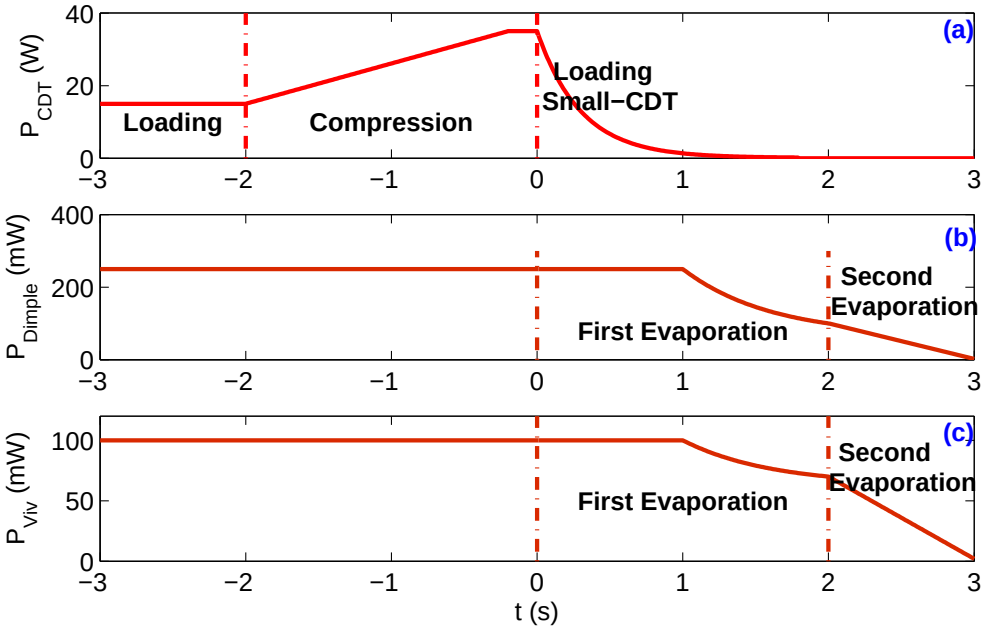


Figure 2.3: Schema of the laser powers of the three dipole traps during the experiment (Large-CDT Loading, Compression, First and Second Evaporation). Fig. (a), (b), (c) represent the Large-CDT, Small-VDT and Small-HDT, respectively.

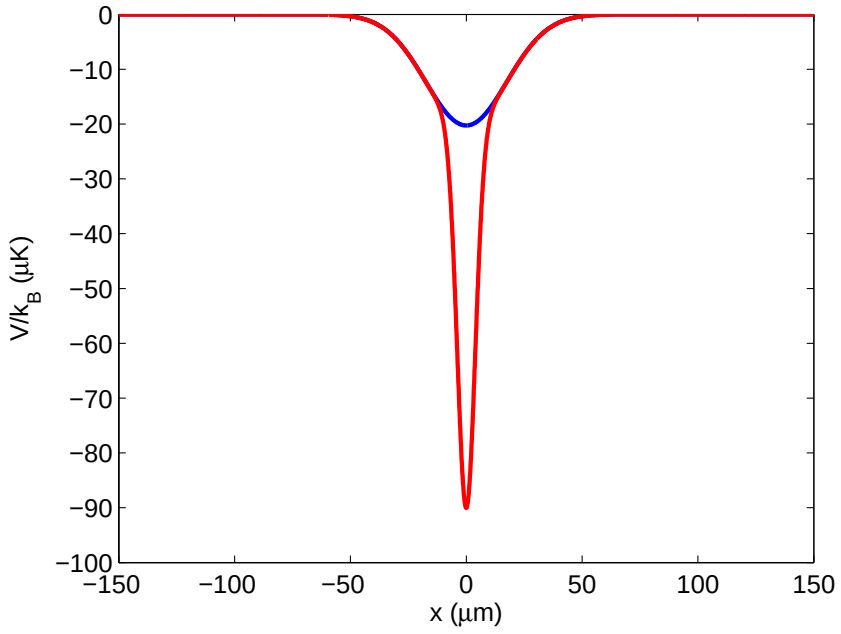


Figure 2.4: Potential of the Small-VDT and the Large-CDT. The blue line represents the Large-CDT only, the red line represents the Small-VDT+large-CDT. During the first evaporation, atoms will fill the more confined, smaller trap.

Fig. 2.3, the power of the Large-CDT decreases exponentially from 35 W to about 1.5 W with $\tau = 300$ ms, the powers of the Small-VDT and Small-HDT keep constant, 250 mW and 100 mW respectively. The atoms loading from the Large-CDT to Small-CDT is mainly during this stage. We keep the powers of Small-VDT and Small-HDT always at high level in order to make the loading process more efficient. After this "Small-CDT loading" process, we have about 4×10^4 atoms with temperature $T \approx 6$ mK. But the most important is that the phase space density reach $\mathcal{D} \approx 0.25$, which can not be achieved without the help of the Small-CDT. In section 2.3.1, we have mentioned that with only Large-CDT, we can only reach $\mathcal{D} \approx 10^{-3}$.

In the next second, the power of the Large-CDT continues to decrease. We switch off completely the Large-CDT 200 ms before the beginning of the second evaporation, in order to eliminate the influence of the Large-CDT. The power of the Small-VDT decrease exponentially from 250 mW to 100 mW with $\tau = 600$ ms. The power of the Small-HDT decrease exponentially from 100 mW to 70 mW with $\tau = 600$ ms. After the switch-off of the Large-CDT, the Small-HDT serves to hold the atoms counter the gravity. In fact, the powers shown above are chosen empirically, in order to have more atoms and make the shape of the atom cloud as isotropic as possible.

After the 2 seconds first evaporation, we have about 1.4×10^4 atoms with temperature $T \approx 4$ μK, phase space density $\mathcal{D} \approx 0.8$, very close to the threshold for Bose-Einstein condensation.

2.3.3.2 Second evaporation

The second evaporation follows immediately after the first evaporation. It is the final step to the Bose-Einstein condensation. The second evaporation lasts 1s. As illustrated in Fig. 2.3, the power of Small-VDT decreases linearly from 100 mW to 2 mW and the power of the Small-HDT decreases linearly from 70 mW to 2mW. In this stage, the Large-CDT is already switched off. The atoms are evaporated purely in the Small-CDT composed by Small-VDT and Small-HDT.

We show in Fig. 2.5 the atom number N, temperature T, and the condensate fraction f_c as a function of the second evaporation time t' ($t' = t - 2$). We also show the condensate fraction f_c as a function of the temperature. We find that at about $t' = 0.2$ s, we reach the threshold of BEC where f_c is no longer zero. Finally, at the end of the second evaporation, we have a almost pure condensate with about 5000 atoms. We remark that in Fig. 2.5, f_c is only about 0.6 at the end of the evaporation. In fact, this condensate fraction is fitted by Eq. (2.27), which is not reliable for large f_c. We will return to this point in section 2.6.1.

In conclusion, after MOT cooling, Large-CDT loading, compression, first and second evaporation, finally, we have a almost pure condensate with about 5000 atoms. This is the ultra-cold atom sample for our future experiments.

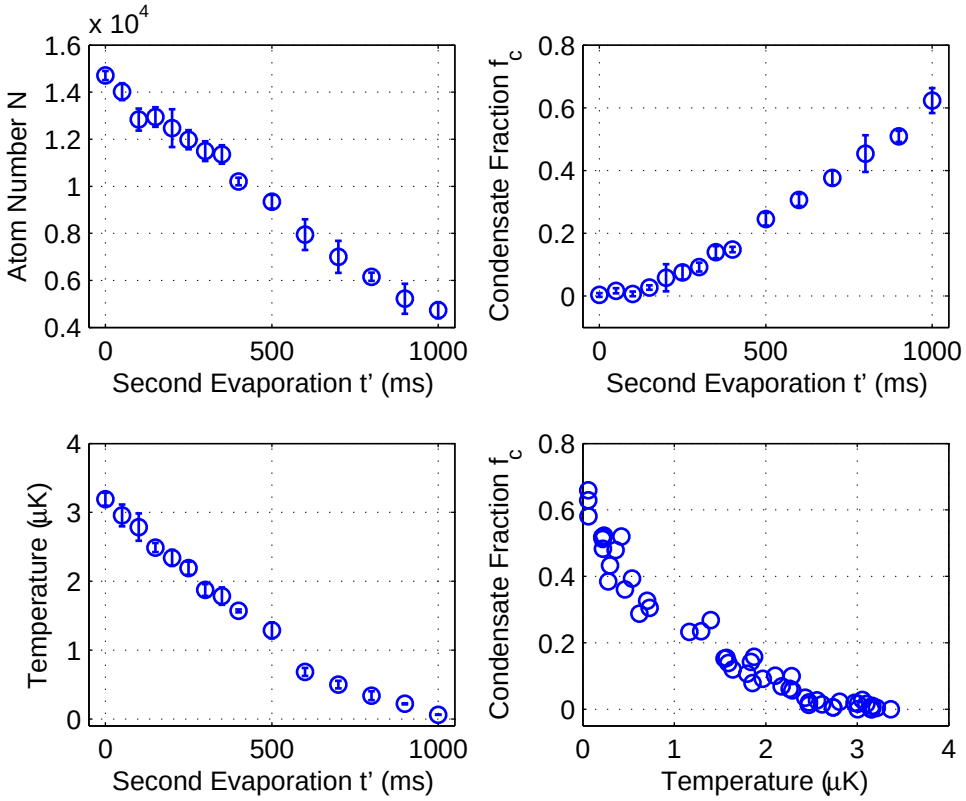


Figure 2.5: Atom number, condensate fraction, phase space density, as a function of the second evaporation time t'.

2.4 Spinor condensate preparation and diagnosis

We have reached the Bose-Einstein condensation after the two steps evaporative cooling. Finally, we obtain the spinor condensate of sodium on $F = 1$ hyperfine state, with three Zeeman sub-levels, $m_F = +1, 0, -1$. In our experiment, we need both to control and to diagonalize the magnetization $m_z = (N_{+1} - N_{-1})/N$ of the spinor condensate sample. As we have pointed out in chapter 1, the magnetization m_z is conserved, and do not change during the evaporation. However, there are several techniques to change the magnetization. We adopt here the spin distillation and Radio-Frequency (RF) magnetic field oscillation to increase and decrease the magnetization respectively [58, 59].

In this section, we begin with the introduction of the coils which serve to control the magnetic field. In the second part, we introduce the methods to control the magnetization of the sample. In the last part, we talk about the diagnosis of the spinor gas, which means how to measure the magnetization m_z.

2.4.1 Magnetic field control

We show in Fig. 2.6 the configuration of the coils we use to generate magnetic field in our experiment. The currents in the coils are alimented by *High Finesse* power supplies.

The ensemble of the coils in Fig. 2.6 can be divided into 4 groups.

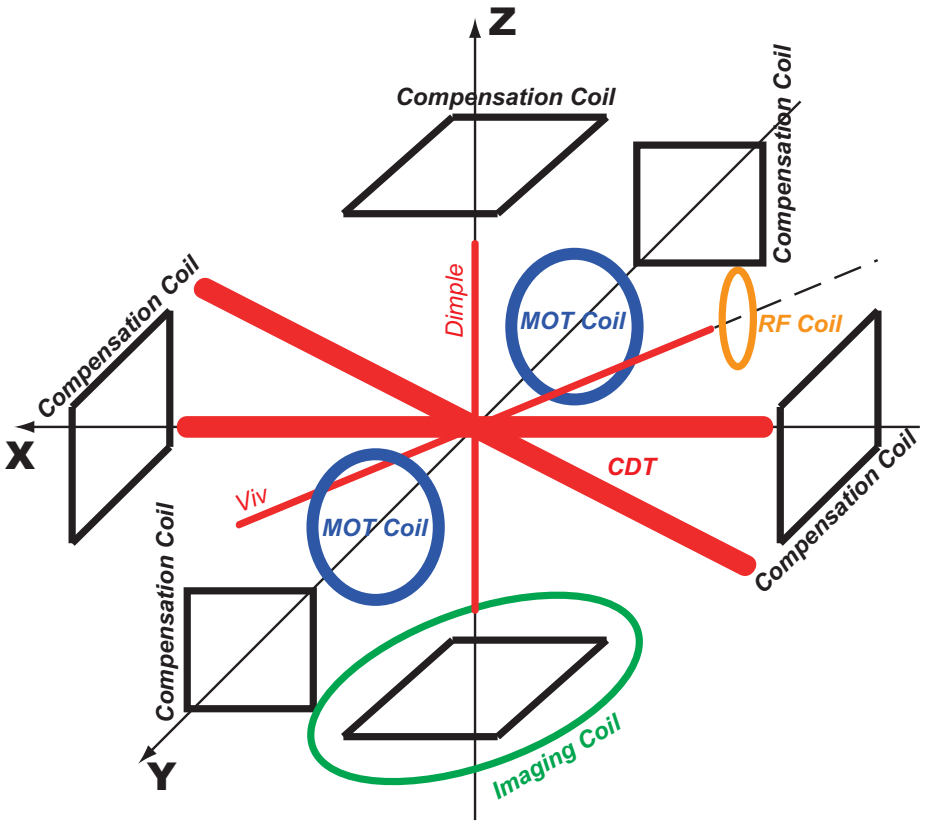


Figure 2.6: Illustration of the coils with dipole traps in the experiment

The first group consists of three Helmholtz pairs, which are illustrated in Fig. 2.6 by black squares. These three pairs of coils are along 3 axis, x, y, z, creating approximately uniform magnetic field in the science chamber in three directions.

In order to well control the value of the magnetic field at the position of the condensate, we should calibrate these coils, relating directly the current in each coil I_x, I_y, I_z with the magnetic field at condensate B_x, B_y, B_z. We have

$$B_{\text{tot}} = \sqrt{(\alpha_x I_x + B_{0x})^2 + (\alpha_y I_y + B_{0y})^2 + (\alpha_z I_z + B_{0z})^2} \tag{2.8}$$

Here, B_{tot} is the total magnetic field. In Eq. (2.8), we have assumed that the coils for one axis create only the magnetic field in the corresponding axis in neglecting the magnetic field created perpendicular to the axis of the coil.. The calibration of the coils is to determine the coefficient α_x, α_y, α_z and the bias field B_{0x}, B_{0y}, B_{0z}, which are external bias fields present in the lab (*e.g.* Earth magnetic field). We adopt the Rabi oscillation to calibrate the magnetic field. With a given magnetic field B_{tot}, the three sub-levels ($m_F = +1, 0, -1$) split because of the linear Zeeman effect. We measure the resonant frequency f_{res} of the Rabi oscillation among these sub-levels. We have

$$f_{\text{res}} = g_F \mu_B \times B_{\text{tot}} \approx 700 \text{ kHz/G} \times B_{\text{tot}}. \tag{2.9}$$

A systematic series of measurements varying I_x, I_y, I_z gives

- $\alpha_x = 0.29$ G/A, $B_{0x} = -107.4$ mG;
- $\alpha_y = 0.51$ G/A, $B_{0y} = -70.9$ mG;
- $\alpha_z = 1.79$ G/A, $B_{0z} = -346.9$ mG;

The vertical bias is the largest, presumably due to the contribution of Earth magnetic field.

The second group is a pair of anti-Helmholtz MOT coils, illustrated in Fig. 2.6 in blue circle. They can generate a magnetic field gradient (up to about 15 G/cm) for MOT and spin distillation and diagnosis which will be discussed in section 2.4.2.1 and section 2.4.3.

The third group is the RF coil, illustrated in Fig. 2.6 in yellow circle. It is used to create a magnetic field oscillation at Radio-Frequencies (RF), typically at 100 kHz which can excite the Rabi-oscillation mentioned above and can depolarize magnetization of the condensate. This depolarization process will be discussed later in section 2.4.2.2

The last group is the imaging coil, illustrated in Fig. 2.6 in green circle. It is used to generate the magnetic field to fix the quantization axis on z for the facility of the imaging. We will return to this point later in section 2.5.

2.4.2 Magnetization controlled spinor gas preparation

In our experiment, the "natural" magnetization after laser cooling is $m_z \approx 0.5$ which is kept constant during the evaporation. In the next chapter, we will study the phase diagram at low temperature for different magnetizations. Therefore, we need to control the magnetization in our experiment. In this part, we discuss two methods to change the magnetization. The spin distillation [58, 59] is used to increase the magnetization and the RF field oscillation is used to decrease the magnetization.

2.4.2.1 Polarization by magnetic field gradient

In order to increase the magnetization of the condensate, we adopt the so-called "spin distillation" during the compression stage. As the normal distillation which separates mixtures based on differences in volatility of components in a boiling liquid mixture, the spin distillation separates different spin components based on differences in the energy shift by the magnetic field. In order to increase the magnetization, we should distill more atoms in $m_F = -1$ compared with atoms in $m_F = +1$. We apply a constant field B_0 in vertical direction z by the Helmholtz pair in z axis, and use the anti-Helmholtz pair (axis along y) to generate a strong magnetic field gradient ∇B, leading to a spin dependent potential in $+z$ direction given by

$$U_{\nabla B} = \frac{\mu_B m_F b'}{4}, \tag{2.10}$$

where b' is the field gradient defined by Eq. (A.4). In addition, atoms are influenced also by the gravity potential which is independent of m_F,

$$U_G = m_{\mathrm{Na}} g. \tag{2.11}$$

with g the gravitational acceleration, m_{Na} the mass of sodium atom.

In order to distill more atoms in $m_F = -1$ and remains as many as possible $m_F = +1$. The potential by magnetic field gradient $U_{\nabla B}$ should be compensated by the gravity potential U_G for $m_F = +1$, as illustrated in Fig. 2.7, the net potential for $m_F = +1$ is almost not inclined, whereas the potentials for $m_F = 0, -1$ are both inclined. The slope for $m_F = -1$ is larger than that for $m_F = 0$ and $m_F = +1$, more atoms in $m_F = -1$ are distilled. The condition of the compensation between $U_{\nabla B}$ and U_G is give by

$$b' = \frac{4 g m_{\mathrm{Na}}}{\mu_B} \approx 16.2 \text{ G/cm}. \tag{2.12}$$

In our experiment, the vertical bias field is about 0.5 G. We vary the b' to get different magnetization larger than 0.5. We illustrate in Fig. 2.8, the magnetization m_z as a function of $\mu_B b'/4 g m_{\mathrm{Na}}$ for $m_z > 0.5$. We find that with stronger magnetic field gradient, m_z is larger and for $\mu_B b'/4 g m_{\mathrm{Na}} \sim 1$, we have $m_z \sim 0.9$.

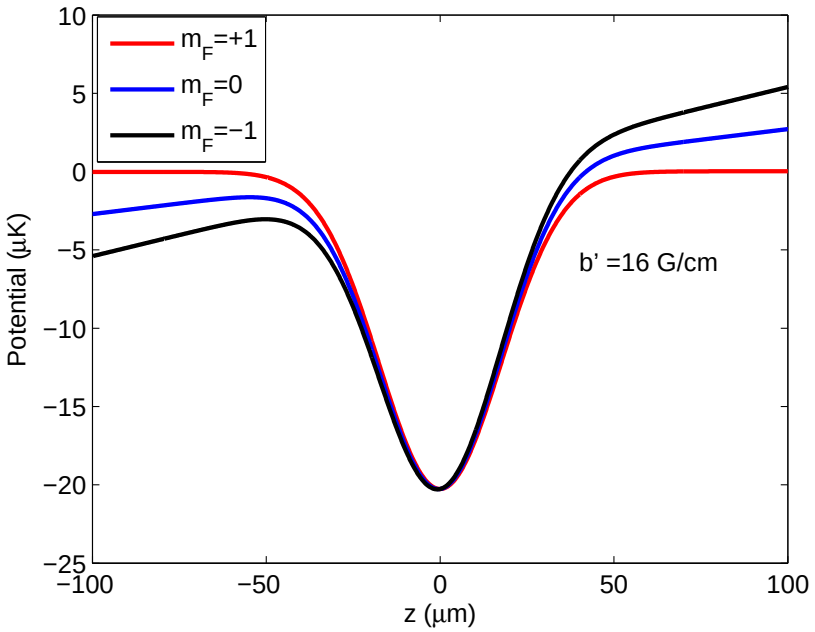


Figure 2.7: Illustration of the potential for different spin component for the distillation. ($m_F = +1, 0, -1$)

2.4.2.2 Depolarization by radio frequency (RF) magnetic field oscillation

In order to get lower magnetization ($m_z \approx 0 \sim 0.5$), we apply a horizontal bias magnetic field about 250 mG and apply a Radio-Frequency (RF) oscillating magnetic field resonant

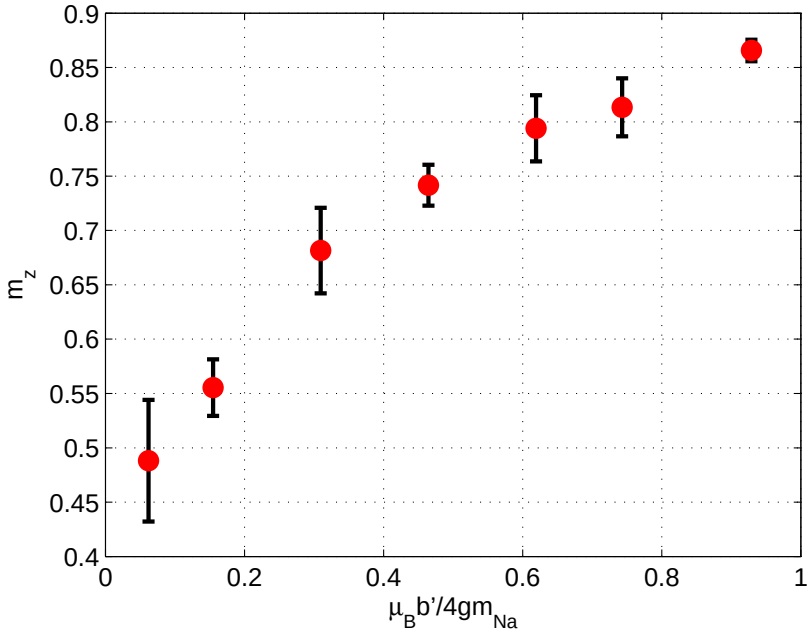


Figure 2.8: Spin distillation for high magnetization preparation ($m_z > 0.5$).

at the Rabi frequency for a variable duration during the compression stage. According to Eq. (2.9), the resonant frequency $f_{\rm res} = 700$ kHz/G $\times$ 0.25 G = 175 kHz. With the help of the RF, as the atoms move and collide in the Large-CDT, their spin quickly decohere, and produce a spin-isotropic mixture. By adjusting the RF field depolarization time, we can adjust the final magnetization as will, as shown in Fig. 2.9. The RF resonance is about 2kHz wide, presumably limited by inhomogeneous broadening (introduced by the magnetic field gradient b'). To ensure that small frequency drifts do not perturb significantly the preparation, the frequency of the oscillating field is swept over 20 kHz at a slow rate during the whole depolarization sequence.

2.4.3 Spin diagnosis

In this part, we will discuss the spin diagnosis, which means how to measure the magnetization m_z [38]. In order to count the population in each Zeeman sub-levels, we should first separate different spin component by a magnetic field gradient, as in the Stern-Gerlach experiment. The gradient of the magnetic field is set to $b' \approx 15$ G/cm, which is almost the maximum value we can reach with the MOT coils. We apply an additional bias field in x direction with $B_x \approx 2$ G, this produces a force along the horizontal x axis that separate the atoms in $m_F = \pm 1$ states from the atoms in $m_F = 0$ by a distance $d_{\rm SG}$ after a period of time t. We have

$$d_{\rm SG} = \frac{\mu_B \eta b' t^2}{4 m_{\rm Na}}, \tag{2.13}$$

with μ_B the Bohr magneton and t the expansion time. The factor η takes into account the temporal profile of the gradient, which rises in a few ms after the beginning of the expansion. In Fig. 2.10, we show the vertical trajectory of the atoms measured in the

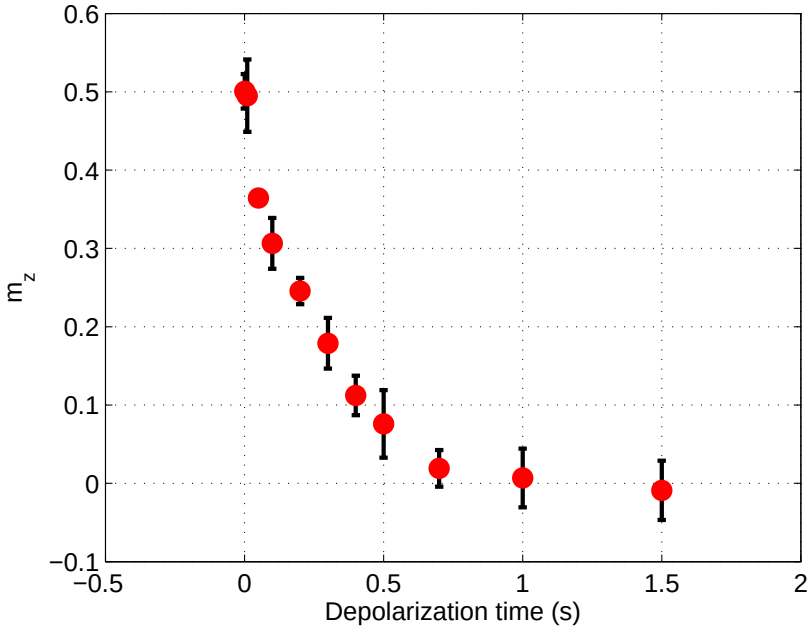


Figure 2.9: Depolarization to prepare samples with low magnetizations ($m_z < 0.5$). The time shown corresponds to the length of a radio-frequency pulse at the Larmor frequency.

experiment, and we compare it with the result calculated form the measured gradient variations $b'(t)$. The good agreement indicates that the gradient behavior is well understood.

After a given expansion time (typically $t \approx 3.5$ ms), we take an absorption image of the clouds and count the atom number in each Zeeman component. In order to obtain reliable images, the separation distance d_{SG} must be much larger than the cloud size R_t after expansion to clearly separate each Zeeman component. In our experiment, when the trap is switched off instantaneously, we typically achieve $d_{\mathrm{SG}}/R_t \sim 1$ only. This is due to the tight trap frequencies and the resulting fast expansion. Therefore, we can not distinguish clearly each Zeeman component when they are overlapped over each other. The magnetic field gradient can not be increased further due to technical limitations, and the expansion time is also limited by the necessity to keep a sufficiently large signal-to-noise ratio to detect atoms in each component.

As a result, we adopt a so-called slow attenuation technique during the Stern-Gelarch separation. We slowly ramp down the laser intensity to approximately 1/10th of its initial value within 5.5 ms before switching it off abruptly. In fact, if we switch off the trap at the beginning, the interaction energy will all convert to kinetic energy for the atoms [60], therefore, the atom cloud expand very quickly. If we switch off the trap at 1/10th of its initial value, the initial interaction energy is lowered. As a result, the expansion speed will be much less. At the same time, this slow attenuation also leaves time for the magnetic gradient to increase to its maximum value, leading finally to $d_{\mathrm{SG}}/R_t \approx 10$ for an expansion time $t \approx 3.5$ ms. We show in Fig. 2.11, the sizes of the expanding clouds

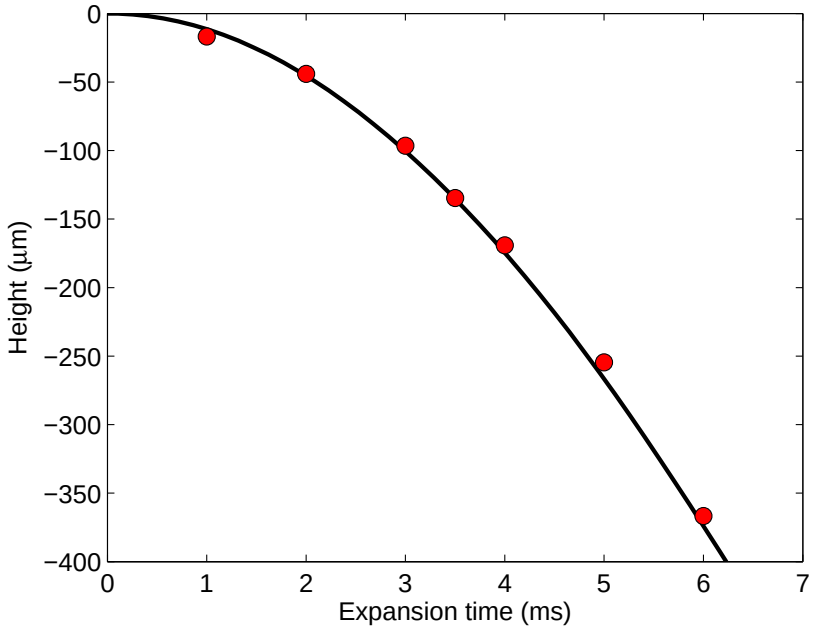


Figure 2.10: Trajectory of atoms in $m_F = +1$ along the vertical direction z. The red point is the measured results, the solid line shows the calculated trajectory taking the measured magnetic field gradient and gravity into account.

after an expansion time both for an instantaneous release and a smooth release. We find the expanding speed is slower after the attenuation by a factor ~ 2. In Fig. 2.12, we illustrate the atom number counted for instantaneous release and smooth release, we find that the atoms are not lost during this slow attenuation process (This is no longer true for very hot clouds near T_c, but holds for the experiments described in this thesis).

2.5 Imaging

In this section, we will introduce the imaging system in our experiment. In order to study the physics of the Bose-Einstein condensate, we should have method to diagnose the sample. The normal probe which contact the sample to diagnose can not be adopted. Simply because the atom sample has much less atoms than the smallest material probe, this will cause the atoms to equilibrate with the probe rather than the opposite. As a result, the optical diagnosis is the only choice [33].

There are many kinds of imaging methods, fluorescent or absorption, *in-situ* or Time-Of-Flight (TOF) [33]. In this section, we will focus on the imaging method which use most frequently in our experiment, the absorption image after a period of TOF. In fact, in our "micro-condensate" experiment, we realize the BEC sample with relatively small atom number ($3000 \sim 5000$). The size of the sample is around the resolution of our imaging system (several μm). As a result, we take the image after a period of TOF.

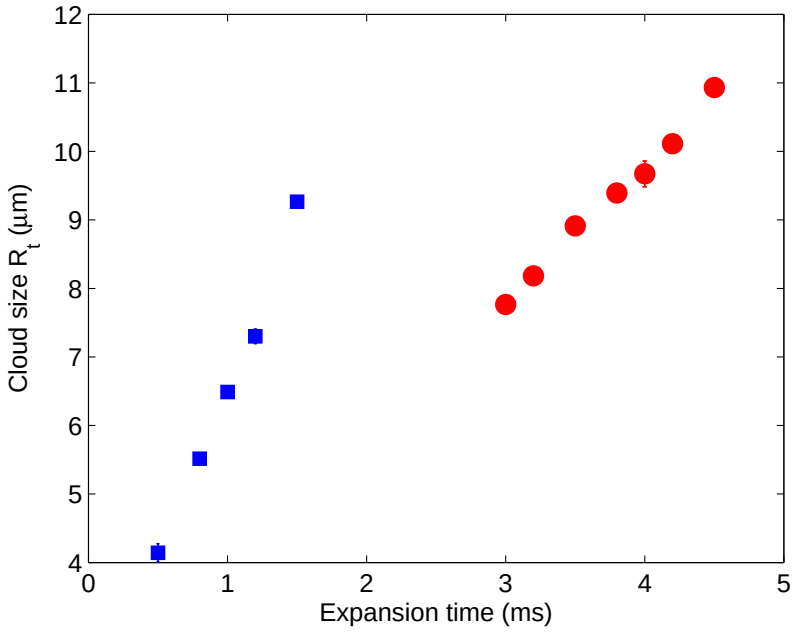


Figure 2.11: Sizes of the expanding clouds after an expansion time for an instantaneous release (blue squares) or a smooth release (red circles).

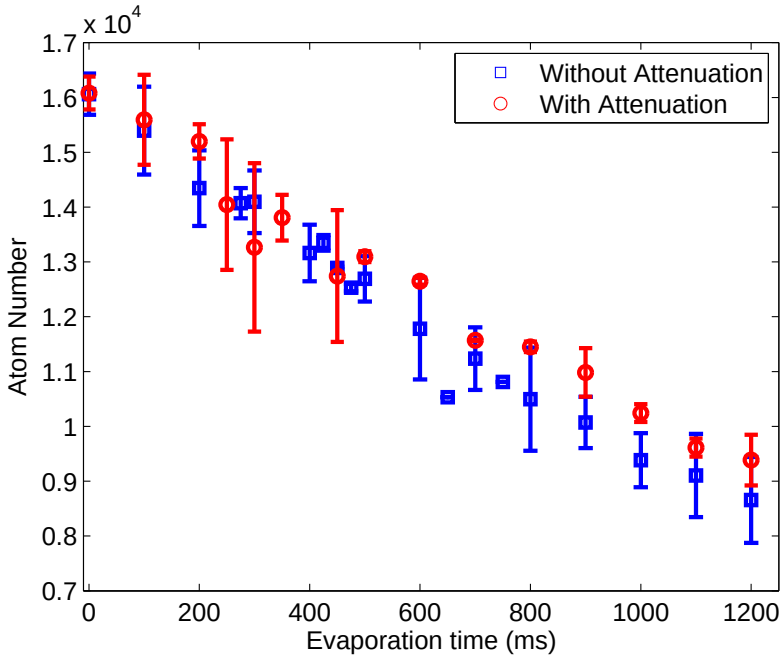


Figure 2.12: Atom number measured for instantaneous (blue squares) and smooth (red circles) releases, for various evaporation times.

In this section, we begin with the basic ideas of the absorption imaging. In the second part, we will introduce our imaging system in detail. In the last part, we will talk about a special method to take absorption image, the "Kinetics mode".

2.5.1 Absorption imaging

The purpose of the absorption imaging is to measure the column space density distribution of the atom sample $n_c(x, y)$ which is the normal space density distribution $n(x, y, z)$ integrated along the direction of the probe light, in our case, in direction z,

$$n_c(x, y) = \int n(x, y, z)\ \mathrm{d}z. \tag{2.14}$$

We denote I the light intensity, according to the Beer-Lambert law, in the presence of the saturation effect and for a resonant incident light, we model the probe absorption by [61]

$$\frac{\mathrm{d}I}{\mathrm{d}z} = -n(x, y, z)\frac{\sigma_0}{\alpha^*}\frac{1}{1 + I/I_{\mathrm{eff}}^{\mathrm{sat}}} \cdot I \equiv -n\sigma(I)I, \tag{2.15}$$

where $\sigma_0 = 3\lambda^2/2\pi$ is the resonant cross section for a two-level atom, $I_{\mathrm{eff}}^{\mathrm{sat}}$ is the effective saturation intensity, with $I_{\mathrm{eff}}^{\mathrm{sat}} = \alpha^* I_0^{\mathrm{sat}}$ (I_0^{sat} is the saturation intensity for a two-level atom). $I_{\mathrm{eff}}^{\mathrm{sat}}$, together with α^* describe the deviation from the two-level atom model, where we have $\alpha^* = 1$, thus $I_{\mathrm{eff}}^{\mathrm{sat}} = I_0^{\mathrm{sat}}$.

Integrating Eq. (2.15) over z, we have

$$n_c(x, y) = -\frac{\alpha^*}{\sigma_0}\ln\Big(\frac{I_t(x, y)}{I_i(x, y)}\Big) + \frac{1}{\sigma_0}\frac{I_i(x, y) - I_t(x, y)}{I_0^{\mathrm{sat}}}, \tag{2.16}$$

with $I_t(x, y)$ the transmitted light intensity and $I_i(x, y)$ the incident light intensity.

If we work at low intensity, which means $I \ll I_{\mathrm{eff}}^{\mathrm{sat}}$, the Beer-Lambert law (Eq. (2.15)) can be simplified as

$$\frac{\mathrm{d}I}{\mathrm{d}z} = -n(x, y, z)\frac{\sigma_0}{\alpha^*}, \tag{2.17}$$

which leads to

$$n_c(x, y) = -\frac{\alpha^*}{\sigma_0}\ln\Big(\frac{I_t(x, y)}{I_i(x, y)}\Big). \tag{2.18}$$

In the absorption imaging, we take three images. $I_{\mathrm{atom}}(x, y)$, which denote the intensity with atoms, I_{no}, which denote the intensity without atoms as a reference, and I_{dark}, which denote the intensity without probe light (background signal). Therefore, we have

$$I_t = I_{\mathrm{atom}} - I_{\mathrm{dark}}, \tag{2.19}$$

$$I_i = I_{\mathrm{no}} - I_{\mathrm{dark}}. \tag{2.20}$$

For the simplicity of our later discussion, we introduce OD the optical depth, defined as

$$\mathrm{OD} = \sigma_0 \cdot n_c(x, y). \tag{2.21}$$

2.5.2 Imaging systems

In Fig. 2.13, we show the configuration of the imaging system in our experiment. The resonant probe light is from the 589 nm laser system introduced in section A.2 (probe 2), the probe light illuminate the atoms at the center of the science chamber from the CF63 viewport upside. The intensity of the probe light $I_i \approx 1$ mW/cm^{-2}, the saturation intensity $I_0^{\text{sat}} \approx 6.26$ mW/cm^{-2} for sodium D_2 line with polarization σ^+. Therefore the saturation parameter $s = I_i/I_0^{\text{sat}} \approx 0.16$. For each image, the pulse of probe light lasts 10 μs.

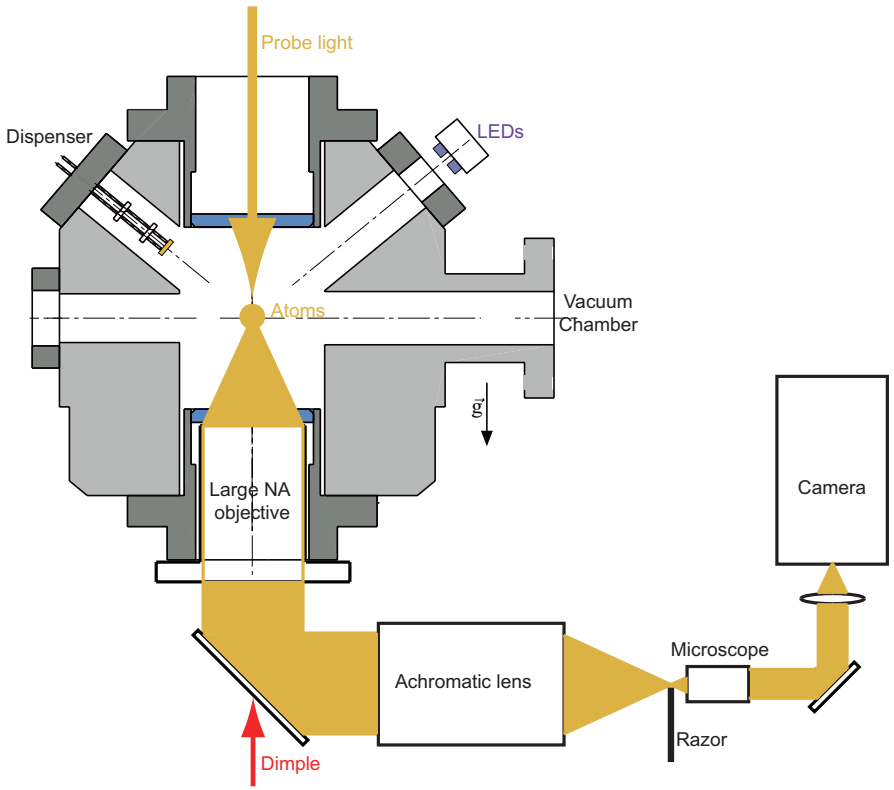


Figure 2.13: The optical imaging system of the absorption imaging

The scattered light is accumulated by a large numerical aperture (NA) objective designed for our experiment. This objective is mounted very close to the CF63 viewport downside in order to be as close as possible to the atoms to get larger NA. In our experiment, NA $\approx$ 0.33, for a diffraction limited optical system, the resolution is limited by this objective, therefore, the resolution limited by this objective can be calculated by the Rayleigh criterion [62],

$$r = \frac{0.61\lambda}{\text{NA}} = \frac{0.61 \times 589 \text{ nm}}{0.33} \approx 1.1 \ \mu\text{m}. \tag{2.22}$$

We have measured directly the resolution of the objective by the test chart USAF 1951, we have $r_m \approx 1.4$ μm which is close to the result calculated by the diffraction limit [43]. In addition, this objective is also served to focus the Small-VDT mentioned in section 2.3.2.

The beam is then focused by a achromatic lens system and collimated by a microscope, at last focused to a Charge-Coupled Device (CCD) camera (Pixis, Princeton Instruments, USA), as illustrated in Fig. 2.13. The overall magnification of this imaging system about 7.8.

2.5.3 Kinetics mode

During the absorption imaging process, we have to take 3 images, with atoms, without atoms and the dark image. The time interval between images is limited by the reading and re-initializing speed of the CCD camera which lasts about several hundred ms. This duration is long compared to typical mechanical and acoustic vibration frequencies in the range 1 Hz $\sim$ 1kHz. As a result, during the time that the image is read and all the pixels of the CCD are re-initialized, the vibrations can change slightly the position or orientation of the probe beam, whose profile, in fact, is far from the Gaussian, possibly because of the speckle or multiple reflection of the windows. This will cause a noise (usually fringes) in the final absorption image. The fringes in the final image come from imperfect division between the "atoms" and "reference" images. To minimize them, it is advantageous to take the two images with as little delay as possible. In the next section, we will introduce an algorithm to reduce the noise in the division process, but here we explain how to reduce the noise experimentally for each separate image.

In order to reduce the time interval between two images, we adopt a "Kinetics mode" (or sometimes referred as the "frame transfer mode") for absorption imaging. In the normal imaging mode, we use all the pixels of the camera to get a image, then read the image, re-initialize all the pixels of the CCD. This takes a substantial time (several 100 ms) so that the "atoms" and "reference" images are suffering from fringes with different patterns, as explained before. In the kinetics mode, we divided the CCD into several parts. Each time, we only use a fixed part of CCD to get the image, then transfer the data of this part to another part of CCD, preparing for the next imaging. We repeat this process until all the images are taken. The benefit of this new mode is that, the transfer time lasts much less than the reading and re-initializing time. Therefore, this kinetics mode can save much time between two images and reduce the noise of the absorption image.

In practice, only a 1024×271 pixels region at the top of the CCD chip is imaged. We use a razor blade (see Fig. 2.13) to hide the rest of the CCD.

We show in Fig. 2.14 the experimental sequence for the kinetics mode. After the exposure which lasts about 10 μs, we shift the pixels. The time required to shift each line is 12.2 μs. We have 170 lines for each frame, therefore the time interval for the frame shift is $\Delta t = 170 \times 12.2\ \mu\text{s} = 2.072$ ms, as shown in Fig. 2.14.

We show in Fig. 2.15 an image taken by the kinetics mode. We list below the usage for each CCD regions.

- FRAME 1: The first region from line 1 to 178 are exposed from the end of a imaging process to the beginning of the next imaging process, which lasts more

than 10 seconds. This part is just over-exposed and useless.

- FRAME 2: The second region from line 179 to 348 is the image with atoms, corresponding $I_{\text{atom}}(x, y)$.
- FRAME 3: The third region from line 349 to 518 is the separation region. In fact, even if we have hidden the rest of the CCD by a razor, there is still diffracted light leaking to other frames. Therefore, in order to prevent the signal of the image 2 (image with atoms) influence the image without atoms, we add this region of separation.
- FRAME 4: The fourth region from line 519 to 688 is the image without atoms, corresponding to $I_{\text{no}}(x, y)$.
- FRAME 5: The fifth region from line 689 to 858 is the dark image, corresponding to I_{dark}.

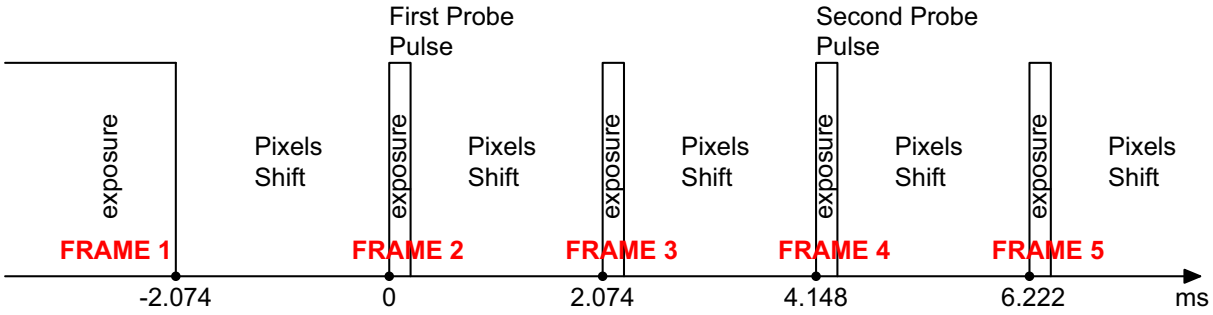


Figure 2.14: Sequence of the kinetics mode. The time interval between two images is 4.148 ms, which is the time required to shift 170 lines of pixels.

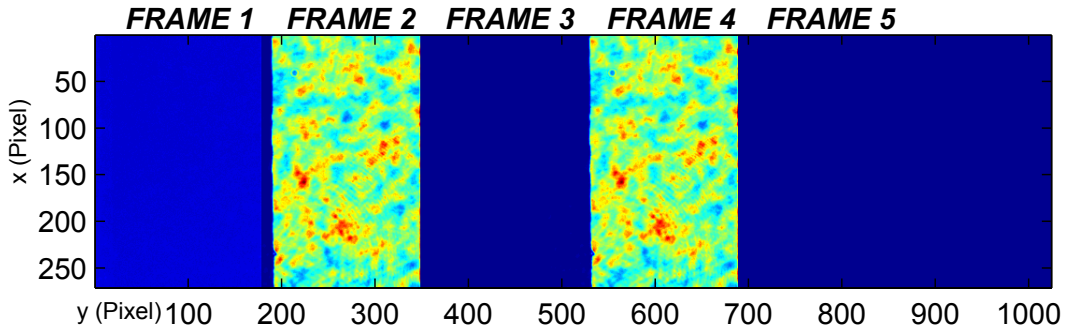


Figure 2.15: Kinetics mode with all frames.

With I_{atom}, I_{no} and I_{dark}, we can calculate the column density distribution n_c by using Eq. (2.19), (2.20), (2.16). (see example in Fig. 2.16)

In this section, we have introduced our imaging system and finally get the column space density distribution. In the next section, we will talk about how to analyze the image to get useful informations and how to reduce the noise of the image.

2.6 Image analysis

After we have got the absorption images, the next step is to get useful informations from them. Besides, the noises in the images due to various reasons will introduce an uncertainty in the atom number counting.

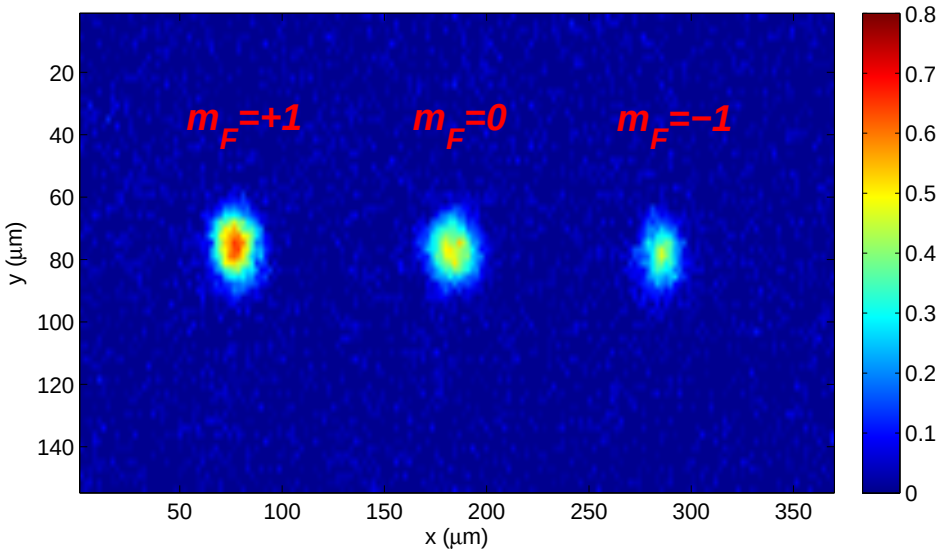


Figure 2.16: An example of absorption image showing three spin components after Stern-Gelarch expansion (see section 2.4.3). The colormap shows the optical depth by Eq. (2.21))

In this section, we will first introduce briefly how to do the fitting to understand the system. A more detailed discussion is in [33]. Then we will focus on the algorithms which aim to reduce the noises of the images. We analyze different kinds of noises and introduce different algorithms to reduce, including the so-called "eigen-face" method which is widely used in other research area [63, 64].

2.6.1 Fitting

In the sections above, we have sometimes mentioned important features of the atom sample, including the temperatures, atom number, or even condensate fraction. But we have not yet discussed how we obtain these parameters. The absorption image reflects the density distribution after TOF, more precisely, the column density in the direction of the probe light. We fit the density profile by a function with several parameters. The fitting function is based on some physical model. Therefore, from the fitting parameters, we will extract important characteristic quantities of the system.

For $T \geq T_c$, the density distribution of atoms trapped in the harmonic trap is described by the Bose function,

$$n_{\mathrm{th}}(\mathbf{r}) = \frac{1}{\lambda_{\mathrm{dB}}^3} g_{3/2}\left(\mathrm{e}^{(\mu - V(\mathbf{r}))/k_B T}\right), \tag{2.23}$$

with

$$V(\mathbf{r}) = \frac{1}{2}m(\omega_x^2 x^2 + \omega_y^2 y^2 + \omega_z^2 z^2). \tag{2.24}$$

For $T \to 0$, under Thomas-Fermi approximation, the density distribution of the pure condensate can be well described as

$$n_c(\mathbf{r}) = \frac{1}{g}\max(\mu - V(\mathbf{r}), 0) \tag{2.25}$$

Therefore, as the simplest model adopted, in the intermediate temperature regime, the mixture of the condensate and the thermal cloud can be described as the sum of the density distribution of the condensate (Eq. (2.23)) and the thermal cloud (Eq. (2.25)),

$$n(\mathbf{r}) = n_c(\mathbf{r}) + n_{\text{th}}(\mathbf{r}). \tag{2.26}$$

In our experiment, we realize the imaging after a period of Time-Of-Flight (TOF). In fact, after TOF without the trap, the density distribution Eq. (2.23) and (2.25) are just *rescaled* along each axis [60]. Besides, the image reflects the column density distribution which is the integration along the probe direction of the density distribution in space. As a result, in our experiment, the images are fitted by the function below

$$\begin{aligned} F(c_1 \dots c_9) = c_1 + c_2\, g_2\Big(\exp\Big(-\frac{(x-c_5)^2}{c_3^2} - \frac{(y-c_6)^2}{c_4^2}\Big)\Big) + \\ c_7 \max\Big(0, \Big(1 - \frac{(x-c_5)^2}{c_8^2} - \frac{(y-c_6)^2}{c_9^2}\Big)^{3/2}\Big). \end{aligned} \tag{2.27}$$

In this fitting function, c_1 is the global offset of the image. The second term, which begin with c_2, is g_2 Bose function obtained by integration of Eq. (2.23) along the imaging axis, which describes the thermal cloud. The third term, which begins with c_7, is obtained by integration of Eq. (2.25) which describes the condensate. We adjust $(c_1 \cdots c_9)$ to minimize the least mean squares,

$$\sum_{\text{pixel}} (F(c) - I)^2. \tag{2.28}$$

Here I is the value of each pixel in absorption image. With all these parameters fitted $(c_1 \cdots c_9)$, we can count the atom number of condensate and thermal cloud, thus calculate the condensate fraction f_c. We can also calculate the temperature of the sample by the size of the Bose function.

In fact, as pointed out in [33], the condensate fraction obtained here is not always reliable. First, for high condensate fraction, the assumption of non-interacting thermal, condensate is not reasonable. Second, the condensate fraction depends on the assumed shape of the bimodal distribution. In our experiment, we are not very deep in Thomas-Fermi limit ($\chi = Na/a_{\text{ho}} \approx 10$ at most). Therefore, the condensate wavefunction, although reasonably close to a Thomas-Fermi distribution around the center region, develops substantial wings near the edges. Although small, these wings can be confusing for the fitting routine which expects a sharp drop near the Thomas-Fermi distribution radius. In Fig.

2.17, we show the numerical simulation of the expansion of the density distribution of a condensate after a TOF = 5 ms (condensate with 1000 atoms in a isotropic harmonic trap with $\omega = 2\pi \times 1000$ Hz, $\chi \equiv N|a|/a_{\rm ho} \approx 3.9$). In the same figure, we also fit the density distribution by Eq. (2.27). The real condensate fraction $f_c^{\rm real} = 1$, but the condensate fraction fitted $f_c^{\rm fit} \approx 0.41$. The fitting function attribute the tail of the density distribution to the thermal cloud, which under-estimate the condensate fraction.

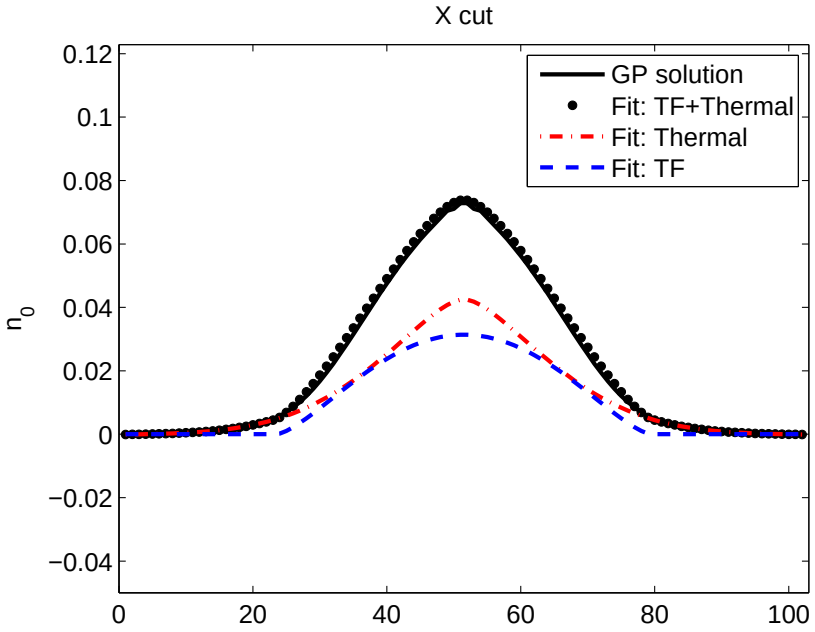


Figure 2.17: Pure condensate ($\chi \equiv N|a|/a_{\rm ho} \approx 3.9$) simulated by the Gross-Pitaevskii equation, fitted by bimodal model (Eq. (2.27)). The black solid line shows the density distribution solved by Gross-Pitaevskii equation. The blue dashed line and the red dash-dotted line is the condensate and the thermal distribution respectively fitted by Eq. (2.27). The black dotted line is fitted total density distribution, which is the sum of the blue dashed line and the red dash-dotted line.

In fact, in order to calculate seriously the condensate fraction, we should solve, or fit, the Gross-Pitaevskii equation for each image, which requires too much time. We conclude that this fitting is only suitable for low condensate fraction $f_c < 0.5$ because for low f_c, all the problems above are mitigated, because the thermal cloud is much larger than the condensate. However, when $f_c \gtrsim 0.5$, both have similar sizes, and the algorithm tends to fit the wings of the condensate distribution by a *pseudo*-thermal distribution. In chapter 4, we will introduce a new method to measure the reliable condensate fraction by measuring the fluctuation of the atom number in $m_F = 0$ state, which is free of these drawbacks.

2.6.2 Counting spin populations

So far, we discussed images taken without Stern-Gerlach procedure, atoms are counted without distinguishing their spin states. Now, we count atom number in each spin component. We show in Fig. 2.19 how to count the atom number in the absorption image. The atom number in each spin component is given by

$$N_i = \frac{S}{\sigma_{\text{eff}}} \sum_{B_i} n_i, \tag{2.29}$$

where $i = +1, 0, -1$ denote the 3 Zeeman sub-levels, S is the size in the atom plan represented by each pixel of the camera and σ_{eff} is the effective scattering cross section. The sum is done in the region of B_{+1}, B_0, B_{-1} for $m_F = +1, 0, -1$ respectively.

2.6.3 Imaging noises

Noise in the absorption image (see for example Fig. 2.16) can be classified in several categories. In this part, we will first introduce the different kinds of noises in our experiment, and then the algorithms to reduce them.

2.6.3.1 Shot Noise

In Fig. 2.16 we can see clearly the noises in the background. The origin of the noise is mainly contributed by the shot noise, which is originated from the particle nature of the light. For a given pixel on the CCD, during a fixed time interval, the photon number received from the probe light follows the Poisson distribution [65], which means the intensity I follows also the Poisson distribution, with $\Delta I \propto \sqrt{I}$. At large photon number, the distribution of I will converge to the Gaussian distribution [66].

In order to identify the nature of the noise in our experiment, we take 100 images without atoms. We realize this by canceling the gradient during the MOT sequence or by switching off the MOT beams. We note $n(x, y)$ the absorption image, $I(x, y)$ the probe light intensity signal. Because there are no atoms, the first and the second image of the absorption imaging are the same except the shot noise. We denote $G_1(x, y)$ and $G_2(x, y)$ the noise of the first and second image respectively which are random variables from pixel to another.

Therefore, we have,

$$n(x, y) = \ln\left(\frac{I(x, y) + G_1(x, y)}{I(x, y) + G_2(x, y)}\right) \approx \frac{G_1(x, y) - G_2(x, y)}{I(x, y)} \qquad G_1, G_2 \ll I \tag{2.30}$$

We note $G'(x, y) = G_1(x, y) - G_2(x, y)$, thus

$$n(x, y) \approx \frac{G'(x, y)}{I(x, y)}. \tag{2.31}$$

For large photon number, $G_1(x, y)$ and $G_2(x, y)$ will follow the Gaussian distribution, with $\langle G_1 \rangle = \langle G_2 \rangle = 0$ and $\Delta G_1 = \Delta G_2 \propto \sqrt{I}$. It can be proved that if G_1 and G_2 both

follow the Gaussian distribution, $G' = G_1 - G_2$ also follows the Gaussian distribution [66], with $\langle G' \rangle = 0$ and $\Delta G' = \sqrt{2}\Delta G_1 \propto \sqrt{I}$.

Therefore, according to Eq. (2.31), we have

$$\langle n(x,y) \rangle = 0, \tag{2.32}$$

and

$$\Delta n(x,y) \propto 1/\sqrt{I(x,y)}. \tag{2.33}$$

Shot noise will influence the atom number counting. From Eq. (2.29), the atom number uncertainty ΔN_i in the region B_i is

$$\Delta N_i = \frac{S}{\sigma_{\text{eff}}} \sum_{B_i} \Delta n_i = \frac{S}{\sigma_{\text{eff}}} \sqrt{\mathcal{N}} \langle \Delta n_i \rangle, \tag{2.34}$$

where $\mathcal{N}$ is the pixel number in the counting region. In our experiment, $S/\sigma \approx 29$, $\mathcal{N} \approx 900$ and $\langle \Delta n_i \rangle \approx 0.04$. Therefore, the atom number uncertainty $\Delta N_i \approx 36$ for each spin component. To simplify our discussion, we suppose here that each pixel is independent, which is not the case if there are some noise structure in the image, which will be discussed in the next section.

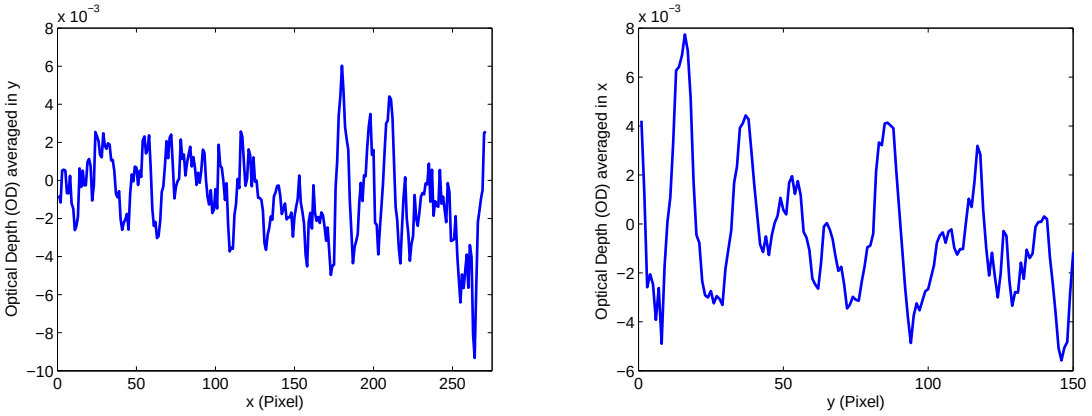
This uncertainty will transfer to the magnetization m_z measurement. Normally, we have in total $N \approx 3000$ atoms. Consider for example $N_{+1} = N_0 = N_{-1} = 1000$, thus $m_z = 0$. If we have $N_{+1} = 1000 + 30$, $N_0 = 1000$, $N_{-1} = 1000 - 30$, thus $m_z' \approx 0.02$. In our experiment, the measurement of the atom number for each spin component and magnetization is very crucial. Reducing this uncertainty by suppressing the noise is therefore an important goal.

2.6.3.2 Structural Noise

Shot noise shows no special spatial structure and will only introduce an *uncertainty* in the atom number counted. If we watch and analyze the images carefully, we will observe other kinds of noise, which are structural, such as background slope and fringes. These kinds of noise are more annoying than the shot noise, because they introduce a *bias* in the atom number counted.

a. Background Slope In Fig. 2.18, we show the background slope. First, we average the 100 images without atoms, and then average another time in y (or x) direction of the image to get Fig. 2.18a (or 2.18b) respectively.

Fig. 2.18 first shows clearly a slope in the image as a function of x and y in Fig. 2.18a and 2.18b, respectively, as well as fringes. Remark that the slope in the y direction is larger than the x direction. The three spin components are separated in the x direction in the absorption image, as a result, the slope in the x direction will influence the atom number counted in each spin component. In Fig. 2.18a, the slope is negative, thus we will *over-estimate* atom number in $m_F = +1$ state and *under-estimate* atom number in $m_F = -1$ state. In practice, we fit *locally* the three spin component, which means



(a) (b)

Figure 2.18: Show the Background slope in x and y direction. This figure show also fringes, especially in (b).

attribute independently three background offset (c_1 in Eq. (2.27)) for the three spin component, this will mitigate the bias. We have tried to fit the slope in excluding the atom region, but the procedure was not found to be stable. We will return to this point in the next section.

b. Fringes Fig. 2.18 also shows fringes, especially in Fig. 2.18b. These fringes will also be harmful in atom number counting. Because the background level oscillates in a larger scale compared with the background slope shown in Fig. 2.18a, the local fit can not solve the problem.

The structural noises, as background slope and fringes shown in Fig. 2.18 may originate from small vibrations of the probe beam, or index fluctuations, as mentioned in section 2.5.3. Etalon effects caused by the windows of the vacuum chamber can also contribute.

2.6.4 Methods to reduce structural noise

2.6.4.1 Slope removal

In order to remove the background slope, we have tried a simple method shown in Fig. 2.19. We choose a region marked B_i in which atoms occupy the $m_F = i$ Zeeman sub-level. A_i and C_i are two regions with the same size as B_i which locate approximately above and below the B_i region. In the A_i and C_i regions, there are no atoms. The modified absorption image in the B_i region is corrected by the average of the A_i and C_i region,

$$n'_{B_i} = n_{B_i} - \frac{n_{A_i} + n_{C_i}}{2}. \tag{2.35}$$

This method can correct the linear background slope and facilitate the Fringe-removal algorithm in the next step. We have also tried to fit the background slope directly in the background region (excluding the atom region, see Fig. 2.20). But the fitting result does

not seem stable. It is possibly because of the fringe structure shown above, but most likely also because the slope itself seems to change on a slow time scale (several minutes) and the background is sometimes not very well described by the model linear in $x - y$ for the background.

We conclude that this slope removal method is simple and effective for linear background slope, but not optimal. This method is used for the analysis of the phase diagram experiment data in chapter 3.

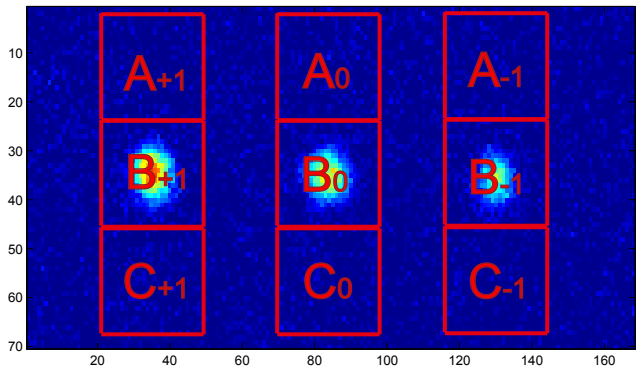


Figure 2.19: Different regions for slope removal algorithm.

2.6.4.2 Fringe-removal

We will introduce here an very effective fringe-removal algorithm, which is closely related to the so-called "Eigen-face algorithm" [67, 68]. The Eigen-face algorithm was first used in the face recognition application. In our experiment, we will use a simpler version of this algorithm. The basic idea is to use a linear combination of a set of reference images to calculate the "best" reference image in order to reduce the noise.

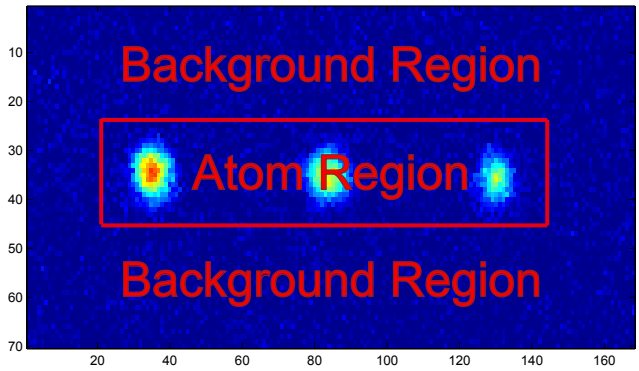


Figure 2.20: Different regions for fringe removal algorithm.

We denote A_x the atom image, R_x the reference image. We need to calculate the "best" reference image, which is a linear combination of a set of reference images, thus, we have

$$Q_x = \sum_k c_k R_{x,k}. \tag{2.36}$$

Here we sum over different reference images, with c_k the coefficient. Q_x is the optimal reference image which minimize the least square difference between the atom and reference images, within a specified background region ($m_x = 1$) excluding the atom region ($m_x = 0$) shown in Fig. 2.20. Therefore we have to minimize

$$\sum_x m_x (A_x - Q_x)^2. \tag{2.37}$$

In minimizing Eq. (2.37), we obtain a linear system of equation

$$\sum_k c_k B_{j,k} = \sum_x m_x R_{x,j} A_x \tag{2.38}$$

with

$$B_{j,k} = \sum_x R_{x,j} R_{x,k} \tag{2.39}$$

For each atom image A_x, the algorithm gives the optimal group of c_k to construct the optimal reference image Q_x by Eq. (2.36). In our experiment, we save both atom images and reference images. We calculate $B_{j,k}$ in using all the reference images during the day (typically several hundreds of images).

In order to estimate the improvement of the fringe-removal algorithm, we use 100 images without atoms to test. We note

$$n_x^R = -\ln(A_x/R_x), \tag{2.40}$$

absorption image calculated by original reference image, and

$$n_x^Q = -\ln(A_x/Q_x), \tag{2.41}$$

absorption image calculated by the optimal reference image.

We calculate $\langle \mathrm{var}(n_x^R) \rangle$ and $\langle \mathrm{var}(n_x^Q)) \rangle$. The "var" is the variance for different pixel for a given image, and the average $\langle \cdot \rangle$ is over different images. This quantity represent the average amplitude of the noise in the 100 images. We have

$$\frac{\langle \mathrm{var}(n_x^R) \rangle}{\langle \mathrm{var}(n_x^Q) \rangle} = 1.8 \pm 0.1. \tag{2.42}$$

It means the algorithm improves the image quality by reducing the noise. According to Eq. (2.34), after the fringe removal algorithm, the atom number uncertainty for each spin component $\Delta N_i \approx 26$ compared with $\Delta N_i \approx 36$ before the fringe removal algorithm.

In Fig. 2.21, we compare the noise before and after the algorithm. The fringe mentioned above in Fig. 2.18b is mitigated. The amplitude of the fringe is decreased. This algorithm is used on the analysis of the spin fluctuation experiments in chapter 4 (The data analysis of the experiment of chapter 3 is done using the simple counting procedure explained in section 2.6.2).

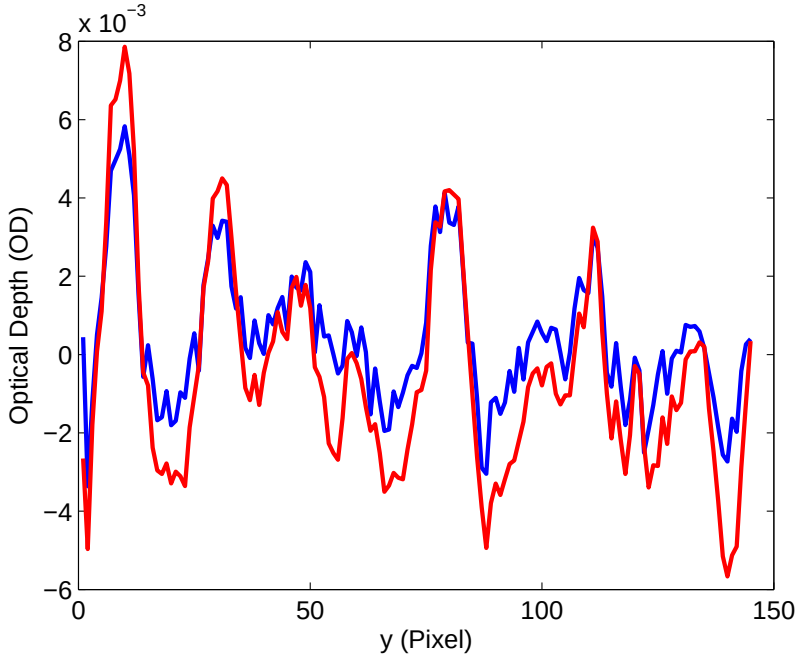


Figure 2.21: Optical denpth (OD) averaged in x as a function of y. The red and blue lines show the OD before and after the fringe removal algorithm, respectively, corresponding to a factor of 2 improvement on atom number determination.

2.7 Conclusion

In this chapter, we have discussed step by step how to reach the Bose-Einstein condensation in our experiment. The first step is the Magneto-Optical trap (MOT), which serves as the pre-cooling stage. We load the MOT directely from the background gas with the help of Light Induced Atomic Desorption (LIAD). Next, we transfer the atoms from the MOT to the Large-Crossed Dipole Trap (Large-CDT). After loading the atoms from the MOT to the Large-CDT, we increase the power of the Large-CDT to compress the atom along the arm of the trap to the crossed region in order to increase the elastic collision rate and to facilitate the evaporative cooling in the next stage.

In our experiment, the evaporative cooling is realized in two steps. First evaporation is mainly in the Large-CDT and at the same time, fill the Small-VDT. It helps to overcome the decrease of the evaporation efficiency caused by the decrease of the frequency of the Large-CDT during the evaporation. Second evaporation is in the more confined Small-CDT composed by Small-VDT and Small-HDT. During the second evaporation,

we reach the regime of the BEC and at the end of the evaporation, we have an almost pure condensate.

We introduce in section 2.4 the method to control and diagnose the spinor condensate. With the magnetic field gradient and the Radio-Frequency (RF) pulse, we can polarize and depolarize the spinor condensate respectively. At the end of the evaporation, with the help of the magnetic field gradient and attenuation ramp of Small-CDT, we can separate the 3 Zeeman sub-levels for imaging.

Optical diagnosis is the only way to study the property of the BEC. We introduced our imaging system, and the kinetics mode of absorption imaging to reduce the noise caused by the mechanical vibration. After we get the absorption image, we use a fitting model to extract physical informations in the images. Finally we introduce several algorithms to reduce the noise of the image in order to reduce the atom number counting uncertainty.

Chapter 3

Phase diagram of spin 1 antiferromagnetic Bose-Einstein condensates

The study of the phase diagram of spin-1 Bose-Einstein condensates with antiferromagnetic interactions is well summarized in [38]. The content of this chapter is directly extracted from that article, with titles of section added. The Supplementary Informations *referred in the main text have been partly discussed in chapter 2 and are reproduced in appendix C.*

3.1 Introduction

We study experimentally the equilibrium phase diagram of a spin 1 Bose-Einstein condensate with antiferromagnetic interactions, in a regime where spin and spatial degrees of freedom are decoupled. For a given total magnetization m_z, we observe for low magnetic fields an "antiferromagnetic" phase where atoms condense in the $m = \pm 1$ Zeeman states, and occupation of the $m = 0$ state is suppressed. Conversely, for large enough magnetic fields, a phase transition to a "broken axisymmetry" phase takes place: The $m = 0$ component becomes populated and rises sharply above a critical field $B_c(m_z)$. This behavior results from the competition between antiferromagnetic spin-dependent interactions (dominant at low fields) and the quadratic Zeeman energy (dominant at large fields). We compare the measured B_c as well as the global shape of the phase diagram with mean-field theory, and find good quantitative agreement.

One of the most active topics in the field of ultra cold quantum gases is the study of interacting many-body systems with spin [29, 30, 69, 26]. Atoms with arbitrary Zeeman structure can be trapped using far-detuned optical traps. Quantum gases of bosons with spin 1 [69, 26], 2 [70, 71], or 3 [72] and fermions with spin larger than 1/2 [73, 74] have been demonstrated experimentally. This opens a whole class of new experiments with spinful many-body systems, such as coherent spin mixing dynamics analogous to an internal Josephson effect [70, 71, 31, 75, 76, 77, 78], squeezing among the different spin components [79, 80, 81], or the study of sudden quenches across magnetic phase transitions [82, 83].

The simplest example is the spin-1 Bose gas. The spin-dependent interaction between two atoms with spins $\mathbf{s}_1$ and $\mathbf{s}_2$ can be written as $V_{12} = g_s \mathbf{s}_1 \cdot \mathbf{s}_2$. Depending on the sign of the coupling constant g_s, this interaction leads to either ferromagnetic ($g_s < 0$, the case of atomic ^{87}Rb [31]) or antiferromagnetic ($g_s > 0$, the case of atomic ^{23}Na [28]) behavior. This naturally leads to different equilibrium phases. An additional but essential feature in experiments with gases of alkali atoms is the conservation of the longitudinal magnetization $m_z = n_{+1} - n_{-1}$, which follows from the spin rotational symmetry of V_{12}. Here n_m denotes the relative populations of the Zeeman state labeled by the magnetic quantum number $m = 0, \pm 1$. The only possible spin-changing two-body process is

$$m = 0 \; + m = 0 \rightarrow m = +1 \; + \; m = -1, \tag{3.1}$$

where two $m = 0$ atoms collide to yield one atom in each state $m = \pm 1$ (or vice-versa), leaving m_z unchanged. In most physical systems, the magnetization would relax by coupling to an external environment. In contrast, quantum gases are almost perfectly isolated and the conservation of magnetization plays a major role [1].

In spite of intense theoretical activity [26], the equilibrium properties of spinor gases remain relatively unexplored experimentally. Most experimental work so far have focused on dynamical properties. For ferromagnetic Rubidium condensates, a recent experimental study concluded that the time needed to reach an equilibrium state, typically several seconds or tens of seconds, could easily exceed the condensate lifetime [84]. For antiferromagnetic ^{23}Na, the stationary regime after damping of spin-mixing oscillations has been studied for relatively high magnetization ($m_z \lesssim 0.5$) [78]. Here also, long equilibration times on the order of 10 s were observed. Both experiments worked with condensates with large atom numbers, well in the Thomas-Fermi regime, where spin domains are expected and observed in transient regimes.

In this Rapid Communication, we present an experimental study of the phase diagram of spin 1 Sodium Bose-Einstein condensates with antiferromagnetic interactions. We work with small atomic samples containing a few thousands atoms held in a tightly focused optical trap. In this regime, spin domains are energetically costly, and spatial and spin degrees of freedom are largely decoupled. We prepare the sample well above the condensation temperature with a well-defined longitudinal magnetization and no spin coherence. At the end of the cooling stage, equilibration times of 3 s are used to ensure that thermal equilibrium is reached. We find, in agreement with theoretical predictions, a phase transition from an "antiferromagnetic" phase where only the $m = \pm 1$ Zeeman components are populated to a mixed "broken axisymmetry" phase where all three Zeeman states can coexist. We determine the phase boundary and the shape of the phase diagram versus applied magnetic field and magnetization by measuring the population of the $m = 0$ state. Our measurements can be explained quantitatively by mean-field theory in the single-mode regime, where the atoms condense in the same spatial wave function irre-

[1] This statement holds when magnetic dipole-dipole interactions are negligible, which is the case for alkali atoms. For some atomic species with large magnetic moments, such as Chromium [72], dipolar relaxation can be dominant.

spective of their internal state.

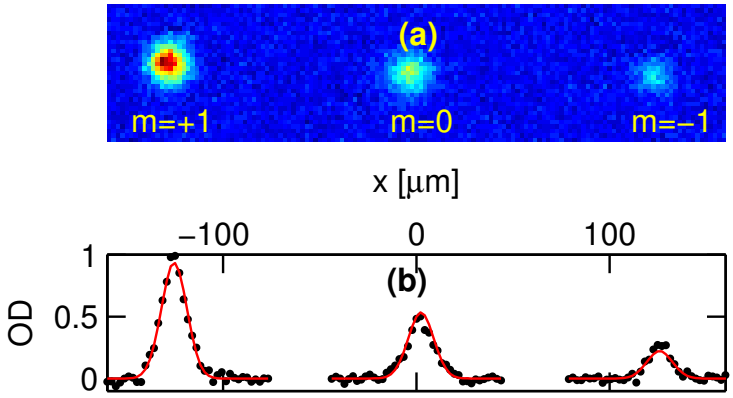


Figure 3.1: (Color online) **a:** Absorption image of a spin 1 BEC after expansion in a magnetic gradient. **b:** Horizontal cuts through the images in (**a**). The same function (shown by straight lines), only recentered and reweighted, is used to fit the density profile of each Zeeman state.

3.2 Experimental configuration

We work with Sodium atoms cooled deeply in the quantum degenerate regime using an all-optical cooling sequence [52, 49]. In order to prepare the sample with a well-defined longitudinal magnetization and no spin coherences, we start from a cold cloud in a crossed optical dipole trap loaded from a magneto-optical trap [49], with a magnetization $m_z \approx 0.6$ resulting from the laser cooling process. To obtain higher degrees of spin polarization, we perform evaporative cooling in the presence of a vertical magnetic field gradient for about 1 s. Each Zeeman state sees a slightly different potential depth. Because of the combined action of gravity and of the magnetic gradient, evaporative cooling in this configuration favors the Zeeman state with the higher trap depth [59, 85]. This results in partially or almost fully polarized samples with magnetization up to $m_z \approx 0.85$. To obtain lesser degrees of polarization than the initial value $m_z \approx 0.6$, we remove the gradient and apply instead an additional oscillating field resonant at the Larmor frequency. The two procedures together allow to prepare well-defined magnetizations ranging from 0 to ≈ 0.85 with good reproducibility and keeping the same evaporative cooling ramp in all cases. After spin preparation, we transfer the cloud in the final crossed dipole trap and resume evaporative cooling (see section 1 in the Supplementary Informations).

After the evaporation ramp, we obtain quasi-pure spin 1 Bose-Einstein condensates (BEC) containing $N \approx 5000$ atoms in a trap with average frequency $\overline{\omega} \approx 2\pi \times 0.7$ kHz. To ensure that the cloud has reached a steady state, we allow for an additional hold time of 3 s after the evaporation ramp. We have investigated the dynamics of the spin populations as this hold time is varied for several values of magnetization and applied magnetic

field. We found that the populations relaxed to steady-state values with a characteristic $(1/e)$ time smaller than 1 s, much less than the finite lifetime of our sample, around 10 s.

The populations of the Zeeman states $m = 0, \pm 1$ are analyzed after expansion in a magnetic field gradient producing a Stern-Gerlach force that accelerates atoms in $m = \pm 1$ in opposite directions. After a given expansion time (typically $t \approx 3.5$ ms), we take an absorption picture of the clouds (see Fig. 3.1a), and count the normalized populations n_m of the Zeeman state $m = 0, \pm 1$. Note that the condensate is in a regime intermediate between the ideal gas and the Thomas-Fermi limits (we estimate a chemical potential $\mu \approx 4\hbar\overline{\omega}$ from a numerical solution of the Gross-Pitaevskii equation).

3.3 Experimental results and interpretation

For a Bose-Einstein condensate held in a tight trap as in our experiment, the energetic cost of spin domains is large (comparable to $\hbar\overline{\omega}$ per atom, much larger than the spin-dependent interaction energy). In this limit, it is reasonable to make the single mode approximation (SMA) for the condensate wavefunction [46, 47], which amounts to consider that all atoms share the same spatial wavefunction independently of their internal state; The condensate spin remains as degree of freedom. To support this approximation, we note that absorption images as in Fig. 3.1a do not reveal any spatial structures or spin domains during the 3 s hold time. Furthermore, we compare in Fig. 3.1b the observed distributions with a common mode distribution. This common mode function is extracted from a Gaussian fit to the most populated cloud ($m = +1$ in this example), and then recentered and reweighed to match the populations of the other Zeeman states. We find very good agreement between the three spatial distributions in the whole range of parameters explored, and conclude that the SMA is indeed a good approximation in our case.

Because the longitudinal magnetization $m_z = n_{+1} - n_{-1}$ is conserved, the relevant magnetic energy in an applied magnetic field is the second-order (quadratic) Zeeman shift of magnitude $q = q_B B^2$, with B the applied magnetic field and $q_B \approx 277$ Hz/G^2. The larger (first-order) linear Zeeman shift has no influence (it can be absorbed in the Lagrange multiplier associated to the fixed magnetization [26]). As other spin-changing mechanisms than collisions are possible, this conservation law is only approximate. For example, it no longer holds when spin-flips are induced on purpose by applying oscillating fields as described above, or for systems with magnetic dipole-dipole interactions [72]. In the absence of such applied fields, we find no evidence for violation of this conservation law within our experimental limit of a few percents.

We show in Fig. 3.2 the measured values of n_0 for a range of applied magnetic fields B and $m_z \approx 0.4$. The population in $m = 0$ is small at low applied fields and rises sharply above a critical value B_c before settling at an asymptotic value. We have repeated these measurements for a wide range of B and m_z, and generically observed this behavior. We show the results in a reconstructed contour plot in Fig. 3.3a. The phase diagram shows unambiguously the presence of two different phases which differ in their spin composition, or

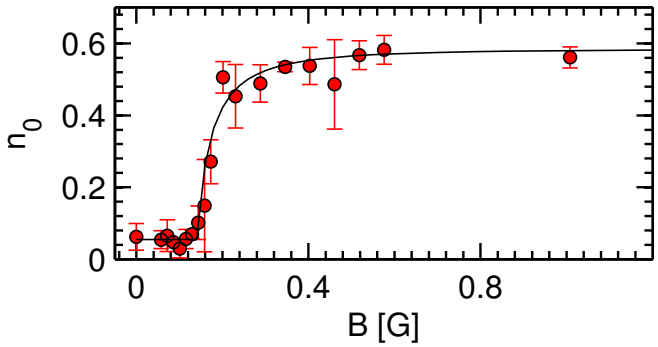


Figure 3.2: (Color online) Sample data showing the population n_0 of the $m = 0$ Zeeman state versus applied magnetic field B, for a magnetization $m_z \approx 0.4$. The solid line is a fit to the data using Eq. (3.5). Vertical error bars show statistical uncertainties on the measured values (one standard deviation).

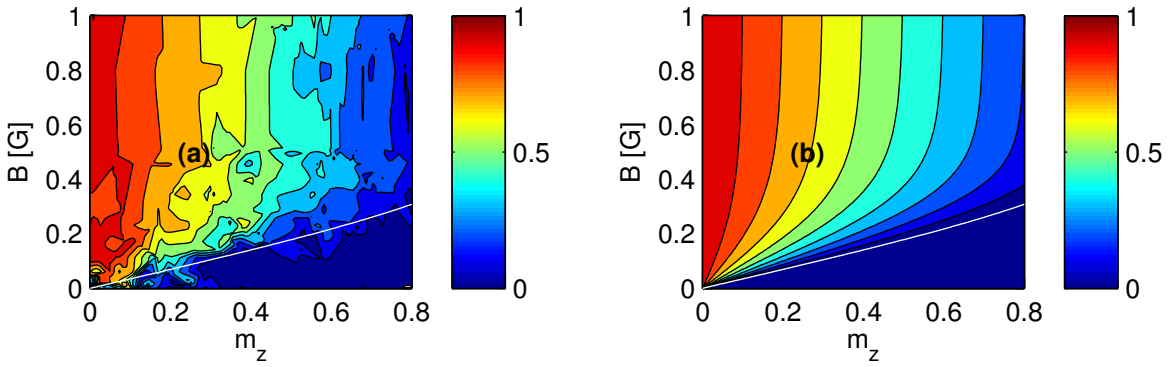


Figure 3.3: (Color online) **a:** Experimental phase diagram showing the population n_0 of the $m = 0$ Zeeman state versus magnetization m_z and applied magnetic field B. The plot shows a contour interpolation through all data points, with magnetization ranging from 0 to 0.8. The white line is the predicted critical field B_c separating the two phases, deduced from Eq. (3.4) by $q_c = q_B B_c^2$. **b:** Theoretical prediction for n_0 at $T = 0$ K.

more precisely are characterized by the absence or presence of condensed atoms in $m = 0$.

We now explain the observed behavior of n_0 in terms of the competition between the spin-dependent interactions and the applied magnetic field (entering quadratically through the second order Zeeman effect). The mean-field energy functional in the single-mode approximation is given by [26]

$$\frac{E_s}{N} = \frac{U_s}{2} |\boldsymbol{S}|^2 - q n_0. \tag{3.2}$$

Here, $\boldsymbol{S} = \langle \boldsymbol{\zeta} | \hat{\boldsymbol{S}} | \boldsymbol{\zeta} \rangle$ is the expectation value of the spin operator $\hat{\boldsymbol{S}}$ taken in the normalized spinor $\boldsymbol{\zeta}$ describing the condensate spin wavefunction, and U_s denotes the spin-spin interaction energy (see section 3 in the Supplementary Informations). For antiferromagnetic interactions ($U_s > 0$), no applied field ($q = 0$) and zero magnetization, the spin 1 BEC realizes a polar, or "spin-nematic", phase according to mean-field theory [29, 30]. The spin wave function $\boldsymbol{\zeta}$ belongs to the family of eigenstates of $\hat{\boldsymbol{S}} \cdot \boldsymbol{n}$ with zero eigenvalue (and zero average spin), with $\boldsymbol{n}$ a headless vector called "nematic director" in analogy with the analogous order parameter characterizing nematic liquid crystals. When $q = 0$, any direction $\boldsymbol{n}$ is a possible solution, while any positive q favors occupation of the $m = 0$ state (along z) and pins the nematic director in the z direction.

When m_z is non zero, there is a competition between the spin-dependent interactions and the quadratic Zeeman energy. The constraint of a fixed magnetization is essential to understand the spin structure of the condensate [86]. The BEC spin wavefunction can be parameterized generically as [29, 30, 86]

$$\boldsymbol{\zeta} = \begin{pmatrix} \sqrt{\frac{1}{2}(1 - n_0 + m_z)}\, e^{i\phi_{+1}} \\ \sqrt{n_0}\, e^{i\phi_0} \\ \sqrt{\frac{1}{2}(1 - n_0 - m_z)}\, e^{i\phi_{-1}} \end{pmatrix}. \tag{3.3}$$

We introduced the phases ϕ_m of the components of $\boldsymbol{\zeta}$ in the standard basis. The effect of antiferromagnetic spin-dependent interactions ($U_s > 0$) is two-fold: First, they lock the relative phase $\phi_{+1} + \phi_{-1} - 2\phi_0$ to π in the minimal energy state. Second, they favor the coexistence of the $m = \pm 1$ component and disfavor mixing them with the $m = 0$ component [28]. As the quadratic Zeeman energy favor the latter, the competition between the two results in two distinct phases as observed experimentally.

The equilibrium population n_0 is found by minimizing the mean-field energy functional [86]. For low q and non-zero magnetization m_z, spin-dependent interactions are dominant, and result in a two-component condensate where the Zeeman states $m = \pm 1$ are populated ($n_0 = 0$). Following [69], we will call this phase "antiferromagnetic" (AF). When $m_z \to 0$, this gives an "easy-plane" polar phase where the nematic director is confined to the $x - y$ plane. Above a critical value q_c given by

$$q_c = U_s \left(1 - \sqrt{1 - m_z^2}\right), \tag{3.4}$$

n_0 increases continuously from zero, indicating a second-order quantum phase transition. Again following [69], we call this phase"broken axisymetry" (BA). For large q, the energy

is minimized by increasing n_0 as much as possible given the constraint of a given m_z: The spin populations therefore tend to $n_{+1} = m_z$, $n_0 = 1 - m_z$, $n_{-1} = 0$ for $m_z > 0$. When $m_z \to 0$, one recovers the easy-axis polar phase with all atoms in the $m = 0$ state along z. More generally, the BA state with $n_0 \neq 0$ has non-zero longitudinal and transverse magnetization (both vanish when m_z goes to zero), and a nematic director orthogonal to the direction of the magnetization vector [87].

We measured the critical line separating the AF and BA phases using the following procedure. We bin the data according to the measured magnetization, in bins of width 0.1 around an average magnetization from $m_z \approx 0$ to $m_z \approx 0.8$, with residual fluctuations around $\delta m_z \approx 0.02$. Each dataset with given magnetization is fitted with a function of the form

$$n_0 = \begin{cases} A_0, q < q_c \\ A_0 + A_1 \frac{q-q_c}{q-q_c+\Delta q}, q \geq q_c. \end{cases} \tag{3.5}$$

This form ensures the existence of a sharp boundary determined by q_c, a constant background value for low q and a well-defined asymptotic value for large q, and reproduces the observed data fairly well, as shown in Fig. 3.2 for a specific example with $m_z \approx 0.4$. At low fields, n_0 is not strictly zero but takes values of a few percents, which can be explained by the presence of a small non-condensed fraction ($f' \approx 2 - 3$ % per component). As such small populations are near our detection limit (~ 3 % for the fractional populations, limited by the optical shot noise associated with the imaging process), we do not attempt to determine them and consider in the following that the condensate is essentially at zero temperature. At high fields, n_0 is very close to the expected value $1 - m_z$ (see Fig. 3.4a), again within a few percents.

We show in Fig. 3.4b the measured boundary $B_c = \sqrt{q_c/q_B}$ between the two phases, which we find in good agreement with the prediction of Eq. (3.4) in the whole range investigated. The comparison is made with the value $U_s/h \approx 65.6$ Hz, obtained from a numerical solution of the Gross-Pitaevskii equation using the scattering lengths given in [42] and the measured trapping parameters and average atom number, and thus does not require any fitting parameter. Our results are in line with previous measurements in [78], which were restricted to the range $m_z > 0.5$ and $B > 0.2$ G and performed with much larger samples well in the Thomas-Fermi regime. Here, we are able to characterize this transition down to zero magnetization and zero applied field, in a system where spin domains (as observed in [78] during the relaxation towards equilibrium) are not expected to form.

Mean-field theory also quantitatively describes our data above the critical line. We compare the calculated n_0 directly to the data in Fig. 3.3a and b. There is no adjustable parameters in this comparison, since the parameters used in the theory are either measured or computed independently. The shape and magnitude of the calculated phase diagrams matches the measured one within 10 % at worst, except very close to the origin $B \approx 0$ and $m_z \approx 0$. In this corner of the phase diagram, we observe larger deviations from the mean field prediction and correspondingly higher fluctuations in n_0. We will present detailed study on these findings in another publication.

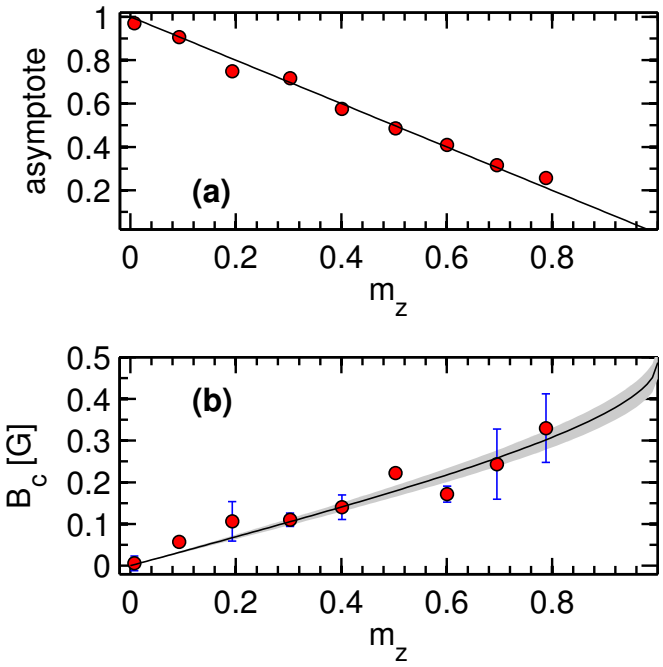


Figure 3.4: (Color online) **a:** Asymptotic value of n_0 for large q (determined from $A_0 + A_1$ in Eq. 3.5). The solid line shows the value $1 - m_z$ expected at zero temperature. **b:** Measured critical field B_c versus magnetization. The solid line shows the values expected from Eq. (3.4) and $q_c = q_B B_c^2$, using $U_s/h \approx 65.6$ Hz. The gray area show the uncertainty on the theoretical value of B_c, dominated by the 15 % uncertainty on the spin-dependent scattering length a_s. For both plots, vertical error bars show statistical uncertainties on the measured values (one standard deviation).

3.4 Conclusion and perspectives

In conclusion, we have explored experimentally the phase diagram of spin 1 BECs with antiferromagnetic interactions. Two phases are found, reflecting the competition between the spin-dependent interactions and the quadratic Zeeman energy. The measurements are in quantitative agreement with mean-field theory, which quantitatively predicts the phase boundary but also the observed spin populations above the transition. In this paper, the population of non-condensed atoms was small (a few percents, below our detection level). Although interesting effects beyond mean-field are predicted at very low temperatures [88], they would require much better sensitivity and lower temperatures to be addressed. On the other hand, at higher temperatures he thermodynamics should differ substantially from the scalar case [72, 48]. Both paths provide interesting directions for future work.

We summarize all the experimental results for different magnetizations in Fig. 3.5.

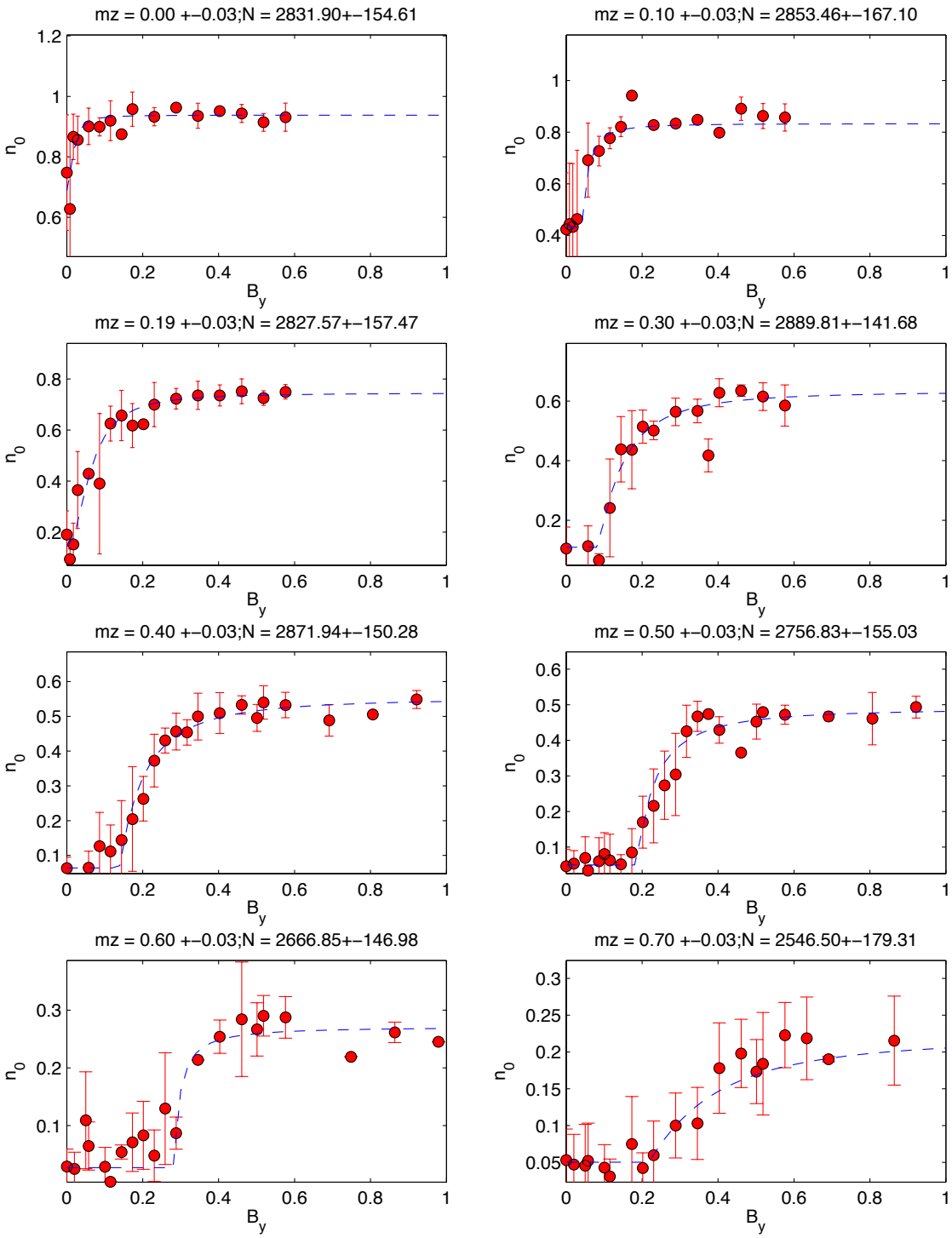


Figure 3.5: Individual datasets (binned by magnetization).

Chapter 4

Collective fluctuations of spin-1 antiferromagnetic Bose-Einstein condensates

4.1 Introduction

At the end of the chapter 3, we have remarked the abnormally large fluctuation of n_0 at $m_z = 0$ and small magnetic field B. These fluctuations, which, in principle, can not be explained by the mean-field approach in chapter 1 section 1.3, are the main subject of this chapter.

In chapter 1, section 1.4, we have studied the behavior of the spinor BEC in the Hartree-Fock approximation. However, we have also pointed out that this description is not complete because we have used a mean-field approach to analyze $\hat{H}_{\mathrm{SMA}}$, the single-mode approximation Hamiltonian of the spin-dependent part. This mean-field approach neglects completely the fluctuations. When $m_z = 0$, the mean-field approach predicts that an arbitrary small magnetic field will break the symmetry and force all the atoms to accumulate in the $m_F = 0$ state. However, in the experiment, we observe large fluctuations of n_0 at low q in $m_z = 0$ case, the average of n_0 is also smaller than 1. We use the spin depolarization process (introduced in chapter 2, section 2.4.2.2) to prepare a spinor condensate sample with $m_z = 0$. After the second evaporation, we keep the power of Small-HDT and small-VDT (see chapter 2, section 2.3) during a period of "hold time", typically several seconds, to give the system sufficient time to reach equilibrium. We apply a bias magnetic field along x direction during the evaporation and the hold time T_{hold}. The imaging is done just after the "hold time". For a given magnetic field B, we repeat the same experimental sequence many times, typically 100 times, in order to measure the expected value of the relative atom number in $m_F = 0$ state, the depletion $\langle n_0 \rangle$, and the standard deviation Δn_0, which are used to characterize the fluctuation. We show in Fig. 4.1 and 4.2, two examples of our experimental measurements in different evaporation time T_{evap} in the second evaporation (thus in different trap depth). We plot $1 - \langle n_0 \rangle$ and Δn_0 as a function of q (quadratic Zeeman energy) for $T_{\mathrm{evap}} = 900$ and 975 ms ($T_{\mathrm{hold}} = 6$ s in both case). We observe large fluctuations (Δn_0 is unity order) and $\langle n_0 \rangle \neq 1$ for small q, which cannot be explained by the mean-field theory introduced in

chapter 1. The main subject of this chapter is to study theoretically and experimentally the behavior of $1 - \langle n_0 \rangle$ and Δn_0.

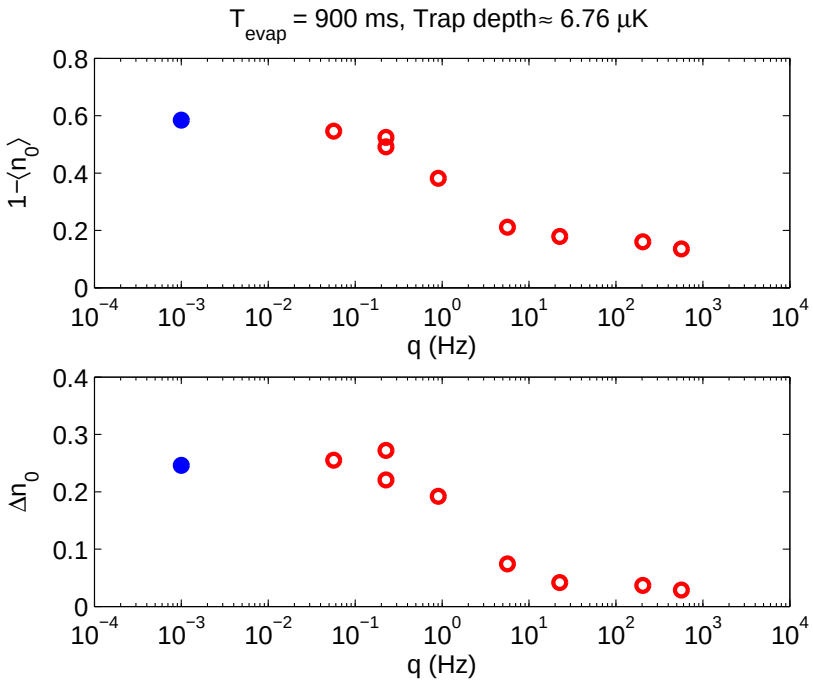


Figure 4.1: Second evaporation $T_{\text{evap}} = 900$ ms, trap depth ~ 6.76 μK, hold time 6 s. The point closet to $q = 0$ (the solid blue circle) corresponds to zero applied field, and bas been set arbitrarily at $q = 10^{-3}$ Hz.

In fact, what we observed in the experiment is an example of a so-called *fragmented condensate*, which means atoms condense simultaneously in *several* single-particle states, instead of one state for the "normal" condensate. The fragmentation has been studied in several kinds of systems, including fragmentation due to orbital or to internal degeneracies [39, 89]. The spin 1 Bose gas, which is studied in our experiment, is a good example of a fragmented condensate [90]. In absence of the magnetic field, the rotational symmetry of the anti-ferromagnetic interaction $V_{1,2} = g_s \mathbf{s}_1 \cdot \mathbf{s}_2$ between two atoms leads to a many-body spin singlet ground state [89, 46], where all three Zeeman sub-levels $m_F = +1, 0, -1$ are equally populated (see Eq. (4.23)). As pointed out in [46, 91, 89], the signature of fragmentation is the appearance of the anomalously large fluctuations of the atom number in each Zeeman sub-levels (see Eq. (4.24)) with super-Poissonian fluctuation ($\Delta N_0^2 \sim \langle N_0 \rangle^2$), which deviate strongly from the value expected for a single condensate or any ensemble without correlations where $\Delta N_0^2 \sim \langle N_0 \rangle$, as we observe in Fig. 4.1 and 4.2. These two first moments of n_0 are clear signatures to illustrate whether the system is fragmented or not. It was also pointed out by [91] that such state was likely not realized in typical experiments, due to its fragility toward any perturbation breaking spin rotational symmetry [92, 93, 94, 95, 96, 97]. In the thermodynamic limit $N \to \infty$, an arbitrary small symmetry-breaking perturbation, for example a small magnetic field, is enough to favor a regular condensed state, where all atoms occupy the same (spinor) wave function and $\Delta N_0 \ll N$. In our situation, spin rotational symmetry is broken explicitly

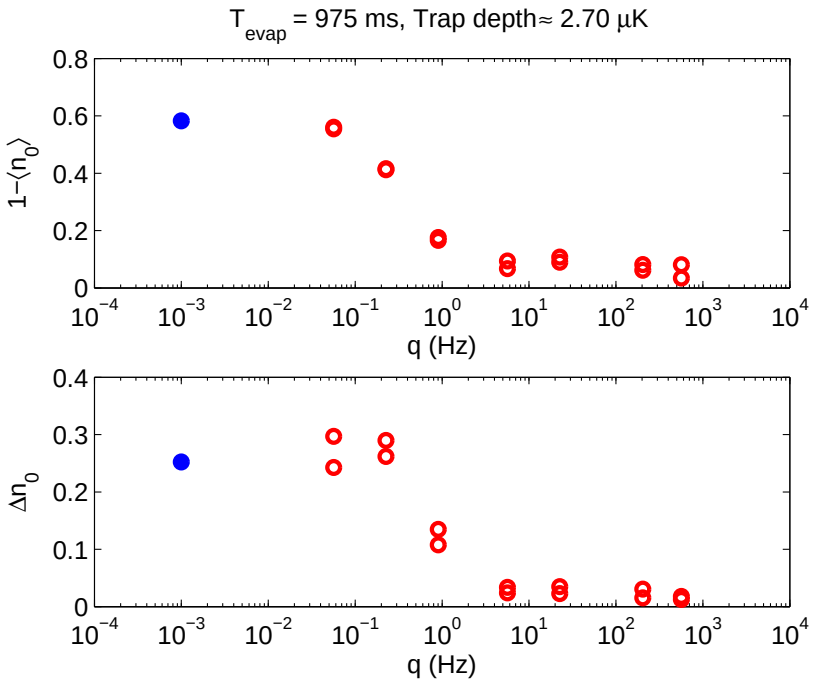


Figure 4.2: Second evaporation $T_{\text{evap}} = 975$ ms, trap depth ~ 2.70 μK, hold time 6 s.The point closet to $q = 0$ (the solid blue circle) corresponds to zero applied field, and bas been set arbitrarily at $q = 10^{-3}$ Hz.

by the quadratic Zeeman effect, characterized by an energy q. For finite N, a finite q is required to suppress the fluctuations of n_0.

This chapter is organized as follows: in section 4.2, we focus on the quantum solution of the single mode Hamiltonian $\hat{H}_{\text{SMA}}$ (see chapter 1, Eq. (1.57)), which describes the spin-1 Bose-Einstein condensate with antiferromagnetic interactions. Previous work analyzed theoretically how the ground state evolved with quadratic Zeeman energy [93, 94, 95, 96]. Experiments are of course performed at finite temperature, and the first goal in this chapter is to generalize the theory to such finite temperature. We adopt two approaches to solve this problem. First, we directly diagonalize the Hamiltonian H_{SMA} and compute the moments of n_0 from this diagonalization. Second, we introduce a so-called "broken symmetry" approach, where the spinor condensate is described as a statistical mixture of mean-field states with fluctuating "direction" in spin space. This approach is shown to reproduce the exact results very well, with two additional advantages: accelerate the calculation and better physical picture. After this basic theory is developed, we note that in order to describe the experiment results in details, it needs to be extended in two ways. In section 4.3, we generalize the distribution of M (definition in section 4.2) and in section 4.4, we take the thermal atoms that surround the condensate into account using semi-ideal Hartree-Fock approximation, introduced in chapter 1. In section 4.5, we use the extended theory to fit the experimental results. Finally, we give an detailed interpretation to these results in section 4.6.

4.2 Quantum analysis of a spin-1 antiferromagnetic BEC

As mentioned in section 4.1, in our experiment, we measure $\langle n_0 \rangle$ and Δn_0 as a function of the quadratic Zeeman energy q. Our purpose is to develop a theory to understand this behavior. We adopt the same strategy as in chapter 1. We analyze separately the condensate and the thermal cloud. The condensate is described by $\hat{H}_{\mathrm{SMA}}$ which will be analyzed in this section, and the thermal cloud will be discussed later.

In order to understand the behavior of the $\langle n_0 \rangle$ and Δn_0 caused by the condensate, the most natural way is to study the spectrum of the Hamiltonian $\hat{H}_{\mathrm{SMA}}$, calculate $\langle n_0 \rangle$ and $\langle n_0^2 \rangle$ for each eigenstate, then average in the canonical ensemble (we assume here a constant total atom number N) with a certain temperature. We remind here the SMA Hamiltonian,

$$\hat{H}_{\mathrm{SMA}} = \frac{U_s}{2N}\hat{\mathbf{S}}^2 - q\hat{N}_0, \tag{4.1}$$

where U_s is the spin interaction energy per atom, N the total atom number, $\hat{\mathbf{S}}$ the total spin operator, $q > 0$ the quadratic Zeeman energy with $q = 276.434\ \mathrm{Hz/G^2} \times B^2$, and $\hat{N}_\alpha$ the atom number operator of the Zeeman sub-level α ($\alpha = +1, 0, -1$).

We denote the temperature of the canonical ensemble "spin temperature" T_s, which determines the distribution in the eigenstates of $\hat{H}_{\mathrm{SMA}}$. Therefore, we have for example

$$\langle N_0^m \rangle_{T_s} = \frac{1}{\mathcal{Z}} \sum_k \langle N_0^m \rangle_k \times \mathrm{e}^{-\beta_s E_k}, \tag{4.2}$$

for integer m, with E_k the energy of eigenstate k, $\beta_s = 1/k_B T_s$ and the partition function $\mathcal{Z} = \sum_k \mathrm{e}^{-\beta_s E_k}$. We denote

$$\langle n_0 \rangle = \frac{\langle N_0 \rangle}{N}, \quad \Delta n_0 = \frac{\Delta N_0}{N}, \tag{4.3}$$

where N is the total atom number, with ΔN_0 the standard deviation of N_0.

In this section, we begin with the introduction to the total spin basis $|N, S, M\rangle$, which is the eigenstate of $\hat{H}_{\mathrm{SMA}}$ at $q = 0$. Here, S is the eigenvalue of the total spin operator $\hat{S}^2$, and M is the eigenvalue of $\hat{S}_z$. This basis is used to develop most of our theory. In the second part of this section, we diagonalize directly the Hamiltonian to calculate $\langle n_0 \rangle$ and Δn_0 for generic q. In the third part, we introduce a so-called "broken symmetry" approach to calculate the moments of n_0, by which the calculation is faster and precise enough.

4.2.1 Formulation in the basis of total spin eigenstates $|N, S, M\rangle$

4.2.1.1 Represention of $\hat{H}_{\mathrm{SMA}}$ in the $|N, S, M\rangle$ basis

We begin with the simplest case, $q = 0$. In this case, $\hat{H}_{\mathrm{SMA}}$ can be solved analytically. The eigenstates of $\hat{H}_{\mathrm{SMA}}$ (Eq. (4.1)) are given by the total spin states $|N, S, M\rangle$ with

energy $E(S) = (U_s/2N)S(S+1)$. We assume that the number of atoms N is even for simplicity. Odd values of N could be treated in a similar way, without modifying the final results to order $1/N$.

The degeneracy of energy level S is $2S+1$. We plot in Fig. 4.3 the illustration of the energy levels for $q = 0$. Remark that S can only be even, because the spatial wave function is symmetric in the s-wave scattering regime, as mentioned in chapter 1, section 1.3.2.1.

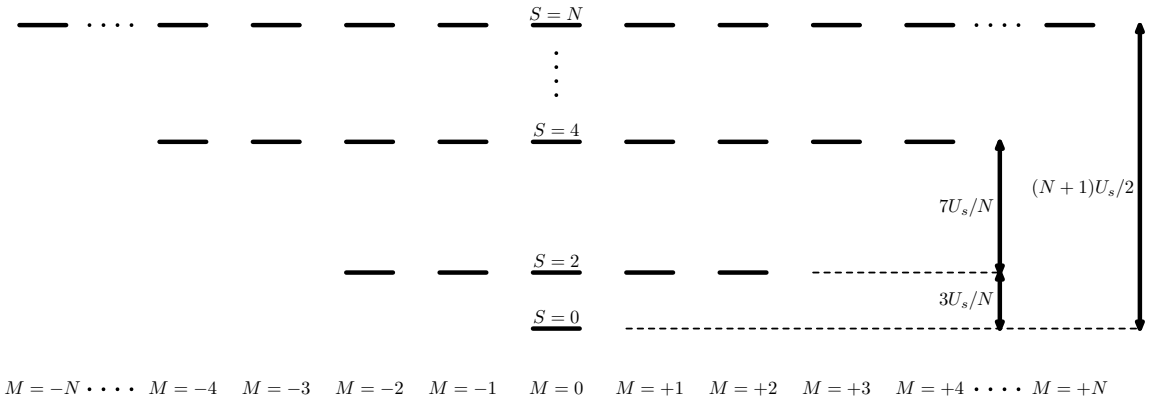


Figure 4.3: Energy level of $\hat{H}_{\mathrm{SMA}}$ for $q = 0$

The total spin eigenstates $|N, S, M\rangle$ can be constructed as follows [89, 46, 91],

$$|N, S, M\rangle = \frac{1}{\sqrt{\mathcal{N}(N, S, M)}} \big(\hat{S}^-\big)^P \big(\hat{A}^\dagger\big)^Q (\hat{a}^\dagger_{+1})^S |\mathrm{vac}\rangle, \tag{4.4}$$

with

$$P = S - M, \tag{4.5}$$

$$2Q = N - S. \tag{4.6}$$

and with the normalization factor

$$\mathcal{N}(N, S, M) = \frac{S!(N-S)!!(N+S+1)!!(S-M)!(2S)!}{(2S+1)!!(S+M)!}. \tag{4.7}$$

Here we introduce the operators

$$\hat{S}^- = \sqrt{2}(\hat{a}^\dagger_{-1}\hat{a}_0 + \hat{a}^\dagger_0\hat{a}_{+1}), \tag{4.8}$$

$$\hat{A}^\dagger = \hat{a}^\dagger_0 - 2\hat{a}^\dagger_{-1}\hat{a}^\dagger_{+1}, \tag{4.9}$$

with $[\hat{S}^-, \hat{A}^\dagger] = 0$.

The operator $\hat{S}^-$ is the total spin lowering operator. The operator $\hat{A}^\dagger$ creates a pair of atoms in the singlet state which can be described by Fock basis $|N_{+1}, N_0, N_{-1}\rangle_{\mathrm{Fock}}$ as

$$\psi_{\mathrm{singlet}} = \sqrt{\frac{1}{3}}\,|0, 2, 0\rangle_{\mathrm{Fock}} - \sqrt{\frac{2}{3}}\,|1, 0, 1\rangle_{\mathrm{Fock}}, \tag{4.10}$$

or directly by the total spin basis $|N, S, M\rangle_{\mathrm{NSM}}$ as

$$\psi_{\mathrm{singlet}} = |2, 0, 0\rangle_{\mathrm{NSM}}. \tag{4.11}$$

In the following discussion, we use only the total spin eigenstates, therefore, we neglect the subscript for indicating the basis.

For $q \neq 0$, the total spin eigenstates are no longer the eigenstates of the $\hat{H}_{\mathrm{SMA}}$, since $[\hat{\mathbf{S}}^2, \hat{N}_0] \neq 0$. However, since $[\hat{S}_z, \hat{N}_0] = 0$, M, which is the eigenvalue of $\hat{S}_z$, is still a good quantum number. As a result, we can diagonalize $\hat{H}_{\mathrm{SMA}}$ by block for each M. For each M, the energy eigenstates can be expressed in the total spin basis,

$$|\phi_M\rangle = \sum_{S=|M|}^{N} c_{S,M} |N, S, M\rangle. \tag{4.12}$$

In order to diagonalize the $\hat{H}_{\mathrm{SMA}}$ in the $|N, S, M\rangle$ basis, we have to calculate the matrix elements of the $\hat{H}_{\mathrm{SMA}}$ in this basis,

$$\langle N, S', M'|\hat{H}_{\mathrm{SMA}}|N, S, M\rangle = \frac{U_s}{2N} S(S+1)\delta_{S,S'}\delta_{M,M'} - q\langle N, S', M'|\hat{N}_0|N, S, M\rangle. \tag{4.13}$$

According to Eq. (4.13), we have to calculate the matrix elements of $\hat{N}_0$ in $|M, S, M\rangle$ basis, we use the following relation

$$\hat{a}_0\,|N, S, M\rangle = \sqrt{A_-(N, S, M)}|N-1, S-1, M\rangle + \sqrt{A_+(N, S, M)}|N-1, S+1, M\rangle, \tag{4.14}$$

with coefficients

$$A_-(N, S, M) = \frac{(S^2 - M^2)(N + S + 1)}{(2S - 1)(2S + 1)}, \tag{4.15}$$

$$A_+(N, S, M) = \frac{((S+1)^2 - M^2)(N - S)}{(2S + 1)(2S + 3)}. \tag{4.16}$$

This gives the matrix elements of $\hat{H}_{\mathrm{SMA}}$ in the $|N, S, M\rangle$ basis as

$$h^M_{S,S} = \frac{U_s}{2N} S(S+1) - q\langle S|\hat{N}_0|S\rangle = \frac{U_s}{2N} S(S+1) - q[A_+(N, S, M) + A_-(N, S, M)], \tag{4.17}$$

$$h^M_{S,S+2} = -q\langle S+2|\hat{N}_0|S\rangle = -q\sqrt{A_-(N, S+2, M) \cdot A_+(N, S, M)}, \tag{4.18}$$

$$h^M_{S,S-2} = -q\langle S-2|\hat{N}_0|S\rangle = -q\sqrt{A_+(N, S-2, M) \cdot A_-(N, S, M)}. \tag{4.19}$$

where we abbreviate $|N, S, M\rangle$ as $|S\rangle$ to simplify the notation of the states.

The Schrödinger equation then takes the form of a tridiagonal matrix equation,

$$h^M_{S,S+2}\, c_{S+2,M} + h^M_{S,S-2}\, c_{S-2,M} + h^M_{S,S}\, c_{S,M} = E\, c_{S,M}, \tag{4.20}$$

with E the energy eigenvalue. After the diagonalization, we get the spectrum of $\hat{H}_{\mathrm{SMA}}$. In principle, we can calculate the spectrum by this method, however, the dimension of the matrix of Hamiltonian D increases when N increases (see in Fig. 4.3, $S = 0, 2, 4, \ldots, N$, we remind that S should be even). The time complexity of the diagonalization is $\mathcal{O}(D^3)$, which makes the direct diagonalization in general hard to access for atom number ~ 5000 [1].

[1] In fact, during the Hartree-Fock simulation (see section 4.4), we have to diagonalize many times the matrix, which makes it important to reduce the time complexity.

4.2.1.2 Calculation of $\langle n_0 \rangle$ and Δn_0 for $|N, S, M\rangle$

According to Eq. (4.14), we can calculate the expected value and standard deviation of N_0 for a given total spin eigenstate $|N, S, M\rangle$:

$$\langle \hat{N}_0 \rangle_{S,M} = \langle N, S, M | \hat{a}_0^\dagger \hat{a}_0 | N, S, M \rangle = A_-(N, S, M) + A_+(N, S, M). \tag{4.21}$$

For the fluctuation, we should first calculate $\langle N, S, M | (\hat{a}_0^\dagger)^2 (\hat{a}_0)^2 | N, S, M \rangle$ in using Eq. (4.14) twice. The variance of $\hat{N}_0$ is then given by

$$\begin{aligned}(\Delta \hat{N}_0^2)_{S,M} &= \langle N, S, M | \hat{a}_0^\dagger \hat{a}_0 \hat{a}_0^\dagger \hat{a}_0 | N, S, M \rangle - \langle N, S, M | \hat{a}_0^\dagger \hat{a}_0 | N, S, M \rangle^2 \\ &= \langle N, S, M | (\hat{a}_0^\dagger)^2 (\hat{a}_0)^2 | N, S, M \rangle + \langle N, S, M | \hat{a}_0^\dagger \hat{a}_0 | N, S, M \rangle - \langle N, S, M | \hat{a}_0^\dagger \hat{a}_0 | N, S, M \rangle^2.\end{aligned} \tag{4.22}$$

As a example, we apply Eq. (4.21), (4.22) to the *ground state* $|N, 0, 0\rangle$. We have

$$\langle n_0 \rangle_{00} = \frac{1}{3}, \tag{4.23}$$

$$(\Delta n_0)_{00} = \sqrt{\frac{4N^2 + 12N}{45N^2}} \approx \sqrt{\frac{4}{45}}. \tag{4.24}$$

Numerically, the leading term in the expression for the standard deviation of n_0 is $\sqrt{4/45} \approx 0.298$. We remark that the ground state display a super-Poissonian fluctuation, which means $\Delta N_0^2 \propto N^2$, different from the thermal atom number fluctuations $\Delta N_{\rm th}^2 \propto N_{\rm th}$.

Eq. (4.23) and (4.24) give only the expected value and standard deviation for the ground state ($q = 0$). In the following discussion, we mainly focus on the temperature regime where the thermal weight will favor states with $1 \ll S \ll N$. For $q = 0$, the eigenvalues of $\hat{H}_{\rm SMA}$ are $E(S) = (U_s/2N)S(S+1)$. Therefore, the temperature regime in which we are interested is

$$\frac{U_s}{N} \ll k_B T_s \ll N U_s. \tag{4.25}$$

In our experiment [38], at the end of the evaporation, $U_s \approx 66$ Hz, $N \approx 5000$, therefore

$$0.64 \text{ pK} \ll T_s \ll 16 \ \mu\text{K}. \tag{4.26}$$

Since $T_s \sim 10 - 100$ nK (as we will see in the experiment part of this chapter), we work well in the temperature regime in Eq. (4.25).

In fact, in the case $1 \ll S \ll N$, we can simplify the diagonalization of $\hat{H}_{\rm SMA}$ (Eq. (4.20)) just by reducing the dimension of the matrix. For example, for $N = 5000$, in principle, we have to diagonalize a 2501×2501 matrix. However, since $S \ll N$, we can neglect matrix elements with large S. if we choose $S_{\max} = 1000$, we only have to diagonalize a 501×501 matrix, which accelerates a lot the calculation.

For the states with $1 \ll S \ll N$, we can also approximate the coefficients $A_\pm$ by keeping the leading order in S and $|N - S|$:

$$A_\pm(N, S, M) \approx \frac{N \mp S}{4S^2} (S^2 - M^2), \tag{4.27}$$

This leads to

$$\langle \hat{N}_0 \rangle_{S,M} \approx \frac{N(S^2 - M^2)}{2S^2}, \tag{4.28}$$

$$\langle \hat{N}_0^2 \rangle_{S,M} \approx \frac{(S^2 - M^2)^2(3N^2 - S^2)}{8S^4}. \tag{4.29}$$

$$(\Delta \hat{N}_0^2)_{S,M} = \langle \hat{N}_0^2 \rangle_{S,M} - \langle \hat{N}_0 \rangle_{S,M}^2 \approx \frac{(S^2 - M^2)^2(N^2 - S^2)}{8S^4}. \tag{4.30}$$

We note that the low-energy eigenstates with $S \ll N, |M| \ll S$ display super-Poissonian fluctuations as found in the ground state ($(\Delta N_0^2)_{\mathrm{S0}} \propto N^2$), whereas eigenstates with $M = S$ display no fluctuations in this approximation. This is the origin of the "abnormal" fluctuations at low B around the critical field B_c (see Fig. 3.5) in chapter 3.

4.2.2 Thermal equilibrium for $\langle \hat{S}_z \rangle = 0$

In this subsection, we use the total spin basis to calculate the first two moments of n_0 at finite temperature T_s. We suppose that all the sectors of M are populated with $\langle \hat{S}_z \rangle = 0$, *i.e.*, the magnetization vanishes in average but fluctuations around zero are possible. In this case, we should diagonalize the $\hat{H}_{\mathrm{SMA}}$ block by block for different M (see Fig. 4.3). In [98] (see in g E, published articles 2), we consider a simpler case, in which we suppose only $M = 0$ sector is populated. All the approximation methods used in that article (*e.g.* tight-binding model) can be applied in $\langle \hat{S}_z \rangle = 0$ case and most of the results in [98] are qualitatively the same as in this subsection.

4.2.2.1 Depletion and fluctuation at $q = 0$

We begin with the system with $q = 0$ at finite temperature T_s. The eigenstates in this case is thus total spin basis $|N, S, M\rangle$, with $E(S) = (U_s/2N)S(S+1)$. If $k_B T_s \ll U_s/N$, only the ground state $|N, 0, 0\rangle$ is populated, as a result, the depletion and the fluctuation of n_0 is given by Eq. (4.23) and (4.24), which display a super-Poissonian fluctuation.

Calculation for $U_s/N \ll k_B T_s \ll N U_s$:

In this temperature regime, the partition function $\mathcal{Z}$ is given by

$$\mathcal{Z} = \sum_{S,M} \mathrm{e}^{-\beta' S(S+1)} \approx \int_0^{+\infty} \mathrm{e}^{-\beta' S^2} \mathrm{d}S \int_{-S}^{+S} \mathrm{d}M = \frac{1}{\beta'}, \tag{4.31}$$

with $\beta' = U_s/(2N k_B T_s)$. This replacement from discrete sum to an integer is valid as long as $1 \ll S \ll N$. The thermal average of $\langle N_0 \rangle_{T_s}$ and $\langle N_0^2 \rangle_{T_s}$ in the canonical ensemble is given by (using Eq. (4.28) and (4.29))

$$\langle N_0 \rangle_{T_s} = \frac{1}{\mathcal{Z}} \sum_{S,M} \mathrm{e}^{-\beta' S(S+1)} \langle N_0 \rangle_{S,M} \approx \frac{N}{3}, \tag{4.32}$$

and to leading order

$$(\Delta N_0^2)_{T_s} = \langle N_0^2 \rangle_{T_s} - \langle N_0 \rangle_{T_s}^2 \approx \frac{4N^2}{45}. \tag{4.33}$$

Calculation for $k_BT_s \gg NU_s$:

For the temperature $k_BT_s \gg NU_s$, the calculations above are *not* valid (the upper bound of the integer, *e.g.* in Eq. (4.31), cannot be extended to $+\infty$). In this regime, the temperature is even large compared with the largest eigenvalue of spectrum (see Fig. 4.3), all the eigenstates are essentially equally populated. We can therefore replace the Boltzmann factor by 1, and thus $\mathcal{Z} \approx N^2$. We have

$$\langle N_0 \rangle_{T_s} \approx \frac{N}{3}. \tag{4.34}$$

$$(\Delta N_0^2)_{T_s} = \langle N_0^2 \rangle_{T_s} - \langle N_0 \rangle_{T_s}^2 \approx \frac{N^2}{18}. \tag{4.35}$$

In conclusion, we have calculated the depletion and the fluctuation at $q = 0$. First, for any temperature T_s, the fluctuation ΔN_0^2 is always super-Poissonian. The temperature will not degrade the large quantum fluctuation at $q = 0$, simply because the temperature will not break the symmetry of the system. Second, the values of the depletion is alway $1/3$, almost independent of temperature T_s, from zero, where the system is in the ground state, until very large temperature $k_BT_s \gg NU_s$. The value of fluctuation is alway $2/3\sqrt{5} \approx 0.298$ from $T_s \sim 0$ until $k_BT_s \ll NU_s$, and decreases to $1/3\sqrt{2} \approx 0.236$ at very large temperature $k_BT_s \gg NU_s$. We remind that the typical level spacing $U_s/N \sim$pK, and the upper bound $NU_s \sim 10\mu$K. As a result, for our experiment, the intermediate temperature limit $U_s/N \ll k_BT_s \ll NU_s$ is always the relevant one. The values for $\langle n_0 \rangle$ and Δn_0 at $q = 0$ are summarized in Tab. 4.1, including the $M = 0$ case, which is discussed in detail in [98].

	$k_BT \ll U_s/N$	$U_s/N \ll k_BT \ll NU_s$	$k_BT \gg NU_s$	
$M = 0$	$1/3$	$1/2$	$1/2$	$\langle n_0 \rangle$
	$2/3\sqrt{5} \approx 0.298$	$1/2\sqrt{2} \approx 0.354$	$1/2\sqrt{3} \approx 0.289$	Δn_0
$\langle \hat{S}_z \rangle = 0$	$1/3$	$1/3$	$1/3$	$\langle n_0 \rangle$
	$2/3\sqrt{5} \approx 0.298$	$2/3\sqrt{5} \approx 0.298$	$1/3\sqrt{2} \approx 0.236$	Δn_0

Table 4.1: Summary of the value of $\langle n_0 \rangle$ and Δn_0 for different situations : a system prepared in the eigenstates of $\hat{S}_z$ with $M = 0$, and a system prepared in a mixture of different M, with $\langle \hat{S}_z \rangle = 0$.

4.2.2.2 Calculation for generic q

For generic q, we diagonalize directly the SMA Hamiltonian $\hat{H}_{\text{SMA}}$ in total spin basis $|N, S, M\rangle$. We summarize in Fig. 4.4, Δn_0 in the $q - T$ plane, which is calculated by

exactly diagonalizing the SMA Hamiltonian for relatively small atom number $N = 300$ (Eq. (4.1)). Large fluctuations and depletion of the $m_F = 0$ state are observed for small q. We can distinguish three different regimes. For low magnetic field $q \ll U_s/N^2$ and low temperatures $k_B T_s \ll U_s/N$ the system is close to the ground state in a regime we call "quantum spin fragmented" [89, 46, 91, 95]. We also observe a thermal regime for $k_B T_s \gg Nq, U_s/N$ dominated by thermally populated excited states. We call this second regime "thermal spin fragmented". Finally, for q large enough and temperature low enough, the bosons condense into the single-particle state $m_F = 0$, forming a so-called "polar" condensate [29, 30]. In this limit, $\langle n_0 \rangle \approx 1$ and $\Delta n_0 \ll 1$. We indicate this third regime as "BEC $m = 0$" in Fig. 4.4 [2].

4.2.3 Broken-symmetry approach

We have treated until now the problem by the most natural method, by studying the spectrum of the SMA Hamiltonian Eq. (4.1). There is another approach to the problem of the spin 1 bosons with antiferromagnetic interactions [89, 39], which relies on the set of so-called "polar" or "spin-nematic" states, defined as

$$|N : \mathbf{\Omega}\rangle = \frac{1}{\sqrt{N!}} (\mathbf{\Omega} \cdot \hat{\mathbf{a}}^\dagger)^N |\text{vac}\rangle, \tag{4.36}$$

where in the standard basis, the vector $\mathbf{\Omega}$ is expressed as

$$\mathbf{\Omega} = \mathrm{e}^{i\gamma} \begin{pmatrix} \frac{1}{\sqrt{2}} \sin(\theta) \mathrm{e}^{i\phi} \\ \cos(\theta) \\ -\frac{1}{\sqrt{2}} \sin(\theta) \mathrm{e}^{-i\phi} \end{pmatrix}, \tag{4.37}$$

These states arise in the mean-field approach in chapter 1, section 1.3.3 when $q = 0$, they minimize the mean-field energy. For a single particle, the state $|1 : \mathbf{\Omega}\rangle = \sum_{i=+1,0,-1} \Omega_i |m_F = i\rangle$ form a family of spin 1 wave functions with

$$\langle 1 : \mathbf{\Omega}| \, \hat{\mathbf{s}} \, |1 : \mathbf{\Omega}\rangle = \mathbf{0}. \tag{4.38}$$

In fact, $|\mathbf{\Omega}\rangle$ is the eigenvector with zero eigenvalue of the operator $\mathbf{\Omega} \cdot \hat{\mathbf{s}}$, with $\hat{\mathbf{s}}$ the spin 1 operator. The states $|N : \mathbf{\Omega}\rangle$ correspond to a many-body wave function where all particle occupy the single particle state $|\mathbf{\Omega}\rangle$. As a result, we have $\langle N : \mathbf{\Omega}| \, \hat{\mathbf{S}} \, |N : \mathbf{\Omega}\rangle = 0$.

4.2.3.1 Zero temperature

We begin with considering the simplest case: the system at zero temperature. We can connect the spin nematic states (Eq. (4.36)) to the total spin states $|N, S, M\rangle$ discussed in the previous section. In fact, spin nematic states form an over-complete basis of the

[2] This phase diagram is calculated in $M = 0$ case [98]. The numerical values are not the same as $\langle \hat{S}_z \rangle = 0$ case, however, the conclusion holds.

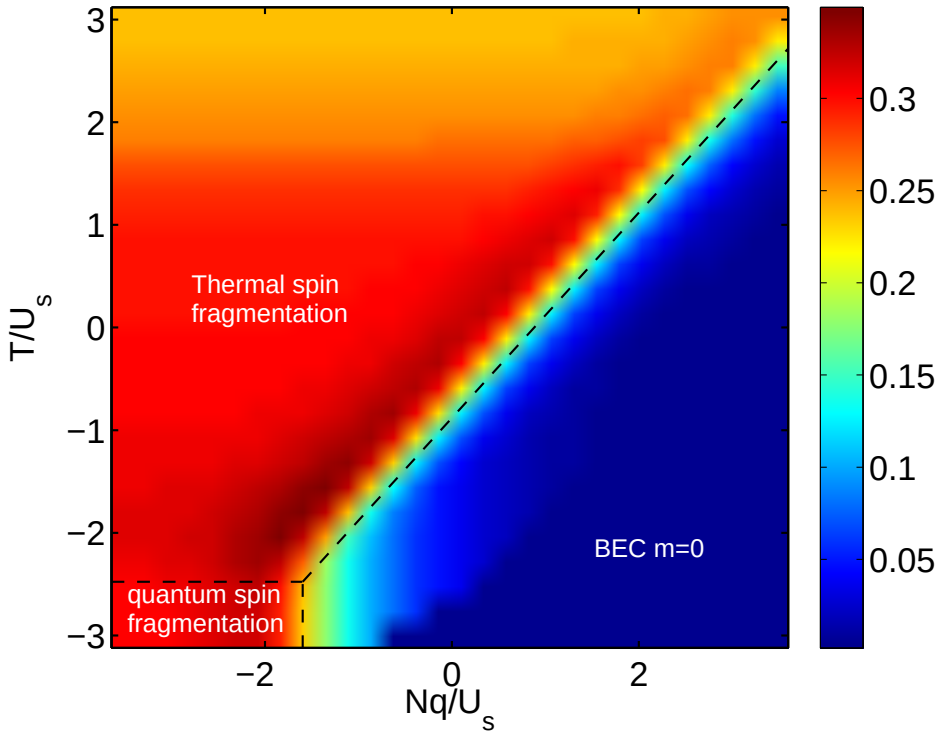


Figure 4.4: Standard deviation Δn_0 in the $q-T$ plane. We mark three different regimes in the $q-T$ plane. "Spin fragmentation" refers to a fragmented spin state with large population fluctuations, where $\Delta n_0 \sim 1$. In the quantum regime ($Nq/U_s \ll 1/N$ and $k_B T_s/U_s \ll 1/N$), this is due to quantum fluctuations: the system is then close to the singlet ground state. In the thermal regime ($k_B T_s \gg Nq, U_s/N$), on the other hand, thermal fluctuations dominate over the quantum one and over the effect of the quadratic Zeeman energy. Conversely, "BEC m=0" refers to atoms forming a regular polar condensate with almost all atoms in $m_F = 0$, and $\Delta n_0 \ll 1$. The plot was drawn by numerically diagonalizing the SMA Hamiltonian (Eq. (4.1)) and computing thermodynamic averages from the spectrum and eigenstates, using $N = 300$. Note the logarithmic scales on both the horizontal and the vertical axis.

bosonic Hilbert space. Expressing the total spin states in this basis, we have [3] [89, 39, 95]

$$|N, S, M\rangle = \int \mathrm{d}\mathbf{\Omega}\, Y_{S,M}(\mathbf{\Omega})|N : \mathbf{\Omega}\rangle, \tag{4.39}$$

where $Y_{S,M}(\mathbf{\Omega})$ is the spherical harmonics and $\mathrm{d}\mathbf{\Omega} = \sin(\theta)\mathrm{d}\theta\mathrm{d}\phi$. For example, at zero magnetic field and zero temperature, the system is in the singlet state $|N, 0, 0\rangle$. According to Eq. (4.39), the singlet ground state and be expressed as a coherent superposition of the spin nematic states with equal weights.

$$|N, 0, 0\rangle = \frac{1}{\sqrt{4\pi}} \int \mathrm{d}\mathbf{\Omega}\, |N : \mathbf{\Omega}\rangle. \tag{4.40}$$

Consider now the average value in the singlet state of a k-body operator $\hat{O}_k$

$$\langle \hat{O}_k \rangle_{\text{singlet}} = \langle N, 0, 0|\hat{O}_k|N, 0, 0\rangle = \frac{1}{4\pi} \int \mathrm{d}\mathbf{\Omega}\mathrm{d}\mathbf{\Omega}' \langle N : \mathbf{\Omega}'|\hat{O}_k|N : \mathbf{\Omega}\rangle. \tag{4.41}$$

As shown in [89], for few-body operators with $k \ll N$, this average value can be approximated to order $1/N$ by a much simpler expression

$$\langle \hat{O}_k \rangle_{\text{singlet}} \approx \frac{1}{4\pi} \int \mathrm{d}\mathbf{\Omega}\, \langle N : \mathbf{\Omega}|\hat{O}_k|N : \mathbf{\Omega}\rangle + \mathcal{O}(1/N). \tag{4.42}$$

In fact, according to Eq. (4.40), the density matrix of the singlet state is

$$\hat{\rho}_{\text{singlet}} = \frac{1}{4\pi} \int \mathrm{d}\mathbf{\Omega}\mathrm{d}\mathbf{\Omega}'\, |N : \mathbf{\Omega}'\rangle\langle N : \mathbf{\Omega}|. \tag{4.43}$$

We can also define a "Broken symmetry" density matrix which is the statistical mixture of the spin-nematic states

$$\hat{\rho}_{\text{BS}} = \frac{1}{4\pi} \int \mathrm{d}\mathbf{\Omega}\, |N : \mathbf{\Omega}\rangle\langle N : \mathbf{\Omega}|. \tag{4.44}$$

Therefore, the approximation Eq. (4.42) means that the average value in the singlet state can be approximated by the average value in the "Broken symmetry" state [89],

$$\langle \hat{O}_k \rangle_{\text{singlet}} \approx \langle \hat{O}_k \rangle_{\text{BS}} + \mathcal{O}(1/N). \tag{4.45}$$

and the spin singlet state can be approximated by the "Broken symmetry" density matrix [89]

$$\hat{\rho}_{\text{singlet}} \approx \hat{\rho}_{\text{BS}} + \mathcal{O}(1/N). \tag{4.46}$$

This approach (Eq. (4.45) and (4.46)) is known as the "Broken symmetry" picture. To the leading order of $1/N$, the exact and the broken symmetry approaches will give

[3] In fact, $|N, S, M\rangle$ defined by Eq. (4.39) is normalized to N, which means $\langle N, S, M|N, S, M\rangle = N$. This factor is compensated in all calculations we do by the same factor N in the scalar product $\langle N : \mathbf{\Omega}|N : \mathbf{\Omega}'\rangle = 2\pi N[\delta(\mathbf{\Omega} - \mathbf{\Omega}') + \delta(\mathbf{\Omega} + \mathbf{\Omega}')]$. We write the the scalar product as $\langle N : \mathbf{\Omega}|N : \mathbf{\Omega}'\rangle = 4\pi\delta(\mathbf{\Omega} - \mathbf{\Omega}')$ for simplicity in the rest of the thesis.

the same results after averaging over the ensemble. The difference between the two approaches vanish in the thermodynamic limit as $1/N$. Briefly speaking, the validity of the approximation Eq. (4.45) rely on that the overlap integral $\langle N:\mathbf{\Omega}|N:\mathbf{\Omega}'\rangle$ between two spin-nematic states vanishes very fast with the distance $|\mathbf{\Omega}-\mathbf{\Omega}'|$. This allows us to use the approximation $4\pi\delta(\mathbf{\Omega}-\mathbf{\Omega}')+\mathcal{O}(1/N)$.

We can thus calculate the moments of N_0 in the singlet state by the "Broken symmetry" approach. We begin with calculating the moments of N_0 in the spin-nematic states $|N:\mathbf{\Omega}\rangle$. In using Eq. (D.2) in appendix D.1, we have

$$\langle N:\mathbf{\Omega}|\hat{N}_0|N:\mathbf{\Omega}\rangle=\langle N:\mathbf{\Omega}|a_0^\dagger a_0|N:\mathbf{\Omega}\rangle=N\cos^2(\theta). \tag{4.47}$$

and the variance of N_0 reads

$$\langle N:\mathbf{\Omega}|\hat{N}_0^2|N:\mathbf{\Omega}\rangle=\langle N:\mathbf{\Omega}|a_0^\dagger a_0 a_0^\dagger a_0|N:\mathbf{\Omega}\rangle=N(N-1)\cos^4(\theta)+N\cos^2(\theta). \tag{4.48}$$

Therefore, the moments of N_0 averaged over $\hat{\rho}_{\mathrm{BS}}$ is

$$\langle N_0\rangle=\frac{1}{4\pi}\int_0^{2\pi}\mathrm{d}\phi\int_0^{\pi}\mathrm{d}\theta\,\sin(\theta)\cos^2(\theta)=\frac{N}{3}, \tag{4.49}$$

$$\Delta N_0^2=\langle N_0^2\rangle-\langle N_0\rangle^2=\frac{4N^2+6N}{45}. \tag{4.50}$$

The moments calculated in "Broken symmetry" picture thus only differ from the results (Eq. (4.23) and (4.24)) in the exact ground state (spin singlet state $|N,0,0\rangle$) by the sub-leading term $\propto N$. This is in agreement with the general statement made above.

4.2.3.2 Moments of N_0 at finite temperatures

In the previous part, we have calculated the moments for the spin singlet state $|N,0,0\rangle$ which is the ground state at zero temperature and zero magnetic field. In this part, we generalize the broken symmetry approach to the finite temperature and non-zero field. The broken symmetry density matrix should include the Boltzmann factor $\mathrm{e}^{-\beta\hat{H}_{\mathrm{SMA}}}$. To leading order in $1/N$, the spin nematic states have zero interaction energy and a mean quadratic Zeeman energy $-Nq\cos^2(\theta)$. In the spirit of the mean-field approximation, we replace the Boltzmann factor by its mean value, and the broken symmetry density matrix is given by

$$\hat{\rho}_{\mathrm{BS}}\approx\frac{1}{\mathcal{Z}}\int\mathrm{d}\mathbf{\Omega}\,|N:\mathbf{\Omega}\rangle\langle N:\mathbf{\Omega}|\mathrm{e}^{N\beta q|\Omega_z|^2}, \tag{4.51}$$

with $\beta=1/k_BT_s$. The partition function can be expressed as

$$\mathcal{Z}=\int_0^{2\pi}\mathrm{d}\phi\int_0^{\pi}\mathrm{d}\theta\,\sin(\theta)\mathrm{e}^{N\beta q\cos^2(\theta)}=2\pi F_{-1/2}(N\beta q). \tag{4.52}$$

Here we introduce the family of functions

$$F_\alpha(\eta)=\int_0^1 x^\alpha\mathrm{e}^{\eta x}\mathrm{d}x, \tag{4.53}$$

which are related to the lower incomplete gamma functions. As a result, the moments of N_0 is

$$\langle N_0^m \rangle = \frac{1}{\mathcal{Z}} \int \mathrm{d}\mathbf{\Omega} \, \langle N : \mathbf{\Omega} | \hat{N}_0^m | N : \mathbf{\Omega} \rangle \mathrm{e}^{N\beta q \cos^2(\theta)}. \tag{4.54}$$

In using Eq. (D.2), to leading order of N

$$\langle n_0^m \rangle = \frac{F_{m-1/2}(N\beta q)}{F_{-1/2}(N\beta q)}. \tag{4.55}$$

From Eq. (4.55), we can calculate easily the expected value and the standard deviation of n_0, not necessary to diagonalize the large matrix of $\hat{H}_{\mathrm{SMA}}$. According to Eq. (4.55), the moments of N_0 depend only on a dimensionless parameter $Nq/k_B T_s$.

We compare in Fig. 4.5, the expected value and the standard deviation calculated by broken symmetry approach and by the exact diagonalization. We find a good agreement between the two.

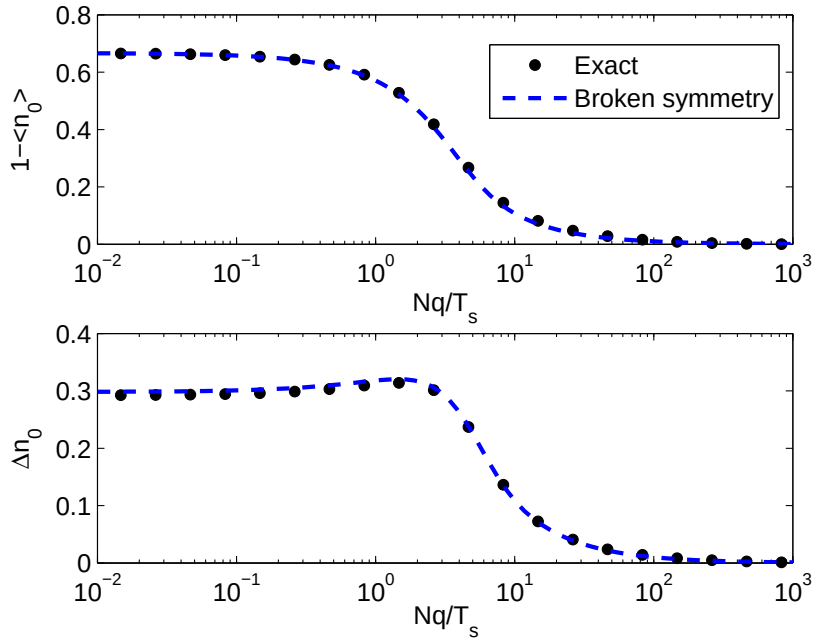


Figure 4.5: Comparison between the broken symmetry approach and exact diagonalization for $N = 1000$, $T = 10U_s$. The black dots are calculated by exact diagonalization, the blue dashed line is calculated by the broken symmetry approach.

4.3 Generalization to arbitrary distribution of M

In section 4.2, we have discussed the quantum solution of SMA Hamiltonian $\hat{H}_{\mathrm{SMA}}$, which describes the condensate. However, in comparing Fig. 4.5 with the experiment results, Fig. 4.1, 4.2, we find two major discrepancies. First, at large q, the theory predicts $1 - \langle n_0 \rangle \to 0$, however, there is a offset in the experimental results, especially in Fig.

4.1. This can be explained by taking the thermal atoms surrounding the condensate into account. We will discuss this in the next section. Second, at $q \to 0$, the theory predicts $1 - \langle n_0 \rangle = 2/3$, however, we measure experimentally $1 - \langle n_0 \rangle \approx 0.6$. Moreover, the theory which restricts atoms on $M = 0$ sector predicts $1 - \langle n_0 \rangle = 0.5$ at $q = 0$ (see Tab. 4.1). Therefore, a possible explanation is that the real distribution of M is between these two cases. Indeed, since $[\hat{H}_{\mathrm{SMA}}, \hat{S}_z] = 0$, the distribution of M is expected to be non-thermal as it cannot relax to the equilibrium distribution predicted by statistical mechanics. In this section, we use the broken symmetry description to generalize to an arbitrary distribution of M, more precisely, we suppose that the density matrix of the spin 1 system can be described by

$$\hat{\rho} = \frac{1}{\mathcal{Z}} \sum_{\nu,M} w_M \mathrm{e}^{-\beta E_{\nu,M}} |\nu, M\rangle\langle\nu, M|. \tag{4.56}$$

with $\hat{H}|\nu, M\rangle = E_{\nu,M}|\nu, M\rangle$, $\mathcal{Z} = \sum_{\nu,M} w_M \mathrm{e}^{-\beta E_{\nu,M}}$. This amounts to introducing a "generalized statistical ensemble" where the energy is fixed on average, while the population of each M_z sector and the total atom number are fixed exactly. For $q > 0$, S is no longer a good quantum number, we indicate ν as the quantum number for marking the eigenstates. Comparing to Eq. (4.2), the additional term w_M in Eq. (4.56) describes a "prior" distribution of M. As we will see, depending on how narrow w_M is, the value of $1 - \langle n_0 \rangle$ at $q = 0$ can lie anywhere between $1/2$ and $2/3$.

We denote $\hat{P}_M$, the projector on the subspace of M

$$\hat{P}_M = \sum_{\nu} |\nu, M\rangle\langle\nu, M|. \tag{4.57}$$

Because $[\hat{H}_{\mathrm{SMA}}, \hat{S}_z] = 0$, we have $\mathrm{e}^{-\beta\hat{H}_{\mathrm{SMA}}}\hat{P}_M = \mathrm{e}^{-\beta\hat{H}_{\mathrm{SMA}}}\hat{P}_M^2 = \hat{P}_M \mathrm{e}^{-\beta\hat{H}_{\mathrm{SMA}}}\hat{P}_M$. As a result, the density matrix Eq. (4.56) can also be expressed as

$$\hat{\rho} = \frac{1}{\mathcal{Z}} \sum_{M} w_M \hat{P}_M \mathrm{e}^{-\beta\hat{H}_{\mathrm{SMA}}} \hat{P}_M. \tag{4.58}$$

Using the results in appendix D.2, we finally get the expression of $\hat{\rho}$ and $\mathcal{Z}$ for the arbitrary distribution w_M

$$\langle N : \mathbf{\Omega}|\hat{\rho}|N : \mathbf{\Omega}\rangle \simeq \frac{1}{\mathcal{Z}} f(\mathbf{\Omega})\, \mathrm{e}^{\beta N q \Omega_z^2}, \tag{4.59}$$

$$\mathcal{Z} \simeq \int \mathrm{d}\mathbf{\Omega}\, f(\mathbf{\Omega})\, \mathrm{e}^{\beta N q \Omega_z^2}, \tag{4.60}$$

with

$$f(\mathbf{\Omega}) = \sum_{M=-N}^{N} \sum_{S=|M|}^{N} w_M |Y_{SM}(\mathbf{\Omega})|^2 = \sum_{S=0}^{N} \sum_{M=-S}^{S} w_M |Y_{SM}(\mathbf{\Omega})|^2. \tag{4.61}$$

Here, we use Eq. (4.59), (4.60), (4.61) to verify whether we can reproduce the results obtained before by assuming $w_M = 1$ and $w_M = \delta_{M,0}$, which correspond to the magnetization unconstrained ($\langle \hat{S}_z \rangle = 0$) and to the magnetization constrained ($M = 0$) cases, respectively.

- $w_M = 1$:

$$f(\mathbf{\Omega}) = \sum_{S=0}^{N} \sum_{M=-S}^{S} |Y_{SM}(\mathbf{\Omega})|^2 = \frac{(N+1)^2}{4\pi}. \tag{4.62}$$

In this case, Eq. (4.59) is the same as Eq. (4.51). Therefore, using $w_M = 1$, we recover all previous results calculated in the $\langle \hat{S}_z \rangle = 0$ case.

- $w_M = \delta_{M,0}$:

$$f(\mathbf{\Omega}) = \sum_{S=0}^{N} |P_S(\cos(\theta))|^2 \cdot \frac{2S+1}{4\pi} \approx \frac{N}{2\pi^2 \sin(\theta)}. \tag{4.63}$$

Therefore, we find

$$\langle n_0 \rangle = \frac{\int_0^\pi \mathrm{d}\theta \, \mathrm{e}^{\eta \cos^2(\theta)} \, \cos^2(\theta)}{\int_0^\pi \mathrm{d}\theta \, \mathrm{e}^{\eta \cos^2(\theta)}} = \frac{1}{2}\Big(1 - \frac{I_1(\eta/2)}{I_0(\eta/2)}\Big), \tag{4.64}$$

$$\langle n_0^2 \rangle = \frac{\int_0^\pi \mathrm{d}\theta \, \mathrm{e}^{\eta \cos^2(\theta)} \, \cos^4(\theta)}{\int_0^\pi \mathrm{d}\theta \, \mathrm{e}^{\eta \cos^2(\theta)}} = \frac{1}{2} + \frac{a-1}{2a} \frac{I_1(\eta/2)}{I_0(\eta/2)}. \tag{4.65}$$

with $\eta = N\beta q$ and $I_n(x)$ the n-order first kind modified Bessel function.

Eq. (4.64) and (4.65) reproduce very well the results of $M = 0$ case, calculated by exact diagonalization.

In the following sections, we always assume a Gaussian distribution for w_M

$$w_M = \mathrm{e}^{-\frac{M^2}{2(N\sigma)^2}}, \tag{4.66}$$

with σ the parameter describing the width of the distribution of M. Therefore, $w_M = \delta_{M,0}$ and $w_M = 1$ correspond to $\sigma = 0$ and $\sigma \to +\infty$, respectively. In Fig. 4.6, we plot $1 - \langle n_0 \rangle$ and Δn_0 as a function of Nq/T_s for $\sigma = 0, 0.3, +\infty$. We see clearly that as σ increases, the value of $1 - \langle n_0 \rangle$ (Δn_0) at $q \sim 0$ increases (decreases). In Fig. 4.7, we plot directly $1 - \langle n_0 \rangle$ and Δn_0 value at $q = 0$ as a function of σ.

4.4 Hartree-Fock Approach

In section 4.2 and 4.3, we have studied the theory for the condensate. In the experiment, there is always a thermal fraction, which is detectable. In this section, we start to consider this thermal part. Like in chapter 1, we separate the system into two parts, condensate and thermal cloud, and solve them separately. We adapt the semi-ideal Hartree-Fock approximation introduced in chapter 1, in which we neglect the influence of the thermal part on the condensate, to describe a fluctuating spinor BEC. Like in chapter 1, section 4, we focus on $m_z = 0$. We calculate $\langle n_0 \rangle$ as a function of B as well as the fluctuations Δn_0 as a function of B.

In principle, the same temperature should characterize at equilibrium the fluctuation

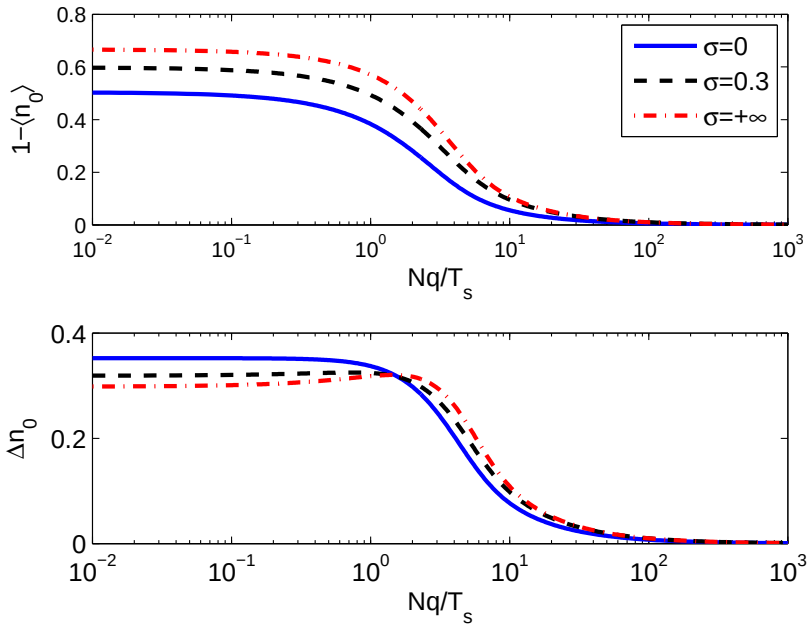


Figure 4.6: $1-\langle n_0\rangle$ and Δn_0 as a function of Nq/T_s for different σ ($\sigma = 0, 0.3, +\infty$).

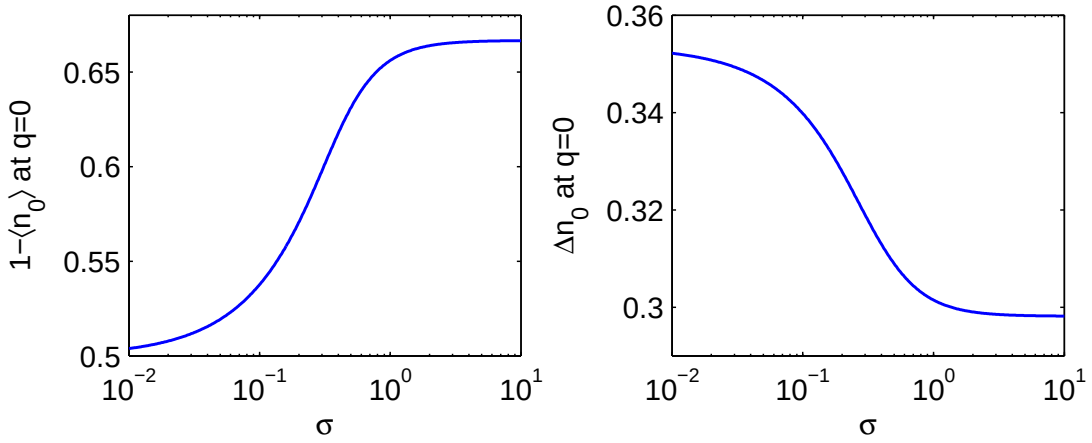


Figure 4.7: $1-\langle n_0\rangle$ and Δn_0 value at $q = 0$ as a function of σ.

of the spinor condensate and of the thermal components. We found that this does not describe the experimental data well, and that we need to introduce two different temperatures, the so-called "spin temperature" T_s, introduced in section 4.2 and the kinetic temperature T_k to characterize the spinor condensate and the thermal cloud, respectively. Therefore, the temperature used in the semi-ideal Hartree-Fock approximation is the kinetic temperature T_k, which determines the population of the various modes that compose the condensed component (one "phonon" mode, and two "spin waves" modes [29]). However the temperature used in the solution of the SMA Hamiltonian $\hat{H}_{\mathrm{SMA}}$, is the spin temperature T_s, which determines the excitations of the $\hat{H}_{\mathrm{SMA}}$. We find in the experiment (see next section) that the spin temperature T_s is much lower than the kinetic temperature T_k

$$T_s \ll T_k. \tag{4.67}$$

In this section, we first discuss how we adapt the semi-ideal Hartree-Fock approximation to fragmented spinor condensates. Next, we show the results of the simulation and in the end, we discuss the informations we can obtain from these simulations and how to use them in the experiment. For definiteness, all the simulations in this section assume that apart from $\langle \hat{S}_z \rangle = 0$, the magnetization is not constrained ($\sigma \to +\infty$ in the prior-distribution in Eq. (4.66)).

4.4.1 Semi-ideal Hartree Fock approximation for spinor BEC

The process of the HF simulation is almost the same as introduced in chapter 1, section 1.4. The density distribution is calculated by using Thomas-Fermi approximation and Single Mode Approximation (SMA), where we neglect the influence of the thermal cloud. The density distribution of the thermal cloud is calculated by the Bose distribution with an effective chemical potential and an effective external potential.

We follow the same iteration in chapter 1, section 1.4.1 which consists of 7 steps for the simulation, except that in step 3, $N^c_{+1}, N^c_0, N^c_{-1}$, the condensate atom number in $m_F = +1, 0, -1$ respectively, are calculated by Eq. (4.55) instead of the mean-field approach. Additionally, we calculate also the fluctuation ΔN_0. In fact, the fluctuation ΔN_0 is composed of two parts, the condensate and the thermal cloud. As we have discussed in the previous sections, the fluctuation of condensate is super-Poissonian ($\Delta N_0^2 \sim N^2$) which is much larger than the normal atom number fluctuation which is Poissonian ($\Delta N_0^2 \sim N$). The fluctuation of the thermal component are expected to be Poissonian, $\Delta N_{\mathrm{th}}^2 \sim N_{\mathrm{th}}$. As a result, the fluctuation is determined only by the condensate to a good approximation,

$$\Delta n_0^2 \approx f_c^2 \cdot (\Delta n_0^2)_{\mathrm{SMA}}. \tag{4.68}$$

The mean population in $m_F = 0$ is, however, affected by the thermal component,

$$\langle n_0 \rangle = f_c \cdot \langle n_0 \rangle_{\mathrm{SMA}} + \langle n_0 \rangle_{\mathrm{th}}. \tag{4.69}$$

This approximation is possibly challenged for the highest temperature we study, where $f_c \approx 0.3$.

4.4.2 Simulation results and analysis

In the following simulations, we always take the total atom number $N = 5000$, and an isotropic harmonic trap with $\bar{\omega} = \omega_x = \omega_y = \omega_z = 2\pi \times 1000$ Hz. We show in Fig. 4.8, the plots of $1-\langle n_0\rangle$ and Δn_0 as a function of q. We plot for different kinetic temperatures $T_k = 200, 300, 400$ nK with the same spin temperature $T_s = 30$ nK.

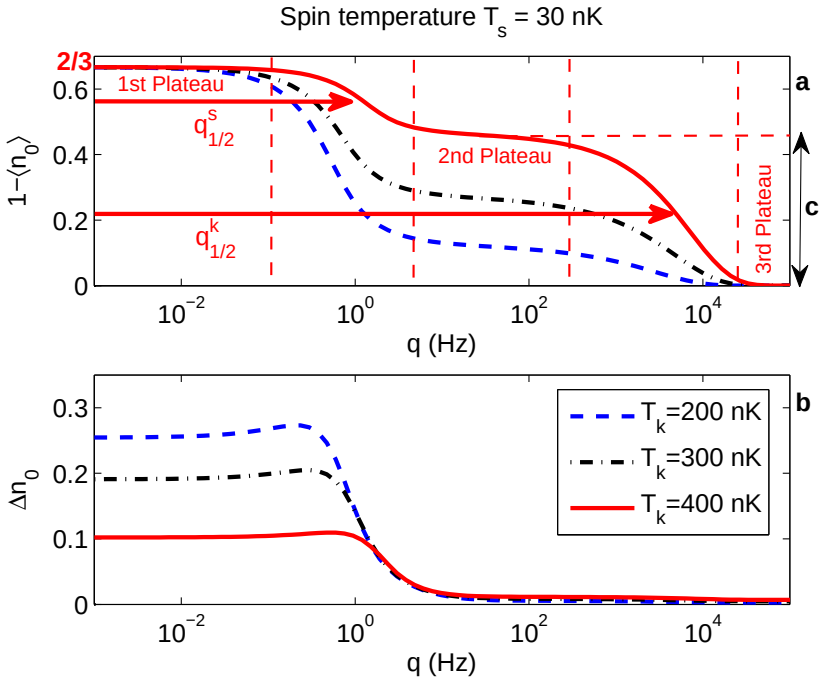


Figure 4.8: Plot of 1-$\langle n_0\rangle$ and Δn_0 as a function of q, with fixed spin temperature $T_s = 30$ nK. The kinetic temperature $T_k = 200, 300, 400$ nK for the blue dashed line, the black dash-dotted line and the red solid line, respectively.

In Fig. 4.8a, we plot $1 - \langle n_0\rangle$ as a function of q. We find for each kinetic temperature, there are three plateaux regions in $1 - \langle n_0\rangle$ curve, which means during an interval of q, $1 - \langle n_0\rangle$ stays almost constant. We take the curve with $T_k = 400$ nK an example and mark the three plateau regions in the figure.

The first plateau region is at low q. For $q \to 0$, we find $1 - \langle n_0\rangle \to 2/3$, which is independent of the kinetic temperature T_k. This is expected because of the spin rotational invariance for both condensate and thermal cloud. In the first plateau region, the magnetic field is not yet strong enough to break this spin rotational invariance, therefore, $1 - \langle n_0\rangle$ is almost unchanged.

Between the first and the second plateau region, as q increases, $1 - \langle n_0\rangle$ decreases until the value of the second plateau, which we denote c. As we will show later in Fig. 4.11, the spin isotropy of the thermal part is valid until the second plateau region, which also means the decrease of the $1-\langle n_0\rangle$ is mainly caused by the condensate. The magnetic field depletes the condensate atoms from $m_F = +1$ and $m_F = -1$ to $m_F = 0$ state because of the quadratic Zeeman effect.

In fact, the plateau value c in the second plateau region is the same as the plateau at low q in chapter 1, Fig. 1.6. Because we did not use the quantum solution of $\hat{H}_{\mathrm{SMA}}$, in chapter 1, the plateau will extend until $q \to 0$. In this plateau region, almost all the condensate atoms occupy the $m_F = 0$ state. Together with the spin isotropy of the thermal cloud, we can connect this plateau value c directly with the condensate fraction f_c, as in chapter 1, section 1.4.2. We have

$$f_c^{\mathrm{iso}} = 1 - \frac{3c}{2}. \tag{4.70}$$

This explains why c depends on the kinetic temperature T_k (larger T_k means smaller f_c thus larger c).

Further, we denote $q^s_{1/2}$, the Half width of q at Half Maximum (HWHM), with the half maximum here define as the mean value of the first and the second plateau. Therefore $1 - \langle n_0 \rangle (q^s_{1/2}) = 1/3 + c/2$. In fact, $q^s_{1/2}$ reflects the spin temperature T_s of the system, as we have discussed in the last section. We can verify that $q^s_{1/2}$ for different T_k in Fig. 4.8 are almost the same, with

$$k_B T_s \sim N q^s_{1/2}. \tag{4.71}$$

Between the second and the third plateau region, magnetic field begins to deplete thermal atoms from $m_F = +1$ and $m_F = -1$ to $m_F = 0$ state. The decrease of $1 - \langle n_0 \rangle$ value is thus caused by the thermal atoms. We denote $q^k_{1/2}$, the Half width of q at Half Maximum (HWHM), with the half maximum here define as the mean value of c and 0 (the second and the third plateau value), $1 - \langle n_0 \rangle (q^k_{1/2}) = c/2$. Because $1 - \langle n_0 \rangle$ value in this region corresponds to removing thermal atoms from $m_F = \pm 1$ states, we have

$$k_B T_k \sim q^k_{1/2} \tag{4.72}$$

Finally, in the third plateau region with very large q, all the atoms are in $m_F = 0$ state, because of the quadratic Zeeman effect.

In Fig. 4.8b, we plot Δn_0 as a function of q. The value of Δn_0 at $q \to 0$ depends on the kinetic temperature T_k (Eq. (4.68)). Higher T_k means smaller f_c thus smaller Δn_0. We show in Fig. 4.9, the plots of $1 - \langle n_0 \rangle$ and Δn_0 as a function of q. We plot for different spin temperatures $T_s = 10, 50, 200$ nK with the same kinetic temperature $T_k = 200$ nK. In Fig. 4.9a, we plot $1 - \langle n_0 \rangle$ as a function of q. Most of the characters of $1 - \langle n_0 \rangle$ curve are explained above. Here, we just remark two points. First, the plateau value c is almost independent of the spin temperature T_s. Second, $q^s_{1/2}$ is larger for larger spin temperature T_s (Eq. (4.71)). In Fig. 4.9b, we plot Δn_0 as a function of q. We find for the different spin temperatures, Δn_0 takes the same value at $q \to 0$ (Eq. 4.68). And the HWHM of q for Δn_0 is larger for larger T_s. All these features confirm that the condensate fraction f_c depends only on kinetic temperature T_k and not on spin temperature T_s.

We illustrate in Fig. 4.10, the condensate fraction f_c as a function of q for different spin temperatures and kinetic temperatures. We find that, in Fig. 4.10a, f_c is almost independent of T_s. In Fig. 4.10b, we find that the condensate fraction f_c is almost independent

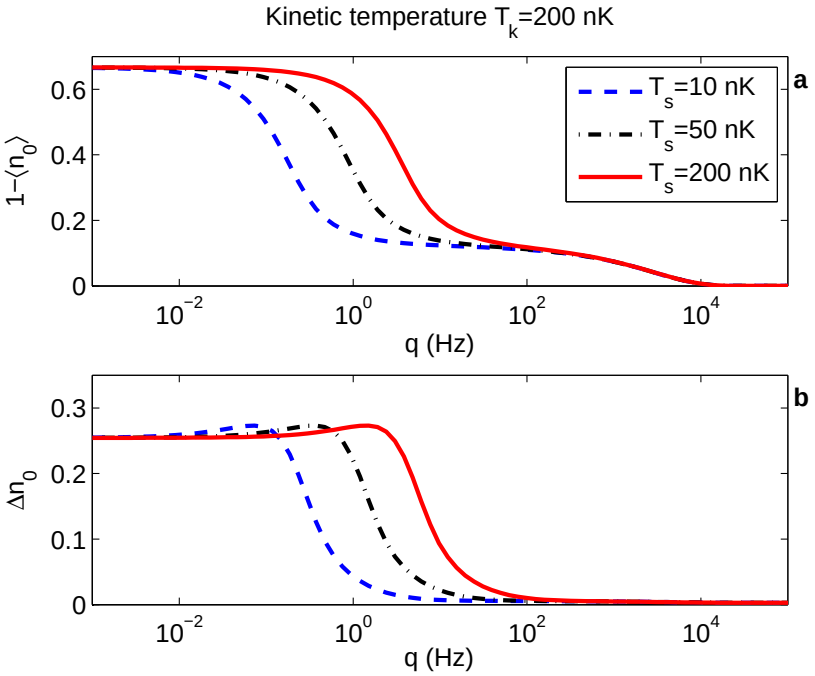


Figure 4.9: Plot of $1-\langle n_0\rangle$ and Δn_0 as a function of q, with fixed kinetic temperature $T_k = 200$ nK. The spin temperature $T_s = 10, 50, 200$ nK for the blue dashed line, the black dash-dotted line and the red solid line, respectively.

of q until the second plateau region.

In Fig. 4.11, we illustrate the deviation (of the spin isotropy) parameter Q as a function of q for different spin and kinetic temperatures. We remind here the definition of Q

$$Q = \frac{N_{+1}^{\rm th} + N_{-1}^{\rm th} - 2N_0^{\rm th}}{N}. \tag{4.73}$$

which is zero if the spin isotropy is perfectly satisfied. In Fig. 4.11(a), (b), we find that until the second plateau region, Q is small, indicating that the spin isotropy of the thermal clouds is not broken. When q increases slightly from 0, Q increases slightly. This is because as q increases, there are more condensed atoms in $m_F = 0$, which prefer more thermal atoms in $m_F = \pm 1$. For large $q \sim k_B T_k$, thermal atoms are depleted from $m_F = \pm 1$ to $m_F = 0$ state, because of the quadratic Zeeman energy, breaking the spin isotropy of the thermal clouds.

In conclusion, in this section, we have used the semi-ideal Hartree-Fock approximation to study our spin-1 system with the presence of the thermal cloud. Comparing to chapter 1, section 1.4, we used the quantum solution developed in the previous section in this chapter to describe the condensate. We focused as usual on $1-\langle n_0\rangle$ and Δn_0 as a function of q. We found that, these plots reveals several important characters of our system, as pointed out in chapter 1, section 1.4, including the spin temperature T_s, the kinetic temperature T_k, and the condensate fraction f_c. In the end, we pointed out that the spin isotropy of the thermal cloud is well satisfied until the second plateau region, as a result, it allows us to connect directly the plateau value c in the $1-\langle n_0\rangle$ plot with the condensate fraction

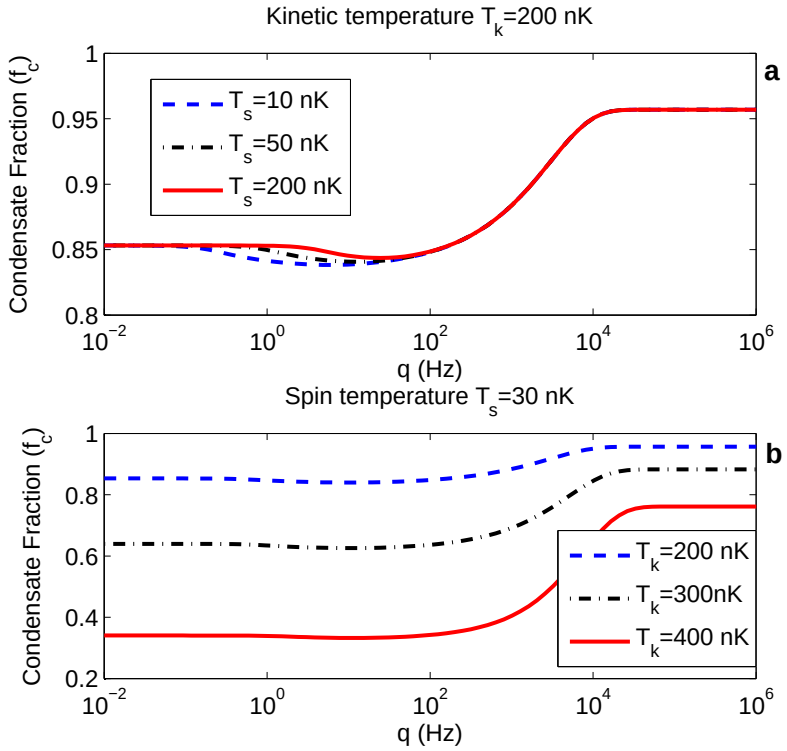


Figure 4.10: Condensate fraction f_c as a function of q for different spin temperatures and kinetic temperature. (a). fixed kinetic temperature. (b). fixed spin temperature.

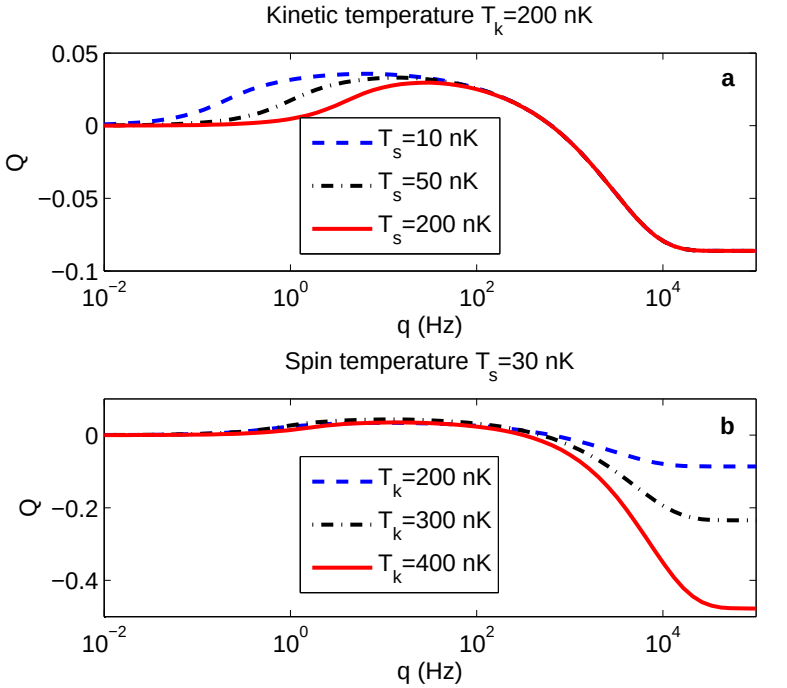


Figure 4.11: Deviation of spin isotropy of the thermal clouds. $Q = (N_{+1}^{\rm th} + N_{-1}^{\rm th} - 2N_0^{\rm th})/N$ as a function of q for different spin temperatures and kinetic temperature. (a). fixed kinetic temperature. (b). fixed spin temperature.

f_c, shown in Eq. (4.70). In the next section, we will introduce our experiment to study the large collective fluctuation, and we will use the model introduced in this section to analyze the data from the experiments.

4.5 Analysis of experimental results

In the previous sections, we introduced the theory of spin-1 antiferromagnetic condensate. In combining the quantum solution of SMA Hamiltonian $\hat{H}_{\rm SMA}$ (Eq. (4.1)) for the condensate and the semi-ideal Hartree Fock approach, we calculated the behavior of $1-\langle n_0\rangle$ and Δn_0 as a function of q. In comparing with the results in chapter 1, section 1.4, in which mean-field theory is used to describe the condensate, we find that the difference is mainly in low q regime. In this section, we show our experimental study of this collective fluctuation and use the theory developed in section 4.2 to 4.4 to analyze the experimental data. We begin this section by introducing the data analysis methods. We show, in the next two parts, the results measured during evaporation and during hold time, respectively. In the last part of this section, we concentrate on another aspect of the spin-1 BEC, the fluctuation of magnetization Δm_z at $q=0$. The interpretation and discussion of the results will be discussed in the next section.

4.5.1 Data analysis

In Fig. 4.12 and 4.13, we show our fitting results of Fig. 4.1 and 4.2 by the model introduced in the previous sections. In fact, for a given total atom number $N_{\rm tot}$ and trap frequency $f_{\rm trap}$, we have 3 parameters to fit:

- kinetic temperature T_k,
- spin temperature T_s,
- σ, the width of the prior-distribution of M (see chapter 4, section 4.3).

The χ_2 function of the fit is given by

$$\chi_2=\sum_{q_m}(\langle n_0\rangle_{\rm HF}-\langle n_0\rangle_m)^2+((\Delta n_0)_{\rm HF}-(\Delta n_0)_m)^2, \tag{4.74}$$

where q_m is the measured q value in the experiment, the subscript "HF" and "m" of $\langle n_0$ and Δn_0 indicate "calculated by Hartree-Fock simulation" and "measured", respectively. In these two figures, we can see features in the $1-\langle n_0\rangle$ and Δn_0 curves discussed in the previous section. For example, in $1-\langle n_0\rangle$ plot, the plateau value at intermediate q in Fig 4.12 is larger than that in Fig. 4.13, indicating that the condensate fraction f_c at $T_{\rm evap}=900$ ms is smaller than that at $T_{\rm evap}=975$ ms (Eq. (4.70)).

We use Eq. (4.74) as the χ_2 function to minimize. This fitting, considering both $1-\langle n_0\rangle$ and Δn_0 curve together, is denoted "global fit" (temperatures fitted are marked by a superscript G). Besides, we can obtain temperatures from $1-\langle n_0\rangle$ or Δn_0 curve individually (marked by a superscript $\langle n_0\rangle$, Δn_0, respectively). In comparing temperatures

fitted by these three methods, we find that the $T^{G}_{k/s}$ is normally between $T^{\langle n_0 \rangle}_{k/s}$ and $T^{\Delta n_0}_{k/s}$ and in general, they are in good agreement except at high temperature, suggesting that the Hartree-Fock model, introduced in chapter 4, is valid at low temperature and reaches its limit at high temperature (low condensate fraction). We should also point out that the parameter σ is essentially used to adjust the $1 - \langle n_0 \rangle$ value at $q \to 0$. We also realize the Hartree-Fock simulation with $\sigma \to +\infty$ and find the same kinetic temperature T_k and spin temperature T_s for all the trap depths and hold times within the error bars. This shows that the temperatures fitted are not affected by σ.

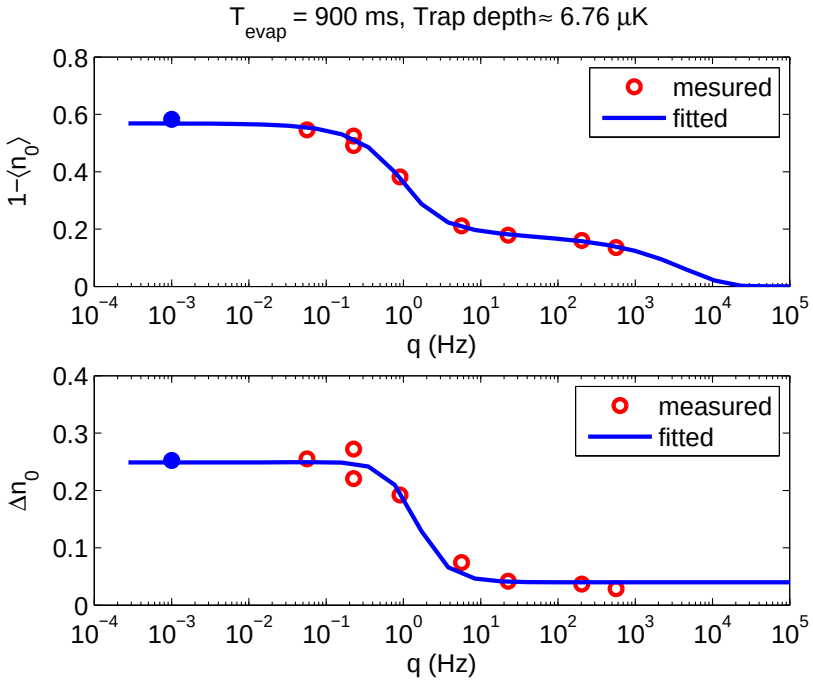


Figure 4.12: Second evaporation $T_{\text{evap}} = 900$ ms, trap depth ~ 6.76 μK. The point closet to $q = 0$ (the solid blue circle) corresponds to zero applied field, and bas been set arbitrarily at $q = 10^{-3}$ Hz.

In our experiment, we realize two kinds of experiment sequences.

- hold time fixed at 6 seconds, we vary the evaporation time T_{evap} from 750 ms to 1000 ms, which is shown in section 4.5.2,
- evaporation time fixed at 1000 ms (end of the second evaporation), we vary the hold time from 1 second to 15 seconds, which is shown in section 4.5.3.

4.5.2 Experimental results of temperature during evaporation

We illustrate in Fig 4.14 and 4.15 the analysis results of temperature with error bars (confidence interval with 68% [99]) during evaporation (with fixed hold time 6 s). The fitting results of σ will be shown in section 4.5.4. We illustrate, in Fig. 4.14, the kinetic and spin temperature (T_k, T_s) as a function of trap depth V_{trap} (with fixed hold time 6 seconds). During the second evaporation, since the trap depth decreases linearly

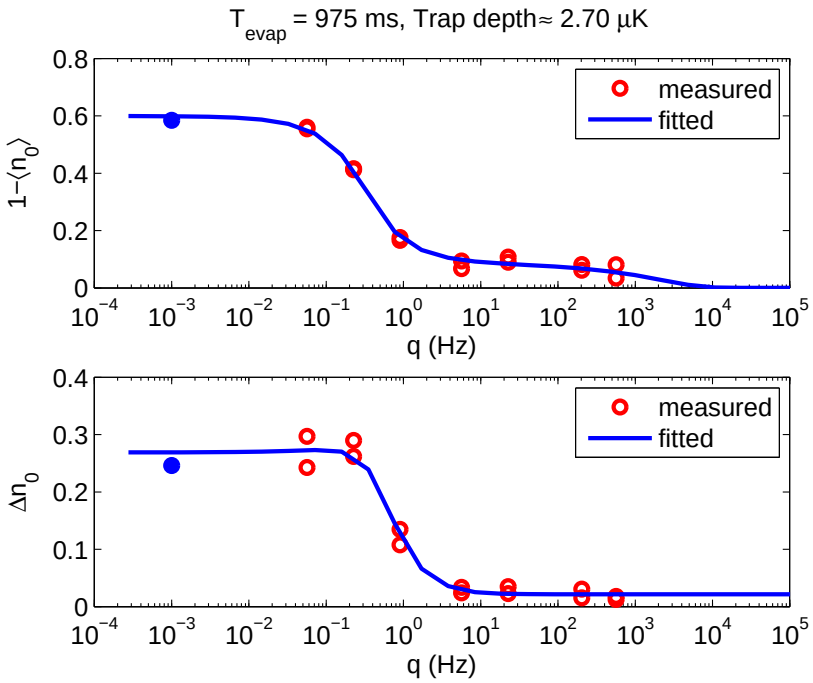


Figure 4.13: Second evaporation $T_{\text{evap}} = 975$ ms, trap depth ~ 2.70 μK. The point closet to $q = 0$ (the solid blue circle) corresponds to zero applied field, and bas been set arbitrarily at $q = 10^{-3}$ Hz.

(chapter 2, section 2.3.3), the kinetic temperature T_k also decreases linearly (chapter 2, section 2.3.1). However, the spin temperature T_s behaves quasi-independent of the trap depth and remains almost unchanged for a wide range of trap depth (4 μK $\sim$ 12 μK). Moreover, spin temperature T_s is always much less than the kinetic temperature T_k, even after a hold time during 6 seconds, which indicates that the system seems not reach the "equilibrium". We will discuss in detail the reason in the next section.

We plot, in Fig 4.15a, kinetic temperature T_k measured by two methods, Hartree-Fock approach mentioned above (blue triangle) and TOF expansion (red circle). In measuring the expansion of the thermal distribution during the Time-Of-Flight (TOF), we can calculate the kinetic temperature T_k [33]. However, at very low temperature, since the condensate fraction is near 1, it is very difficult to distinguish thermal distribution from the dominant condensate (chapter 2, section 2.6.1), whose expansion is caused by both quantum pressure and interaction [12]. This is the reason why kinetic temperature T_k by TOF expansion method is only reliable for relatively large trap depth. However, in the overlapping region, the kinetic temperatures obtained by both methods accord well with each other. Moreover, the slopes of both T_k curves accord also well with each other, indicating that the kinetic temperature T_k calculated by Hartree-Fock method is reliable. We plot, in Fig. 4.15b, the condensate fraction f_c as a function of trap depth (with fixed hold time 6 seconds). At the end of the second evaporation, we reach to a almost pure condensate. Condensate fraction f_c, calculated by Hartree-Fock simulation, is more reliable than that fitted directly by Eq. (2.27), (see Fig. 2.5 and discussion in chapter 2, section 2.6.1).

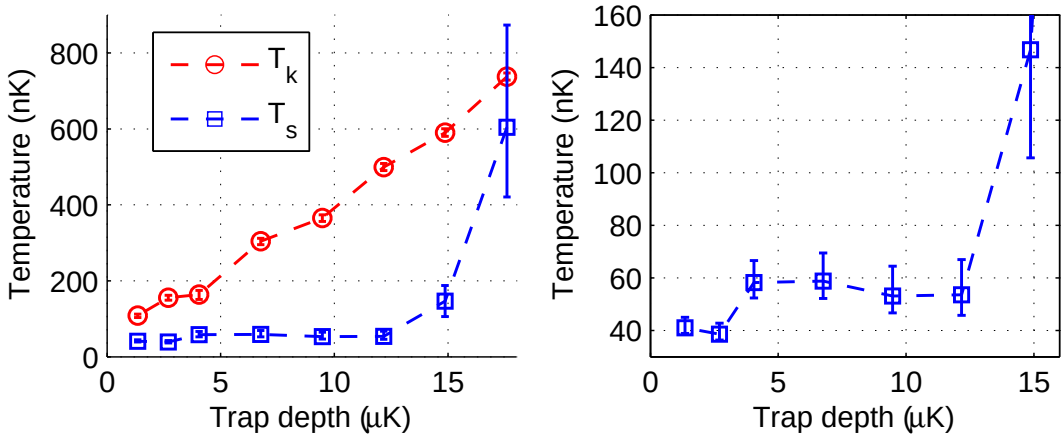


Figure 4.14: (a). Kinetic temperature T_k and spin temperature T_s as a function of trap depth (with hold time 6 seconds). (b). Zoom on the spin temperature T_s.

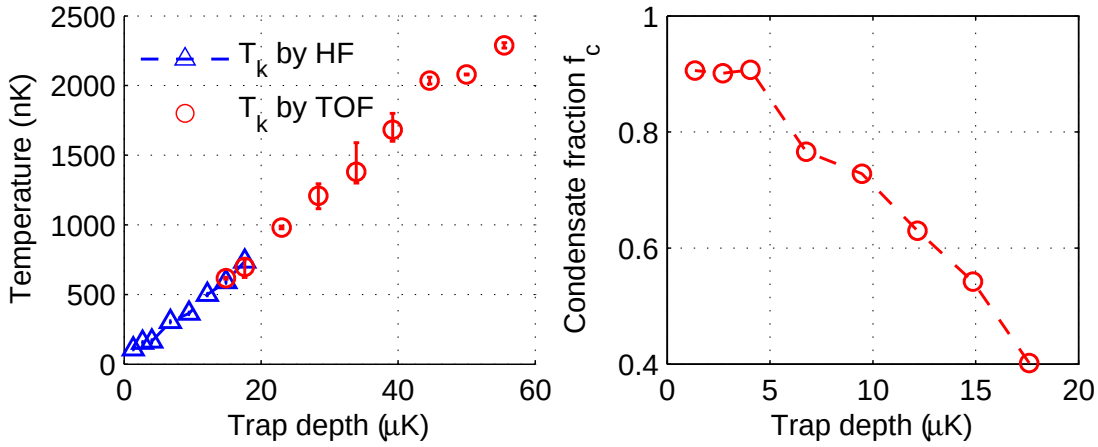


Figure 4.15: (a). Kinetic temperature T_k calculated by HF approach (blue triangle) and by TOF expansion (red circle). (b). Condensate fraction f_c as a function of trap depth (with hold time 6 s).

4.5.3 Experimental results of temperature during hold time

We illustrate in Fig. 4.16, the analysis results of temperature during hold time (with fixed $T_{\text{evap}} = 1000$ ms, trap depth $V_{\text{trap}} \approx 1.35$ μK, at the end of the second evaporation). The fitting results of σ will be shown in section 4.5.4. We illustrate in Fig 4.16a, (T_k, T_s) as a function of hold time, with fixed trap depth (at the end of the second evaporation). The kinetic temperature T_k continues to decrease slowly during the hold time, since the evaporation continues in the trap. The spin temperature T_s keeps almost unchanged, and always smaller than the kinetic temperature T_k. In Fig. 4.16b, we show the condensate fraction f_c as a function of hold time. The condensate fraction increases during the hold

time, since the evaporation continues during the hold.

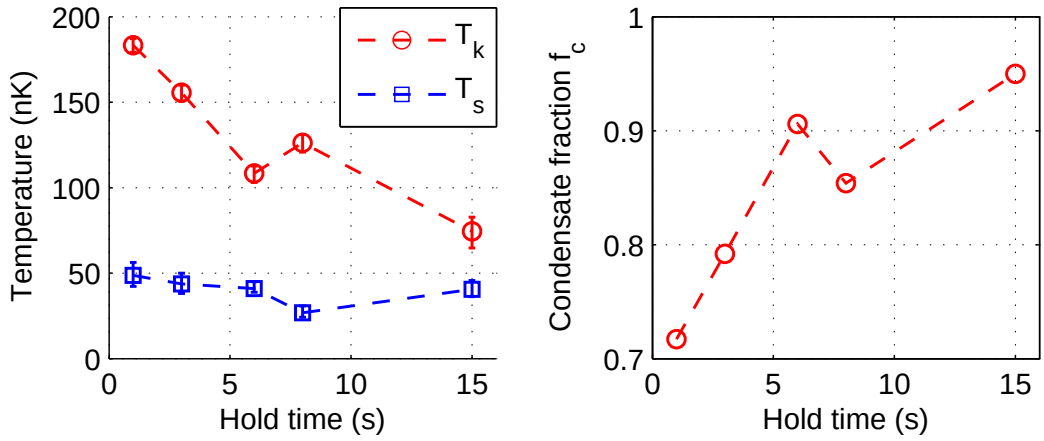


Figure 4.16: (a). Kinetic temperature T_k and spin temperature T_s as a function of hold time (with $T_{\text{evap}} = 1000$ ms, trap depth ~ 1.35 μK). (b). Condensate fraction f_c as a function of hold time (with $T_{\text{evap}} = 1000$ ms).

4.5.4 Fluctuation of magnetization Δm_z at $q = 0$

All discussions above concentrate on the moments of n_0 ($1 - \langle n_0 \rangle$ and Δn_0). In this part, we discuss the fluctuation of magnetization Δm_z as a supplement. In fact, because $\langle m_z^2 \rangle \sim 1/N$, it cannot be calculated by the broken symmetry approach, according to Eq. (4.45). Therefore, in this part, we consider only a simple case, $q = 0$, where the eigenstates of $\hat{H}_{\text{SMA}}$ are known analytically.

4.5.4.1 Theoretical analysis of Δm_z at $q = 0$

In this section, we consider a pure condensate $f_c = 1$ described by $\hat{H}_{\text{SMA}}$. We suppose a Gaussian prior-distribution for w_M (see section 4.3). The partition function is [4]

$$\mathcal{Z} = \sum_{S=0}^{N} \sum_{M=-S}^{S} \mathrm{e}^{-\beta \frac{U_s}{2N} S(S+1)} \mathrm{e}^{-\frac{M^2}{2(N\sigma)^2}} \approx \sum_{S=0}^{N} \sum_{M=-S}^{S} \mathrm{e}^{-\beta' S^2} \mathrm{e}^{-\gamma M^2}, \tag{4.75}$$

with $\beta' = U_s/(2Nk_BT_s)$ and $\gamma = 1/(2(N\sigma)^2)$. The sum can be replaced by an integral if $\beta', \gamma \ll 1$, which means $k_BT \gg U_s/N$ and $\sigma \gg 1/N$. These two conditions are satisfied for our experimental parameters. We get directly $\langle M \rangle = 0$, and after some algebra (see appendix D.3) we find the fluctuation of m_z at $q = 0$ is given by

$$\Delta m_z = \sqrt{\frac{\Delta M^2}{N^2}} = \sigma \sqrt{1 - \frac{\sqrt{\alpha}}{(1+\alpha)\arctan(1/\sqrt{\alpha})}}. \tag{4.76}$$

[4] It should be aware that N in this subsubsection is the condensate atom number, not the total atom number.

with σ the width of the prior-distribution of M, $\alpha = NU_s\sigma^2/k_BT_s$. According to Eq. (4.78), α can also be expressed as

$$\alpha = NU_s\sigma^2/k_BT_s = \frac{2}{3}\Big(\frac{\sigma}{\Delta m_{z,\infty}}\Big)^2. \tag{4.77}$$

We calculate Δm_z in two extreme cases, $\sigma \to 0$ and $\sigma \to +\infty$:

- if $\sigma \to 0$, $\alpha \to 0$, $\Delta m_z \to 0$. This is natural, since $\sigma \to 0$ corresponds to $M = 0$ case.
- if $\sigma \to +\infty$, $\alpha \to +\infty$,

$$\Delta m_z \to \sqrt{\frac{2}{3}\frac{k_BT_s}{NU_s}} \equiv \Delta m_{z,\infty}, \tag{4.78}$$

  corresponding to $\langle \hat{S}_z \rangle = 0$ case in section 4.2.2.

Finally, we can connect directly the spin temperature T_s with spin interaction energy (at $q = 0$). We calculate $\langle S^2 \rangle$ in appendix D.3. As a result, we find

$$\langle E_s \rangle = \frac{U_s}{2N}\langle S^2 \rangle = g(\alpha) \cdot k_BT_s \tag{4.79}$$

with

$$g(\alpha) = \frac{1}{2} \cdot \Big(1 + \frac{\sqrt{\alpha}}{(1+\alpha)\arctan(1/\sqrt{\alpha})}\Big). \tag{4.80}$$

when $\alpha \to 0$, $g(\alpha) \to 1/2$; when $\alpha \to +\infty$, $g(\alpha) \to 1$, as illustrated in Fig. D.1. In fact, Eq. (4.78), (4.79) connects directly the averaged spin interaction energy $\langle E_s \rangle$ and spin temperature T_s, which is very important to explain the origin of the spin temperature T_s in our system. We will return to this point in the last section in this chapter.

4.5.4.2 Experimental results of Δm_z at $q = 0$

The discussion in section 4.5.4.1 concentrates on the fluctuation of the magnetization of the condensate. The atom number fluctuations of the thermal atoms in each component (normally Poissonian) are small compared with those of the condensates (normally super-Poissonian). As a result, we suppose that only condensates contribute to the total fluctuation of the magnetization. We have

$$\Delta m_{z,\mathrm{tot}}^2 = \Delta m_{z,c}^2 \times f_c^2. \tag{4.81}$$

Here, $\Delta m_{z,\mathrm{tot}}$ is the total fluctuation of magnetization, $\Delta m_{z,c}$ is fluctuation of the magnetization of the condensate, expressed in Eq. (4.76). In the following discussion, we denote $\Delta m_{z,\mathrm{tot}}$ directly by Δm_z for simplicity.

We illustrate, in Fig. 4.17a, the width σ of the prior-distribution of M as a function of trap depth (with fixed hold time 6 seconds), which is used to calculate Δm_z. We neglect the contribution of the fluctuation of thermal atoms (see section 4.4.1, Eq. (4.68))

and plot in Fig. 4.17b, the measured (red circle) and calculated (blue square) fluctuation of magnetization Δm_z at $q = 0$ as a function of trap depth (with hold time 6 s). We find good agreement except for $T_{\rm evap} = 700, 750, 800$ ms, corresponding to trap depth $V_{\rm trap} \approx 17.6, 14.9, 12.2$ μK (high trap depth, high temperature and low condensate fraction), indicating that the Hartree-Fock model describes well our spin-1 system for low enough temperatures. For highest temperatures, it becomes suspicious, indicating a possible failure of our Hartree-Fock model.

We plot in Fig. 4.17c, the width σ of the prior-distribution of M as a function of hold time, which is used to calculate Δm_z in Eq. (4.76). We compare in Fig. 4.17d the measured (red circle) and calculated (blue square) fluctuation of magnetization Δm_z at $q = 0$ as a function of hold time and find a good agreement within a precision of 15%.

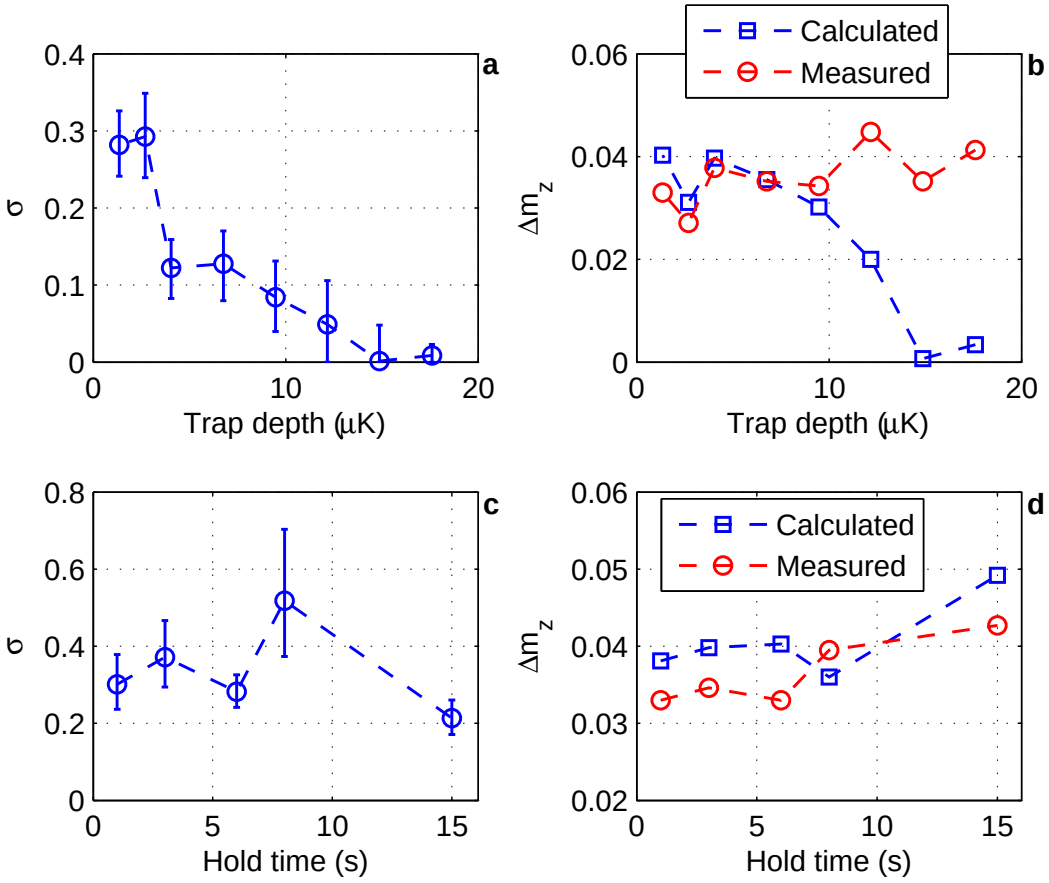


Figure 4.17: (**a**). σ as a function of trap depth (with hold time 6 s). (**b**). Measured and calculated fluctuation of magnetization Δm_z at $q = 0$ as a function of trap depth (with hold time 6 s). (**c**). σ as a function of hold time (with $T_{\rm evap} = 1000$ ms). (**d**). Measured and calculated fluctuation of magnetization Δm_z at $q = 0$ as a function of hold time (with $T_{\rm evap} = 1000$ ms).

We list in Tab. 4.2 and 4.3, $\sigma/\Delta m_{z,\infty}$ during evaporation and during hold time, respectively. We remind that $\Delta m_{z,\infty}$ is calculated in making $\sigma \to +\infty$ (Eq. (4.78)). In fact,

$\sigma/\Delta m_{z,\infty}$ reflects the influence of σ on the *real*-distribution of M. If $\sigma \gg \Delta m_{z,\infty}$, system is only slightly influenced by the prior-distribution factor $e^{-\frac{M^2}{2(N\sigma)^2}}$ (see Eq. (4.75)), which is almost valid for the low trap depths.

T_{evap} (ms)	700	750	800	850	900	950	975	1000
V_{trap} (μK)	17.6	14.9	12.2	9.47	6.76	4.05	2.70	1.35
$\sigma/\Delta m_{z,\infty}$	< 0.05	< 0.05	1.07	1.68	2.51	2.55	8.41	6.24

Table 4.2: $\sigma/\Delta m_{z,\infty}$ during evaporation with fixed hold time 6 s.

Hold (s)	1	3	6	8	15
$\sigma/\Delta m_{z,\infty}$	5.54	7.31	6.24	12.25	3.96

Table 4.3: $\sigma/\Delta m_{z,\infty}$ during hold time with fixed trap depth ($T_{\text{evap}} = 1000$ ms, $V_{\text{trap}} \approx 1.35$ μK, end of evaporation).

4.6 Discussion of the results

In this chapter, we show the experiment results and data analysis concerning the large collective fluctuations of our spin-1 BEC system. We plot the kinetic temperature T_k, spin temperature T_s and condensate fraction f_c as a function of trap depth V_{trap} and hold time. We find that the measurement of the fluctuation behavior of the spinor condensate can not only serve as a thermometry to measure both the kinetic temperature T_k, which can hardly measured at very low temperature (because of high condensate fraction), and spin temperature T_s of our system, but also offers a method to get reliable condensate fraction f_c of our system.

We noticed that the spin temperature T_s is in general lower than the kinetic temperature T_k. More precisely, the kinetic temperature T_k depends directly on the trap depth V_{trap}, because of the mechanism of evaporative cooling. However, the spin temperature T_s is almost independent (sometimes keeps constant for a wide range) of trap depth and hold time, indicating very weak coupling between spin and kinetic degree of freedom. We show in Fig. 4.18 an illustrative energy structure with both SMA modes and the first "spin wave" mode. The spin wave modes are quantized due to the finite size of our system. The energy spacing of SMA modes is typically $U_s/N \sim 1$ pK, however, the first spin wave mode is in $\hbar\omega \approx 8$ nK. This vast difference in energy scale means coupling between SMA modes and spin wave modes is realized by multi-level process and thus very inefficient. We therefore expect a very weak coupling between the SMA modes, which relate to the spin temperature T_s and other collective modes (phonons and spin waves, which relate to the kinetic temperature).

In fact, kinetic and spin degree of freedom have independent mechanism to reach equilibrium. The kinetic degree of freedom (phonons and spin waves) reaches equilibrium by

the evaporative cooling with standard thermalization process, whereas the spin degree of freedom reaches equilibrium by dephasing of single-mode collective spin excitations [100] (or in other words, collective oscillations of the condensate that eventually relax to a steady state [77]). In conclusion, the independent mechanisms to reach equilibrium and the weak coupling between different modes lead to different kinetic and spin temperatures and this difference can hold for very long time, forming a quasi-equilibrium state [101], as Bose-Einstein condensate in alkali gases [3].

One more question is what energy scale determines the spin temperature. In an isolated system (here, the condensate spin degree of freedom), the temperature after thermalization is determined by the available energy, which is given by Eq. (4.79): $\langle E_s \rangle \sim k_B T_s$. Let us first discuss a "quench" scenario, where the gas is brutally cooled from above critical temperature T_c to well below, then the reaches the equilibrium after a period of time. Because the condensate forms from the thermal cloud, it seems to be reasonable to assume that the condensate inherit the same fluctuation of magnetization as the thermal gas from which it forms, *i.e.* $\langle S_z^2 \rangle \sim 2N/3$. [5] As a result, we have

$$\langle E_s \rangle = \frac{U_s}{2N} \langle \mathbf{S}^2 \rangle \sim \frac{U_s}{2N} \times 3 \langle S_z^2 \rangle \sim U_s. \tag{4.82}$$

In our experiment, U_s is typically $2 - 6$ nK, leading to a spin temperature lower than measured. However, a number of other factors are important. First, the evaporative cooling and the thermalization are two simultaneous process and they are gradual, not sudden. Therefore, the discussion above, assuming that the atom "first" emerge from the thermal cloud and "then" reach equilibrium, is not directly applicable. Second, the atoms lose during the evaporation. Third, the fluctuation of magnetization can also be limited by the imperfections in the preparation of the sample. Therefore, we propose a quench experiment for our future work. We first apply a sufficient large magnetic field in order to force all the atoms to $m_F = 0$ state, then switch off abruptly the field to zero. By this way, we prepare at the beginning a well defined state with zero fluctuation of magnetization and can observe how this state evolves and reaches the equilibrium. We can measure the spin temperature during this process, which will help us to better understand the origin of the spin temperature.

4.7 Conclusion

In this chapter, we studied theoretically and experimentally the collective fluctuations of the spin-1 Bose-Einstein condensate with antiferromagnetic interactions. More precisely, we focused on the behaviors of $1 - \langle n_0 \rangle$ and Δn_0 as a function of q, and the fluctuation of magnetization Δm_z at $q = 0$.

In section 4.2, we focused on the quantum analysis of the SMA Hamiltonian $\hat{H}_{\mathrm{SMA}}$, which describes the behavior of the condensate. We began with the direct diagonalization of the

[5] Here, we suppose the isotropy of the thermal cloud ($N_{+1}^{\mathrm{th}} = N_{+1}^{\mathrm{th}} = N_{+1}^{\mathrm{th}}$), which is valid if q is not very large (see chapter 4, section 4.4.2).

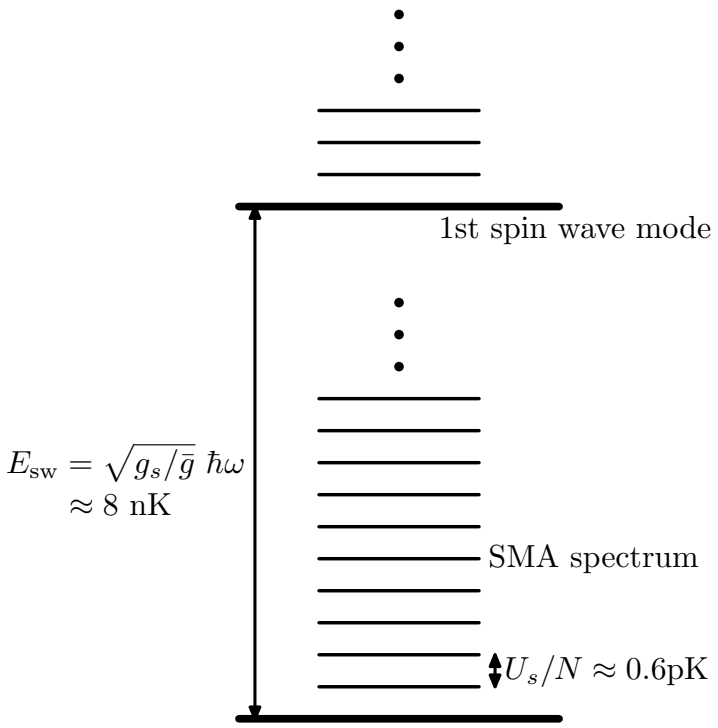


Figure 4.18: Sketch of the energy ladder showing SMA modes and spin wave modes. Other excitation branches lie higher in energy (> 50 nK).

SMA Hamiltonian $\hat{H}_{\rm SMA}$ in total spin basis $|N, S, M\rangle$. We introduced later the so-called "broken symmetry" approach, which is a very powerful method to calculate the first two moments of n_0 to a good approximation, and much faster than the direct diagonalization.

We noticed two major discrepencies between the experimental results and the SMA theory. Therefore, we developed in the next two sections the extensions of the theory. In section 4.3, we generalized to arbitrary distribution of M, which changes the $1 - \langle n_0 \rangle$ value at $q = 0$. In section 4.4, we used the semi-ideal Hartree-Fock approximation, which is discussed in detail in chapter 1, section 1.4, to take the thermal atoms into account. As in chapter 1, we plot $1 - \langle n_0 \rangle$ and Δn_0 as a function of q. From these plots, we could extract many physical informations of our system. For example, the two different HWHM of q ($q^s_{1/2}$, $q^k_{1/2}$) reflect two different temperatures, spin temperature T_s and kinetic temperature T_k, respectively. The second plateau value c reflects the condensate fraction (Eq. (4.70)). We also identified two crossover regions between the three plateau regions, in which condensate and thermal cloud behaves individually in each.

In section 4.5, we introduced our experiment of the collective spin fluctuation. We used the model introduced in the previous two sections to fit the $1 - \langle n_0 \rangle$ and Δn_0 curves measured in the experiments. We found that the spin temperature T_s is much lower than the kinetic temperature T_k and is not quite affected by the evaporation process. Finally in section 4.6, we gave an detailed analysis and explanation to our experiment results.

Conclusion

In this thesis, we focused on the spin-1 Bose Einstein condensate with antiferromagnetic interactions both in theory and in experiment.

In chapter 1, we introduced the basic mean-field theory of the spin-1 Bose-Einstein condensate, both at zero temperature, in which a pure condensate is formed, and at non-zero temperature, in which both condensate and thermal cloud are present. We began this chapter with a discussion of the scalar condensate, which is a condensate described by a scalar order parameter. We discussed the condensate with or without interactions, and introduced the so-called "semi-ideal Hartree Fock approximation", which was used to solve the problem at non-zero temperature where both condensate and thermal atoms are present and interact between each other. In this method, we neglect the influence of the thermal atoms on the condensate, which is proven to be efficient and precise enough. This approximation was also adopted in the spinor case in this chapter and in chapter 4. Next, we discussed the pure spin-1 condensate at zero temperature, which is described by a three components order parameter. In studying the Hamiltonian of interaction, we found that the magnetization m_z is conserved, which is important for the discussion in the following chapters. We gave a mean-field solution of $\hat{H}_{\mathrm{SMA}}$, the Hamiltonian describing the spin-1 condensate in using the Single Mode Approximation (SMA). This mean-field solution predicted a phase transition as magnetic field changes, which was studied experimentally in chapter 3. Finally, in using the semi-ideal Hartree Fock approximation, we studied the spinor condensate at non-zero temperature. We focused on the plots of $1 - n_0$ as a function of q, which contains many physical information about the system, such as temperature, condensate fraction, *etc.*

In chapter 2, we introduced step by step how we realize, control, detect and analyze the spin-1 Bose-Einstein condensate in our experiment. We discussed particularly compression and evaporation in a Large Crossed Dipole Trap (Large-CDT), then evaporation in a Small Crossed Dipole Trap (Small-CDT). We finally obtain an almost pure condensate with about 5000 atoms in the trap. We then discussed how to control the condensate, especially the magnetization. We use spin distillation and depolarization process and achieve a control over the magnetization m_z from about 0 to 0.9. Finally, we introduced how to detect and analyze the condensate. In our experiment, we use absorption imaging after a period of Time Of Flight (TOF) to diagnose the condensate, which reflects the column spatial density distribution of the atoms in the trap. For the analysis of the image, we constructed a model to fit the absorption images, by which we can get physical information of the system, such as atom number, temperature, condensate fraction, *etc.* We also introduced several methods to reduce the noise of the images, including fringe-

removal method, which is based on the eigen-face algorithm. In reducing the noise of the image, we can reduce also the atom number uncertainty counted from the absorption images.

In chapter 3, we introduced the experimental study of the phase diagram of the spin-1 condensate with antiferromagnetic interactions at very low temperature, which was discussed in theory in chapter 1. We found experimentally a phase transition from the antiferromagnetic phase to the broken axisymmetry phase as magnetic field B increases. This phase transition is caused by the competition between antiferromagnetic spin-dependent interactions, which is dominant at low fields, and the quadratic Zeeman energy, which is dominant at high fields. We found that the measurements were in quantitative agreement with mean-field theory, which predicts very well the phase boundary and the observed spin population above the transition. We observed also that at small field and small magnetization, large fluctuation of n_0 which could not be explained by the mean-field theory.

In chapter 4, we studied both in theory and in experiment the large collective fluctuations of spin-1 condensate. First, we gave a detailed quantum many-body analysis on $\hat{H}_{\mathrm{SMA}}$, the single mode approximation Hamiltonian describing the spin-1 condensate. We first diagonalized directly the Hamiltonian in total spin basis $|N, S, M\rangle$, and then developed a so-called "broken-symmetry approach", an alternative method to analyze the SMA Hamiltonian. In this approach, the spinor condensate is described as a statistical mixture of mean-field states with fluctuating "direction" in spin space. This approach reproduced very well the results by exact diagonalization. According to the quantum solution of the SMA Hamiltonian, two major differences between theory and experiment were noticed, which led to two theoretical extensions. First, we generalized the distribution of M in order to change the value of $1-\langle n_0\rangle$ at $q=0$. Second, we use the semi-ideal Hartree-Fock method to take the thermal atoms into account. We distinguished two kinds of temperatures, the spin temperature T_s, which characterizes the statistical behavior of the collective spin of the condensate, and the kinetic temperature T_k, which reflects the thermodynamical behavior of the non-condensed component. We plot $1-\langle n_0\rangle$ and Δn_0 as a function of q. Compared with the results in chapter 1, the quantum description of the condensate changed the behavior of $1-\langle n_0\rangle$ vs q curve especially at low q, where the deviations from the mean-field solution are large and where large fluctuations are observed. We used the theory developed in this chapter to fit the experimental data. From the fitting, we obtained the kinetic and spin temperatures and condensate fraction. We found that the spin temperature is always much smaller than the kinetic temperature ($T_s \ll T_k$) and is not influenced much during the evaporation and the hold time. The reason is possibly because of the large difference between the energy scale of the SMA modes, which is related to the spin temperature T_s and that of the other modes (*e.g.* spin wave mode), which is related to the kinetic temperature T_k. In fact, our observations indicate that the condensate spin acts as an almost isolated system which thermalizes "on its own", almost independent of the regular thermalization occurring via collisions inside the thermal cloud. We can thus see this system as being in a "pseudo-equilibrium" state that is reached even without dissipation or an external reservoir.

For the work in the next step, we have proposed a quench experiment in chapter 4, section 4.6, in order to clarify the origin of the spin temperature. For the far future work, we have constructed a micro trap which is much smaller compared with the Vertical dipole trap and the Horizontal dipole trap mentioned in chapter 2, in which we hope to control the atom number of condensate, with only about hundreds of atoms. This micro dipole trap allows us to produce the strong correlated spin states, such as schrödinger's cat state [102] or Fork twin state [103].

Appendix A

Magneto-Optical Trap (MOT)

The first step to the Bose-Einstein condensation is the Magneto-Optical Trap (MOT). In our experiment, we load the MOT directly from the background gas with the help of the *Light Induced Atomic Desorption* (LIAD) [52]. The MOT can cool down sodium atoms from the room temperature (~ 300 K) down to ~ 50 μK [52]. However, the efficiency of the evaporative cooling makes the "first step" laser cooling a preliminary cooling which do not serve to cool as much as possible but to load the conservative trap more efficiently [33]. This pre-cooled sample will be transferred to the "large crossed dipole trap" which will be discussed in the next section.

In this appendix, we begin with a brief introduction to the principle of Doppler cooling, and illustrate the energy structure of the sodium atom to explain how to realize a MOT. In the second part, we present the 589 nm laser used in our group [104, 105]. Finally, we will discuss the application of the LIAD technique in our experiment [52]. Most of the information is contained in the PHD thesis of Emmanuel Mimoun [44] and is included here for completeness.

A.1 Elements of Doppler cooling and MOT

The interactions between atoms and light are in general complex. Here we consider a simple model: two-level system which is illustrated in Fig A.1a. The energy structure of the atom consists of only two levels with the energy gap $\hbar\omega_A$. We note the ground state $|g\rangle$ which is stable, and the excited state $|e\rangle$ which is unstable. The natural width of the exited state is Γ. The atom interacts with the light of the frequency ω_L. Here we suppose the quasi-resonant condition is satisfied which means the detuning $\Delta = \omega_L - \omega_A \ll \omega_A, \omega_L$.

This quasi-resonant light can be absorbed by the atoms, and re-emitted in cycles. Because the photons carry momentum, after many cycles, the average atomic momentum changes. The atom thus "feel" a force exerted by the laser beams. The force from the laser to the atom can be divided into two parts [5], the radiative part which originates from the gradient of the phase of the light and the dipole part which originates from the gradient of the intensity of the light. If the atom is at rest, the radiative force

$$F_{\text{rad}} = \hbar k_L \frac{\Gamma}{2} \frac{s}{1+s}, \tag{A.1}$$

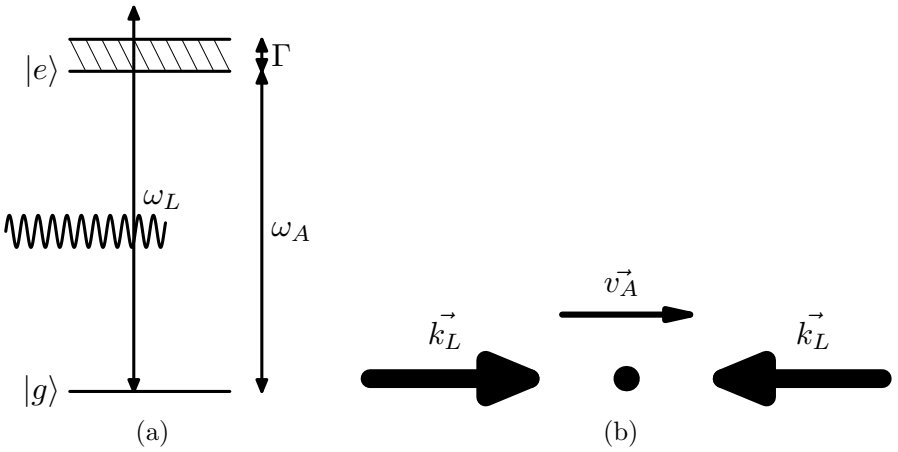


Figure A.1: (a). Two level system. Atom with two energy levels interacts with light. (b). Doppler cooling: two counter-propagating laser beams with $\omega_L < \omega_A$ induce a viscous cooling force on the atoms.

with

$$s = \frac{I/I_{\text{sat}}}{1 + 4(\Delta/\Gamma)^2}. \tag{A.2}$$

Here s denotes the saturation parameter, I_{sat} the saturation intensity.

Considering here the 1-D situation illustrated in Fig. A.1b, the atom moves in $+x$ direction with the velocity v. Two laser beams counter-propagate with the detuning Δ. According to the Doppler effect, the detuning "felt" by the atom will be changed compared with the detuning at rest, $\Delta_\pm \approx \Delta \mp k_L v$. The combined radiative force then becomes (for small v and small light intensity) equivalent to a viscous force,

$$F = F_+ - F_- \approx -\alpha v, \tag{A.3}$$

with a damping coefficient $\alpha \propto -\Delta$. The combined radiative force is frictional if the detuning $\Delta < 0$ ($\alpha > 0$). As a result, this force can decelerate the atoms and thus decrease the temperature of the sample. This is the so-called "Doppler cooling". At the region of the crossed laser beams, the atoms are decelerated by the frictional force but also diffuse randomly because of the spontaneous emission. This "recoil heating" effect counter balances Doppler cooling and leads to a minimal temperature $T_D \approx \hbar\Gamma/2$.

In order to trap the atoms in the region, we have to add a magnetic gradient. As a result, the energy shifts of the sub-levels are inhomogeneous because of the magnetic field gradient. Laser cooling forces in the magnetic gradient can be reduced to a friction force, as before, plus a restoring force that ensures trapping. This is known as "Magneto-optical trap" (MOT).

We illustrate in Fig. A.2, the real energy structure of sodium and all the lasers we use for the MOT. For cooling, we choose the transition between $|3^2S_{1/2}, F = 2\rangle$ and $|3^2P_{3/2}, F' = 3$ with the detuning $\Delta_c = -20$ MHz. Once atoms are excited to the $|3^2P_{3/2}, F' = 3\rangle$ state, they can easily decay to the ground state $3^2S_{1/2}, F = 1$ because of

the spontaneous emission. The atoms in the ground state are no longer resonant with the cooling beam because of the 1.77 GHz gap between $3^2S_{1/2}, F = 1$ and $3^2S_{1/2}, F = 2$. As a result, we need additional ("Repumper") beams to "re-pump" the atoms from $3^2S_{1/2}$ to $3^2P_{3/2}$. This repumper laser is tuned on the $3^2S_{1/2}, F = 1$ to $3^2P_{3/2}, F = 2$ transition with detuning $\Delta_R = 0$.

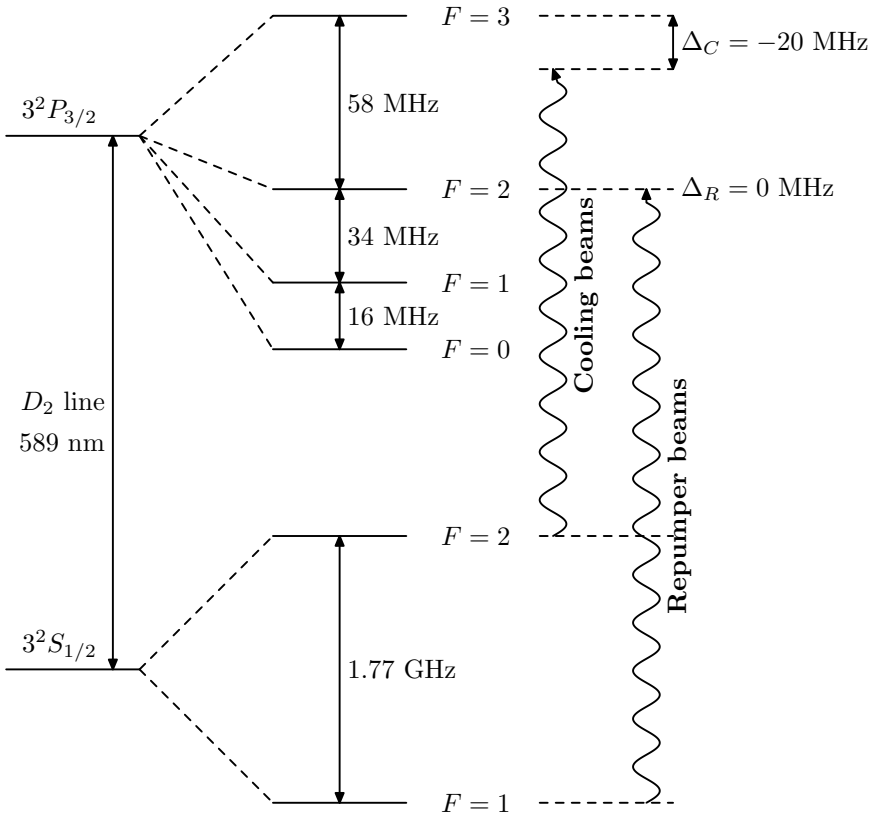


Figure A.2: Sodium energy structure with cooling and re-pumping lasers, with respective detunings Δ_c and Δ_R with respect to the $2 \to 3$ and $1 \to 2$ transitions.

A.2 589 nm laser system

As described in the section above, to perform the laser cooling, one needs quasi-resonant light, around 589 nm in our case. At the beginning of the experiment, the group designed and built a 589 nm laser system using a non-linear optics approach [104, 105, 44].

The basic ideas is to sum up the frequencies of two infrared lasers. We illustrate in Fig. A.3 the main setup of the 589 nm laser system. The 589 nm yellow laser comes from two commercial solid lasers with $\lambda_1 = 1064$ nm and $\lambda_2 = 1319$ nm. These two lasers are both commercial YAG laser, with output power $P_1 \approx 1.2$ W and $P_2 \approx 0.5$ W. The sum-frequency is generated in the non-linear optical material, ppKTP (periodically polarised KTP). Normally, the efficiency of the non-linear process is very low if the light passes once through the crystal. As a result, an optical cavity is used to enhance the effi-

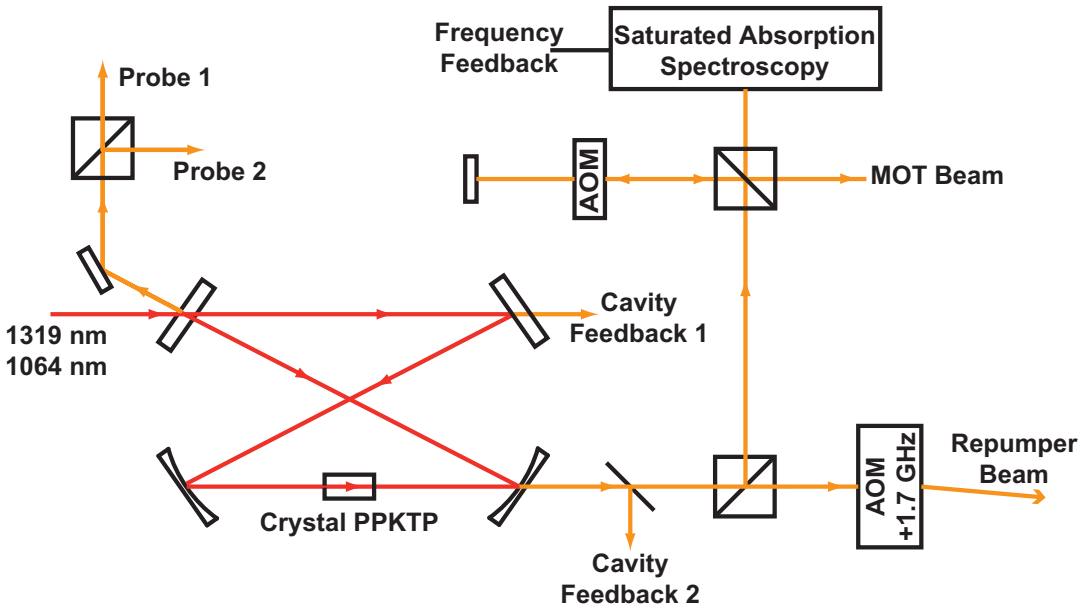


Figure A.3: Schematic layout of the 589nm laser system in our experiment.

ciency. In our experiment, we can maintain a output power $P_{\text{out}} \approx 650$ mW of the 589 nm laser, slightly less than the maximum value obtained in [104, 105, 44] for technical reasons.

The feedback system of 589 nm laser is also shown in Fig. A.3. The feedback system consists of two main parts, the intensity stabilization and frequency stabilization. The "intensity stabilization" system ensures that both pump lasers are maintained resonant with the cavity at all times. The frequency feedback system use the saturated absorption spectrum to lock the laser frequency exactly to the $3^2S_{1/2}$ to $3^2P_{3/2}$ transition, which is 589.159 nm. In our experiment, we lock the 589 nm laser frequency to one of the iodine molecule transition instead of the normally used sodium vapor. The benefit is that the iodine can work at room temperature, whereas sodium vapor should be heated to 120°C. The transition frequency of the iodine molecule shift about 467 MHz below the cooling transition, so we have to use an Acoustic-Optical Modulator (AOM) to shift back this difference.

As shown in Fig. A.3, the output of the 589 nm laser from cavity is divided into three parts. The first part is the cooling beam (Fig. A.2) which is detuned by 20 MHz using an AOM. The second part is the repumper beam (Fig. A.2) which is detuned by AOM about 1.7 GHz. The third part is further divided into two probe beams used for imaging (detail in section 2.5). All these beams are controlled by a AOM and a shutter. The AOM can switch off the beam within several μs. But in order to maintain the thermal stability of the AOM, we should switch off the AOM as shortly as possible. The shutter can continue to cut the beams if we need.

The cooling beam and the re-pumper beam are transmitted via the optical fibers to a fiber cluster in which they are mixed and re-distributed into 6 identical beams. These beams are transmitted also by optical fibers to the vacuum chamber. In Fig. 2.1, we

illustrate the configuration of the 6 laser beams around the science chamber. The waist of the beams are about 11 mm. The power $P \approx 1.8$ mW for each (of 6) cooling beam and $P \approx 450$ μW for each re-pump beam. The two probe beams are also transmitted by optical fiber to the science chamber.

A.3 Sodium MOT

The anti-Helmholtz coils pair shown in Fig. 2.1 creates a magnetic field around the center of the science chamber given by

$$\mathbf{B}(x, y, z) \approx \frac{b'x}{2}\,\mathbf{e_x} - b'y\,\mathbf{e_y} + \frac{b'z}{2}\,\mathbf{e_z}. \tag{A.4}$$

In our experiment, the current in the coil $I \approx 120$ A and $b' \approx 12$ G/cm. They are made from hollow copper tubes, and water cooled to prevent damage.

In most sodium experiments, a Zeeman slower [106] is adopted to load the MOT. However, the large magnetic field generated by the magnets in the Zeeman slower prevent us to adopt this option. In our experiment, we load the MOT directly from the background pressure in the vacuum chamber. The background pressure, or the density of the atoms of sodium can be controlled by the *dispenser*. The dispenser is formed by a powder of sodium oxide, which can release the sodium by heating current. Unfortunately, the response time constant of the pressure in the vacuum chamber to the current is too long, typically seconds. This will decrease the life time in the optical dipole trap because of the collisions with background "hot" atoms. Normally, we heat the dispenser once every several months just to compensate the atoms absorbed by the pumps.

In order to control "instantly" the density, we adopt the *Light Induced Atomic Desorption* (LIAD). In fact, after we switch off the dispenser, many atoms are absorbed on the wall and especially on the windows of the vacuum chamber. We use the ultraviolet LED ($\lambda \approx 370$ nm) to release the atoms back to the vacuum chamber, which will increase abruptly the pressure of the chamber. When we switch off the ultraviolet light, the atoms will be re-absorbed again very fast. The pressure decreases very fast (within less than 100 ms), and is thus not harmful for the loading of the optical dipole trap. In using the LIAD, we can control almost "instantly" the pressure of the vacuum chamber. In our experiment, the LED current is $I_{\mathrm{LED}} \approx 0.7$A.

We show in Fig. A.4 the loading behavior of the MOT with the help of the LIAD [52]. We load the MOT until 12 s with the LED on, and at 12 s, we shut off the LED. The MOT loading time constant $\tau \approx 6$ s, and saturate at $N \approx 2 \times 10^7$ atoms. After we shut off the LED, the atom number decrease because of the atom absorption by the science chamber. The life time constant $\tau \approx 27$ s. In the experiment, after $\sim$10 s MOT loading, we obtain about 2×10^7 atoms with temperature $T \approx 200$ μK. This loading process is fast, and the atom number and temperature is suitable for the next step optical dipole trap loading.

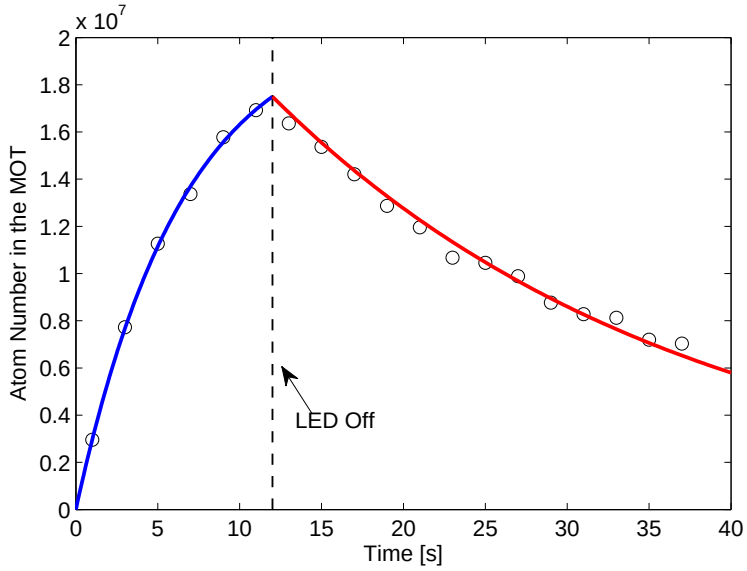


Figure A.4: MOT loading before and after switching off the LED. Figure from [52].

Appendix B

Loading the Large Crossed Dipole Trap (Large-CDT)

The phase space density $\mathcal{D}$ can reach $10^{-5} \sim 10^{-6}$ in a Magneto-optical trap [33]. This is still far from the threshold of the Bose-Einstein condensation $\mathcal{D} \sim 1$. There are several factors which limit the temperature and the density of the atoms in the MOT, and thus the phase space density [107, 108]. Because of the high efficiency of the evaporative cooling on the enhancement of the phase space density, the MOT sequence is now served as a pre-cooling step [33].

Evaporative cooling can be realized in several kinds of traps. We adopt the optical dipole trap in which all the Zeeman sub-levels can be conserved for the spinor BEC study. The typical depth of the optical dipole trap is only several mK, this is the reason why we need the MOT pre-cooling [109]. Before the realization of the evaporative cooling, we should first transfer the atoms pre-cooled in the MOT to the optical dipole trap. The loading process will be explained in this section. In fact, in our experiment, we transfer the atoms from the MOT to the Large Crossed Dipole Trap (Large-CDT) with the size of the waist about 40μm [49]. We call it "Large", because in the following evaporation, we will use a smaller crossed dipole trap with the size of the waist only about several μm which will be discussed in section 2.3.

This appendix is organized as follows. In the first part, we will introduce the basic ideas of the optical dipole trap. In the second part, we will show the configuration of the Large-CDT in our experiment, including the characteristic parameters of our trap and the feedback system. In the third part, we will explain how we load the Large-CDT from the MOT. And in the last part, we will show that by increasing the power of the Large-CDT, we can accumulate the atom to the crossed region (central region) in order to obtain good conditions for evaporative cooling in the next step. Most of the information is contained in the PHD thesis of David Jacob [43] and is included here for completeness.

B.1 Elements of optical dipole traps

The basic idea of the far-off resonant optical dipole trap is to use the interactions between the induced dipole moment of a neutral atom and the electrical field of the light [109]. Consider an atom described by the two-level system in section A.1 interacts with a linear polarized laser $\mathbf{E}(\mathbf{r}) = \mathbf{E}_0(\mathbf{r})\mathrm{e}^{-i\omega_L t} + c.c.$, with $\mathbf{E}_0(\mathbf{r}) = E_0(\mathbf{r})\mathbf{e}_q$. ω_L is the frequency of the laser and $\mathbf{e}_q$ is the polarization axis. Under the condition that $\Delta \gg \Gamma$ and saturation parameter $s \ll 1$, the potential of the optical dipole trap which originate from this interaction is [109]:

$$U_{\mathrm{dip}} = \frac{3\pi c^2 \Gamma}{2\omega_A^3}\left(\frac{1}{\omega_L - \omega_A} - \frac{1}{\omega_L + \omega_A}\right) \cdot I(r). \tag{B.1}$$

where $I(r) = \epsilon_0 c|\mathbf{E}_0(\mathbf{r})|^2$ is the intensity of the beam at position $\mathbf{r}$, ϵ_0 the vacuum permittivity and Γ the natural width of the excited state. The dipole force is thus: $F_{\mathrm{dip}}(\mathbf{r}) = -\nabla U(\mathbf{r})$. Remark that the dipole trap potential U_{dip} is proportional to the local intensity of the laser beam, as a result, we should use high-power laser in order to get a deeper dipole trap.

According to the sign of the detuning $\Delta = \omega_L - \omega_A$, we can classify the dipole potential by two kinds:

- if $\Delta < 0$, the trap is called *red* detuned, the atoms are trapped around the maxima of the intensity.
- if $\Delta > 0$, the trap is called *blue* detuned, the atoms are trapped around the minima of the intensity.

In this thesis, all the optical dipole traps are red detuned *i.e* $\Delta < 0$.

Even though the trapping laser is far-detuned, the atoms can still have the possibility to be scattered by the non-resonant light because of the high power of the trapping laser [109]. The life time of atom is thus limited by the scattering rate of the atoms by the laser, Γ_{sc},

$$\hbar\Gamma_{\mathrm{sc}} = \frac{\Gamma}{\Delta} U_{\mathrm{dip}}. \tag{B.2}$$

According to Eq. (B.2), the scattering rate Γ_{sc} is proportional to the trapping depth $U_{\mathrm{dip}}(\mathbf{r})$ and inversely proportional to the detuning Δ. This means we can not increase the laser power and decrease the detuning as we wish to increase the depth of the trap, because it will also increase the scattering rate, and leads to the heating of the cloud. We should compromise between the trap depth and the heating to choose our laser parameters including the power and detuning.

Another important feature of the optical dipole trap is that the trapping potential is almost spin-independent [109], which is very helpful for our spinor BEC experiment. All our optical dipole trap satisfy the spin-independent condition and thereby can trap all the spin states by the same way.

B.2 Experimental setup

B.2.1 Configuration of the Large-CDT

The basic configuration of the Large-CDT in our experiment is shown in Fig. B.1. The trap is composed by two linear polarized laser beams crossed at the center of the vacuum chamber. Each beam comes from the same laser folded onto itself [49].

These two beams are in the horizontal plane. The first beam is along the x direction and the second along the $x + y = 0$ direction as illustrated in Fig. B.1. The angle between the two beams is about 45°. Between the two beams, there is a $\lambda/2$ wave plate in order to turn the polarization of the first beam by $\pi/2$. As a result, the polarization of the two beams are orthogonal in order to minimize residual interference which could heat the atoms.

Both beams cross at the position of each waist $w_0 = 42$ μm. The laser beams are generated by a high power fiber laser (IPG) of which the output power is about 40 W and the wavelength $\lambda_{\mathrm{CDT}} = 1064$ nm which is far-off resonant with the sodium D line transition approximately 589 nm [35].

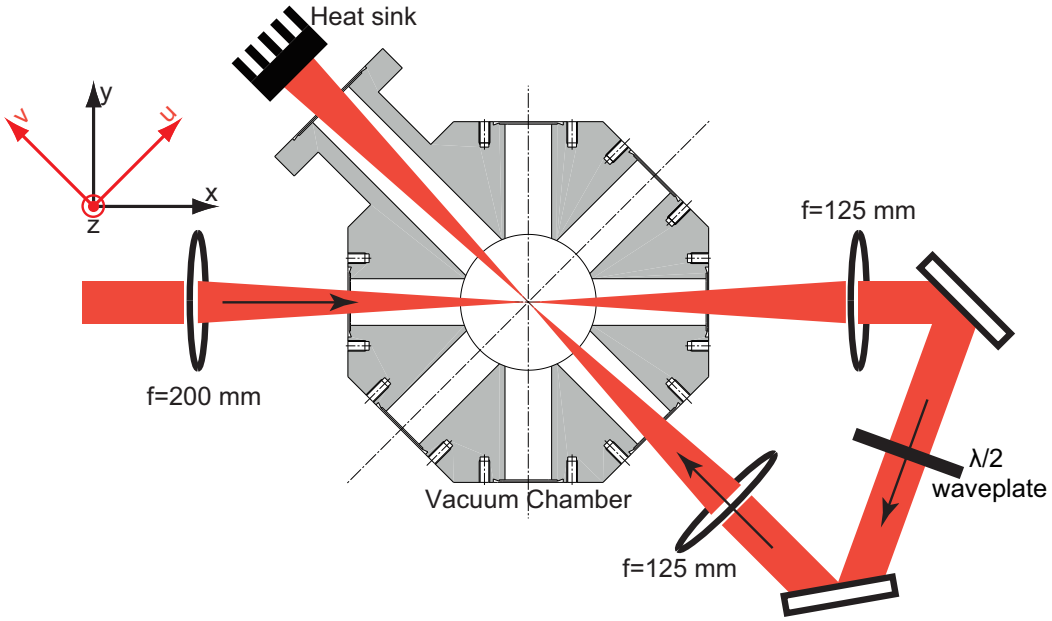


Figure B.1: Large crossed dipole trap configuration with science chamber

According to Eq. (B.1), the potential of the trap is proportional to intensity of the beam. As a result, the trapping potential of the Large-CDT is proportional to the total intensity which is directly the sum of the individual Gaussian beam intensities because of no interference between the two beams (orthogonal polarizations). The trapping potential can thus be described as follows [49]

$$V_{\mathrm{CDT}}(x,y,z) = \frac{V_0}{2}\Big(\frac{\mathrm{e}^{-2(y^2+z^2)/w(x)^2}}{(w(x)/w_0)^2} + \frac{\mathrm{e}^{-2(u^2+z^2)/w(v)^2}}{(w(v)/w_0)^2}\Big). \tag{B.3}$$

with

$$w(x) = w_0\sqrt{1 + x^2/l_R^2}, \tag{B.4}$$

$$w(v) = w_0\sqrt{1 + v^2/l_R^2}, \tag{B.5}$$

with $l_R = \pi w_0^2/\lambda_{\mathrm{CDT}} \approx 5.2$ mm the Rayleigh length, and with V_0 is the potential depth at the center, given by

$$V_0 = \frac{3\pi c^2 \Gamma}{2\omega_A^2}\Big(\frac{1}{\omega_L - \omega_A} + \frac{1}{\omega_L + \omega_A}\Big) I_0 \tag{B.6}$$

We have introduced here the (u, v) coordinate system which is the 45° counter-clockwise rotation of the (x, y) system.

$$(u, v) = (x\cos(\theta) + y\sin(\theta), -x\sin(\theta) + y\cos(\theta)), \tag{B.7}$$

with $\theta = 45°$. In this coordinate system, the second beam is along the v direction.

At the end of the compression stage, which will be discussed in section B.4, atoms are accumulated mainly at the central region of the intersection of the two beams, prepared for the consequent evaporative cooling. The Gaussian trap Eq. (B.3) can then be approximated safely to a harmonic form which is much more easier for theoretical analysis.

In Tab. B.1 we list the parameters of the Large-CDT with laser power $P = 36$ W, including the trap frequencies $(\omega_x, \omega_y, \omega_z)/2\pi$, the trap depth V_0, and the scattering rate Γ_{sc}.

$w_{\mathrm{CDT}}(\mu\mathrm{m})$	$(\omega_x, \omega_y, \omega_z)/2\pi$ (kHz)	V_0/k_B (mK)	Γ_{sc} (s^{-1})
42	(2.5,4.5,5.1)	1.2	9

Table B.1: Parameters of the Large-CDT with $P = 36$ W. $(\omega_x, \omega_y, \omega_z)/2\pi$ is trap frequencies, V_0 is the trap depth, and Γ_{sc} is the scattering rate at the center of the Large-CDT. Table from [43].

B.2.2 Feedback system of the Large-CDT

During the experiment, we need, in several cases, to control or to modulate the depth of the trapping potential, for example, during the compression and the evaporative cooling stages. Therefore, we need to control very well the laser intensity which is proportional to the trapping depth. We adopt a intensity feedback system to control the Large-CDT. We illustrate in Fig. B.2 the feedback system and the optical system adapted in order to generate the intensity controlled, linear polarized, collimated laser beam. The laser beams are drawn in red color, and the electrical signals are drawn in blue. The whole system is enclosed in a metal box for the security reason (high power laser beam).

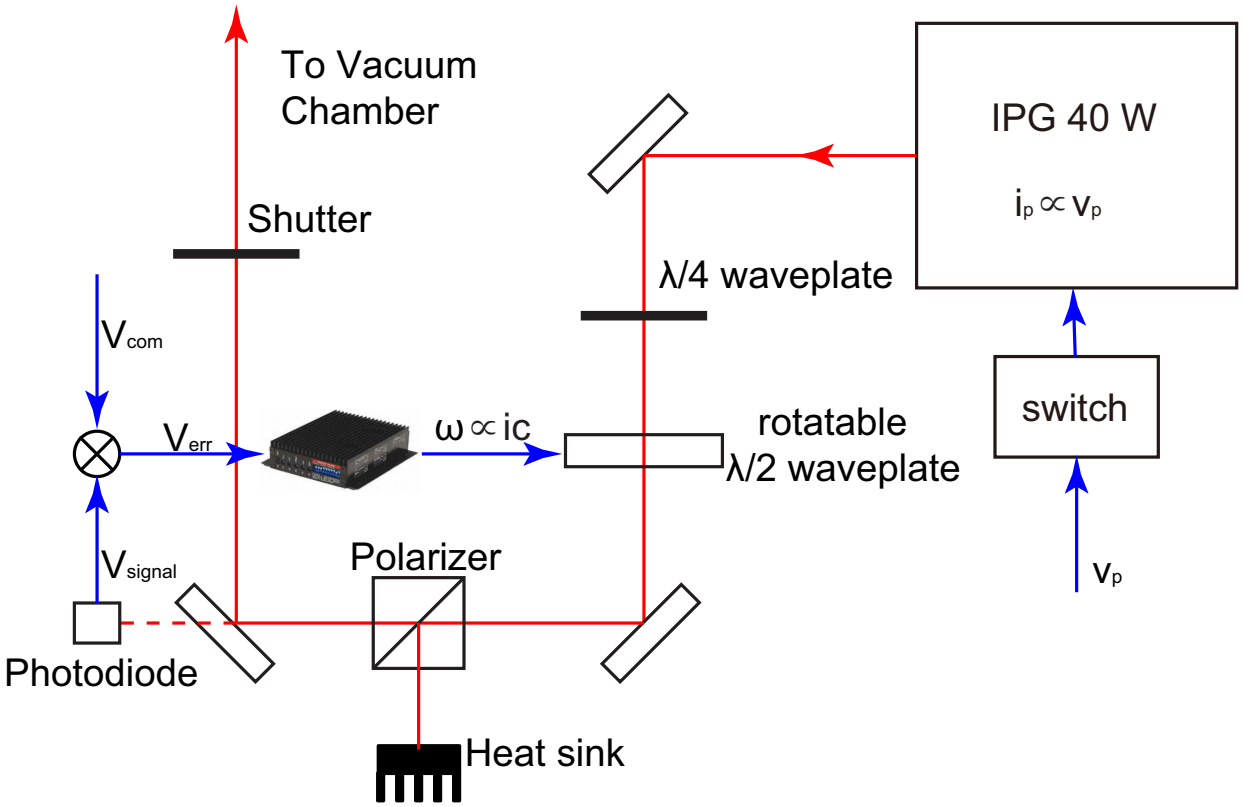


Figure B.2: IPG with feedback configuration

The output laser intensity is mainly controlled by two different elements. The first is the current of the pump diode of IPG fiber laser i_p which can be controlled by an analog input voltage v_p. The second is a rotatable $\lambda/2$ waveplate controlled by a motor with feedback. The $\lambda/2$ waveplate is followed by a Glan-Taylor polarizer. In fact, the output beam of the 40 W IPG laser is not completely linear but with some ellipticity. The $\lambda/4$ waveplate with appropriate main axis direction is to eliminate this ellipticity. Followed by a rotatable $\lambda/2$ waveplate combined with the polarizer, we can control the power of the laser beam behind. The minimal power that can be reached is about 0.5% of the maximum available.

By measuring by a photo-diode the residual light intensity behind a high-reflectivity mirror in the optical path of the high power laser beam, we get a signal V_signal proportional to the *real* beam intensity. Comparing to a command value V_com, we get an error signal $V_\mathrm{err} = V_\mathrm{com} - V_\mathrm{signal}$. This error signal is sent to a controller unit, which is adapted to the motor, in order to get a control current i_c. The speed of the motor is proportional to the control current i_c, thus the angular velocity of the rotatable $\lambda/2$ waveplate is also proportional to i_c, $\dot{\theta} \propto i_c$.

The bandwidth of the waveplate feedback system is about 10 Hz which is slow compared to some process during the realization of the BEC. As a result, we modulate, at the same time, the output power of the IPG laser directly via the injection current in the pump diode i_p. The bandwidth of this modulation can be up to 50 kHz which is sufficient to our experiment. However, if we decrease too much the injection current i_p to about

10% of its maximum, we come close to the laser threshold and the laser noise dramatically increases. Therefore, we limit the control voltage to stay away from this value above 30%.

During the experiment, we sometimes need to shut down abruptly the Large-CDT. We can cut off the injection current i_p in less than 10 μs with laser intensity drop to 10%, using an additional TTL input on the laser controller.

B.3 Loading the Large Crossed Dipole Trap

After we have pre-cooled and trapped atoms in the MOT, the next step is to transfer the atoms from the MOT to the Large Crossed Dipole Trap, whose features are discussed in section B.2. The loading process from MOT to Large-CDT is in general complex. The presence of the Large-CDT perturbs the dynamics of laser cooling [110]. The loading efficiency depends on the loading power of the Large-CDT and the density and temperature of the MOT. With lower temperature, the atoms are more easily trapped by the Large-CDT, and with higher density, the loading efficiency will be obviously higher.

At the end of the MOT stage, we realize two short stages, "Dark MOT" and "Cold MOT". During these two stages, the power and the frequency of the cooling and repumper beams are adjusted for several purposes. First, to increase loading efficiency by increasing the density and decrease the temperature of the MOT, second, because the high power Large-CDT beams can modify the atom energy level by light shift, we should adjust the laser in order to make the MOT cooling still efficient, and third, transfer atoms to the electronic ground state $|3^2S_{1/2}, F = 1\rangle$, in which the atoms will be trapped in the optical dipole trap.

In our experiment, the optimal loading power of the Large-CDT is not the highest available [49]. We optimize the loading power and explain the reason.

B.3.1 Optimization of the MOT lasers

B.3.1.1 Dark MOT

The Dark MOT [111] starts right after the MOT stage and lasts 100 μs. We decrease the power of the repumper beam from 300 μW/cm^2 down to 10 μW/cm^2, and change the detuning of the cooling laser from -20 MHz to -18 MHz. As a consequence of the reduced power of repumper, large population of atoms will accumulate in the electronic ground state $3^2S_{1/2}$ $F = 1$ which will not take part in the cooling cycle ($|3^2S_{1/2}, F = 2\rangle \leftrightarrow |3^2P_{3/2}, F = 3\rangle$). As a result, the light-induced collisions [40] (leading to trap loss) and the reabsorption of scattered laser light (weakening the trapping potential and limiting the density) are both suppressed [107, 108]. In this stage, MOT appears much less bright because of much less resonant cooling cycles.

B.3.1.2 Cold MOT

The Cold MOT start just after the Dark MOT stage and lasts 30 μs. We change the detuning of the cooling laser from -2Γ to -3.8Γ (Γ is the natural line width, $\Gamma = 2\pi \cdot 9.795(11)$ MHz). During this stage, sub-Doppler cooling continues to decrease the temperature down to 50 μK. At the end of the Dark MOT, cooling laser lasts 300 μs longer than the repumper laser in order to transfer all the atoms to the $|3^2S_{1/2}, F = 1\rangle$ ground state. The values for the detuning and the power of the cooling and repumper lasers during these 2 phases are optimized to obtain the maximum atom number in the Large-CDT.

B.3.2 Optimization of the Large-CDT power

We search for the optimum power of Large-CDT beams for loading. We maintain the power of the beams for 100 μs to see the atom number loaded in the two arms. We illustrate in Fig. B.3 the image of the atoms loaded in the arms of crossed dipole trap. During this short time, the thermalization process, which makes the atoms trapped in the Large-CDT to equilibrium, has not yet been important. In the following section, we will see the time scale of the thermalization is order of seconds.

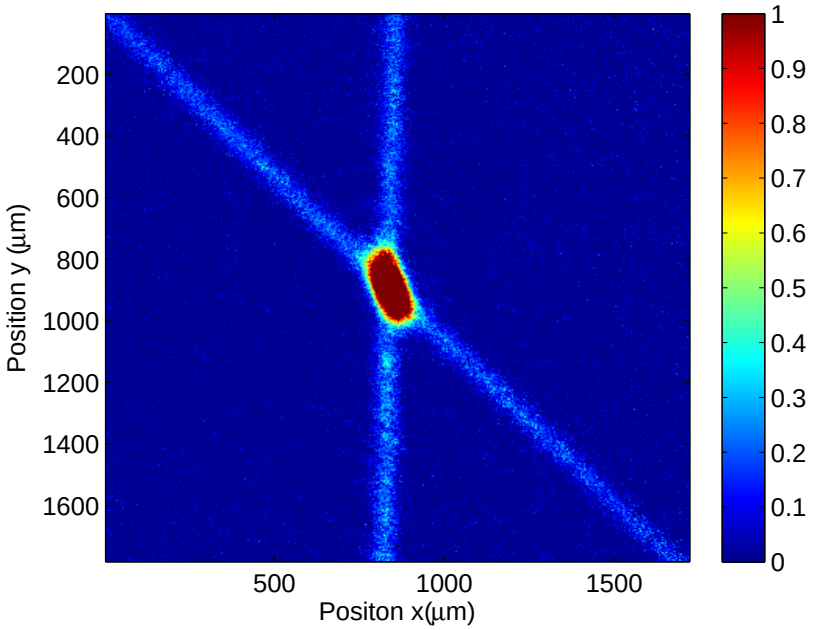
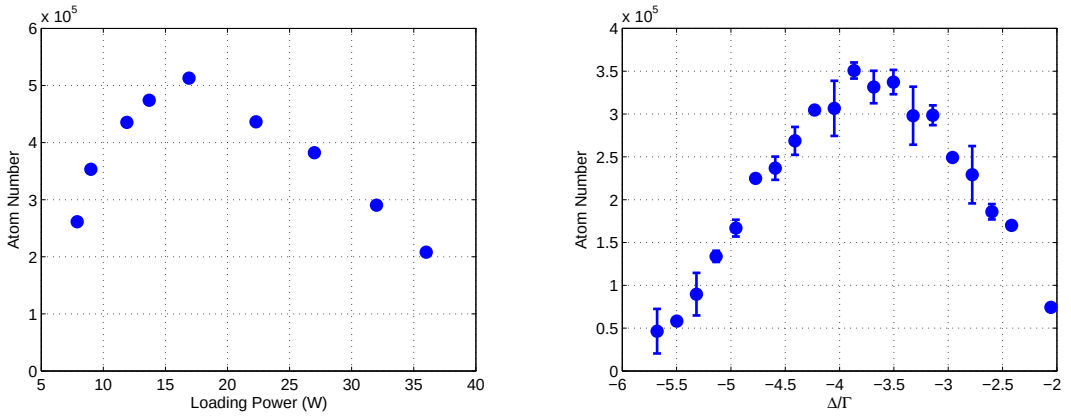


Figure B.3: Atoms loaded in the arms of the Large Optical Dipole Trap. (The colormap shows the optical depth by Eq. (2.21))

In Fig. B.4, we illustrate the optimization of the loading process. In Fig. B.4a, we plot the loaded atom number as a function of the loading power. The optimum power is about 16 W, corresponding to the light intensity about 5.4×10^5 W/cm^2. In this loading power, we plot in Fig. B.4b the loaded atom number as a function of the detuning of the cooling laser during Cold MOT stage. The optimum detuning is about -3.8Γ.



(a) (b)

Figure B.4: (a) The loaded atom number as a function of the loading power of the Large-CDT. The optimum power is about 16 W, corresponding to the light intensity about 5.4×10^5 W/cm^2. (b) In the optimum loading power 16 W, the loaded atom number as a function of the detuning of the cooling laser during Cold MOT stage. The optimum detuning is about -3.8Γ. Figure from [43]

We found that for very high power, the loading process is not as efficient as we naively expected. There are two main reasons. First, the high loading power makes the induced light shift large and difficult to compensate. Because of the inhomogeneity of the intensity of the beams, if we compensate the light shift at central region, the atoms farther will not be effectively cooled, and *vice versa*. Second, when the light shift is sufficiently large, the frequency of the cooling laser will approach the transition of $|3^2S_{1/2}, F = 2\rangle$ and $|3^2P_{3/2}, F = 2\rangle$. This will depump the atoms to $3^2S_{1/2}, F = 1\rangle$ stage.

In conclusion, because of the light shift induced by the Large-CDT, both the loading power and the cooling laser parameters should be adjusted in order to make the loading process efficient. At the end of the loading process, we obtain 5×10^5 atoms distributed along the arms of the Large-CDT with the temperature about 50 μK [49].

B.4 Compression in the Large-CDT

At the end of the loading process, the atoms are distributed along the arms of the Large-CDT (Fig. B.3). We wish to "compress" the atoms to the center region of the Large-CDT for two reasons. First, increase the space density in the center region in order to increase the collision rate, which is important for the evaporation. Second, we will evaporate in a smaller crossed dipole trap which cross at the center of the Large-CDT. In this part, we will optimize this compression process for the next evaporation step.

In Fig. B.5, we show the different results of the threes different compression process. First, we hold on the power of the Large-CDT at 13.7 W and let the atoms spontaneously accumulate to the center of the Large-CDT. Second, we increase the power of the

Large-CDT within 50 ms from the loading power to the maximum power 36 W. Third, we increase the power of the Large-CDT within 50 ms from the loading power to the maximum power 36 W. In Fig. B.5a, we plot the atom number at the center of the Large-CDT N_c as a function of the compression duration. In Fig. B.5b, we plot the $\alpha_{\mathrm{CDT}} = N_c/N_{\mathrm{tot}}$ as a function of the compression duration. α_{CDT} is the proportion of the N_c to the total atom number N_{tot} ($N_{\mathrm{tot}} = N_c + N_{\mathrm{arm}}$).

From the two figures, we conclude that, the optimum compression is the 2 seconds power ramp from loading power to the maximum power [49]. We increase the power of the Large-CDT to increase the depth of the center region of the Large-CDT, which will make the center region more attractive to the atoms trapped in the arms of the Large-CDT. After 2 seconds of compression, about 60% of atoms are in the center region. After that the trap loss will surpass the accumulation process. As a result α_{PDC} still increases, but both the atom number in the center region N_c and the total atom number N_{tot} decrease.

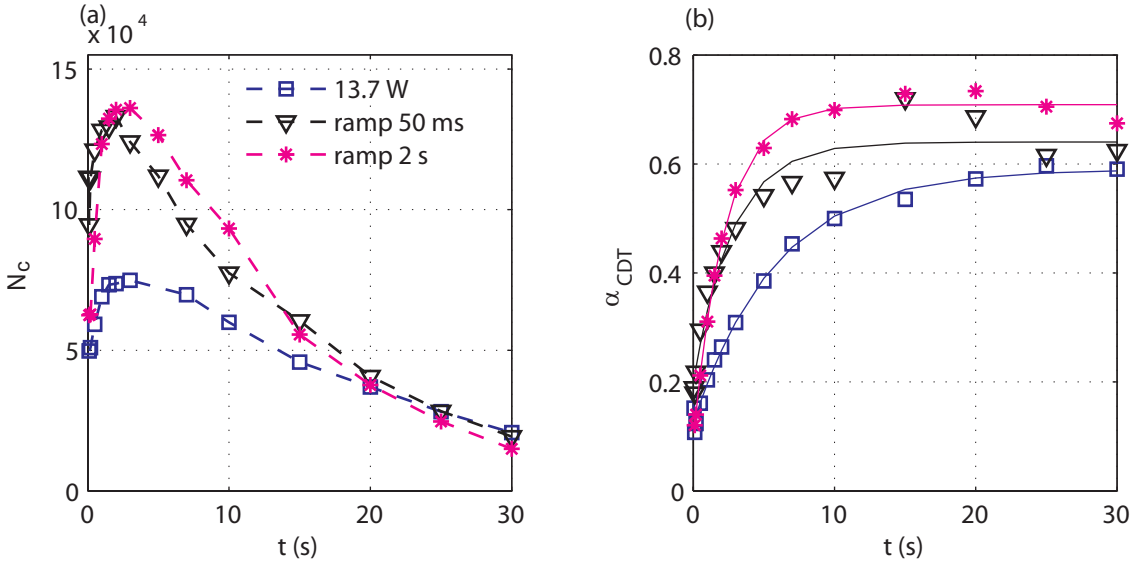


Figure B.5: (a). Atom number at the center region of the Large-CDT N_c as a function of the compression duration. (b). $\alpha_{\mathrm{CDT}} = N_c/N_{\mathrm{tot}}$ as a function of compression duration. (Figures from [49])

In conclusion, we adopt the 2 s ramp compression from 13.7 W to 36 W. At the end of the compression, we have 1.4×10^5 atoms with the temperature about 100 μK, and the phase space density $\mathcal{D} \approx 5.6 \times 10^{-4}$, prepared for the evaporation stage.

Appendix C

Supplementary Material : Phase diagram of spin 1 antiferromagnetic Bose-Einstein condensates

The content of this appendix is directly extracted from the Supplementary Informations *of [38].*

C.1 Sample preparation

In this section, we give a more comprehensive account of the preparation sequence used in the experiment. Evaporative cooling is done in two steps as explained in [49], starting from a large-volume optical trap that is subsequently transferred to a smaller trap with tighter confinement (which is used for the experiments described in the main text). This sequence allows one to maintain a high collision rate throughout the whole evaporation ramp. We start from atoms loaded in the large-volume trap from a magneto-optical trap (MOT). The loading is done at a reduced trap laser power, which was found in [49] to optimize the loading. After all MOT lasers are switched off, the large-volume trap is compressed by ramping up the laser power in 2 s. This increases the collision rate in the arms of the trap, helps filling the crossing region and overall provides a better starting point for the subsequent evaporative cooling ramp. The laser cooling sequence before the compression is found to result in a mixed spin state, with spin populations in the Zeeman states $m = +1, 0, -1$ in a ratio $0.7 : 0.2 : 0.1$, approximately.

To increase the degree of spin polarization, the compression ramp is done with an additional vertical bias field (~ 0.5 G) and magnetic field gradient (20 G/cm). As shown in [59, 85], this results in a spin distillation which polarizes the sample into the $m = +1$ state. The reason is that the trapping potential in the vertical direction are now slightly different for each Zeeman state, due to the potential drop caused by the gradient (see inset of Fig. C.1). One can choose a value such that the magnetic potential almost compensates gravity for the $m = +1$ state. The $m = 0$ state still feels the gravitational potential, and the $m = -1$ state then feels a potential drop twice as strong as $m = 0$. As a result, the effective potential depths for $m = 0, -1$ are slightly reduced compared to the $m = +1$ state, and evaporative cooling removes the former atoms preferentially. After the

spin distillation is complete, we obtain a partially polarized cloud with m_z ranging from ≈ 0.6 to ≈ 0.85 depending on the strength of the magnetic field gradient (see Fig. C.1a). We found that keeping the gradient for longer times was no longer effective to increase the polarization further. Our interpretation is that as the cloud size becomes too small, the magnetic potential drop becomes almost unnoticeable.

To obtain lesser degrees of polarization, we apply a horizontal bias field ~ 0.25 G and apply an additional radio-frequency (rf) field resonant at the Larmor frequency for a variable amount of time. As the atoms move and collide in the dipole trap, their spins quickly decohere, and produce a spin-isotropic mixture. By adjusting the strength of the rf field, we can adjust the final magnetization at will, as shown in Fig. C.1b. The radio-frequency resonance is about 2 kHz wide, presumably limited by inhomogeneous broadening and stray magnetic fields (which are estimated to a few mG due to environmental noise). To ensure that small frequency drifts do not perturb significantly the preparation, the frequency of the oscillating field is swept over 20 kHz at a slow rate during the whole depolarization sequence.

After this preparation stage, the magnetic field is set at its final value, and we perform evaporative cooling by reducing the depth of the crossed dipole trap until a temperature ~ 10 μK is reached, at which point the cloud is transferred to the final trap with tighter focus to boost the spatial density [49]. This final trap is formed by two red-detuned laser beams, one propagating vertically with a waist ($1/e^2$ radius) of ≈ 8 μm and the other propagating horizontally with a waist ≈ 11 μm. At the end of the evaporation ramp, where the experiments are performed, the trap frequencies are $\{\omega_{x,y,z}\} = 2\pi \times (910, 1000, 425)$ Hz.

C.2 Stern-Gerlach expansion

The populations of the Zeeman states are analyzed after expansion in a magnetic field gradient $b' = 15$ G/cm, which is switched on at the start of the expansion sequence together with an additional bias field $B_x \approx 2$ G. This produces a force along the horizontal x axis that separates the $m = \pm 1$ clouds from the $m = 0$ one by a distance $d_{SG} = \mu_B \eta b' t^2 / 4M_{Na}$, with μ_B the Bohr magneton and t the expansion time. The factor η takes into account the temporal profile of the gradient, which rises in a few ms after the beginning of the expansion. Fig. C.2a shows the vertical trajectory of the atoms, and compares it with the one calculated from the measured gradient variations. The excellent agreement indicates that the gradient behavior is well understood. After a given expansion time (typically $t \approx 3.5$ ms), we take an absorption picture of the clouds, and count the relative populations. The image is taken in a vertical magnetic field $B_z \approx 1$ G applied 1 ms before the image is taken. The horizontal bias field B_x is switched off at the same time that B_z is switched on. In order to obtain reliable images, the separation d_{SG} must be much larger than the cloud sizes R_t after expansion to clearly separate each Zeeman component. In our experiment, when the trap is switched off instantaneously, we typically achieve $d_{SG}/R_t \approx 1$ only. This is due to the tight trap frequencies, and

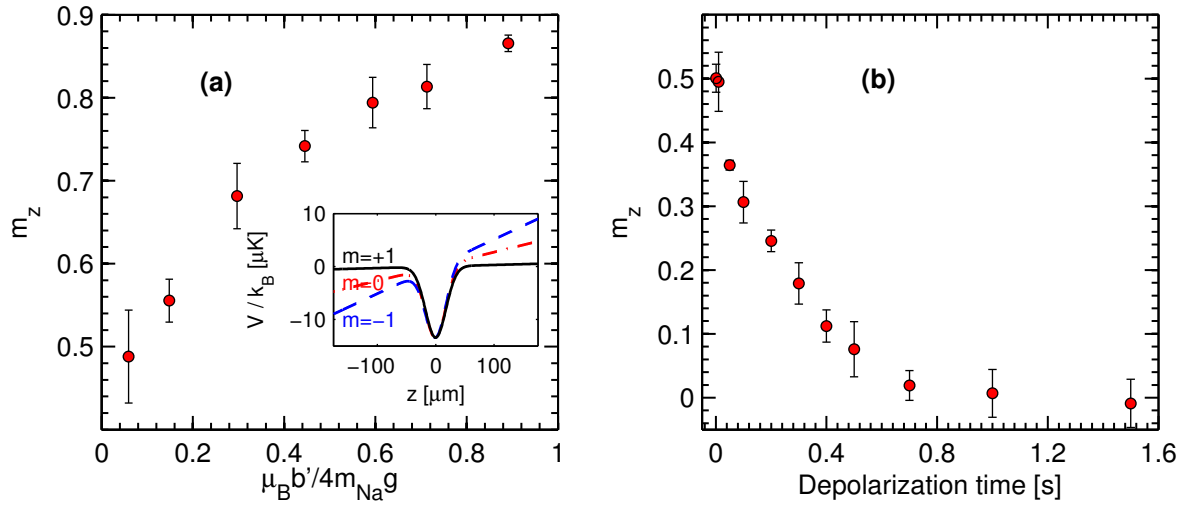


Figure C.1: **Supplementary Material-** (Color online) **(a):** Spin distillation to prepare samples with high magnetization ($m_z > 0.5$). The plot shows the magnetization measured for cold clouds, as a function of the magnetic gradient b' in units of $m_{Na}g/\mu_B$, with g the acceleration of gravity and μ_B the Bohr magneton. The inset shows a sketch of the potential energies for each Zeeman state along the vertical axis z. The potential drop is exaggerated for clarity, and is smaller than depicted in the actual experiment. **(b):** Depolarization to prepare samples with low magnetizations ($m_z < 0.5$). The time shown corresponds to the length of a radio-frequency pulse at the Larmor frequency.

the resulting fast expansion. The gradient strength cannot be increased further due to technical limitations, and the expansion time is also limited by the necessity to keep a sufficiently large signal-to-noise ratio to detect atoms in each component.

We thus resort to a slow opening of the trap, by ramping down the laser intensity to approximately 1/10th of its initial value in 5.5 ms before switching it off abruptly. As shown in Fig. C.2b, this reduces the expansion speed (of both the condensate and the thermal gas). At the same time, this leaves time for the gradient to settle to its maximum value, leading finally to $d_{SG}/R_t \approx 10$ for an expansion time $t = 3.5$ ms. We have checked that this procedure do not affect the measured atom number (see Fig. C.2c) or condensed fraction.

C.3 Spin interaction energy

The spin-spin interaction energy (positive for antiferromagnetic interactions) is given in the SMA by

$$U_s = \frac{4\pi\hbar^2 N a_s}{m_{\rm Na}} \int |\overline{\phi}(\mathbf{r})|^4 \, d^3\mathbf{r}, \tag{C.1}$$

with $m_{\rm Na}$ the mass of a Sodium atom, $a_s \approx 0.1$ nm the spin-dependent scattering length [42] and $\overline{\phi}$ the single-mode wave function. In terms of the commonly used singlet and

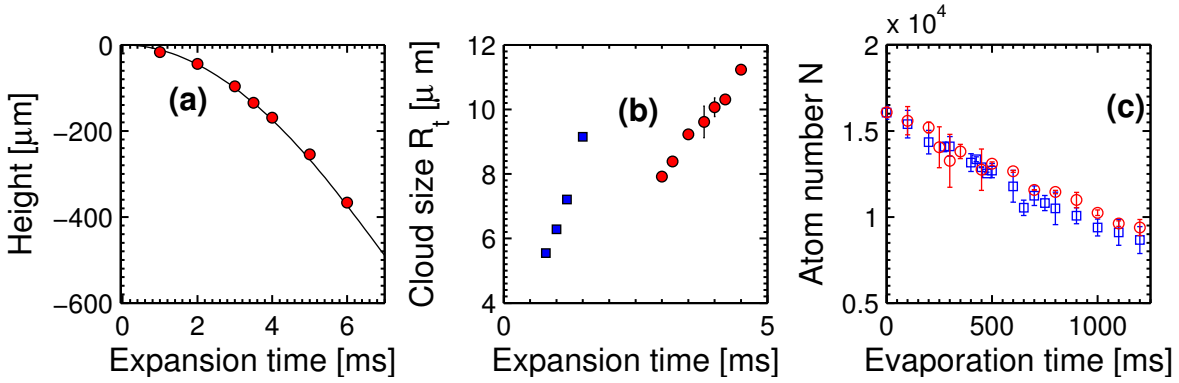


Figure C.2: **Supplementary Material-** (Color online) Free expansion after trap opening. **(a):** Center-of-mass trajectory along the vertical direction z for the $m = +1$ state; The solid line shows the calculated trajectory taking the measured magnetic gradient and gravity into account. **(b):** Sizes of the expanding clouds after an expansion time for an instantaneous release (blue squares) or a smooth release (red circles). **(c):** Atom number measured for instantaneous (blue squares) and smooth (red circles) releases, for various evaporation times.

quintet scattering lengths a_0 and a_2 [26], one has $a_s = (a_2 - a_0)/3$. We obtain the latter by solving numerically the Gross-Pitaevskii equation [47]

$$-\frac{\hbar^2}{2m_{\mathrm{Na}}}\Delta\overline{\phi}(\mathbf{r}) + \frac{1}{2}m_{\mathrm{Na}}\overline{\omega}^2\overline{\phi} + N\overline{g}|\overline{\phi}|^2\overline{\phi} = \mu\overline{\phi}. \tag{C.2}$$

We assumed the real, slight anisotropic trap potential could be approximated by an isotropic harmonic potential, with $\overline{\omega}/2\pi \approx 0.7$ kHz the geometric average of the three trap frequencies. The spin-independent interaction strength is $\overline{g} = 4\pi\hbar^2\overline{a}/m_{\mathrm{Na}}$, with $\overline{a} \approx 2.79$ nm [42], and in accordance with the single-mode assumption we have neglected spin-dependent interaction terms of order $\sim a_s/\overline{a}$.

C.4 Conservation of magnetization

We discuss in this section the key assumption behind this work, the conservation of longitudinal magnetization. As already discussed, this is true as far as short-range interactions are concerned. However, there are other weak effects that could in principle relax the magnetization. Two main effects come to mind. First, a dipole-dipole interaction exists in principle between atoms with non-zero spin. These effects are very weak compared to short-range spin-dependent interactions. A typical relaxation rate due to dipole-dipole interactions is less than 0.02 Hz for a fully polarized gas for our parameters, assuming the dipolar loss constant is given by the upper bound $L_2 \approx 5 \cdot 10^{-16}$ at.cm^2/s given in [112]. Dipolar relaxation can therefore be neglected for the experiments reported here. Second, the cloud held in the optical trap is subject to permanent evaporative cooling, leading to a $1/e$ lifetime around 10 s. If the potential depends on the internal state, in general magnetization is not conserved (this is the principle behind spin distillation [59, 85]). However, even in this case the remaining trapped atoms will relax to a new equilibrium

state through magnetization-conserving collisions, and thus to the equilibrium state expected with fixed magnetization. In other words, assuming the spin degrees of freedom equilibrate faster than the magnetization relaxes, the system should adiabatically follow the slow relaxation of magnetization due to evaporation. We note that if the potential is spin-independent, and the thermal gas isotropic the magnetization will not change on average, although one can expect fluctuations to increase in time. Experimentally, we found no evidence for these effects, which we believe to exist but lie beyond our sensitivity (a few percent, limited by the optical shot noise in the detection process).

Appendix D

Calculation details for Broken symmetry picture

D.1 Spin nematic states $|N:\mathbf{\Omega}\rangle$

According to Eq. (4.36), the spin nematic states can be expressed as

$$\begin{aligned} |N:\mathbf{\Omega}\rangle &= \frac{1}{\sqrt{N!}}(\mathbf{\Omega}\cdot\hat{\mathbf{a}}^{\dagger})^{N}|\mathrm{vac}\rangle \\ &= \frac{1}{\sqrt{N!}}(\Omega_{+1}a_{+1}^{\dagger}+\Omega_{0}a_{0}^{\dagger}+\Omega_{-1}a_{-1}^{\dagger})^{N}|\mathrm{vac}\rangle \\ &= \sum_{\substack{k,l,m \\ k+l+m=N}} \sqrt{\frac{N!}{k!l!m!}}\Omega_{+1}^{k}\Omega_{0}^{l}\Omega_{-1}^{m}\,|k,l,m\rangle_{\mathrm{Fock}}. \end{aligned} \tag{D.1}$$

The N-order moment of N_0 in this state is given by

$$\langle N:\mathbf{\Omega}|\hat{N}_{0}^{m}|N:\mathbf{\Omega}\rangle = P_{N}^{m}\cos^{2m}(\theta)+c_{2}P_{N}^{m-1}\cos^{2m-2}(\theta)+\cdots+c_{m}P_{N}^{1}\cos^{2}(\theta). \tag{D.2}$$

where the coefficients $c_2,\cdots,c_m$ are defined such as

$$l^{m} = l(l-1)\cdots(l-m+1)+c_{2}\cdot l(l-1)\cdots(l-m+2)+\cdots+c_{m}\cdot l. \tag{D.3}$$

D.2 Calculation of $\hat{\rho}$ in section 4.3

The density matrix in the generalized ensemble where the distribution of M is constrained can be expressed as

$$\hat{\rho} = \frac{1}{\mathcal{Z}}\sum_{M} w_{M}\hat{P}_{M}\mathrm{e}^{-\beta\hat{H}_{\mathrm{SMA}}}\hat{P}_{M}. \tag{D.4}$$

In order to calculate the average of a k-body observable $\hat{\mathcal{O}}^{(k)}$ for the density matrix $\hat{\rho}$, we have

$$\begin{aligned} \langle\hat{\mathcal{O}}^{(k)}\rangle &= \mathrm{Tr}(\hat{\mathcal{O}}^{(k)}\hat{\rho}) \\ &= \int \mathrm{d}\mathbf{\Omega}\int \mathrm{d}\mathbf{\Omega}'\,\langle N:\mathbf{\Omega}|\hat{\mathcal{O}}^{(k)}|N:\mathbf{\Omega}'\rangle\langle N:\mathbf{\Omega}'|\hat{\rho}|N:\mathbf{\Omega}\rangle, \end{aligned} \tag{D.5}$$

with

$$\langle N:\mathbf{\Omega}|\hat{\rho}|N:\mathbf{\Omega}'\rangle = \frac{1}{\mathcal{Z}}\sum_M w_M \langle N:\mathbf{\Omega}|\hat{P}_M \mathrm{e}^{-\beta\hat{H}_{\mathrm{SMA}}}\hat{P}_M|N:\mathbf{\Omega}'\rangle. \tag{D.6}$$

In using Eq. (D.1), the action of annihilation operator $\hat{a}_\sigma$ on $|N:\mathbf{\Omega}\rangle$ leads to

$$\hat{a}_\sigma|N:\mathbf{\Omega}\rangle = \sqrt{N}\Omega_\sigma|N-1:\mathbf{\Omega}\rangle, \tag{D.7}$$

with $\sigma = +1, 0, -1$, thus

$$\hat{a}_{\sigma_1}\hat{a}_{\sigma_2}\cdots\hat{a}_{\sigma_k}|N:\mathbf{\Omega}\rangle = \sqrt{N(N-1)\cdots(N-k+1)}\,\Omega_{\sigma_1}\Omega_{\sigma_2}\cdots\Omega_{\sigma_k}|N-k:\mathbf{\Omega}\rangle. \tag{D.8}$$

Therefore, the average of a normally ordered k-body observable $\hat{\mathcal{O}}^{(k)} = a^\dagger_{\sigma_1}a^\dagger_{\sigma_2}\cdots a^\dagger_{\sigma_k}a_{\sigma_1}a_{\sigma_2}\cdots a_{\sigma_k}$ for $|N:\mathbf{\Omega}\rangle$ leads to

$$\begin{aligned}\langle N:\mathbf{\Omega}|\hat{\mathcal{O}}^{(k)}|N:\mathbf{\Omega}'\rangle = N(N-1)\cdots(N-k+1)\Omega^*_{\sigma_1}\Omega'_{\sigma_1}\Omega^*_{\sigma_2}\Omega'_{\sigma_2}\cdots\Omega^*_{\sigma_k}\Omega'_{\sigma_k}\\ \times\langle N-k:\mathbf{\Omega}|N-k:\mathbf{\Omega}'\rangle.\end{aligned} \tag{D.9}$$

As we have pointed out in section 4.2.3, $\langle N:\mathbf{\Omega}|N:\mathbf{\Omega}'\rangle \approx 4\pi\delta(\mathbf{\Omega}-\mathbf{\Omega}') + \mathcal{O}(1/N)$. As a result, in Eq. (D.6), only the diagonal elements of $\hat{\rho}$ counts. According to the discussion in section 4.2.3, we have

$$\hat{H}_{\mathrm{SMA}}|N:\mathbf{\Omega}\rangle = -Nq\cos^2(\theta)|N:\mathbf{\Omega}\rangle + \mathcal{O}(1). \tag{D.10}$$

Therefore,

$$\begin{aligned}\mathrm{e}^{-\beta\hat{H}_{\mathrm{SMA}}}|N:\mathbf{\Omega}\rangle &= \sum_{m=0}^{\infty}\frac{1}{m!}(-\beta\hat{H}_{\mathrm{SMA}})^m|N:\mathbf{\Omega}\rangle\\ &\approx \mathrm{e}^{\beta Nq\cos^2(\theta)}|N:\mathbf{\Omega}\rangle.\end{aligned} \tag{D.11}$$

As a result, Eq. (D.6) leads to

$$\langle N:\mathbf{\Omega}|\hat{\rho}|N:\mathbf{\Omega}\rangle \simeq \frac{1}{\mathcal{Z}}\sum_M w_M \mathrm{e}^{\beta Nq\cos^2(\theta)}\langle N:\mathbf{\Omega}|\hat{P}_M|N:\mathbf{\Omega}\rangle. \tag{D.12}$$

In order to calculate $\langle N:\mathbf{\Omega}|\hat{P}_M|N:\mathbf{\Omega}\rangle$, we note that the eigenstates $|N,S,M\rangle$ (for $S = |M|\cdots N$) form a basis for each subspace of given M. From Eq. (4.39), we have

$$P_M = \sum_{S=|M|}^{N}|N,S,M\rangle\langle N,S,M| = \sum_{S=|M|}^{N}\int \mathrm{d}\mathbf{\Omega}\mathrm{d}\mathbf{\Omega}'\, Y^*_{SM}(\mathbf{\Omega})Y_{SM}(\mathbf{\Omega}')|N:\mathbf{\Omega}\rangle\langle N:\mathbf{\Omega}'|. \tag{D.13}$$

Therefore, using the quasi-orthogonality of the $|N:\mathbf{\Omega}\rangle$ states, we have (to an error $\sim 1/N$)

$$\langle N:\mathbf{\Omega}|P_M|N:\mathbf{\Omega}\rangle \approx \sum_{S=|M|}^{N}|Y_{SM}(\mathbf{\Omega})|^2. \tag{D.14}$$

Finally, we get the expression of $\hat{\rho}$ and $\mathcal{Z}$ for the arbitrary distribution w_M

$$\langle N:\mathbf{\Omega}|\hat{\rho}|N:\mathbf{\Omega}\rangle \simeq \frac{1}{\mathcal{Z}}f(\mathbf{\Omega})\,\mathrm{e}^{\beta Nq\Omega_z^2}, \tag{D.15}$$

$$\mathcal{Z} \simeq \int \mathrm{d}\mathbf{\Omega}\, f(\mathbf{\Omega})\, \mathrm{e}^{\beta N q \Omega_z^2}, \tag{D.16}$$

with

$$f(\mathbf{\Omega}) = \sum_{M=-N}^{N} \sum_{S=|M|}^{N} w_M |Y_{SM}(\mathbf{\Omega})|^2 = \sum_{S=0}^{N} \sum_{M=-S}^{S} w_M |Y_{SM}(\mathbf{\Omega})|^2. \tag{D.17}$$

D.3 Fluctuation of magnetization Δm_z at $q = 0$

We begin with the fluctuation of M,

$$\begin{aligned} \Delta M^2 &= \langle M^2 \rangle \\ &= \frac{\int_0^{+\infty} \mathrm{e}^{-\beta' S^2} \mathrm{d}S \cdot \int_{-S}^{S} M^2 \mathrm{e}^{-\gamma M^2} \mathrm{d}M}{\int_0^{+\infty} \mathrm{e}^{-\beta' S^2} \mathrm{d}S \cdot \int_{-S}^{S} \mathrm{e}^{-\gamma M^2} \mathrm{d}M} \\ &= \frac{1}{2\gamma} - \frac{1}{2(\beta'+\gamma)\sqrt{\pi} \int_0^{+\infty} \mathrm{e}^{-\alpha x^2} \mathrm{erf}(x)\, \mathrm{d}x}. \end{aligned} \tag{D.18}$$

with $\mathrm{erf}(x) = \frac{2}{\sqrt{\pi}} \int_0^x \mathrm{e}^{-t^2} \mathrm{d}t$, $\beta' = \beta U_s/(2N)$, $\gamma = 1/(2N^2\sigma^2)$, $\alpha = \beta'/\gamma = N\beta U_s \sigma^2$. Moreover, we have

$$\sqrt{\pi} \int_0^{+\infty} \mathrm{e}^{-\alpha x^2} \mathrm{erf}(x)\, \mathrm{d}x = \frac{1}{\sqrt{\alpha}} \arctan(\frac{1}{\sqrt{\alpha}}). \tag{D.19}$$

Finally, the fluctuation of m_z at $q = 0$ is

$$\Delta m_z = \sqrt{\frac{\Delta M^2}{N^2}} = \sigma \sqrt{1 - \frac{\sqrt{\alpha}}{(1+\alpha)\arctan(\frac{1}{\sqrt{\alpha}})}}. \tag{D.20}$$

We can also calculate $\langle \mathbf{S}^2 \rangle$,

$$\begin{aligned} \langle \mathbf{S}^2 \rangle &= \frac{\int_0^{+\infty} \mathrm{d}S\, S^2 \mathrm{e}^{-\beta' S^2} \int_{-S}^{+S} \mathrm{d}M\, \mathrm{e}^{-\gamma M^2}}{\int_0^{+\infty} \mathrm{d}S\, \mathrm{e}^{-\beta' S^2} \int_{-S}^{+S} \mathrm{d}M\, \mathrm{e}^{-\gamma M^2}} \\ &= \frac{1}{2\gamma} \Big(\frac{1}{\alpha} + \frac{1}{\sqrt{\alpha}(1+\alpha)\arctan(1/\sqrt{\alpha})} \Big). \end{aligned} \tag{D.21}$$

$$\int_0^{+\infty} \mathrm{d}x\, x^2 \mathrm{e}^{-\alpha x^2} \mathrm{erf}(x) = \frac{1}{2\sqrt{\pi}} \Big(\frac{1}{\alpha + \alpha^2} + \frac{\arctan(1/\sqrt{\alpha})}{\alpha^{3/2}} \Big). \tag{D.22}$$

As a result, the spin interaction energy $\langle E_s \rangle$ at $q = 0$ is

$$\langle E_s \rangle = \frac{U_s}{2N} \langle \mathbf{S}^2 \rangle = k_B T_s \cdot g(\alpha). \tag{D.23}$$

with

$$g(\alpha) = \frac{1}{2} \cdot \Big(1 + \frac{\sqrt{\alpha}}{(1+\alpha)\arctan(1/\sqrt{\alpha})} \Big). \tag{D.24}$$

Moreover, according to Eq. (D.20), we have

$$\frac{U_s}{2N} \times 3\langle S_z^2 \rangle = f(\alpha) \cdot k_B T_s. \tag{D.25}$$

with

$$f(\alpha) = \frac{3}{2} \cdot \alpha \Big(1 - \frac{\sqrt{\alpha}}{(1+\alpha)\arctan(1/\sqrt{\alpha})} \Big). \tag{D.26}$$

We plot in Fig. D.1, function $f(\alpha)$ and $g(\alpha)$ in Eq. (D.26) and (D.24), respectively.

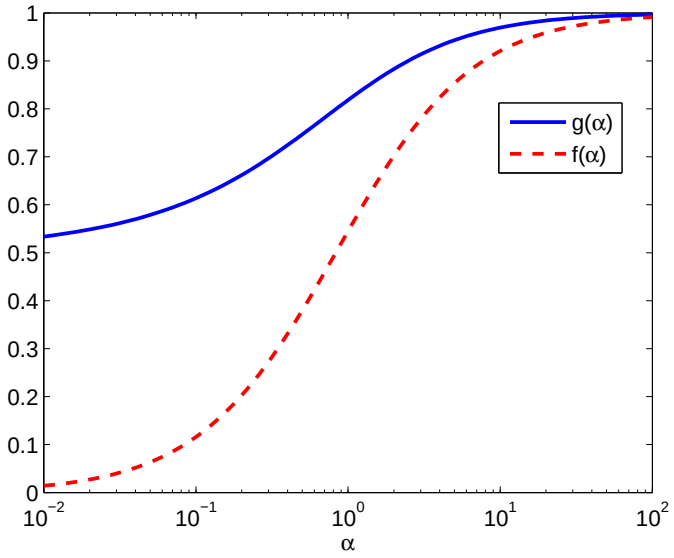


Figure D.1: Function $f(\alpha)$ and $g(\alpha)$ in Eq. (D.26) and (D.24), respectively.

Appendix E

Published articles

- **Phase diagram of spin-1 antiferromagnetic Bose-Einstein condensates**

  David Jacob, Lingxuan Shao, Vincent Corre, Tilman Zibold, Luigi De Sarlo, Emmanuel Mimoun, Jean Dalibard, and Fabrice Gerbier. *Phys. Rev. A* **86**, 061601(R) (2012)

  This article is cited in chapter 3 (main text) and in appendix C (supplementary material), and will not be included in this appendix.

- **Spin fragmentation of Bose-Einstein condensates with antiferromagnetic interactions**

  Luigi De Sarlo, Lingxuan Shao, Vincent Corre, Tilman Zibold, David Jacob, Jean Dalibard and Fabrice Gerbier. *New Journal of Physics* **15** (2013) 113039 (18pp)

New Journal of Physics
The open access journal for physics

Spin fragmentation of Bose–Einstein condensates with antiferromagnetic interactions

Luigi De Sarlo[1], Lingxuan Shao, Vincent Corre, Tilman Zibold, David Jacob, Jean Dalibard and Fabrice Gerbier[2]

Laboratoire Kastler Brossel, CNRS, ENS, UPMC, 24 rue Lhomond, F-75005 Paris, France
E-mail: fabrice.gerbier@lkb.ens.fr

New Journal of Physics **15** (2013) 113039 (18pp)
Received 2 July 2013
Published 19 November 2013
Online at http://www.njp.org/
doi:10.1088/1367-2630/15/11/113039

Abstract. We study spin fragmentation of an antiferromagnetic spin 1 condensate in the presence of a quadratic Zeeman (QZ) effect breaking spin rotational symmetry. We describe how the QZ effect turns a fragmented spin state, with large fluctuations of the Zeeman populations, into a regular polar condensate, where the atoms all condense in the $m = 0$ state along the field direction. We calculate the average value and variance of the population of the Zeeman state $m = 0$ to illustrate clearly the crossover from a fragmented to an unfragmented state. The typical width of this crossover is $q \sim k_B T/N$, where q is the QZ energy, T the spin temperature and N the atom number. This shows that the spin fluctuations are a mesoscopic effect that will not survive in the thermodynamic limit $N \to \infty$, but are observable for a sufficiently small atom number.

[1] Current address: SYRTE, Observatoire de Paris, CNRS, UPMC; 61 Avenue de l'Observatoire, 75014 Paris, France.
[2] Author to whom any correspondence should be addressed.

Content from this work may be used under the terms of the Creative Commons Attribution 3.0 licence. Any further distribution of this work must maintain attribution to the author(s) and the title of the work, journal citation and DOI.

© IOP Publishing Ltd and Deutsche Physikalische Gesellschaft

Contents

1. Introduction **2**
2. Single-mode description of spin-1 condensates **5**
3. Spectrum and eigenstates for $M = 0$ **5**
3.1. Continuum approximation for large q 6
3.2. Ground state 6
3.3. Excited states for $M = 0$ 7
4. Spin fragmentation at finite temperatures **8**
4.1. Spin fragmentation for $q = 0$ 9
4.2. Bogoliubov approximation for $q \neq 0$ 10
4.3. Comparison between the different approximations 11
5. Comparison with the broken-symmetry picture **12**
5.1. Zero temperature 12
5.2. Moments of N_0 at finite temperatures 14
6. Conclusion **15**
Acknowledgments **15**
Appendix A. Total spin eigenstates **16**
Appendix B. Continuum approximation **17**
References **17**

1. Introduction

The natural behavior of bosons at low enough temperatures is to form a Bose–Einstein condensate (BEC), i.e. a many-body state where one single-particle state becomes macroscopically occupied [1]. There are, however, situations where bosons can condense simultaneously in several single-particle states, forming a so-called *fragmented condensate*. Several examples are known, where fragmentation occurs due to orbital (Bose gases in optical lattices or in fast rotation) or to internal degeneracies (pseudo-spin-1/2 or spin-1 Bose gases). These examples have been reviewed in [2, 3].

The spin-1 Bose gas, first studied by Nozières and Saint James [4], is a striking example where fragmentation occurs due to rotational symmetry in spin space. For antiferromagnetic interactions of the form $V_{12} = g_s \mathbf{s}_1 \cdot \mathbf{s}_2$ between two atoms with spins $\mathbf{s}_1$ and $\mathbf{s}_2$ ($g_s > 0$), the many-body ground state is expected to be a spin singlet state [2, 5]. In such a state, the three Zeeman sublevels are occupied, leading to three macroscopic eigenvalues of the single-particle density matrix (instead of just one for a regular condensate). As pointed out in [2, 5, 6], the signature of fragmentation is then the occurrence of anomalously large fluctuations of the populations N_m in the Zeeman states $m = 0, \pm 1$ (see also [7, 8], where similar behavior is predicted in a pseudo-spin-1/2 system). In the singlet state, for instance, the expectation value and variance of N_0 are $\langle N_0 \rangle = N/3$ and $\Delta N_0^2 \approx 4N^2/45$, respectively ($N$ is the total number of particles). Such super-Poissonian fluctuations ($\Delta N_0^2 \propto \langle N_0 \rangle^2$) deviate strongly from the value expected for a single condensate or any ensemble without correlations where

$\Delta N_0^2 \propto \langle N_0 \rangle$.[3] It was pointed out by Ho and Yip [6] that such a state was probably not realized in typical experiments, due to its fragility toward any perturbation breaking spin rotational symmetry (see also [9–14]). In the thermodynamic limit $N \to \infty$, an arbitrary small symmetry-breaking perturbation is enough to favor a regular condensed state, where almost all the atoms occupy the same (spinor) condensate wave function and $\Delta N_0 \ll N$.

In this paper, we give a detailed analysis of the phenomenon of spin fragmentation for spin-1 bosons. Our analysis assumes the conservation of total magnetization m_z. The fact that magnetization is an (almost) conserved quantity follows from the rotational invariance of the microscopic spin exchange interaction, and from the isolation of atomic quantum gases from their environment. A key consequence is that in an external magnetic field B, the linear Zeeman effect only acts as an energy offset and does not play a role in determining the equilibrium state. The dominant effect of an applied magnetic field is a second-order (or quadratic) Zeeman energy, of the form $q(m^2 - 1)$ for a single atom in the Zeeman state with magnetic quantum number m.[4] The quadratic Zeeman (QZ) energy breaks the spin rotational symmetry, and favors a condensed state with $m = 0$ along the field direction. In [10–13], the evolution of the ground state with the QZ energy q was studied theoretically. Since experiments are likely to operate far from the ground state, it is important to understand quantitatively how the system behaves at finite temperatures. This is the main topic we address in this paper.

Our focus in this paper will be to calculate the first two moments (average value and variance) of N_0. These moments illustrate clearly the evolution of the system from fragmented to unfragmented and thus constitute the main experimental signature of fragmentation. The main findings are summarized in figure 1, where we plot the standard deviation of $n_0 = N_0/N$ in a q–T plane. Large fluctuations of the $m = 0$ state are observed for small q. We can distinguish three different regimes. For low $q \ll U_s/N^2$ and low temperatures $k_B T \ll U_s/N$ ($U_s \propto g_s$ is the spin interaction energy per atom), the system is close to the ground state in a regime we call 'quantum spin fragmented' [2, 5, 6, 12]. We also observe a thermal regime for $k_B T \gg Nq, U_s/N$ dominated by thermally populated excited states. We call this second regime 'thermal spin fragmented'. Finally, for q large enough and temperature low enough, the bosons condense into the single-particle state $m = 0$, forming a so-called 'polar' condensate [16, 17]. In this limit, $\langle N_0 \rangle \approx N$ and $\Delta N_0 \ll N$. We indicate this third regime as 'BEC $m = 0$' in figure 1.

The evolution from the fragmented, singlet condensate to an unfragmented condensate with increasing QZ energy q is similar to a well-known example in the literature on quantum magnetism, the Lieb–Matthis model of lattice Heisenberg antiferromagnets [18]. This model describes collective spin fluctuations of an Heisenberg antiferromagnet on a bipartite lattice. It constitutes a popular toy model for demonstrating the appearance of broken symmetry ground states in condensed matter [19–24]. The ground state of such system (in principle also a spin singlet) was found theoretically to evolve to a Néel state in the thermodynamic limit in the presence of an arbitrarily small *staggered* magnetic field (whose sign alternates from one site to the next). The underlying theory is close to the one presented here. An essential difference

[3] Note that the problem we discuss here is unrelated to the anomalous fluctuations of the *total* condensate number found for ideal gases in the grand canonical ensemble [1]. In this work, we assume implicitly the canonical ensemble, and study the fluctuations of the populations of individual Zeeman states discarding quantum and thermal depletion of the condensate.

[4] This second-order shift originates from the hyperfine coupling between electronic and nuclear spins, and corresponds to the second-order term in an expansion of the well-known Breit–Rabi formula for alkalis (see e.g. [15]).

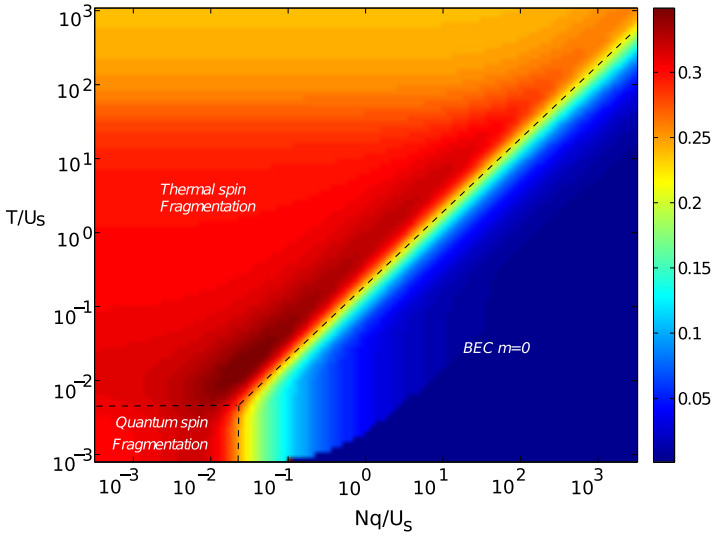


Figure 1. Standard deviation $\Delta n_0 = \Delta N_0/N$ of the population N_0 of the Zeeman state $m = 0$, normalized to the total atom number N. We mark three different regimes in the q–T plane. 'Spin fragmentation' refers to a fragmented spin state with large population fluctuations, where $\Delta n_0 \sim 1$. In the quantum regime ($Nq/U_s \ll 1/N$ and $k_B T/U_s \ll 1/N$), this is due to quantum fluctuations: the system is then close to the singlet ground state. In the thermal regime ($k_B T \gg Nq, U_s/N$), on the other hand, thermal fluctuations dominate over the quantum one and over the effect of the QZ energy. Conversely, 'BEC $m = 0$' refers to the atoms forming a regular polar condensate with almost all the atoms in $m = 0$, and $\Delta n_0 \ll 1$. The plot was drawn by numerically diagonalizing the Hamiltonian (1) and computing thermodynamic averages from the spectrum and eigenstates, using $N = 300$ particles. Note the logarithmic scales on both the horizontal and the vertical axis.

is that the present model of antiferromagnetic spin-1 BECs is expected to accurately describe actual experimental systems [25, 26]. In the antiferromagnet case, the staggered magnetic field is a theoretical object that cannot be produced in the laboratory for real solids. In contrast, the QZ energy is easily controllable in spin-1 BEC experiments. Another important difference is that experiments with ultracold quantum gases are typically conducted with relatively small atom numbers, from $N \sim 10^2$ to 10^6, so that the conclusions that hold in the thermodynamic limit do not necessarily apply and spin fragmentation can be observed experimentally.

The paper is organized as follows. In section 2, we present the basic model that describes an ensemble of spin-1 bosons with antiferromagnetic interactions condensing in the same orbital wave function irrespective of the internal state (single-mode approximation (SMA)). In section 3, we use the basis of total spin eigenstates (exact in the absence of an applied magnetic field, $q = 0$). We derive approximate solutions for the spectrum and eigenstates for $q > 0$ in section 3.1, and discuss how they evolve with increasing QZ energy. By using these results, we compute in section 4 the average value and variance of N_0 at finite temperatures, and compare the approximate solution to numerical diagonalization of the Hamiltonian. We finally present in section 5 an alternative approach, where the fragmented condensate is described as a statistical

mixture of mean-field (symmetry broken) states. We find excellent agreement with the exact diagonalization of the Hamiltonian.

2. Single-mode description of spin-1 condensates

We consider a gas of ultracold spin-1 bosons in a trap with Zeeman components $m = -1, 0$ or +1. We discuss the case of antiferromagnetic interactions and assume the validity of the SMA, i.e. that all bosons condense in the same spatial orbital irrespective of their internal state [27]. The Hamiltonian is [28]

$$\hat{H} = \frac{U_s}{2N}\hat{\mathbf{S}}^2 - q\hat{N}_0, \tag{1}$$

where $U_s > 0$ is the spin interaction energy per atom[5], $q > 0$ is the QZ energy, $\hat{\mathbf{S}}$ is the total spin operator and $\hat{N}_\alpha$ is the number operator in Zeeman state α. We assume that the number of atoms N is even for simplicity. Odd values of N could be treated in a similar way, without modifying the final results to order $1/N$. Typical experimental values for the parameters of the SMA model are $N = 10^3$–10^5, $U_s/k_B \sim 2$–5 nK, while q can be varied from zero to values much larger than U_s by changing the magnetic field [25, 26].

In the absence of an external magnetic field ($q = 0$), the Hamiltonian reduces to a quantum rotor with moment of inertia N/U_s [5, 11]. The energy eigenstates are thus simply the total spin eigenstates $|N, S, M\rangle$, with S the spin quantum number and M its projection on the z-axis. The corresponding eigenvalues are $E(S) = (U_s/2N)S(S+1)$, with a degeneracy $2S+1$. The wave functions for these states are known explicitly in the Fock basis [2, 5, 6] (see also appendix A).

When $q \neq 0$, since $[\hat{S}_z, \hat{N}_0] = 0$, the magnetic quantum number M (eigenvalue of $\hat{S}_z$) remains a good quantum number. One can diagonalize $\hat{H}$ by block in each M sector. For each M, the energy eigenstates can be expressed in the angular momentum basis

$$|\phi_M\rangle = \sum_{S=|M|}^{N} c_{S,M}|N, S, M\rangle. \tag{2}$$

To express the Hamiltonian in (1) in the $|N, S, M\rangle$ basis, we need to compute the action of $\hat{N}_0$. The non-vanishing matrix elements of $\hat{N}_0$ are $\langle N, S, M\,|\hat{N}_0|N, S, M\rangle$, $\langle N, S\pm 2, M|\,\hat{N}_0|N, S, M\rangle$ (see appendix A). The Schrödinger equation then takes the form of a tridiagonal matrix equation

$$h^M_{S,S+2}c_{S+2,M} + h^M_{S,S-2}c_{S-2,M} + h^M_{S,S}c_{S,M} = Ec_{S,M} \tag{3}$$

with E the energy eigenvalue and where the coefficients $h^M_{S,S'}$ are easily obtained from the expressions given in appendix A.

3. Spectrum and eigenstates for $M = 0$

A first approach for finding the spectrum and eigenstates is to diagonalize numerically the matrix h^M in (3). Our goal in this section is to propose an analytical approximation to better understand the structure of the spectrum and the eigenstates. The discussion allows one to describe how the

[5] The spin interaction energy U_s can be calculated from $U_s = g_s \int d\mathbf{x}|\psi(\mathbf{x})|^4$, where $\psi(\mathbf{x})$ is the spatial orbital of the condensate.

ground state evolves with q, and will also be useful to understand qualitatively the behavior of the systems at finite temperatures later in this paper. For simplicity, we focus in this section on the $M = 0$ sector. The conclusions we obtain remain qualitatively correct for $M \neq 0$ provided its value is not too large ($|M| \ll N$).

3.1. Continuum approximation for large q

We make the assumption that the thermodynamic behavior is dominated by states, such that the dominant coefficients in the $|N, S, M\rangle$ basis obey $1 \ll S \ll N$. As we will see later in this paper, this assumption is justified for large enough q at $T = 0$, and for any q at finite temperatures $k_B T \gg U_s/N$. In this limit, the matrix elements $h_{S,S}$, $h_{S,S\pm2}$ can be simplified. We obtain to lowest order in $1/S$, S/N (see appendix B)

$$-J(x+\epsilon)c(x+\epsilon) - J(x-\epsilon)c(x-\epsilon) + \frac{NU_s}{2}x^2 c(x) = \left(E + \frac{Nq}{2}\right) c(x), \tag{4}$$

where we have set $x = S/N$, $\epsilon = 2/N$, $c(x) = c_{S,0}$. This equation maps the spin problem to a tight-binding model for a particle hopping on a lattice, with an additional harmonic potential keeping the particle near $x = 0$. The model is characterized by an inhomogeneous tunneling parameter $J(x) = Nq\,(1 - x^2/2)/4$ and a harmonic potential strength NU_s. Boundary conditions confine the particle to $0 \leqslant x \leqslant 1$.

If $c(x)$ changes smoothly as a function of x, the tight-binding model can be further simplified in a continuum approximation. We show in appendix B that the tight-binding equation reduces to the one for a fictitious one-dimensional harmonic oscillator

$$-\frac{q}{N}c''(x) + \frac{N}{4}(q + 2U_s)\,x^2 c(x) = (E + Nq)\,c(x). \tag{5}$$

The boundary condition $c(0) = 0$ selects the eigenstates of the standard harmonic oscillator with odd parity. The mass m and oscillation frequency ω of the fictitious oscillator are found from $\hbar^2/2m \equiv q/N$ and $m\omega^2 \equiv N(q + 2U_s)/2$. The oscillator frequency is thus

$$\hbar\omega = \sqrt{q(q + 2U_s)}. \tag{6}$$

This collective spectrum was also obtained by the Bogoliubov approach of [10, 12].

3.2. Ground state

In this section, we use the results established previously to examine the evolution of the ground state with increasing q. Our results reproduce the ones from [12] obtained by using a different method. The ground state of the truncated fictitious harmonic oscillator (with boundary condition $c_0(0) = 0$) is given by

$$c_0(x) = \frac{1}{\pi^{1/4}\sigma^{1/2}}\frac{x}{\sigma}\exp\left(-\frac{x^2}{2\sigma^2}\right) \tag{7}$$

with the quantum harmonic oscillator size

$$\sigma = \sqrt{\frac{\hbar}{m\omega}} = \sqrt{\frac{2}{N}}\left(\frac{q}{q + 2U_s}\right)^{1/4}. \tag{8}$$

The continuum approximation is valid only if $c(x)$ varies smoothly on the scale of the discretization step ϵ, or equivalently when $\sigma \gg 1/N$. This gives the validity criterion for this approximation

$$q \gg \frac{U_s}{N^2}. \tag{9}$$

For $q < U_s/N^2$, the ground state is very close to the singlet state, with a width $\sigma \ll 1/N$. Here, spin fragmentation occurs purely due to quantum spin fluctuations (related to antiferromagnetic interactions) of a polar BEC. We indicate this state in figure 1 as 'quantum spin fragmented'.

For $q \gg U_s/N^2$, the continuum approximation is valid. We see from (8) that as q increases, the QZ energy mixes an increasing number of S states. Asymptotically, for $q \gg U_s$, the true ground state is a superposition of $\sim N\sigma \approx \sqrt{2N}$ total spin eigenstates. In this regime, we can compute the moments of N_0 by expressing the depletion operator $N - \hat{N}_0$ in terms of the ladder operators $\hat{b}$ and $\hat{b}^\dagger$ associated with the fictitious harmonic oscillator. We find

$$N - \langle N_0 \rangle = \frac{U_s + q}{2\sqrt{q(q+2U_s)}}, \tag{10}$$

$$\Delta N_0^2 = \frac{U_s^2}{2q(q+2U_s)}. \tag{11}$$

For $U_s/N^2 \ll q \ll U_s$, the depletion $N - \langle N_0 \rangle$ and variance ΔN_0^2 are larger than unity but small compared to N, N^2, respectively, while for $q \gg U_s$, they become less than one particle: in the latter case, the ground state approaches the Fock state $(\hat{a}_0^\dagger)^N|\text{vac}\rangle$ expected from the mean field theory. We indicate both regimes as 'BEC $m = 0$' in figure 1, without marking the distinction.

3.3. Excited states for $M = 0$

We now turn to the description of the excited states, still limiting ourselves to the case $M = 0$ for simplicity. The tight-binding model (4) is characterized by a tunneling parameter $J = Nq(1 - x^2/2)/4$ and a harmonic potential strength $\kappa = NU_s$. Let us examine two limiting cases. For $q = 0$ (no hopping), the energy eigenstates coincide with the 'position' eigenstates with energy $E(S) \approx (U_s/2N)S^2$ for $S \gg 1$. Conversely, when $U_s = 0$ the energy eigenstates are delocalized states, which form an allowed energy band of width $\sim 4J \sim Nq$. The weak inhomogeneity of the tunneling parameter does not play a large role since these states are confined near $x = 0$ by the harmonic potential.

For the general case where $J, \kappa \neq 0$, the eigenstates can be divided into two groups [29, 30]:

- low-energy states with energy $E < 4J$, which are extended 'Bloch-like' states modified by the harmonic potential; the continuum approximation introduced earlier corresponds to an effective mass approximation, valid for low-energy states with $E \ll 4J = Nq$ (the requirement $q \gg U_s/N^2$ found before still holds); and
- high-energy states with $E \gg 4J$, that would be in the band gap in the absence of the potential energy term (and thus forbidden). They are better viewed as localized states, peaked around $x(E) \approx \sqrt{2E/NU_s}$ with a width $\sim 1/N$. As a result, they are very similar to the angular momentum eigenstates $|N, S, 0\rangle$ for the corresponding value of S. For these states, the continuum approximation does not hold.

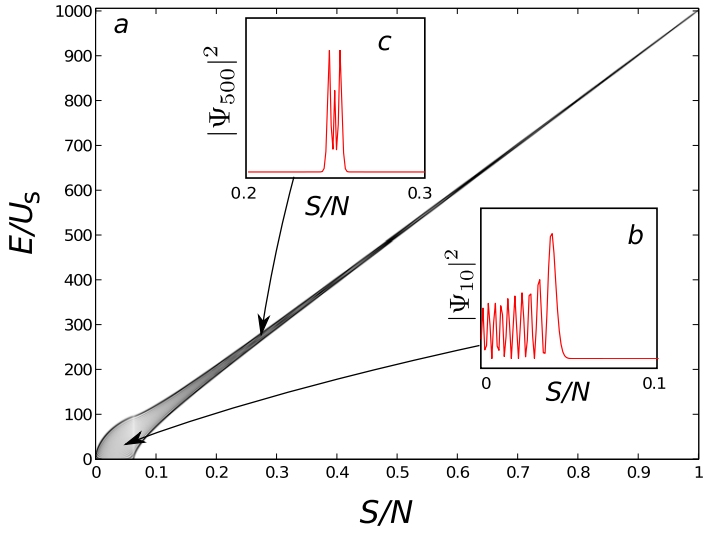


Figure 2. Probability densities (amplitude shown as gray scale) of the eigenstates of the spin-1 Hamiltonian (1) as a function of 'position' $x = S/N$ and energy E/U_s. The plot corresponds to $N = 2000$ and $Nq/U_s = 10$. At low energy, the eigenstates explore the whole available region, from the turning point down to $x = 0$. Conversely, at high energies, the eigenstates are more and more localized around the diagonal, as expected for potential energy eigenstates. We show as insets the probability densities for the 10th (b) and 500th (c) excited states for illustration.

We illustrate this classification in figure 2, where we show the probability densities $|c(S)|^2$ as a function of energy. One can see the change from a 'delocalized' regime at small energies to a 'localized' regime at large energies. The wave functions were calculated exactly by diagonalizing the Hamiltonian for $N = 1000$. We also show the corresponding energy spectrum in figure 3, showing the same crossover from delocalized states at low energies to localized states at high energies. For low energies, the spectrum is given by the harmonic oscillator model, $\epsilon_n \approx \hbar\omega(2n + 3/2)$ with n integer. For high energies, the energy eigenstates are localized around $x_n = n/N$, with a spectrum given by $\epsilon_n \approx U_s n^2/2N$ with n integer. Both expressions agree well with the numerical result in their respective domains of validity.

4. Spin fragmentation at finite temperatures

We have seen in section 3.2 that for a system in its ground state, the depletion and fluctuations of the $M = 0$ state were rapidly collapsing as q was increased above U_s/N^2, and the system turned from a fragmented to a single condensate with all the atoms in the Zeeman state $m = 0$. The energy gap to the first excited state is $3U_s/N$ near $q = 0$. For typical experimental values [25, 26], this corresponds to a few pK, vastly smaller than realistic temperatures for a typical experiment (a few tens of nK) due to the $1/N$ scaling. Therefore, it is natural to ask how the crossover from a fragmented to a single condensate is modified at finite temperatures. In the remainder of the paper, we thus consider the high temperature case $k_B T \gg U_s/N$. We will compute the first two moments of N_0 at finite temperatures, $\langle N_0\rangle_T$ and $(\Delta N_0^2)_T = \langle N_0^2\rangle_T - \langle N_0\rangle_T^2$, and use these quantities to study the fragmented to single condensate crossover.

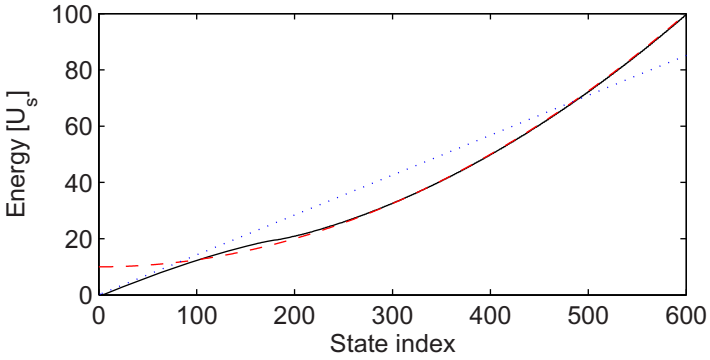


Figure 3. Energy spectrum for $N = 2000$ and $Nq/U_s = 10$. The black solid line is the spectrum calculated by numerical diagonalization of the Hamiltonian (1), shifted up by qN. The red dashed line corresponds to $E(S) = (U_s/2N)S^2 + qN/2$, the blue dotted line to the harmonic oscillator approximation.

4.1. Spin fragmentation for $q = 0$

Let us first consider the case $q = 0$. An important remark is that super-Poissonian fluctuations are not unique to the ground state, but also occur for low-energy eigenstates with $S \ll N$. This is best seen by considering values of S such that $1 \ll S \ll N$. In this limit, we find

$$\langle \hat{N}_0 \rangle_{SM} \approx (N^2 - S^2)(S^2 - M^2)/8, \tag{12}$$

$$\langle \hat{N}_0^2 \rangle_{SM} \approx (3N^2 - S^2)(S^2 - M^2)^2/8, \tag{13}$$

$$(\Delta N_0^2)_{SM} \approx (N^2 - S^2)(S^2 - M^2)^2/8, \tag{14}$$

where $\langle \hat{N}_0^p \rangle_{SM} = \langle N, S, M \mid N_0^{\mathrm{p}} \mid N, S, M \rangle$. Hence, we find super-Poissonian fluctuations for $M \ll S \ll N$, which eventually vanish as S (resp. M) increases to its maximum value N (resp. S).

We calculate now the thermally averaged $\langle n_0 \rangle_T$ and $(\Delta n_0^2)_T$ in the canonical ensemble. The average population in $m = 0$ is given by

$$\langle N_0 \rangle_T = \frac{1}{Z} \sum_{S,M} \mathrm{e}^{-\beta' S(S+1)} \langle N_0 \rangle_{SM}. \tag{15}$$

The second moment $\langle N_0^2 \rangle_T$ and the variance $(\Delta N_0^2)_T$ are given by similar expressions. Here, Z is the partition function and $\beta' = U_s/2Nk_BT$. Assuming that the temperature is large compared to the level spacing ($k_BT \gg U_s/N$), the thermodynamic sums over energy levels is dominated by states with large $S \gg 1$. There are two regimes to consider.

At intermediate temperatures, states with $1 \ll S \ll N$ dominate the thermodynamics. To calculate the thermal average over all S in this regime, we replace the discrete sums by integrals and send the upper bound N of the integral to infinity. A simple estimate of the mean value of S, $\langle S \rangle \sim (Nk_BT/U_s)^{1/2}$, shows that the condition $1 \ll S \ll N$ corresponds to the boundaries

$$\frac{U_s}{N} \ll k_BT \ll NU_s. \tag{16}$$

In this regime, we find

$$\langle N_0\rangle_T \approx \frac{N}{3}, \tag{17}$$

$$(\Delta N_0^2)_T = \langle N_0^2\rangle_T - \langle N_0\rangle_T^2 \approx \frac{4N^2}{45}, \quad k_B T \ll N U_s. \tag{18}$$

We note that to the leading order in $1/N$, the moments of N_0 are identical for those found in the singlet state.

The second regime arises when the temperature becomes very large ($k_B T/NU_s > 1$), where one expects the sum to saturate due to the finite number of states. In this limit, the upper bound of the integral cannot be taken to infinity, and one must take the restriction $S \leqslant N$ into account. On the other hand, the Boltzmann factor can be replaced by unity, and the sums can then be calculated analytically. One finds

$$(\Delta N_0^2)_{T\gg NU_s} \approx N^2/18. \tag{19}$$

To summarize (see figure 1), for $q = 0$ we always find large depletion and super-Poissonian fluctuations ($\Delta N_0^2 \sim \langle N_0\rangle^2$). The average population is always $N/3$ as expected from the isotropy of the Hamiltonian. The relative standard deviation remains approximately constant (to order N) at the value $\Delta N_0/N \approx 2/3\sqrt{5} \approx 0.298$ for $k_B T \ll NU_s$, and changes to $1/3\sqrt{2} \approx 0.236$ for very large temperatures $k_B T > NU_s$ where all the states are occupied with equal probability.

4.2. Bogoliubov approximation for $q \neq 0$

For large $q > 0$ (and $\langle S_z\rangle$ constrained to vanish only in average), we expect that the system will form a condensate in the $m = 0$ Zeeman state, with small fluctuations. Such a system can be described in the Bogoliubov approximation (as described in the appendix of [12]), which extends to any M the harmonic oscillator approximation made earlier for the $M = 0$ sector. One sets $\hat{a}_0 \approx \sqrt{N_0}$, and expresses the fluctuations $\hat{a}_{\pm1}$ in terms of new operators $\hat{\alpha}^{\pm}$,

$$\hat{\alpha}_{\pm} = u\hat{a}_{\pm1} - v\hat{a}_{\mp1}^{\dagger}. \tag{20}$$

Here, the Bogoliubov amplitudes u, v defined by

$$u \pm v = \left(\frac{q}{2U_s + q}\right)^{\pm 1/4} \tag{21}$$

are chosen to put the Hamiltonian in diagonal form

$$H_{\text{Bogo}} = \sum_{\mu=\pm} \hbar\omega \left(\hat{\alpha}_{\mu}^{\dagger}\hat{\alpha}_{\mu} + \frac{1}{2}\right) - (g + q). \tag{22}$$

The energy $\hbar\omega$ of the Bogoliubov mode is identical to the one previously found in the harmonic oscillator approximation for $M = 0$ (equation (6)). Note that we have now two such modes (instead of only one in the case $M = 0$).[6]

[6] We expect, in general, three modes of excitations for a spin-1 system. When the constraint of constant particle number is taken into account, this reduces the number of modes to two. The suppressed mode would correspond to the density fluctuations in an extended system, and is explicitly ruled out by the SMA. When a further constraint $M = 0$ is imposed, another mode is canceled—corresponding to magnetization fluctuations which are explicitly forbidden, thus leaving only one excitation mode.

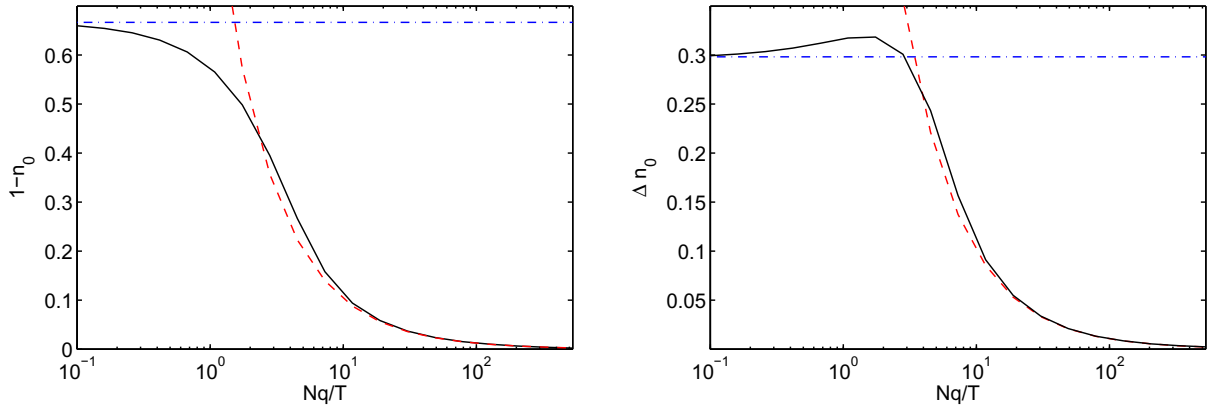


Figure 4. Depletion (left) and standard deviation (right) of N_0. The solid line shows the exact numerical result for $N = 1000$ and $T = 10U_s$, the blue dash-dotted line is the result calculated for $q = 0$ by using equations (17), (18) and the red dashed line shows the Bogoliubov approximation. Deviations are observed for $q/T \sim N$ (not visible at the scale of the figure), which is expected from our approximation: this regime corresponds to a depletion of one atom or less, and corrections $\propto 1/N$ that we neglect become important.

In the Bogoliubov approximation, the moments of N_0 can be obtained analytically. The quantum ($T = 0$) depletion of N_0 is smaller than one atom. The thermal part of the depletion and variance of $n_0 = N_0/N$ read for $k_B T \gg \hbar\omega$:

$$1 - \langle n_0 \rangle = \frac{2(U_s + q)}{q + 2U_s} \frac{k_B T}{Nq}, \tag{23}$$

$$\Delta n_0^2 = \frac{2\left[(U_s + q)^2 + U_s^2\right]}{(q + 2U_s)^2} \left(\frac{k_B T}{Nq}\right)^2. \tag{24}$$

The prefactors take values of order unity, and both the depletion $1 - \langle n_0 \rangle$ and standard deviation Δn_0 scale as $k_B T/Nq$. The above expressions are valid provided they describe small corrections to a regular polar condensate where almost all the atoms accumulate in $m = 0$ ($\langle n_0 \rangle = 1$), or in other words for temperatures

$$k_B T \ll Nq. \tag{25}$$

4.3. Comparison between the different approximations

We compare in figure 4 the predictions for the moments of N_0 obtained from the various approximations discussed in the paper, Bogoliubov approximation and $q = 0$ limit. These approximations are compared to the results obtained by diagonalization of the original Hamiltonian (1) and computing thermodynamic averages by using the exact spectrum and eigenstates.

When $Nq/k_B T \ll 1$, the localized states of section 3.3, which are dominated by their potential energy, will be populated. Since these localized states are close to the angular momentum eigenstates found in the $q = 0$ limit, to a good approximation the formula derived in section 4.1 (see (17), (18) and the continuous blue line in figure 4). On the other hand,

for $Nq/k_BT \gg 1$, thermal states mostly populate states with $E \sim qN$, i.e. 'delocalized' states within the low-energy 'Bloch band' of width $\sim Nq$. Those states correspond to small depletion and fluctuations, and they are well described by the Bogoliubov approximation presented in section 4.2 (see (23), (24) and the red dashed line in figure 4). The numerical solution of the original model (3) interpolates between the two well-defined asymptotic limits, either a thermal mixture of total spin eigenstates for $q \ll k_BT/N$ or a thermal state of Bogoliubov-like excitations for $q \gg k_BT/N$.

We note to conclude this section that in the regime $U_s/N \ll k_BT \ll NU_s$, the tight-binding model defined in equation (3) has a quasi-universal form at finite temperatures, in the sense that the model is entirely specified by two dimensionless parameters, for instance k_BT/U_s and Nq/U_s. We found that the physical quantities $\langle N_0\rangle$, (ΔN_0) depend only on their ratio Nq/k_BT, to a very good approximation. This quasi-universality, which can be explored by experiments, will be easily justified in the broken symmetry approach presented in the next section.

5. Comparison with the broken-symmetry picture

So far, we have treated the problem by the most natural method, by looking for the eigenspectrum of the Hamiltonian. Another approach [2, 3] to the problem of spin 1 bosons with antiferromagnetic interactions relies on the set of so-called polar or spin-nematic states, defined as

$$|N : \mathbf{\Omega}\rangle = \frac{1}{\sqrt{N!}} \left(\mathbf{\Omega} \cdot \hat{\mathbf{a}}\right)^N |\mathrm{vac}\rangle, \tag{26}$$

where the vector $\mathbf{\Omega}$ reads in the standard basis

$$\mathbf{\Omega} = \mathrm{e}^{\mathrm{i}\gamma} \begin{pmatrix} \frac{1}{\sqrt{2}} \sin(\theta)\mathrm{e}^{\mathrm{i}\phi} \\ \cos(\theta) \\ -\frac{1}{\sqrt{2}} \sin(\theta)\mathrm{e}^{-\mathrm{i}\phi} \end{pmatrix}. \tag{27}$$

For a single particle, the states $|\mathbf{\Omega}\rangle = \sum_{i=0,\pm1} \Omega_i |m = i\rangle$ form a continuous family of spin 1 wave functions with vanishing average spin. In fact, $|\mathbf{\Omega}\rangle$ is the eigenvector with zero eigenvalue of the operator $\mathbf{\Omega} \cdot \hat{\mathbf{s}}$, with $\hat{\mathbf{s}}$ the spin 1 operator. The states $|N : \mathbf{\Omega}\rangle$ correspond to a many-body wave function where all the particles occupy the single-particle state $|\mathbf{\Omega}\rangle$. As a result, one has $\langle N : \mathbf{\Omega}|\hat{\mathbf{S}}|N : \mathbf{\Omega}\rangle = 0$.

5.1. Zero temperature

It is interesting to connect the spin nematic states to the angular momentum eigenstates. The spin nematic states form an overcomplete basis of the bosonic Hilbert space. On writing the states $|N, S, M\rangle$ in this basis, one finds [2, 3, 12]

$$|N, S, M\rangle \propto \int \mathrm{d}\mathbf{\Omega}\, Y_{S,M}(\mathbf{\Omega}) |N : \mathbf{\Omega}\rangle, \tag{28}$$

where Y_{SM} denotes the usual spherical harmonics and where $\mathrm{d}\mathbf{\Omega} = \sin(\theta)\mathrm{d}\theta\, \mathrm{d}\phi$. In particular, the singlet ground state $|N, 0, 0\rangle$ appears to be a coherent superposition with equal weights

of the nematic states. Consider now the average value in the singlet state $\langle \hat{O}_k \rangle_{\text{singlet}} = \langle N, 0, 0 | \hat{O}_k | N, 0, 0 \rangle$ of a k-body operator $\hat{O}_k$,

$$\langle \hat{O}_k \rangle_{\text{singlet}} = \frac{1}{4\pi} \int \mathrm{d}\mathbf{\Omega}\, \mathrm{d}\mathbf{\Omega}' \langle N : \mathbf{\Omega}' | \hat{O}_k | N : \mathbf{\Omega} \rangle. \tag{29}$$

As shown in [2], for a few-body operators with $k \ll N$ this expectation value can be approximated to order $1/N$ by the much simpler expression

$$\langle \hat{O}_k \rangle_{\text{singlet}} \approx \frac{1}{4\pi} \int \mathrm{d}\mathbf{\Omega} \langle N : \mathbf{\Omega} | \hat{O}_k | N : \mathbf{\Omega} \rangle. \tag{30}$$

This approximation shows that the system can be equally well described by a statistical mixture of spin-nematic states described by the density matrix [2, 3]

$$\hat{\rho}_{\text{BS}} = \frac{1}{4\pi} \int \mathrm{d}\mathbf{\Omega} | N : \mathbf{\Omega} \rangle \langle N : \mathbf{\Omega} |. \tag{31}$$

At zero temperature and zero field, there is no preferred direction for the vector $\mathbf{\Omega}$ so that each state can appear with equal probability. This approach is known as a 'broken symmetry' point of view, where one can imagine that the atoms condense in the same spin state for each realization of the experiment, but this spin state fluctuates arbitrarily from one realization to the next. The important point is that the overlap integral $\langle N : \mathbf{\Omega}' | N : \mathbf{\Omega} \rangle$ between two spin-nematic states vanishes very quickly with the distance $|\mathbf{\Omega} - \mathbf{\Omega}'|$. This allows one to use the approximation $\langle N : \mathbf{\Omega}' | N : \mathbf{\Omega} \rangle \approx 4\pi \delta(\mathbf{\Omega} - \mathbf{\Omega}') + \mathcal{O}(1/N)$, which leads to

$$\langle \hat{O}_k \rangle_{\text{BS}} = \text{Tr}[\hat{\rho}_{\text{BS}} \hat{O}_k] \approx \langle \hat{O}_k \rangle_{\text{singlet}} + \mathcal{O}(1/N). \tag{32}$$

This result can be written as a general statement concerning the average values of a few-body observables with $k \ll N$ [2]: to the leading order in $1/N$, the exact and broken symmetry approaches will give the same results after averaging over the ensemble. The differences between the two approaches are subtle and vanish in the thermodynamic limit as $1/N$.

It is worth noting the difference between individual states and the ensemble. The moments of N_0 in the state $|N : \mathbf{\Omega}\rangle$ are given by

$$\langle N : \mathbf{\Omega} | \hat{N}_0 | N : \mathbf{\Omega} \rangle = N u^2,$$

$$\langle N : \mathbf{\Omega} | \hat{N}_0^2 | N : \mathbf{\Omega} \rangle = N(N-1)u^4 + N u^2,$$

where $u = \cos(\theta)$. The variance of N_0 for a system prepared in a single spin-nematic state, $Nu^2(1-u^2)$, is thus Poissonian, as expected for a regular condensate. On the other hand, computing the ensemble averages over $\hat{\rho}_{\text{BS}}$ gives

$$\langle N_0 \rangle = N \int_0^1 \mathrm{d}u\, u^2 = \frac{N}{3},$$

$$\langle N_0^2 \rangle = \int_0^1 \mathrm{d}u \left(N(N-1)u^4 + N u^2 \right) = \frac{3N^2 + 2N}{15},$$

$$\Delta N_0^2 = \frac{4N^2 + 6N}{45}.$$

The variance in the ensemble is thus super-Poissonian, and differs from the result in the exact ground state only by the sub-leading term $\propto N$. This is in agreement with the general statement made above.

5.2. *Moments of N_0 at finite temperatures*

We now extend the broken symmetry approach summarized above to finite temperatures. The density matrix should include a weight factor proportional to the energy of the states $|N:\Omega\rangle$. To the leading order in $1/N$, these states have zero interaction energy[7] and a mean QZ energy given by $-Nq\cos^2(\theta)$. In the spirit of the mean-field approximation, we replace the Boltzmann factor by its mean value and write the density matrix as

$$\hat{\rho}_{\mathrm{BS}} \approx \frac{1}{\mathcal{Z}} \int \mathrm{d}\boldsymbol{\Omega} |N:\boldsymbol{\Omega}\rangle\langle N:\boldsymbol{\Omega}| \mathrm{e}^{N\beta q \Omega_z^2} \tag{33}$$

with $\beta = 1/k_{\mathrm{B}}T$. The partition function can then be expressed as

$$\mathcal{Z} = \int_0^{2\pi} \mathrm{d}\phi \int_0^{\pi} \sin(\theta)\mathrm{d}\theta \; \mathrm{e}^{N\beta q \cos^2(\theta)} = 2\pi F_{-1/2}(N\beta q)\,. \tag{34}$$

Here, we introduced the family of functions

$$F_\alpha(y) = \int_0^1 x^\alpha \, \mathrm{e}^{yx} \, \mathrm{d}x, \tag{35}$$

which are related to the lower incomplete gamma functions. In a similar way, we can compute the moments of $n_0 = N_0/N$ to the leading order in N as

$$\langle n_0^m \rangle = \frac{F_{m-1/2}(N\beta q)}{F_{-1/2}(N\beta q)}. \tag{36}$$

From this result, one can easily deduce the average and variance of n_0. This calculation provides an explicit proof of the numerical evidence that, to the leading order in N, the moments of N_0 obey a universal curve depending only on $Nq/k_{\mathrm{B}}T$ and not on q/U_{s} or T/U_{s} separately.

From the properties of the functions F_α, we recover the results established in the previous section. When $x \to 0$, one finds $F_\alpha(x) \sim 1/(\alpha+1)$ and $\langle n_0^m \rangle \sim 1/(2m+1)$. By using this result we recover for $q = 0$ the previous results, i.e. $\langle n_0 \rangle = 1/3$ and $\Delta n_0^2 = 4/45$. When $x \to \infty$, $F_\alpha(x) \sim \mathrm{e}^x/x \times [1 - \alpha/x + \alpha(\alpha-1)/x^2]$. This leads to the asymptotic behavior $\langle n_0^m \rangle \sim 1 - m/(N\beta q) + m(m-3/2)/(N\beta q)^2 + \cdots$ when $N\beta q \gg 1$, which reproduces the Bogoliubov results (23), (24) for $q \ll U_{\mathrm{s}}$.[8]

We finally compare, in figure 5, the results from the broken symmetry approach to the results obtained by diagonalizing the Hamiltonian (1). We find excellent agreement between the two in the regime of thermal fragmentation, supporting the picture of mean-field states with random orientation fluctuating from one realization to the next. We note that the ansatz (33) for the density matrix is by no means obvious, and the good agreement with the numerical results is obtained only because the set of polar states is a good description for sufficiently

[7] Explicitly, one has $\langle N:\boldsymbol{\Omega}|\hat{\mathbf{S}}^2|N:\boldsymbol{\Omega}\rangle = N(1+\cos^2(\theta))$, so that the interaction energy of the state $|N:\boldsymbol{\Omega}\rangle$ is given by $U_{\mathrm{s}}\cos^2(\theta) \sim \mathcal{O}(1)$ compared to the QZ energy $\sim \mathcal{O}(N)$. The same argument applies to the off-diagonal matrix elements $\langle N:\boldsymbol{\Omega}'|\hat{\mathbf{S}}^2|N:\boldsymbol{\Omega}\rangle$.

[8] For $q \gg U_{\mathrm{s}}$, the depletion and standard deviation of $\hat{n}_0$ are of the order $1/N$, of the same order as the error made by using the broken symmetry approach.

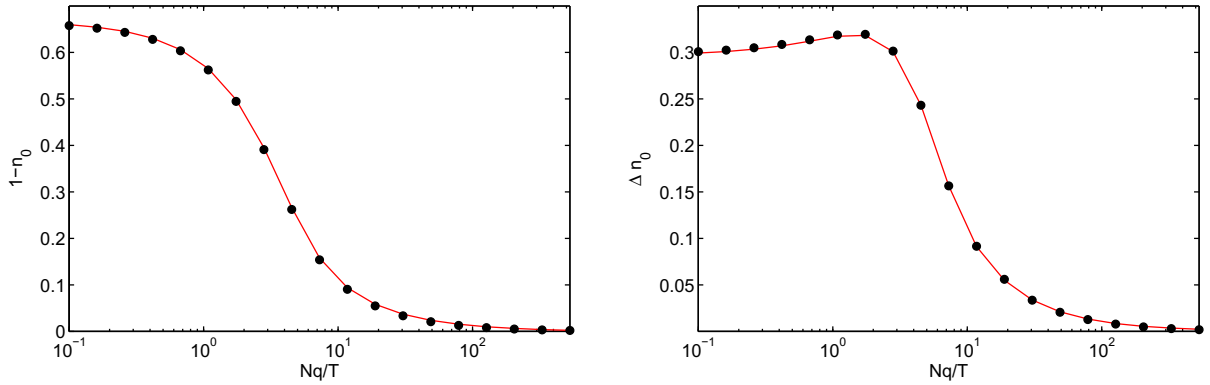


Figure 5. Exact diagonalization (red solid line) versus broken symmetry approach (black dots) for $N = 1000$, $k_B T/U_s = 10$.

low temperatures: although these states are not true eigenstates of the Hamiltonian (1), the action of $\hat{H}$ yields off-diagonal matrix elements scaling as $1/N$ [31], and thus vanishing in the thermodynamic limit. At high temperatures ($k_B T \sim N U_s$), where all the high-energy states are populated the broken-symmetry ansatz is no longer adequate.

6. Conclusion

We have studied the properties of an ensemble of antiferromagnetic spin-1 bosons with QZ energy breaking the spin rotational symmetry. The system evolves with increasing QZ energy from a super-fragmented condensate with large fluctuations to a regular polar condensate where the atoms condense in $m = 0$. We focused, in particular, on the behavior of a thermal mixture of excited states, and discussed the evolution of the moments of N_0 with increasing q. Two approaches were explored, one relying on the diagonalization of the Hamiltonian (either exactly or approximately in certain parameter regimes), and the other relying on a broken symmetry picture where the system is described as a statistical mixture of degenerate polar condensates. Both approaches were found in remarkable agreement. In this paper, we focused on the equilibrium properties and assumed thermal equilibrium from the start. An interesting question is how the physical system (i.e. also including the dynamics of non-condensed modes not described in the SMA) can reach such an equilibrium state, e.g. following a quench in q [32]. This problem, which can be linked to the more general question of thermalization of closed quantum systems [33], provides an interesting direction for future work.

Acknowledgments

We acknowledge discussions with members of the LKB, in particular Yvan Castin. This work was supported by IFRAF, by Ville de Paris (Emergences project) and by DARPA (OLE project).

Appendix A. Total spin eigenstates

The general expression of the states $|N, S, M\rangle$ in the Fock basis is

$$|N, S, M\rangle = \frac{1}{\sqrt{\mathcal{N}}}(\hat{S}^{(-)})^P(\hat{A}^\dagger)^Q(\hat{a}_{+1}^\dagger)^S|\text{vac}\rangle. \tag{A.1}$$

Here, $P = S - M$, $2Q = N - S$, $\hat{S}_-$ is the spin lowering operator and $\hat{A}^\dagger = \hat{a}_0^\dagger - 2\hat{a}_{-1}^\dagger\hat{a}_{+1}^\dagger$ is the singlet creation operator. The two operators commute. The normalization constant reads

$$\mathcal{N} = \frac{S!(N-S)!!(N+S+1)!!(S-M)!(2S)!}{(2S+1)!!(S+M)!}, \tag{A.2}$$

where !! indicates a double factorial.

The action of $\hat{a}_0$ on the angular momentum eigenstates is

$$\hat{a}_0|N, S, M\rangle = \sqrt{A_-(N, S, M)}|N-1, S-1, M\rangle + \sqrt{A_+(N, S, M)}|N-1, S+1, M\rangle, \tag{A.3}$$

where $\hat{a}_0$ is the annihilation operator of a boson in the Zeeman state $m = 0$, and where the coefficients $A_\pm$ are given by

$$A_-(N, S, M) = \frac{(S^2 - M^2)(N+S+1)}{(2S-1)(2S+1)}, \tag{A.4}$$

$$A_+(N, S, M) = \frac{((S+1)^2 - M^2)(N-S)}{(2S+1)(2S+3)}. \tag{A.5}$$

The non-zero matrix elements of $\hat{N}_0$ are

$$\langle S|\hat{N}_0|S\rangle = (A_+(N, S, M) + A_-(N, S, M)), \tag{A.6}$$

$$\langle S+2|\hat{N}_0|S\rangle = \sqrt{A_-(N, S+2, M)A_+(N, S, M)}, \tag{A.7}$$

$$\langle S-2|\hat{N}_0|S\rangle = \sqrt{A_+(N, S-2, M)A_-(N, S, M)}, \tag{A.8}$$

where we abbreviated the notation for the state $|N, S, M\rangle$ as $|S\rangle$ to simplify the notation. We then obtain the matrix elements of $\hat{H}_0$ in the $|N, S, M\rangle$ basis as

$$h_{S,S}^M = \frac{U_s}{2N}S(S+1) - q\langle S|\hat{N}_0|S\rangle, \tag{A.9}$$

$$h_{S,S+2}^M = -q\langle S+2|\hat{N}_0|S\rangle, \tag{A.10}$$

$$h_{S,S-2}^M = -q\langle S-2|\hat{N}_0|S\rangle. \tag{A.11}$$

Appendix B. Continuum approximation

We expand the matrix elements $h_{S,S}$, $h_{S,S\pm2}$ to the first order in $1/S$, S/N, M^2/S^2, and obtain

$$h^M_{S,S\pm2} \approx \frac{N}{4}\left[1-\frac{M^2}{(S\pm1)^2}\right]-\frac{1}{8N}\left[(S\pm1)^2-M^2\right], \tag{B.1}$$

$$h^{M\neq0}_{S,S} \approx \frac{N}{2}\left(1-\frac{M^2}{S^2}\right), \quad h^{M=0}_{S,S} \approx \frac{N}{2}. \tag{B.2}$$

For $M=0$, we obtain

$$-\frac{Nq}{4}\left[\left(1-\frac{(x+\epsilon)^2}{2}\right)c_{S+2}+\left(1-\frac{(x-\epsilon)^2}{2}\right)c_{S-2}\right]+\frac{NU_s}{2}x^2c_S=\left(E+\frac{Nq}{2}\right)c_S, \tag{B.3}$$

where we have set $x=S/N$ and $\epsilon=2/N$. We now take the continuum limit, where $\epsilon\ll1$ is taken as a discretization step and c_s becomes a continuous function $c(S)$. We write

$$\frac{N^2}{4}\left(c_{S+2}+c_{S-2}\right)\approx\Delta c(s)+\frac{N^2}{2}c(s). \tag{B.4}$$

By substituting in (B.4) and neglecting a term $\propto(qx^2/N)\Delta c$, we arrive at (5).

This derivation is valid as long as the relevant states are well localized around $x=0$. This is always the case in the ground state, which has a width at most $\sim1/\sqrt{N}$ for $q\gg U_s$. For the thermal states, the width is $\sim\sqrt{k_BT/[N(2U_s+q)]}$, which gives the condition $k_BT\ll N(U_s+q)$. Finally, the cross-term $\propto(qx^2/N)\Delta c$ is of the order $2E_pE_c c/[N(2U_s+q)]$ in terms of the kinetic and potential energies E_c, E_p of the harmonic oscillator. In the thermal regime, a typical order of magnitude for this term is thus $(k_BT)^2/[N(2U_s+q)]$, small compared to the energy k_BT typical for the other terms we kept in the equation provided the condition above is fulfilled.

References

[1] Pitaevskii L and Stringari S 2003 *Bose Einstein Condensation* (Oxford: Oxford University Press)
[2] Castin Y and Herzog C 2001 *C. R. Acad. Sci. Paris* **2** 419–43
[3] Mueller E J, Ho T L, Ueda M and Baym G 2006 *Phys. Rev.* A **74** 033612
[4] Nozières P and Saint James D 1982 *J. Phys. France* **42** 1133–48
[5] Law C K, Pu H and Bigelow N P 1998 *Phys. Rev. Lett.* **81** 5257
[6] Ho T L and Yip S K 2000 *Phys. Rev. Lett.* **84** 4031
[7] Kuklov A B and Svistunov B V 2002 *Phys. Rev. Lett.* **89** 170403
[8] Ashhab S and Leggett A J 2003 *Phys. Rev.* A **68** 063612
[9] Zhou F 2001 *Phys. Rev. Lett.* **87** 080401
[10] Cui X, Wang Y and Zhou F 2008 *Phys. Rev.* A **78** 050701
[11] Barnett R, Sau J D and Das Sarma S 2010 *Phys. Rev.* A **82** 031602
[12] Barnett R, Hui H Y, Lin C H, Sau J D and Das Sarma S 2011 *Phys. Rev.* A **83** 023613
[13] Lamacraft A 2011 *Phys. Rev.* A **83** 033605
[14] Tasaki H 2013 *Phys. Rev. Lett.* **110** 230402
[15] Foot C 2005 *Atomic Physics* (Oxford: Oxford University Press)
[16] Ho T L 1998 *Phys. Rev. Lett.* **81** 742

[17] Ohmi T and Machida T 1998 *J. Phys. Soc. Japan* **67** 1822
[18] Leib E and Matthis D 1962 *J. Math. Phys.* **3** 749
[19] Kaiser C and Peschel I 1989 *J. Phys. A: Math. Gen.* **22** 4257
[20] Kaplan T A, von der Linden W and Horsch P 1990 *Phys. Rev.* B **42** 4663–9
[21] Bernu B, Lhuillier C and Pierre L 1992 *Phys. Rev. Lett.* **69** 2590–3
[22] Azaria P, Delamotte B and Mouhanna D 1993 *Phys. Rev. Lett.* **70** 2483–6
[23] van Wezel J, van den Brink J and Zaanen J 2005 *Phys. Rev. Lett.* **94** 230401
[24] van Wezel J, Zaanen J and van den Brink J 2006 *Phys. Rev.* B **74** 094430
[25] Black A T, Gomez E, Turner L D, Jung S and Lett P D 2007 *Phys. Rev. Lett.* **99** 070403
[26] Jacob D, Shao L, Corre V, Zibold T, De Sarlo L, Mimoun E, Dalibard J and Gerbier F 2012 *Phys. Rev.* A **86** 061601
[27] Yi S, Müstecaplıoğlu Ö E, Sun C P and You L 2002 *Phys. Rev.* A **66** 011601
[28] Stamper-Kurn D M and Ueda M 2013 *Rev. Mod. Phys.* **85** 1191–244
[29] Hooley C and Quintanilla J 2004 *Phys. Rev. Lett.* **93** 080404
[30] Ott H, de Mirandes E, Ferlaino F, Roati G, Türck V, Modugno G and Inguscio M 2004 *Phys. Rev. Lett.* **93** 120407
[31] Anderson P W 1952 *Phys. Rev.* **86** 694–701
[32] Pu H, Law C K, Raghavan S, Eberly J H and Bigelow N P 1999 *Phys. Rev.* A **60** 1463–70
[33] Polkovnikov A, Sengupta K, Silva A and Vengalattore M 2011 *Rev. Mod. Phys.* **83** 863–83

Bibliography

[1] S. N. Bose. Plancks Gesetz und Lichtquantenhypothese (Plancks Law and Light Quantum Hypothesis). *Z. Phys.*, 26:178, 1924. 7, 11, 13

[2] A. Einstein. Quantentheorie des einatomigen idealen Gases. *Sitzungsber. Kgl. Preuss. Akad. Wiss.*, 7, 13:261(1924), 3(1925), 1924. 7, 11, 13

[3] L. Pitaevskii and S. Stringari. *Bose-Einstein Condensation*. Oxford University Press, Oxford, 2003. 7, 8, 11, 13, 14, 15, 16, 17, 105

[4] Steven Chu. Nobel Lecture: The manipulation of neutral particles. *Rev. Mod. Phys.*, 70:685–706, Jul 1998. 7, 35

[5] Claude N. Cohen-Tannoudji. Nobel Lecture: Manipulating atoms with photons. *Rev. Mod. Phys.*, 70:707–719, Jul 1998. 7, 35, 111

[6] William D. Phillips. Nobel Lecture: Laser cooling and trapping of neutral atoms. *Rev. Mod. Phys.*, 70:721–741, Jul 1998. 7, 35

[7] M. H. Anderson, J. R. Ensher, M. R. Matthews, C. E. Wieman, and E. A. Cornell. Observation of Bose-Einstein Condensation in a Dilute Atomic Vapor. *Science*, 269(5221):198–201, 1995. 7, 11

[8] K. B. Davis, M. O. Mewes, M. R. Andrews, N. J. van Druten, D. S. Durfee, D. M. Kurn, and W. Ketterle. Bose-Einstein Condensation in a Gas of Sodium Atoms. *Phys. Rev. Lett.*, 75:3969–3973, Nov 1995. 7, 11

[9] E. A. Cornell and C. E. Wieman. Nobel Lecture: Bose-Einstein condensation in a dilute gas, the first 70 years and some recent experiments. *Rev. Mod. Phys.*, 74:875–893, Aug 2002. 7, 35

[10] Wolfgang Ketterle. Nobel lecture: When atoms behave as waves: Bose-Einstein condensation and the atom laser. *Rev. Mod. Phys.*, 74:1131–1151, Nov 2002. 7, 35

[11] Immanuel Bloch, Jean Dalibard, and Wilhelm Zwerger. Many-body physics with ultracold gases. *Rev. Mod. Phys.*, 80:885–964, Jul 2008. 7

[12] Franco Dalfovo, Stefano Giorgini, Lev P. Pitaevskii, and Sandro Stringari. Theory of Bose-Einstein condensation in trapped gases. *Rev. Mod. Phys.*, 71:463–512, Apr 1999. 7, 12, 14, 15, 16, 99

[13] Ph. Courteille, R. S. Freeland, D. J. Heinzen, F. A. van Abeelen, and B. J. Verhaar. Observation of a Feshbach Resonance in Cold Atom Scattering. *Phys. Rev. Lett.*, 81:69–72, Jul 1998. 7

[14] S. Inouye, M. R. Andrews, J. Stenger, H.-J. Miesner, D. M. Stamper-Kurn, and W. Ketterle. Observation of Feshbach resonances in a Bose-Einstein condensate. *Nature*, 392:151–154, 03/12 1998. 7

[15] Cheng Chin, Rudolf Grimm, Paul Julienne, and Eite Tiesinga. Feshbach resonances in ultracold gases. *Rev. Mod. Phys.*, 82:1225–1286, Apr 2010. 7

[16] S. L. Cornish, N. R. Claussen, J. L. Roberts, E. A. Cornell, and C. E. Wieman. Stable ^{8}5Rb Bose-Einstein Condensates with Widely Tunable Interactions. *Phys. Rev. Lett.*, 85:1795–1798, Aug 2000. 7

[17] Markus Greiner, Olaf Mandel, Tilman Esslinger, Theodor W. Hansch, and Immanuel Bloch. Quantum phase transition from a superfluid to a Mott insulator in a gas of ultracold atoms. *Nature*, 415:39–44, 01/03 2002. 7

[18] C. C. Bradley, C. A. Sackett, J. J. Tollett, and R. G. Hulet. Evidence of Bose-Einstein Condensation in an Atomic Gas with Attractive Interactions. *Phys. Rev. Lett.*, 75:1687–1690, Aug 1995. 7, 11

[19] Dale G. Fried, Thomas C. Killian, Lorenz Willmann, David Landhuis, Stephen C. Moss, Daniel Kleppner, and Thomas J. Greytak. Bose-Einstein Condensation of Atomic Hydrogen. *Phys. Rev. Lett.*, 81:3811–3814, Nov 1998. 7

[20] F. Pereira Dos Santos, J. Léonard, Junmin Wang, C. J. Barrelet, F. Perales, E. Rasel, C. S. Unnikrishnan, M. Leduc, and C. Cohen-Tannoudji. Bose-Einstein Condensation of Metastable Helium. *Phys. Rev. Lett.*, 86:3459–3462, Apr 2001. 7

[21] G. Modugno, G. Ferrari, G. Roati, R. J. Brecha, A. Simoni, and M. Inguscio. Bose-Einstein Condensation of Potassium Atoms by Sympathetic Cooling. *Science*, 294(5545):1320–1322, 2001. 7

[22] Tino Weber, Jens Herbig, Michael Mark, Hanns-Christoph Ngerl, and Rudolf Grimm. Bose-Einstein Condensation of Cesium. *Science*, 299(5604):232–235, 2003. 7, 36

[23] Y. Takasu, K. Maki, K. Komori, T. Takano, K. Honda, M. Kumakura, T. Yabuzaki, and Y. Takahashi. Bose-Einstein Condensation of Yb atoms. *AIP Conference Proceedings*, 770(1):254–262, 2005. 7

[24] Stefano Giorgini, Lev P. Pitaevskii, and Sandro Stringari. Theory of ultracold atomic Fermi gases. *Rev. Mod. Phys.*, 80:1215–1274, Oct 2008. 7

[25] S. Jochim, M. Bartenstein, A. Altmeyer, G. Hendl, S. Riedl, C. Chin, J. Hecker Denschlag, and R. Grimm. Bose-Einstein Condensation of Molecules. *Science*, 302(5653):2101–2103, 2003. 7

[26] Dan M. Stamper-Kurn and Masahito Ueda. Spinor Bose gases: Symmetries, magnetism, and quantum dynamics. *Rev. Mod. Phys.*, 85:1191–1244, Jul 2013. 7, 11, 21, 22, 65, 66, 68, 70, 130

[27] D. S. Hall, M. R. Matthews, J. R. Ensher, C. E. Wieman, and E. A. Cornell. Dynamics of Component Separation in a Binary Mixture of Bose-Einstein Condensates. *Phys. Rev. Lett.*, 81:4531–4531, Nov 1998. 7

[28] J. Stenger, S. Inouye, D. M. Stamper-Kurn, H.-J. Miesner, A. P. Chikkatur, and W. Ketterle. Spin domains in ground-state Bose-Einstein condensates. *Nature*, 396(6709):345–348, 11/26 1998. 7, 8, 11, 66, 70

[29] Tin-Lun Ho. Spinor Bose Condensates in Optical Traps. *Phys. Rev. Lett.*, 81:742–745, Jul 1998. 7, 21, 22, 24, 26, 65, 70, 84, 92

[30] Tetsuo Ohmi and Kazushige Machida. Bose-Einstein Condensation with Internal Degrees of Freedom in Alkali Atom Gases. *J. Phys. Soc. Jpn.*, 67:1822–1825, 1998. 7, 21, 22, 24, 65, 70, 84

[31] M.-S. Chang, C. D. Hamley, M. D. Barrett, J. A. Sauer, K. M. Fortier, W. Zhang, L. You, and M. S. Chapman. Observation of Spinor Dynamics in Optically Trapped ^{87}Rb Bose-Einstein Condensates. *Phys. Rev. Lett.*, 92:140403, Apr 2004. 8, 65, 66

[32] Kerson Huang. *Introduction to Statistical Physics, 2nd ed.* Taylor & Francis, 2010. 11

[33] W. Ketterle, D. S. Durfee, and D. M. Stamper-Kurn. Making, probing and understanding Bose-Einstein condensates. *eprint arXiv:cond-mat/9904034*, April 1999. 11, 14, 16, 35, 37, 38, 49, 55, 56, 99, 111, 117

[34] Anthony J. Leggett. Bose-Einstein condensation in the alkali gases: Some fundamental concepts. *Rev. Mod. Phys.*, 73:307–356, Apr 2001. 11, 14

[35] Daniel A. Steck. Sodium D Line Data. *Alkali D Line Data*, 2003. 11, 19, 20, 23, 119

[36] S. Giorgini, L.P. Pitaevskii, and S. Stringari. Thermodynamics of a trapped Bose-condensed gas. *Journal of Low Temperature Physics*, 109(1-2):309–355, 1997. 11, 17

[37] M. Naraschewski and D. M. Stamper-Kurn. Analytical description of a trapped semi-ideal Bose gas at finite temperature. *Phys. Rev. A*, 58:2423–2426, Sep 1998. 11, 18

[38] David Jacob, Lingxuan Shao, Vincent Corre, Tilman Zibold, Luigi De Sarlo, Emmanuel Mimoun, Jean Dalibard, and Fabrice Gerbier. Phase diagram of spin-1 antiferromagnetic Bose-Einstein condensates. *Phys. Rev. A*, 86:061601, Dec 2012. 12, 33, 47, 65, 81, 127

[39] Erich J. Mueller, Tin-Lun Ho, Masahito Ueda, and Gordon Baym. Fragmentation of Bose-Einstein condensates. *Phys. Rev. A*, 74:033612, Sep 2006. 14, 76, 84, 86

[40] John Weiner, Vanderlei S. Bagnato, Sergio Zilio, and Paul S. Julienne. Experiments and theory in cold and ultracold collisions. *Rev. Mod. Phys.*, 71:1–85, Jan 1999. 15, 122

[41] C. J. Pethick and H. Smith. *Bose-Einstein Condensation in Dilute Gases*. Cambridge University Press, 2001. 17, 23

[42] S. Knoop, T. Schuster, R. Scelle, A. Trautmann, J. Appmeier, M. K. Oberthaler, E. Tiesinga, and E. Tiemann. Feshbach spectroscopy and analysis of the interaction potentials of ultracold sodium. *Phys. Rev. A*, 83:042704, Apr 2011. 19, 22, 71, 129, 130

[43] David Jacob. *Condensats de Bose-Einstein de spin 1 : étude expérimentale avec des atomes de sodium dans un piège optique*. PhD thesis, Universit Pierre et Marie Curie - Paris VI (25/05/2012), Jean Dalibard (Dir.), 2012. oai:tel.archives-ouvertes.fr:tel-00730750. 20, 33, 35, 36, 52, 117, 120, 124

[44] Emmanuel Mimoun. *Condensat de Bose-Einstein de sodium dans un piège mésoscopique*. PhD thesis, Universit Pierre et Marie Curie - Paris VI (28/09/2010), Jean Dalibard (Dir.), 2010. oai:tel.archives-ouvertes.fr:tel-00527457. 22, 35, 111, 113, 114

[45] G. Breit and I. I. Rabi. Measurement of Nuclear Spin. *Phys. Rev.*, 38:2082–2083, Dec 1931. 23

[46] C. K. Law, H. Pu, and N. P. Bigelow. Quantum Spins Mixing in Spinor Bose-Einstein Condensates. *Phys. Rev. Lett.*, 81:5257–5261, Dec 1998. 24, 68, 76, 79, 84

[47] S. Yi, Ö. E. Müstecaplıoğlu, C. P. Sun, and L. You. Single-mode approximation in a spinor-1 atomic condensate. *Phys. Rev. A*, 66:011601, Jul 2002. 24, 68, 130

[48] Wenxian Zhang, Su Yi, and L. You. Bose-Einstein condensation of trapped interacting spin-1 atoms. *Phys. Rev. A*, 70:043611, Oct 2004. 27, 72

[49] D Jacob, E Mimoun, L De Sarlo, M Weitz, J Dalibard, and F Gerbier. Production of sodium BoseEinstein condensates in an optical dimple trap. *New Journal of Physics*, 13(6):065022, 2011. 33, 67, 117, 119, 122, 124, 125, 127, 128

[50] E. L. Raab, M. Prentiss, Alex Cable, Steven Chu, and D. E. Pritchard. Trapping of Neutral Sodium Atoms with Radiation Pressure. *Phys. Rev. Lett.*, 59:2631–2634, Dec 1987. 35

[51] Wolfgang Ketterle and N.J. Van Druten. Evaporative Cooling of Trapped Atoms. In Benjamin Bederson and Herbert Walther, editors, *Advances In Atomic, Molecular, and Optical Physics*, volume 37 of *Advances In Atomic, Molecular, and Optical Physics*, pages 181 – 236. Academic Press, 1996. 35, 38

[52] Emmanuel Mimoun, Luigi De Sarlo, David Jacob, Jean Dalibard, and Fabrice Gerbier. Fast production of ultracold sodium gases using light-induced desorption and optical trapping. *Phys. Rev. A*, 81:023631, Feb 2010. 36, 67, 111, 115, 116

[53] A. Keshet and W. Ketterle. A distributed, graphical user interface based, computer control system for atomic physics experiments. *Review of Scientific Instruments*, 84(1):015105, January 2013. 36

[54] M. D. Barrett, J. A. Sauer, and M. S. Chapman. All-Optical Formation of an Atomic Bose-Einstein Condensate. *Phys. Rev. Lett.*, 87:010404, Jun 2001. 36

[55] S. R. Granade, M. E. Gehm, K. M. O'Hara, and J. E. Thomas. All-Optical Production of a Degenerate Fermi Gas. *Phys. Rev. Lett.*, 88:120405, Mar 2002. 36

[56] Jean Dalibard. *Atomes ultra-froids (notes de cours rédigées par Jean Dalibard)*. 38

[57] T. A. Savard, K. M. O'Hara, and J. E. Thomas. Laser-noise-induced heating in far-off resonance optical traps. *Phys. Rev. A*, 56:R1095–R1098, Aug 1997. 39, 40

[58] Giovanni Cennini, Gunnar Ritt, Carsten Geckeler, and Martin Weitz. All-Optical Realization of an Atom Laser. *Phys. Rev. Lett.*, 91:240408, Dec 2003. 43, 45

[59] A. Couvert, M. Jeppesen, T. Kawalec, G. Reinaudi, R. Mathevet, and D. Guéry-Odelin. A quasi-monomode guided atom laser from an all-optical Bose-Einstein condensate. *EPL (Europhysics Letters)*, 83(5):50001, 2008. 43, 45, 67, 127, 130

[60] Y. Castin and R. Dum. Bose-Einstein Condensates in Time Dependent Traps. *Phys. Rev. Lett.*, 77:5315–5319, Dec 1996. 48, 56

[61] G. Reinaudi, T. Lahaye, Z. Wang, and D. Guéry-Odelin. Strong saturation absorption imaging of dense clouds of ultracold atoms. *Opt. Lett.*, 32(21):3143–3145, Nov 2007. 51

[62] Eugene Hecht. *Optics (Fourth edition)*. Addison-Wesley, 2002. 52

[63] L. Sirovich and M. Kirby. Low-dimensional procedure for the characterization of human faces. *J. Opt. Soc. Am. A*, 4(3):519–524, Mar 1987. 55

[64] P.N. Belhumeur, J.P. Hespanha, and D. Kriegman. Eigenfaces vs. Fisherfaces: recognition using class specific linear projection. *IEEE Trans. Pattern Anal. Mach. Intell.*, 19(7):711720, 1997. 55

[65] Leonard Mandel and Emil Wolf. *Optical Coherence and Quantum Optics*. Cambridge University Press, 1995. 58

[66] Sylvie Méléard. *Aléatoire*. Éditions de l'École Polytechnique, 2010. 58, 59

[67] C. F. Ockeloen, A. F. Tauschinsky, R. J. C. Spreeuw, and S. Whitlock. Detection of small atom numbers through image processing. *Phys. Rev. A*, 82:061606, Dec 2010. 61

[68] Xiaolin Li, Min Ke, Bo Yan, and Yuzhu Wang. Reduction of interference fringes in absorption imaging of cold atom cloud using eigenface method. *Chin. Opt. Lett.*, 5(3):128–130, Mar 2007. 61

[69] Yuki Kawaguchi and Masahito Ueda. Spinor Bose-Einstein condensates. *Physics Reports*, 520(5):253 – 381, 2012. 65, 70

[70] H. Schmaljohann, M. Erhard, J. Kronjäger, M. Kottke, S. van Staa, L. Cacciapuoti, J. J. Arlt, K. Bongs, and K. Sengstock. Dynamics of $F = 2$ Spinor Bose-Einstein Condensates. *Phys. Rev. Lett.*, 92:040402, Jan 2004. 65

[71] T. Kuwamoto, K. Araki, T. Eno, and T. Hirano. Magnetic field dependence of the dynamics of ^{87}Rb spin-2 Bose-Einstein condensates. *Phys. Rev. A*, 69:063604, Jun 2004. 65

[72] B. Pasquiou, E. Maréchal, L. Vernac, O. Gorceix, and B. Laburthe-Tolra. Thermodynamics of a Bose-Einstein Condensate with Free Magnetization. *Phys. Rev. Lett.*, 108:045307, Jan 2012. 65, 66, 68, 72

[73] Shintaro Taie, Yosuke Takasu, Seiji Sugawa, Rekishu Yamazaki, Takuya Tsujimoto, Ryo Murakami, and Yoshiro Takahashi. Realization of a SU(2) $\times$ SU(6) System of Fermions in a Cold Atomic Gas. *Phys. Rev. Lett.*, 105:190401, Nov 2010. 65

[74] Jasper S. Krauser, Jannes Heinze, Nick Flaschner, Soren Gotze, Ole Jurgensen, Dirk-Soren Luhmann, Christoph Becker, and Klaus Sengstock. Coherent multi-flavour spin dynamics in a fermionic quantum gas. *Nat Phys*, 8(11):813–818, 11 2012. 65

[75] Ming-Shien Chang, Qishu Qin, Wenxian Zhang, Li You, and Michael S. Chapman. Coherent spinor dynamics in a spin-1 Bose condensate. *Nat Phys*, 1(2):111–116, 11 2005. 65

[76] J. Kronjäger, C. Becker, M. Brinkmann, R. Walser, P. Navez, K. Bongs, and K. Sengstock. Evolution of a spinor condensate: Coherent dynamics, dephasing, and revivals. *Phys. Rev. A*, 72:063619, Dec 2005. 65

[77] A. T. Black, E. Gomez, L. D. Turner, S. Jung, and P. D. Lett. Spinor Dynamics in an Antiferromagnetic Spin-1 Condensate. *Phys. Rev. Lett.*, 99:070403, Aug 2007. 65, 105

[78] Y. Liu, S. Jung, S. E. Maxwell, L. D. Turner, E. Tiesinga, and P. D. Lett. Quantum Phase Transitions and Continuous Observation of Spinor Dynamics in an Antiferromagnetic Condensate. *Phys. Rev. Lett.*, 102:125301, Mar 2009. 65, 66, 71

[79] B. Lücke, M. Scherer, J. Kruse, L. Pezzé, F. Deuretzbacher, P. Hyllus, O. Topic, J. Peise, W. Ertmer, J. Arlt, L. Santos, A. Smerzi, and C. Klempt. Twin Matter Waves for Interferometry Beyond the Classical Limit. *Science*, 334(6057):773–776, 2011. 65

[80] C. Gross, H. Strobel, E. Nicklas, T. Zibold, N. Bar-Gill, G. Kurizki, and M. K. Oberthaler. Atomic homodyne detection of continuous-variable entangled twin-atom states. *Nature*, 480(7376):219–223, 12/08 2011. 65

[81] C. D. Hamley, C. S. Gerving, T. M. Hoang, E. M. Bookjans, and M. S. Chapman. Spin-nematic squeezed vacuum in a quantum gas. *Nat Phys*, 8(4):305–308, 04 2012. 65

[82] L. E. Sadler, J. M. Higbie, S. R. Leslie, M. Vengalattore, and D. M. Stamper-Kurn. Spontaneous symmetry breaking in a quenched ferromagnetic spinor Bose-Einstein condensate. *Nature*, 443(7109):312–315, 09/21 2006. 65

[83] E. M. Bookjans, A. Vinit, and C. Raman. Quantum Phase Transition in an Antiferromagnetic Spinor Bose-Einstein Condensate. *Phys. Rev. Lett.*, 107:195306, Nov 2011. 65

[84] J. Guzman, G.-B. Jo, A. N. Wenz, K. W. Murch, C. K. Thomas, and D. M. Stamper-Kurn. Long-time-scale dynamics of spin textures in a degenerate $F = 1$ ^{87}Rb spinor Bose gas. *Phys. Rev. A*, 84:063625, Dec 2011. 66

[85] A. Couvert, M. Jeppesen, T. Kawalec, G. Reinaudi, R. Mathevet, and D. Gury-Odelin. Erratum: A quasi-monomode guided atom laser from an all-optical Bose-Einstein condensate. *EPL (Europhysics Letters)*, 85(1):19901, 2009. 67, 127, 130

[86] Wenxian Zhang, Su Yi, and Li You. Mean field ground state of a spin-1 condensate in a magnetic field. *New Journal of Physics*, 5(1):77, 2003. 70

[87] F. Zhou, M. Snoek, J. Wiemer, and I. Affleck. Magnetically stabilized nematic order: Three-dimensional bipartite optical lattices. *Phys. Rev. B*, 70:184434, Nov 2004. 71

[88] Nguyen Thanh Phuc, Yuki Kawaguchi, and Masahito Ueda. Effects of thermal and quantum fluctuations on the phase diagram of a spin-1 ^{87}Rb Bose-Einstein condensate. *Phys. Rev. A*, 84:043645, Oct 2011. 72

[89] Yvan Castin and Christopher Herzog. BoseEinstein condensates in symmetry breaking states. *Comptes Rendus de l'Acadmie des Sciences - Series {IV} - Physics*, 2(3):419 – 443, 2001. 76, 79, 84, 86

[90] P. Nozières and D. Saint James. Particle vs. pair condensation in attractive Bose liquids. *J. Phys. France*, 43(7)(7):1133 – 1148, july 1982. 76

[91] Tin-Lun Ho and Sung Kit Yip. Fragmented and Single Condensate Ground States of Spin-1 Bose Gas. *Phys. Rev. Lett.*, 84:4031–4034, May 2000. 76, 79, 84

[92] Fei Zhou. Spin Correlation and Discrete Symmetry in Spinor Bose-Einstein Condensates. *Phys. Rev. Lett.*, 87:080401, Aug 2001. 76

[93] Xiaoling Cui, Yupeng Wang, and Fei Zhou. Quantum-fluctuation-driven coherent spin dynamics in small condensates. *Phys. Rev. A*, 78:050701, Nov 2008. 76, 77

[94] Ryan Barnett, Jay D. Sau, and S. Das Sarma. Antiferromagnetic spinor condensates are quantum rotors. *Phys. Rev. A*, 82:031602, Sep 2010. 76, 77

[95] Ryan Barnett, Hoi-Yin Hui, Chien-Hung Lin, Jay D. Sau, and S. Das Sarma. Quantum rotor theory of spinor condensates in tight traps. *Phys. Rev. A*, 83:023613, Feb 2011. 76, 77, 84, 86

[96] Austen Lamacraft. Spin-1 microcondensate in a magnetic field. *Phys. Rev. A*, 83:033605, Mar 2011. 76, 77

[97] Hal Tasaki. Polar and Antiferromagnetic Order in $f = 1$ Boson Systems. *Phys. Rev. Lett.*, 110:230402, Jun 2013. 76

[98] Luigi De Sarlo, Lingxuan Shao, Vincent Corre, Tilman Zibold, David Jacob, Jean Dalibard, and Fabrice Gerbier. Spin fragmentation of BoseEinstein condensates with antiferromagnetic interactions. *New Journal of Physics*, 15(11):113039, 2013. 82, 83, 84

[99] William H. Press, Brian P. Flannery, Saul A. Teukolsky, and William T. Vetterling. *Numerical Recipes*. Cambridge University Press, 1986. 98

[100] M. Gring, M. Kuhnert, T. Langen, T. Kitagawa, B. Rauer, M. Schreitl, I. Mazets, D. Adu Smith, E. Demler, and J. Schmiedmayer. Relaxation and Prethermalization in an Isolated Quantum System. *Science*, 337(6100):1318–1322, 2012. 105

[101] Anatoli Polkovnikov, Krishnendu Sengupta, Alessandro Silva, and Mukund Vengalattore. *Colloquium*: Nonequilibrium dynamics of closed interacting quantum systems. *Rev. Mod. Phys.*, 83:863–883, Aug 2011. 105

[102] A. Micheli, D. Jaksch, J. I. Cirac, and P. Zoller. Many-particle entanglement in two-component Bose-Einstein condensates. *Phys. Rev. A*, 67:013607, Jan 2003. 109

[103] J. A. Dunningham, K. Burnett, and Stephen M. Barnett. Interferometry below the Standard Quantum Limit with Bose-Einstein Condensates. *Phys. Rev. Lett.*, 89:150401, Sep 2002. 109

[104] Emmanuel Mimoun, Luigi De Sarlo, Jean-Jacques Zondy, Jean Dalibard, and Fabrice Gerbier. Sum-frequency generation of 589 nmlight with near-unit efficiency. *Opt. Express*, 16(23):18684–18691, Nov 2008. 111, 113, 114

[105] E. Mimoun, L. Sarlo, J.-J. Zondy, J. Dalibard, and F. Gerbier. Solid-state laser system for laser cooling of sodium. *Applied Physics B*, 99(1-2):31–40, 2010. 111, 113, 114

[106] William D. Phillips and Harold Metcalf. Laser Deceleration of an Atomic Beam. *Phys. Rev. Lett.*, 48:596–599, Mar 1982. 115

[107] Thad Walker, David Sesko, and Carl Wieman. Collective behavior of optically trapped neutral atoms. *Phys. Rev. Lett.*, 64:408–411, Jan 1990. 117, 122

[108] C. G. Townsend, N. H. Edwards, C. J. Cooper, K. P. Zetie, C. J. Foot, A. M. Steane, P. Szriftgiser, H. Perrin, and J. Dalibard. Phase-space density in the magneto-optical trap. *Phys. Rev. A*, 52:1423–1440, Aug 1995. 117, 122

[109] R. Grimm, M. Weidemüller, and Y. B. Ovchinnikov. Optical Dipole Traps for Neutral Atoms. *Advances in Atomic Molecular and Optical Physics*, 42:95–170, 2000. 117, 118

[110] S. J. M. Kuppens, K. L. Corwin, K. W. Miller, T. E. Chupp, and C. E. Wieman. Loading an optical dipole trap. *Phys. Rev. A*, 62:013406, Jun 2000. 122

[111] Wolfgang Ketterle, Kendall B. Davis, Michael A. Joffe, Alex Martin, and David E. Pritchard. High densities of cold atoms in a *dark* spontaneous-force optical trap. *Phys. Rev. Lett.*, 70:2253–2256, Apr 1993. 122

[112] A. Görlitz, T. L. Gustavson, A. E. Leanhardt, R. Löw, A. P. Chikkatur, S. Gupta, S. Inouye, D. E. Pritchard, and W. Ketterle. Sodium Bose-Einstein Condensates in the F=2 State in a Large-Volume Optical Trap. *Phys. Rev. Lett.*, 90:090401, Mar 2003. 130